



**THÈSE DE DOCTORAT**  
**DE L'UNIVERSITÉ PSL**

Préparée à Chimie ParisTech

**Développements méthodologiques pour la simulation de  
l'adsorption des gaz simples dans les matériaux  
nanoporeux**

Methodology developments for the simulation of simple gas adsorption in nanoporous materials

Soutenue par  
**Lionel ZOUBRITZKY**

Le 15/10/2024

École doctorale n°388  
**Chimie Physique et  
Chimie Analytique de  
Paris Centre**

Spécialité  
**Chimie Physique**

**Composition du jury :**

Emeric BOURASSEAU  
CEA Cadarache

*Rapporteur*

François-Xavier COUDERT  
CNRS, Chimie ParisTech – PSL

*Directeur de thèse*

Tina DÜREN  
University of Bath

*Rapporteuse*

Caroline MELLOT-DRAZNIEKS  
CNRS, Collège de France

Pluton PULLUMBI  
Air Liquide



| PSL

ParisTech





---

# TABLE OF CONTENTS

---

Notations and abbreviations . . . . .	1
<b>Introduction</b>	<b>3</b>
<b>1 Topology of crystalline materials</b>	<b>7</b>
1.1 Notion of topology . . . . .	8
1.1.1 Definition . . . . .	8
1.1.2 Existing resources . . . . .	8
1.2 Algorithms and implementation . . . . .	11
1.2.1 From the chemical structure to the net. . . . .	11
1.2.2 Periodic graph structure . . . . .	14
1.2.3 Equilibrium placement . . . . .	17
1.2.4 Minimization of the graph. . . . .	19
1.2.5 Search space exploration . . . . .	21
1.3 Reduction of the search space . . . . .	25
1.3.1 The initial search space . . . . .	25
1.3.2 Categorization of vertices and edges . . . . .	26
1.3.3 Reduction through symmetry . . . . .	28
1.3.4 Ordering of keys . . . . .	28
1.4 Application to materials databases . . . . .	29
1.4.1 RCSR, EPINET and IZA-SC database . . . . .	30
1.4.2 MOF structures . . . . .	32
1.4.3 Database of aluminophosphates . . . . .	39
1.4.4 Hypothetical zeolites . . . . .	40
1.5 Web interface . . . . .	41
1.6 Summary and perspectives . . . . .	44
<b>2 Cation placement in zeolites</b>	<b>47</b>
2.1 Cationic zeolites . . . . .	48
2.1.1 Structure and properties . . . . .	48
2.1.2 Aluminium placement . . . . .	50
2.1.3 Cations . . . . .	54
2.2 Methodology for the prediction of cation placement . . . . .	54
2.2.1 Underlying algorithms . . . . .	56
2.2.2 Meta-algorithms . . . . .	62
2.2.3 Extraction of sites and population from simulation . . . . .	66
2.3 Results . . . . .	68
2.3.1 Case study: FAU . . . . .	68
2.3.2 Other zeolites . . . . .	75

2.4	Energy computation . . . . .	79
2.4.1	Force fields. . . . .	79
2.4.2	Short-term interactions . . . . .	80
2.4.3	Ewald summation . . . . .	81
2.4.4	Precomputation . . . . .	83
2.5	Possible alternatives . . . . .	87
<b>3</b>	<b>Molecular simulation of adsorption</b>	<b>91</b>
3.1	Molecular description. . . . .	92
3.1.1	Physisorption and chemisorption . . . . .	92
3.1.2	Adsorption sites in crystalline materials . . . . .	92
3.1.3	Small gases in zeolites . . . . .	93
3.2	Grand Canonical Monte Carlo . . . . .	94
3.2.1	Principle. . . . .	94
3.2.2	Implementation . . . . .	95
3.2.3	Computational aspects . . . . .	97
3.3	GCMC on a grid . . . . .	99
3.3.1	Principle. . . . .	99
3.3.2	Validation . . . . .	102
3.3.3	Computational aspects . . . . .	103
<b>4</b>	<b>Database approach</b>	<b>109</b>
4.1	Screening studies . . . . .	110
4.2	Adsorption isotherm . . . . .	110
4.2.1	Definition and classification . . . . .	110
4.2.2	Experimental observation and numerical prediction . . . . .	112
4.3	Database constitution. . . . .	112
4.3.1	Aluminium placement . . . . .	113
4.3.2	Cation placement . . . . .	113
4.4	Prediction . . . . .	114
4.4.1	Why isotherms?. . . . .	114
4.4.2	Adsorption models. . . . .	115
4.4.3	Isotherm fitting . . . . .	118
4.4.4	Fitting result . . . . .	119
4.4.5	Simple meta-models . . . . .	122
4.5	Perspectives . . . . .	123
<b>Conclusion and perspectives</b>		<b>127</b>
<hr/>		
<b>List of Publications</b>		<b>131</b>
Peer-reviewed articles. . . . .		131
Open-source software and libraries . . . . .		131
<b>Bibliography</b>		<b>133</b>

## NOTATIONS AND ABBREVIATIONS

***r*** triplet of coordinates in real space.

***k*** triplet of coordinates in Fourier space.

***p*** configuration of a system.

$\|\mathbf{x}\|$  Euclidean norm of vector  $\mathbf{x}$ .

$\|\mathbf{x}\|_p$  periodic distance, *i.e.* the smallest Euclidean norm of a periodic image of vector  $\mathbf{x}$ .

**pcu** (any three-letter bold lowercase name) topology from the Reticular Chemistry Structure Resource (RCSR).

**FAU** (any three-letter capitalized name) zeolite topology from the International Zeolite Association structure commission (IZA-SC).

MC “Monte Carlo”.

GCMC “grand canonical Monte Carlo”.



---

# INTRODUCTION

---

Gas separation is the action of extracting, from a gas mixture, some of the components from the others. This critical industrial process underlies the purification of all gases, as well as the removal of unwanted species from gas mixtures, for instance toxic or polluting components in exhaust fumes. Direct applications include CO<sub>2</sub> capture, either from industrial sources or directly from air, O<sub>2</sub> purification for medical purposes, H<sub>2</sub> production, which is becoming a major stake for the energy transition, cold generation by liquefying pure N<sub>2</sub> or He, radioactive rare gas capture from nuclear plant emissions, and many others. All of these highlight the relevance of this topic both for the industry in general, but also particularly in the current context of environmental crisis.

Unfortunately, gases are difficult to handle. They are often invisible, many of them odorless, and they naturally escape into any reachable space if not properly sealed at all times. Some, like H<sub>2</sub> are flammable and explosive when in contact with the air. Others, like CO or Cl<sub>2</sub>, are highly toxic. Their containment usually involves storing them at high pressure, with other associated risks. For human life in particular, any perturbation of the local oxygen concentration can be dangerous and even lethal, which makes any gas leakage a threat in closed spaces. In the context of chemistry, their low concentration generally makes them poor reactants under normal conditions, and all the previous properties make their manipulation hazardous and impractical.

Nonetheless, a few techniques have been developed to enable gas separation. One consists in doing cryogenic distillation, in which the mixture is first cooled until it liquefies, then undergoes fractional distillation: since the different constituents have distinct boiling temperatures, each component can be extracted selectively. This process is too costly to be operated industrially, except to handle very large quantities of gas. It is thus mainly used for air separation, to collect N<sub>2</sub>, O<sub>2</sub> and Ar typically.

The other main technique is adsorption. This consists in making the mixture flow through a medium, the adsorbent, that selectively traps some of its components while letting the others flow through, where they are collected. In a second stage of the process, the captured gas is also collected and the adsorbent is regenerated, either by increasing the temperature or by decreasing the pressure compared to the first stage, sometimes both. The precise temperatures and pressures used in this process depend on the adsorbent and the nature of the gases to separate.

Other gas separation techniques exist: membranes technology can be used for dehumidification and H<sub>2</sub> extraction, amine scrubbing for H<sub>2</sub>S and CO<sub>2</sub> separation from flue gas, fractional

condensation is used for heavier gas resulting from pyrolysis vapours. But they are not as much used at large in the industry, more for specific cases only.

Adsorption carries the unique promise of being theoretically able to separate any gas composition, as long as a good adsorbent can be found. Such adsorbents need to have a large exchange surface in order to quantitatively interact with the gas mixture, therefore good candidates are usually porous materials, with pore sizes around the nanometer scale. If the two gases being separated have very different molecular sizes, then the perfect adsorbent is one in which the smaller gas can be trapped while the biggest one cannot enter the pore. But apart from this case, there is a large variety of possible materials to try.

Experimentally testing a candidate framework material requires synthesizing it, characterizing its mechanical and thermal properties to ensure it can survive industrial use, and of course checking its adsorption properties with respect to the target gas mixture. This entire process is very costly and time-consuming, so it cannot be used as a primary mean to explore all possibilities. Ideally, only a select few frameworks should be experimentally tested, resulting from a pre-selection based on non-experimental criterion.

In this context, the numerical simulation of nanoporous materials offers a desirable venue. Running such simulations is considerably faster and cheaper than experiments, which makes it possible to screen through the diversity of possible frameworks, and select only those that yield the best properties in simulation, to check against experimental testing. It can also provide insights on structure-property relations in materials, which can be useful to guide the exploration of this search space.

Even in the realm of simulation however, each individual computational method corresponds to a unique compromise between accuracy and cost. Finding optimal candidates thus requires a multi-scale approach, where a first screening covers as many materials as possible, with a possibly low accuracy, and whose resulting candidates are filtered by a second, smaller but more precise study, and so on, until yielding candidates of appropriate quality. It is thus crucial that simulation methodologies be available to cover this range of requirements.

This thesis focuses on the development of such methodologies for the study of adsorption of small gases in crystalline nanoporous frameworks. Most of my work thus consists in the elaboration and the implementation of new algorithms to solve problems of interest in the field. My aim is to provide ready-to-use tools to tackle these problems, as well as methodological guidelines, for both experimentalists and other theoreticians.

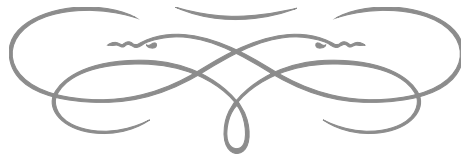
The [first chapter](#) of this manuscript is dedicated to the CrystalNets.jl software I developed, which is a toolbox for the identification of the topology of crystal materials. This notion of “topology”, explained therein, underlies the geometric description of all crystalline frameworks, and should thus correlate with many of their properties. CrystalNets.jl was also adapted into a website, making it easily accessible for non-theoreticians.

The [second chapter](#) covers the problem of placing cations in zeolites. Zeolites are a particular class of crystalline nanoporous materials, already widely used in the industry for adsorption and many other applications. Numerically finding the positions of their extra-framework

cations is a difficult task however, yet it is a necessary step before attempting to predict their adsorption properties. Both existing and new methodologies are discussed, including a new meta-algorithm for accelerating Monte Carlo simulations in sharp potential energy landscapes. This chapter also details a number of useful numerical techniques I used to decrease the computational cost of simulations.

The simulation of the adsorption phenomenon itself is treated in the [third chapter](#). The most commonly used methodology is compared to another Monte Carlo scheme made faster by restricting movements to a grid, and which shows excellent agreement for monoatomic species. Again, a few numerical optimizations are explained.

Finally, the [fourth chapter](#) tackles the issue of very large-scale screening. Using a database approach, it uncovers a few preliminary results on the search for a universal model able to predict adsorption isotherms of small gases in zeolites across topologies, Si / Al ratios, cations and temperature, at minimal computational cost and quantifiable precision.





---

# TOPOLOGY OF CRYSTALLINE MATERIALS

---

---

1.1	Notion of topology . . . . .	8
1.1.1	Definition . . . . .	8
1.1.2	Existing resources . . . . .	8
1.2	Algorithms and implementation . . . . .	11
1.2.1	From the chemical structure to the net . . . . .	11
1.2.2	Periodic graph structure . . . . .	14
1.2.3	Equilibrium placement . . . . .	17
1.2.4	Minimization of the graph . . . . .	19
1.2.5	Search space exploration . . . . .	21
1.3	Reduction of the search space . . . . .	25
1.3.1	The initial search space . . . . .	25
1.3.2	Categorization of vertices and edges . . . . .	26
1.3.3	Reduction through symmetry . . . . .	28
1.3.4	Ordering of keys . . . . .	28
1.4	Application to materials databases . . . . .	29
1.4.1	RCSR, EPINET and IZA-SC database . . . . .	30
1.4.2	MOF structures . . . . .	32
1.4.3	Database of aluminophosphates . . . . .	39
1.4.4	Hypothetical zeolites . . . . .	40
1.5	Web interface . . . . .	41
1.6	Summary and perspectives . . . . .	44

---

This chapter introduces the `CrystalNets.jl` software for crystal topology identification, developed during this PhD. Its content is adapted from [1].

## 1.1 NOTION OF TOPOLOGY

### 1.1.1 Definition

In order to describe the average structure of crystalline materials at the nano-scale, reticular chemistry<sup>2,3</sup> proposes to classify crystals, and in particular framework materials, in light of their topology. This approach consists in abstractly regrouping the atoms of a crystal into clusters, called *vertices*, bonded together by an abstract kind of linkers, called *edges* – the choice of grouping being informed by chemical sense. In simple compounds, such as dense oxides, the mapping can be trivial, with each atom as a separate vertex and each chemical bond as an edge. For zeolites and other aluminosilicates, the tetrahedral atoms T are considered the vertices (T = Al, Si, P, ...) and the T–O–T linkages are the edges. In the case of metal–organic frameworks (MOFs), the vertices would be chosen among the *secondary building units* (SBUs)<sup>4</sup> with more than 2 points of extension, and the edges would correspond to bonds between those, as well as ditopic SBUs, for example. Any crystal can then be simplified into a topological structure, called a *net*, consisting of the sets of vertices and edges (see Figure 1.1).

Like the atomic structure it represents, the net is 3-dimensional and periodic. It contains all the information on the connectivity of the vertices, *i.e.* which pairs of vertices, called *neighbours*, are linked by an edge. Thus, it provides a convenient mathematical abstraction to classify crystal structures. However, it is important to note that this representation is dependent on the choice of vertices and therefore a crystal may be represented by different nets.<sup>11</sup> Moreover, reconstructing the full crystal from the net necessitates additional data, such as the unit cell parameters and the nature and exact geometric placement of the vertices and the edges.<sup>6</sup> A crystal may also be composed of multiple interpenetrating nets,<sup>12</sup> which is common in ultraporous framework materials.

### 1.1.2 Existing resources

Several existing projects, such as the RCSR<sup>8</sup> or Epinet,<sup>13,14</sup> aim at collecting the different nets underlying the structure of real or hypothetical crystals. This is key to allowing researchers to create new materials with a target topology, which is useful to obtain specific physical properties, given the strong link between materials topology and properties for a given chemical composition.<sup>15,16</sup> However, in order to check the accuracy of the collected nets with regard to existing crystals, one needs a way to determine the net from a given crystal structure.

There are currently two different approaches to solve this problem, which correspond to the two main softwares used in the field: ToposPro<sup>17,18</sup> and Systre.<sup>19</sup> ToposPro is a crystallographic tool that allows to retrieve an extensive set of topological properties from crystals. It is a proprietary software, but its topology detection tool can be accessed for free online<sup>20\*</sup> for crystallographic files in CIF format.<sup>21</sup> Its strategy to identify the topology of a net consists in computing three specific properties for each vertex  $u$ :

---

\*available online at <https://topcryst.com/>

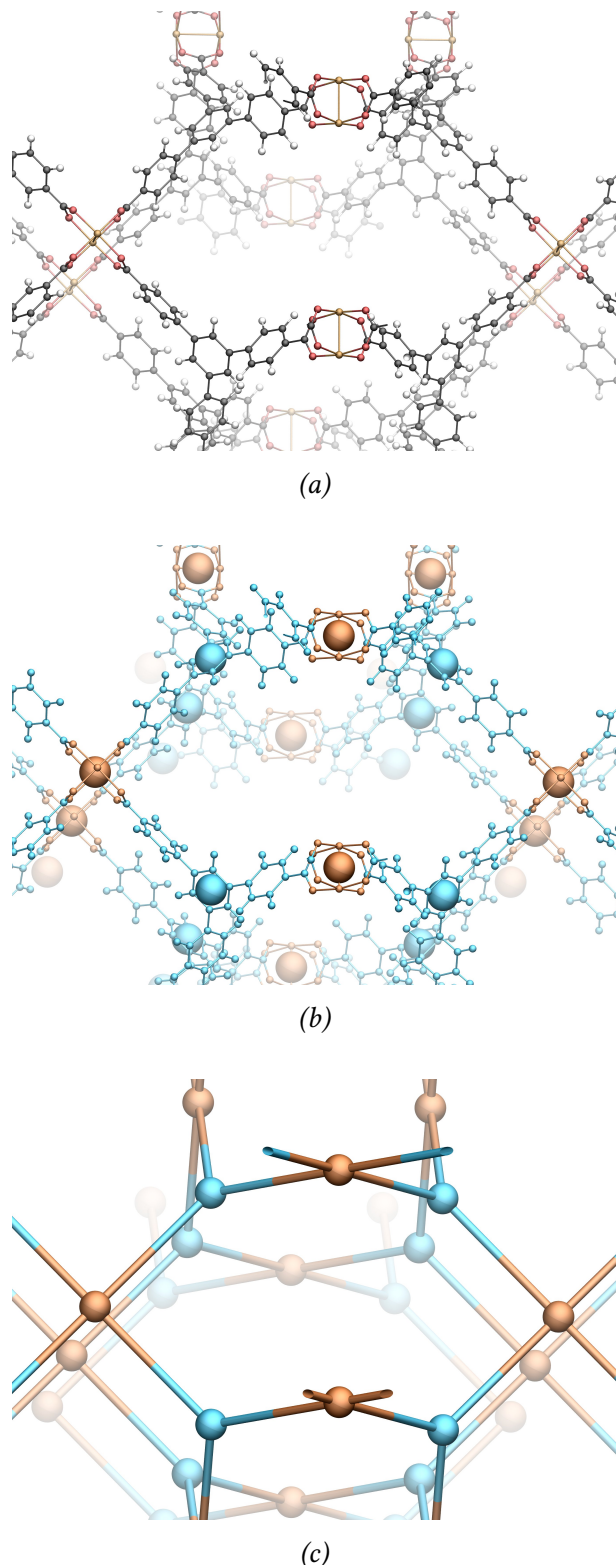


*Figure 1.1: Decomposition of a crystalline framework into its underlying net:*

(a) Crystalline structure of MOF-143.<sup>5</sup>

(b) Identification of the SBUs: Cu-based paddle-wheel<sup>6</sup> and benzene-tribenzoate (BTB).<sup>7</sup>

(c) The underlying net, called **pto** in the database of the RCSR.<sup>8</sup>

Like all other atomistic representations of frameworks present in this thesis, this figure was realized using the Tachyon<sup>9</sup> library in VMD<sup>10</sup>

- The coordination sequence up to distance 10. A vertex  $v$  is at distance  $k$  of  $u$  if there is a chain of  $k + 1$  vertices  $u = u_0, u_1, \dots, u_k = v$  such that for all  $i$  in  $\llbracket 1, k \rrbracket$  (where  $\llbracket a, b \rrbracket$  designates the set of integers between  $a$  and  $b$ ),  $u_{i-1}$  and  $u_i$  are neighbours, and there is no smaller such chain. The  $k$ -th term of the coordination sequence of  $u$  is then defined as the number of vertices at distance  $k$  of  $u$ .
- The point symbol.
- The vertex symbol.

The latter two account for the shortest cycles and rings starting at vertex  $u$ .<sup>22,23</sup> It is found empirically that the combination of these three properties for all vertices forms an almost unique identifier of the topology. However, this approach is not completely sound as there can be different nets that do share these same three properties.

Systre is an open-source software\*; its inputs are files representing the graph underlying the crystal structure, rather than the crystallographic files directly. It implements an algorithm that yields a so-called *topological genome*<sup>24</sup> of the net, which is a finite series of numbers. This genome is provably unique for each net, only depends on the net itself and not its representation, and can be computed in polynomial time of the size of the net. To do so, Systre starts by computing an *equilibrium placement*<sup>25</sup> of the vertices, which attributes to each vertex a position which is the barycentre of that of its neighbours. The net is then minimized, which amounts to finding a unit cell. Afterwards, Systre collects a number of *candidates*, which are frames of reference that do not depend on the current representation of the net. For each candidate, the vertices of the net are ordered according to their position in the frame of reference, and a key is determined which uniquely identifies the net with this ordering in this frame. The genome is then chosen as the lexicographically smallest key. Since the candidates do not depend on the initial representation of the graph, the keys do not either, hence the genome is indeed uniquely determined and only depends on the net itself. In graph theory, the problem Systre solves is called *graph canonization*. It incidentally allows determining whether two input graphs are actually two representations of the same graph (the *graph isomorphism* problem) by comparing their canonical forms (here, the genome), but it can also be used to give a canonical name to graphs for example, by accessing a database of names with the canonical form of the graphs.

Apart from ToposPro and Systre, a few alternative tools have been developed to simplify structures into topological descriptors, but none are suitable for topology identification of chemical structures at large. Indeed, they either only work on specific structures (usually zeolites) like TOTOPOL,<sup>26</sup> or rely on a non-unique representation of the structure (such as a tiling<sup>27</sup>) like the T-ring representation,<sup>28</sup> or because their output is not unique for each input structure, like the Single Repeating Unit representation<sup>29</sup> for example. For finite molecules, the two most common representations are the SMILES<sup>30</sup> file format, which is proprietary and comes with several conflicting implementations, or the IUPAC's International Chemical Identifier (InChi)<sup>31</sup> key, which is open-source and more standardized, but less human-readable. Both include additional chemical information as well.

---

\*available online at <http://gavrog.org/>

In this context, I developed a new tool to efficiently determine the topology of crystal structures: the Julia package `CrystalNets.jl`<sup>\*</sup>. Julia<sup>32</sup> is a modern general-purpose and scientific programming language that offers both great performance and ease of programmability.<sup>33</sup> This, as well as carefully chosen optimizations, allows `CrystalNets.jl` to outperform Systre while leveraging a very similar core algorithm to ensure soundness. Moreover, the package uses the Julia port of chemfiles<sup>†</sup> which allows it to read common chemical file formats like CIF, making it easy to use for the analysis of single cases as well as large databases of crystal structures.

Delgado-Friedrichs and O’Keeffe [19] explained the overall architecture of the Systre algorithm which `CrystalNets.jl` largely reuses: this chapter will mostly follow its structure, only briefly summarizing the key concepts that are already explained elsewhere along the way, while focusing on the implementation choices and some proofs of correctness that do not appear in other publications. A series of new algorithm optimizations will then be explained, which account for the great performance improvement observed for most nets compared with Systre. `CrystalNets.jl` has been used to analyze several existing crystalline databases, which will be detailed afterwards. Finally, the `CrystalNets` web interface will be showcased, along with details of its implementation.

## 1.2 ALGORITHMS AND IMPLEMENTATION

### 1.2.1 From the chemical structure to the net

#### BONDING ALGORITHM

Since the topological information is derived from the bond network, using correct bonds is a necessary prerequisite to any topology recognition tool. Yet, identifying bonds in a crystal is not a clear-cut science. Following the chemical meaning of a bond, the map of electronic density in the system should theoretically be necessary to establish the bond network of the crystal. A bond would then be detected when the density reaches a certain threshold along the interatomic axis, and the nature of the bond (simple, double, triple) can be derived from the overlap of atomic orbitals for instance. However, using this minute vision of the chemical structure, the value of the threshold results from an arbitrary decision.

The fundamental reason why attributing bonds is cannot be made absolute results from the fact that chemical bonds are no more than a useful convention, rather than a measurable observable. Yet, this convention is not without meaning, otherwise any notion built from it, like the topology in case, would lack sense. Therefore, several bond attributing strategies have been devised, none being proven as the ultimate one.

In the case of `CrystalNets.jl`, whenever the bonds are not explicitly given, the automatic bonding algorithm starts from the heuristic strategy used by chemfiles and the visualization software VMD.<sup>10</sup> First, the smallest distance between all pairs of atoms is computed, “smallest” being taken among the translated images of each atom across unit cells. Any distance lower than 0.5 Å is considered an input error. Otherwise, two atoms are bonded if their distance is

---

<sup>\*</sup>available online at <https://github.com/coudertlab/CrystalNets.jl>

<sup>†</sup>available online at <https://chemfiles.org/>

below the minimum of two threshold: the first one is proportional to the maximum Van der Waals radius of all atoms in the structure, and the second is proportional to the sum of Van der Waals radii of the two atoms. The Van der Waals radii were taken from the Blue Obelisk's data repository and slightly modified for a few atoms as in Chemfiles.

From this point, the new algorithm departs from that of Chemfiles and VMD by using multiple additional heuristics. First, the two cutoff values mentioned before are controlled by an option that can be tweaked by the user, to remove some spurious bonds or detect some which are just past the threshold. Additionally, if the structure is a MOF or a zeolite (which is set by the user), then the Van der Waals radius of all metallic atoms is multiplied by 1.5, to account for the larger bonds used in the description of inorganic SBUs.

A number of spurious bonds are then removed from the initial guess resulting from these rules. Some common atoms have fixed maximum valence : hydrogen is limited to 1 neighbour, carbon and nitrogen to a maximum of 4, oxygen to 2 unless it has metallic neighbours, in which case it can have up to 4 neighbours (a typical use case is for metal-oxo clusters). Bonds shorter than 0.65 Å or longer than 4 Å are removed, as well as those longer than 3 Å that are significantly out-of-plane with respect to other bonds around any of the two neighbours. Metal-metal bonds are conditionally removed according to user options. Finally, in a configuration where three atoms are pairwise bonded in a triangle, the longest of the three bonds is removed if it is either too long or too close to the opposite atom.

A special rule is added to allow detecting hydrogen bonds, which is disabled by default. This consists in conditionally accepting one additional H–A bond to a hydrogen atom already bonded to an atom D, when atom A is one of either O, N, F, Cl or S. The additional bond is then only accepted if it is between 1 Å and 2.5 Å long, and if the D–H–A angle is less than 30°, all these parameters being modifiable by the user.

All these heuristics were derived from manual inspection of the result of the bonding algorithm over databases of crystal structures. As with any strategy relying on heuristics, it cannot be made perfect, but it appears to be reasonable enough for all cases encountered so far. Overall, this strategy works well with respect to the time vs precision trade-off required by `CrystalNets.jl`; any input without explicit bond which requires this algorithm will still result in a warning though, to let the user know that the automatically extracted bond network should be carefully checked.

## CLUSTERING ALGORITHMS

Once the bond network is obtained, it undergoes clustering, which consists in grouping together sets of atoms: each such cluster will then be collapsed into a single vertex in the net. This transformation is useful in order to simplify the exact atomistic topology into a higher-level topology that can expose the overall organization of the crystal, without reproducing the low-level details.

I implemented five main clustering options: “All Nodes”, “Single Node”, “Standard”, “PE” and “PE&M”, which are particularly relevant for the decomposition of MOFs into SBUs. All decompositions start by separating metals, on the one hand, and organic carbons, on the other hand. Aromatic cycles are merged into a single pseudo-atom. The “Single Node” strategy<sup>34</sup> consists in growing the metallic clusters, then the organic clusters, with adjacent non-attributed atoms until all have an attributed group. The “All Nodes” clustering<sup>34</sup> additionally puts the

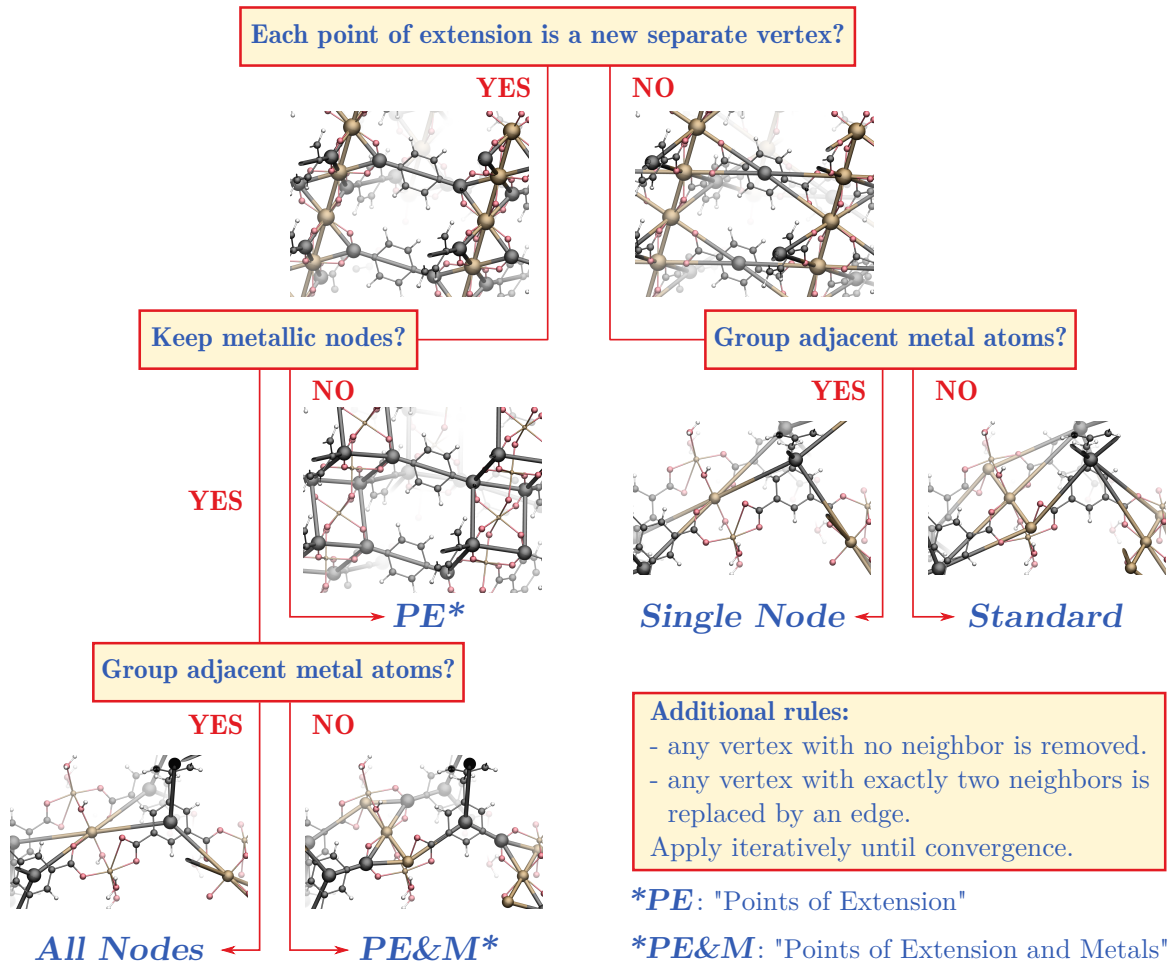


Figure 1.2: Schematic representation of the key differences between clustering choices

points-of-extension,<sup>35,36</sup> which are the organic atoms bonded to an inorganic cluster, into their own separate group. Alternatively, each metal atom can be put into its own separate group, yielding the “Standard” strategy. These three methods have been standardized by IUPAC.<sup>34</sup>

In addition to these three main options, the “Points-of-Extension and Metals” (PE&M) algorithm proposed by Xie et al. [37] consists in retaining the points-of-extension from the initial clustering, but discarding those clusters to only keep one per metal atom and one per point-of-extension. Finally, the “Points-of-Extension” (PE) strategy only retains one cluster per point-of-extension. All of these differences are summarized in Figure 1.2.

Except for the “Standard” representation which is uniquely defined by its implementation in ToposPro,<sup>38,39</sup> the other clustering options are only described, like before, but not uniquely determined by an explicit algorithm.<sup>11,34,37,38,40,41</sup> CrystalNets.jl does not follow the original implementation of the “Standard” representation,<sup>39</sup> primarily because of the required computational cost for determining the minimal ring around each bond. Instead, its custom algorithm consists in the following main steps:

- First, organic cycles are replaced by a new virtual carbon atom. Afterwards, all metallic atoms are assigned to the “inorganic” class and all carbon atoms to the “organic” class. Then, in a loop, each remaining atom that is bonded to an atom in the “inorganic” class is itself classified as “inorganic”, until no such atom remains. All remaining unassigned atoms are then classified as “organic”. P and S atoms are treated differently and considered organic if directly bonded to a carbon, metallic if directly bonded to a metal, and part of a third class otherwise.
- Afterwards, SBUs are formed by regrouping together all adjacent atoms belonging to the same class. Paddle-wheel patterns are identified separately and regrouped into a single inorganic SBU even when the two opposite metal centres are not bonded together. The *points of extension*, which are organic atoms bonded to an inorganic atom, form their own SBU each. The algorithm stops here if there is no periodic SBU, *i.e.* if there is no infinite set of adjacent atoms belonging to the same class.

Otherwise, if there are such periodic SBUs, they are split by virtually removing the atoms with the highest connectivity and regrouping the other atoms of the periodic SBU into the remaining connected components. A few other heuristics are used to ensure that all final SBUs are finite, and to tackle the various possible configurations encountered in framework structures.

This algorithm yields the “All Nodes” representation . It can be converted to “PE” by removing all metallic atoms and bonding their corresponding points of extension to describe the coordination polyhedra around the removed metals. The “All Nodes” representation is also convertible to “Single Node” simply by merging the organic points of extension with their neighbouring organic SBU. It can also be transformed to yield the “PE&M” representation by splitting inorganic clusters to keep only one metal atom per SBU. Combining the algorithm for “PE&M” and “Single Nodes” yields the “Standard” representation.<sup>38</sup> For simple cases, CrystalNets.jl also provides an “Each Vertex” clustering option which bypasses the entire clustering step and keeps each atom as its own vertex in the net, as well as an “Input” option which determines clusters directly from the Residues of the chemfiles-parsed input file, so that the user may provide their own SBUs.

Once the SBUs are determined, they are converted to vertices and bonded together according to the atomic bonds. Finally, as with all nets in CrystalNets.jl, if a vertex has one or zero neighbour, it is removed, and if it has exactly two neighbours it is converted into an edge between its neighbours, and this iteratively until convergence. Once vertices and edges are defined, interpenetrating nets are separated, each of them accounting for a single structure.

Overall, the net which will be identified by CrystalNets.jl heavily depends on a series of choices made when deciding on the bond attribution, as well as the clustering step. Automated tools can only guess so far as to the expected decomposition of the crystal, hence the importance of checking the alignment of the detected net with the expected outcome.

### 1.2.2 Periodic graph structure

Crystal nets are special instances of 3-periodic graphs. In general, a *graph* is a mathematical construct that contains objects, called *vertices*, some of which are linked together by *edges*. Two

linked vertices are said to be *neighbours*. In a crystal, the pattern representing the atoms and their chemical bonds periodically repeats itself across three dimensions: for this reason, the graph representing a crystal is called 3-periodic.

More generally an  $N$ -periodic graph (with  $N \in \mathbb{N}^*$ ) can be represented using the vector model.<sup>42</sup> This model conceptually follows the description of a crystal as a lattice and a pattern. Any point in the lattice is denoted by an offset  $o \in \mathbb{Z}^N$ , whose  $i$ -th coordinate is the offset along the  $i$ -th axis of the lattice compared to a fixed origin. An  $N$ -periodic graph is then defined by a pair  $(V, E)$  where  $V$  is the set of vertex identifiers and  $E \subset V \times V \times \mathbb{Z}^N$  is the set of edges. Any vertex in space is uniquely identified by a pair  $(v, o) \in V \times \mathbb{Z}^N$  where  $v \in V$  is its vertex identifier and  $o \in \mathbb{Z}^N$  is the offset of the cell that contains the vertex. Let's note  $n = |V|$  the number of vertices per cell and identify  $V$  with the integer interval  $\llbracket 1, n \rrbracket$  so that each vertex identifier can be considered to be a number in  $\llbracket 1, n \rrbracket$ . When working in a fixed cell, the vertices will simply be referred to by their vertex identifier. Finally, for most of the rest of this chapter  $N$  will be equal to 3 since nets are 3-dimensional, but the algorithms exposed in the rest of this section actually work for any dimension and `CrystalNets.jl` can identify 2-periodic and 1-periodic graphs as well.

An edge  $e = (u, v, o)$  can be broken down into a source  $u \in V$ , and a destination  $(v, o) \in V \times \mathbb{Z}^3$ . The source can be seen as the vertex of identifier  $u$  and positioned in the cell at the origin of the lattice, and the destination is the vertex to which it is linked. When the source and the destination are in the same cell, the offset  $o$  is zero and noted  $0_{\mathbb{Z}^3} = (0, 0, 0)$ . Edges of the form  $(u, u, 0_{\mathbb{Z}^3})$ , called *loops*, are absent in nets because they do not convey any structural information.

For any edge  $e = (u, v, o) \in E$ , the reverse edge  $(v, u, -o)$  is also in  $E$ : this property makes the graph *undirected*. All graphs used to represent crystals are undirected because chemical bonds are symmetric: if atom A is bonded to atom B, then atom B is bonded to atom A, and likewise for clusters of atoms.

As opposed to periodic graphs, *simple* graphs do not have a concept of offset: an edge of a simple graph is only a pair of vertices. Numerous computational representations of simple graphs exist in the literature, but they cannot be directly transposed to periodic graphs. In order to find a computational representation for crystals relevant to topological analyses, a useful observation is that nets share two distinctive features that come from chemistry:

- The number of edges is at most proportional to the number of vertices, because of the limited valence of atoms. Such graphs are generally called *sparse*. This remains true when vertices represent clusters instead of single atoms, although in that case the number of neighbours can be higher than the maximum valence of an atom — for instance, SBUs with up to 66 points of extension have been built.<sup>4</sup>
- The set of edges is small to medium-sized because the number of vertices per unit cell is, in practice, between 1 and 10 000 in most real-world crystalline structures. This is small compared to the trillion of edges of some graphs in social media modelling for instance.<sup>43</sup>

Finally, the most important operation on graphs that will subsequently be used is finding the set of neighbours of a given vertex. Driven by this, I chose to computationally repre-

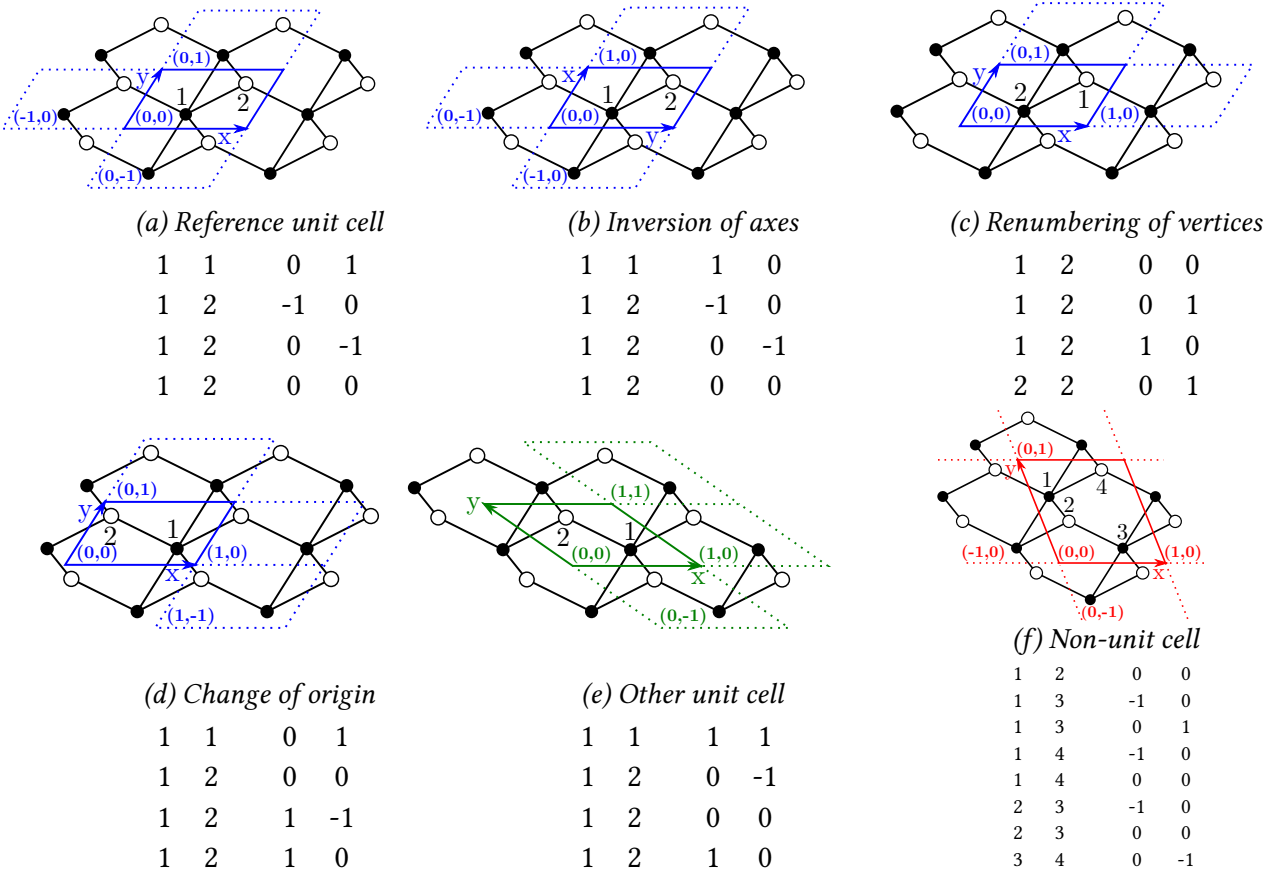


Figure 1.3: Six different representations of the same 2-periodic graph. The first two columns are the source and destination vertices, the last two are the edge offset.

sent a periodic graph by a list of size  $n$  whose  $u$ -th element is the set of neighbours of  $u$ :  $\mathcal{N}_u = \{(v, o) \in V \times \mathbb{Z}^3 \mid (u, v, o) \in E\}$ .  $\mathcal{N}_u$  is stored as a lexicographically sorted list.

Because of the previously mentioned undirectedness of the graph, if  $(v, o) \in \mathcal{N}_u$ , then  $(u, -o) \in \mathcal{N}_v$ . However, it is often convenient to be able to enumerate the edges of the graph without double counting an edge and its reverse. For this reason, the representation comprises another list of size  $n$  whose  $u$ -th element is the first index  $i$  in  $\mathcal{N}_u$  such that  $\mathcal{N}_u[i] = (v, o)$  with either  $v > u$  or  $[v = u \text{ and } o > 0_{\mathbb{Z}^3}]$ . Such an edge  $(u, v, o)$  will be called a *direct* edge. Since loops are forbidden, all edges are either a direct edge, or the reverse of a direct edge. Thus, since each list of neighbours is lexicographically ordered, reading the list of neighbours starting at the given indices  $i$  is guaranteed to yield all direct edges of the graph, hence each edge exactly once without its reverse. The lexicographically ordered sequence of direct edges is a unique identifier of a representation  $(V, E)$  of a periodic graph in the vector model: such a sequence will be called the *key* associated with the representation.

I implemented the graph structure detailed above in `PeriodicGraphs.jl`, a companion Julia package which can be used independently of `CrystalNets.jl`. That package also contains dedicated ring statistics algorithms, of independent interest for the topological analysis of materials.

Figure 1.3 shows several representations of the same 2-periodic graph. The graph is made of two kinds of vertices (represented by open and closed circles), but the choice of the vertex identifiers and of the cell influences the representation. Each choice of cell is characterized by its origin and its axes  $x$  and  $y$ ; some repeated cells are represented as well, along with their offset in the bottom-left corner. For each representation, the key is written below, each line referring to a direct edge. Recall that the Systre algorithm works by choosing the lexicographically smallest key from a set of representations, extracted from candidates that do not depend on the representation of the graph. Hence, if the set of representations was those shown in the figure, the topological genome of the graph would be the smallest key, *i.e.* that under the representation in Figure 1.3a.

Having a working representation for nets, let's now discuss my reimplementation of the Systre algorithm<sup>19</sup> to compute a unique identifier for each net topology.

### 1.2.3 Equilibrium placement

#### DEFINITION

Given a periodic graph, the first step is to compute, for each vertex  $(u, o') \in V \times \mathbb{Z}^3$ , a position  $\mathbf{p}(u, o') \in \mathbb{R}^3$  such that

$$\forall u \in V, o' \in \mathbb{Z}^3, \mathbf{p}(u, o') = \frac{1}{|\mathcal{N}_u|} \sum_{(v, o) \in \mathcal{N}_u} \mathbf{p}(v, o' + o) \quad (1.1)$$

The list of positions  $\mathbf{p}$ , called an *equilibrium placement*, is such that each vertex is at the barycentre of all its neighbours.  $\mathbf{p}$  must also satisfy the additional constraint that

$$\forall u \in V, o \in \mathbb{Z}^3, \mathbf{p}(u, o) = p(u, 0_{\mathbb{Z}^3}) + o \quad (1.2)$$

to enforce the periodicity of the equilibrium placement.

The equilibrium placement has been proven to be unique modulo isometries, because it is the solution of a full-rank linear problem.<sup>25</sup> Equation (1.1) can be rewritten with Equation (1.2) in matrix form,  $A \times P = O$ , where  $A \in \mathcal{M}_{n,n}(\mathbb{Z})$ ,  $O \in \mathcal{M}_{n,3}(\mathbb{Z})$  and unknown  $P \in \mathcal{M}_{n,3}(\mathbb{R})$  such that, noting  $n(u, v)$  the number of neighbors of  $u$  whose identifier is  $v$ :

- $\forall (u, v) \in V^2, A_{u,v} = \begin{cases} |\mathcal{N}_u| - n(u, u) & \text{if } u = v \\ -n(u, v) & \text{otherwise} \end{cases}$
- $\forall u \in V, O_u = \sum_{(v, o) \in \mathcal{N}_u} o$

and from which we determine for all  $u \in V, \mathbf{p}(u, 0_{\mathbb{Z}^3}) = P_u$ .

Since the coefficient of  $A$  and  $O$  are integers, the computed solution  $P$  is always in  $\mathcal{M}_{n,3}(\mathbb{Q})$  with the additional constraint that one of the vertices  $u$  be placed at the origin. The exact solution with coefficients in  $\mathbb{Q}$  is actually necessary for the subsequent computations and not an approximation, so the resolution of the system must be exact. This turns out to be a very costly operation: it requires storing integers of arbitrary size, which are computationally far more expensive than fixed-width machine integers.

#### COMPUTATIONAL ASPECTS

The GNU Multiple Precision Arithmetic Library (GMP)<sup>44</sup> provides access to heavily optimized structures that allow to efficiently perform exact integer and rational computations. Julia has

native support for the arbitrarily-sized integer structure from GMP, through the `BigInt` type, but does not provide a full interface for GMP's rational numbers (although it is internally used for Julia's native `Rational{BigInt}` type). As part of this work, I provide this special support in a separate package, `BigRationals.jl`, which exports the `BigRational` type wrapping GMP's rational type.

In addition to the data structure used, a choice has to be made about the algorithm for solving this linear system. The most straightforward idea would be a general linear algebra technique such as LU decomposition followed by forward and backward substitution. Yet, matrix A is structured since it is both symmetric and sparse, calling for the use of more efficient algorithms.

Several algorithms have been discussed in the literature for the exact resolution of sparse and integer linear systems.<sup>45–48</sup> Following the analysis by Eberly *et al.*,<sup>45</sup> I decided to implement Dixon's algorithm<sup>47</sup> which relies on a modulo-prime inversion of the matrix. In accordance with their conclusion, this algorithm largely outperforms a sparse LU decomposition algorithm (which I also implemented as a reference and for benchmarking), both algorithms leveraging GMP instructions specific to the `BigRational` type for improved performance. Yet, Dixon's algorithm can fail if matrix A happens not to be invertible modulo the chosen prime: hence, I chose to successively invert it modulo three hard-coded large primes and stop at the first succeeding one, and finally resort to LU decomposition if all three fail. This implementation is up to orders of magnitude faster than that used in the original Systre program written in Java. This extra performance is crucial for the use of the topology detection algorithm as part of large-scale screening methodologies.

The equilibrium placement naturally embeds the graph in a Euclidean space, namely  $\mathbb{Q}^3$ . The first vertex of the graph is placed in position  $(0, 0, 0) = 0_{\mathbb{Q}^3}$ , which is allowed because any translation of the equilibrium placement still results in an equilibrium placement. Moreover, because of [Equation \(1.2\)](#), for any vertex identifier  $u \in V$  there is an offset  $o$  such that  $p(u, o) \in [0, 1]^3$ , where  $[a, b]$  designates the set of reals between  $a$  (included) and  $b$  (excluded). In order to simplify the representation, this offset is set to  $0_{\mathbb{Z}^3}$  by adjusting the offsets of the edges of the graph accordingly. In this new representation, equations [1.1](#) and [1.2](#) still hold, as well as the new property:

$$\forall u \in V, \mathbf{p}(u) \in (\mathbb{Q} \cap [0, 1[^3) \quad \text{where } \mathbf{p}(u) = \mathbf{p}(u, 0_{\mathbb{Z}^3}) \quad (1.3)$$

In order to accelerate the subsequent algorithms, the vertices of the graph are lexicographically sorted according to their new position. The first vertex, being at  $0_{\mathbb{Q}^3}$ , remains first.

Nets where at least two vertices have the same position are called *unstable* and, similarly to Systre, are generally not handled by `CrystalNets.jl`. This is usually not problematic since their probability of occurrence is low.<sup>49</sup> My implementation can however handle unstable nets where each collision site comprises at most four vertices if there is no edge between two different collision sites and no collision site is bonded to two representatives of the same vertex. This accounts for roughly half of the encountered unstable nets in the explored databases. I will not detail the case of these unstable nets here but focus on stable ones, so we can thus assume that no two vertices have the same position.

Figure 1.4 represents the equilibrium placement for the net of diamond (called **dia** in the RCSR). Note that the natural embedding in  $\mathbb{Q}^3$  imposes a cubic unit cell for all nets, which is not representative of the actual unit cell of diamond; however, the geometry of the unit cell is irrelevant here because only the topology of the net matters. As a consequence, the bond lengths are not representative of that of diamond either, which explains why not all have the same lengths in this representation. Nonetheless, each vertex is indeed at the barycentre of the positions of its neighbours.

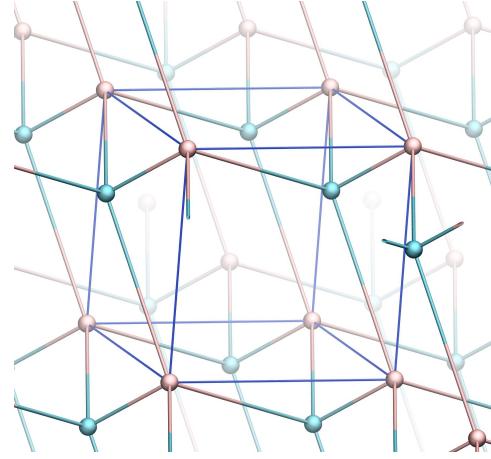


Figure 1.4: Natural Euclidean embedding of the equilibrium placement for the **dia** net.

#### 1.2.4 Minimization of the graph

Once the equilibrium placement is found, the next step of the algorithm is to find a unit cell. In general, a *cell* is a parallelepiped whose three axes ( $\vec{a}, \vec{b}, \vec{c}$ ) are linearly independent translations that constitute symmetries of the graph. Such translations will be called *valid translations*. Another representation for this cell is the matrix  $A$  whose columns are respectively  $\vec{a}, \vec{b}$  and  $\vec{c}$ . Its volume is  $\det(A) = (\vec{a} \wedge \vec{b}) \cdot \vec{c}$ . It is a *unit cell* if it contains the smallest possible number of vertices, which is equivalent to having a minimal volume.

At this point, it is important to recall that the Euclidean space in which the graph is embedded through the equilibrium placement depends on its initial representation, so there is no simple way of finding a unique unit cell independently of the original representation. In particular, common cell reduction techniques such as Delaunay<sup>50</sup> or Niggli,<sup>51,52</sup> which yield a uniquely defined cell, do not solve this problem. Unfortunately, existing libraries implementing these techniques (like *spglib*<sup>53</sup> or *cctbx*<sup>54</sup>) cannot be used either for the simpler problem of finding any unit cell because they do not handle arbitrary precision.

First, note that, by construction of the equilibrium placement, the initial cell is the canonical basis of  $\mathbb{Q}^3$ , so its matrix is the identity  $I$ . Let's now assume that  $I$  is not a unit cell and there is a unit cell  $A \in \mathbb{Q}^{3 \times 3}$  of volume  $\det(A) \in ]0, 1[$ .

Let's define  $f : \mathbb{Q} \rightarrow \mathbb{Q} \cap [0, 1[, \frac{p}{q} \mapsto \frac{p\%q}{q}$  where  $p\%q$  is the remainder of the euclidean division of  $p$  by  $q$  (hence  $p\%q \in [0, q - 1]$ ). Let  $B = (f(A_{i,j}))_{1 \leq i,j \leq 3} \in \mathbb{Q}^{3 \times 3}$ . By definition of  $f$ , the columns of  $B$  are axes within the initial cell; moreover, since  $\forall x \in \mathbb{Q}, x - f(x) \in \mathbb{Z}$ , each axis of  $B$  can be seen as the corresponding axis of  $A$  plus an offset  $o \in \mathbb{Z}^3$ . But since  $I$  is a

repeating unit, such an offset is a valid translation, so each axis of  $B$  is a valid translation. Finally, since  $\det(A) \notin \mathbb{Z}$ , not all coefficients of  $A$  can be integers, so  $A$  has at least one coefficient  $x$  such that  $f(x) \neq 0$ , so at least one axis of  $B$  is not  $0_{\mathbb{Q}^3}$ .

To summarize, the previous observations show that if the initial cell was not a unit cell, then there exists a non-zero valid translation  $t \in (\mathbb{Q} \cap [0, 1[)^3 \setminus \{0_{\mathbb{Q}^3}\})$ .

Let's use this fact to find a unit cell by enumerating all such translations. Symmetries map vertices to vertices, so the first vertex (lexicographically sorted by position) is mapped to another. But since the first vertex was put in position  $0_{\mathbb{Q}^3}$ , the translation is directly given by the position of the other vertex. Hence, only  $n - 1$  translations need to be checked, and if none is valid then the initial cell is a unit cell.

Checking whether a translation is valid can be done with  $O(n \log n)$  time complexity. Vertices are already sorted by position, which allows to efficiently check that all the vertices are mapped to vertices. Doing so first allows to collect the map from initial vertices to their new counterparts and return early if the translation is invalid. Afterwards, it remains to be checked that all edges are also mapped to edges, which can also be done efficiently since the lists of neighbours  $\mathcal{N}_u$  where  $u \in V$  are also lexicographically sorted.

If  $I$  is not a unit cell, then a valid translation  $t = (t_1, t_2, t_3) \in (\mathbb{Q} \cap [0, 1[)^3 \setminus \{0_{\mathbb{Q}^3}\})$  must have been found. Let  $k \in \llbracket 1, 3 \rrbracket$  be such that  $t_k$  is the smallest non-zero coefficient of  $t$ . Then a new smaller cell is given by matrix  $A^{(t)}$  where

$$A^{(t)}_{i,j} = \begin{cases} t_i & \text{if } j = k \\ 1 & \text{if } j \neq k \text{ and } i = j \\ 0 & \text{otherwise} \end{cases} \quad (1.4)$$

The volume of  $A^{(t)}$  is  $\det(A^{(t)}) = t_k \in ]0, 1[$  and by construction its axes are all valid translations, so  $A$  is indeed a new smaller cell. This process can then be iterated in the new Euclidean space created by mapping each point  $x \in \mathbb{Q}^3$  to  $(A^{(t)})^{-1}x$ , until no valid translation is left.

There are several ways to improve the computational complexity of this procedure. The first one consists in observing that if  $t \in \mathbb{Q}^3$  is a valid translation, then so is  $k \times t + o$  where  $k \in \mathbb{Z}$  and  $o \in \mathbb{Z}^3$ . This allows to minimize the volume of the new cell  $A^{(t)}$  thanks to algebraic considerations. Let's illustrate this point in two dimensions for simplicity, although it can be generalized to any number of dimensions.

Let  $t = \left(\frac{p_1}{q_1}, \frac{p_2}{q_2}\right)$  be a valid translation. Let's assume that  $p_1 \neq 0$  and  $q_1 \geq q_2$  (the opposite reasoning can be done in the other case). Let  $k \in \mathbb{Z}$  and  $k' \in \mathbb{Z}$  be Bézout coefficients for  $p_1$  and  $q_1$ , *i.e.* such that  $kp_1 + k'q_1 = 1$ , and let  $o = (k', 0) \in \mathbb{Z}^2$ . Then  $k \times t + o = \left(\frac{1}{q_1}, \frac{kp_2}{q_2}\right)$ .

Hence, matrix  $A^{(kt+o)}$  can replace  $A^{(t)}$  to reduce the cell to a volume  $\frac{1}{q_1}$  instead of  $\frac{p_1}{q_1}$ .

Another potential improvement consists in using all the valid translations instead of stopping at the first one encountered. This way, the translation that minimizes the volume of the new

cell can be chosen instead of any valid translation. However the cost of collecting all valid translations can be up to  $n$  times higher than finding the first valid translation.

Furthermore,  $A^{(t)}$  is just a special case of the set of possible new cells. In general, any invertible matrix whose columns are valid translations (including columns of the identity matrix) is the matrix of a valid cell. The best new cell is the one with the smallest volume, but combinatorial exploration of all possible such matrices that lead to smaller cells has a worst-case complexity of  $O(n^3)$ . In practice, many candidate matrices can be eliminated before computing their determinant so using this method is actually quite efficient.

### 1.2.5 Search space exploration

At this stage in the workflow, the graph has a unit cell and a corresponding equilibrium placement. Let's now look for the topological genome. The strategy follows that implemented in Systre, which consists in taking the lexicographically smallest key among those computed for a number of candidates. Both the computation of the key from a given candidate and the selection of the candidates should not depend on the current representation of the graph.

A candidate is defined as a triplet of linearly independent edges, and represented by a pair {vertex, basis of  $\mathbb{Q}^3$ } where the vertex is the source of the first edge and the columns of the basis are the translations induced by the edges. The process of selecting candidates is explained in section 1.3. This subsection focuses on the computation of a key from a given candidate.

This precise algorithm is explained in [19] and analyzed as Algorithm 5 in [25]. It is detailed in Figure 1.5. The main point is that the algorithm creates a new representation of the graph which is independent of the previous one by redefining both the unit cell and the numbering of vertices thanks to a unique euclidean space derived from the candidate. The first element of the candidate, the vertex, is the origin of the new space and the columns of the basis are its three axes.

Step **(b)** is a simple affine transformation of the positions and steps **(c)** to **(h)** are straightforward to implement, they only require keeping track of the positions of the numbered vertices. Step **(j)** is also straightforward, it consists in multiplying each translation by the inverse of the matrix of the new unit cell to obtain an integer offset. This allows to retrieve the set of edges  $E$  of the graph, and since  $V = \llbracket 1, n \rrbracket$ , this directly yields the representation of a periodic graph in the vector model.

Step **(i)** deserves special consideration. It consists in building a new unit cell from the set of positive translations  $t$  of the edges, positive in the sense of being lexicographically greater than  $0_{\mathbb{Q}^3}$ . Negative translations are negated to only keep positive ones. By construction, this set does not depend on the previous representation of the graph, it only depends on the candidate. As a consequence, any deterministic algorithm that transforms a set of translations into a unit cell can be used for this purpose. Delgado-Friedrichs and O'Keeffe<sup>19</sup> mention this point and suggest triangulating the translations, without detailing their algorithm. Before presenting the one used here, let's sketch the general idea and prove a lemma.

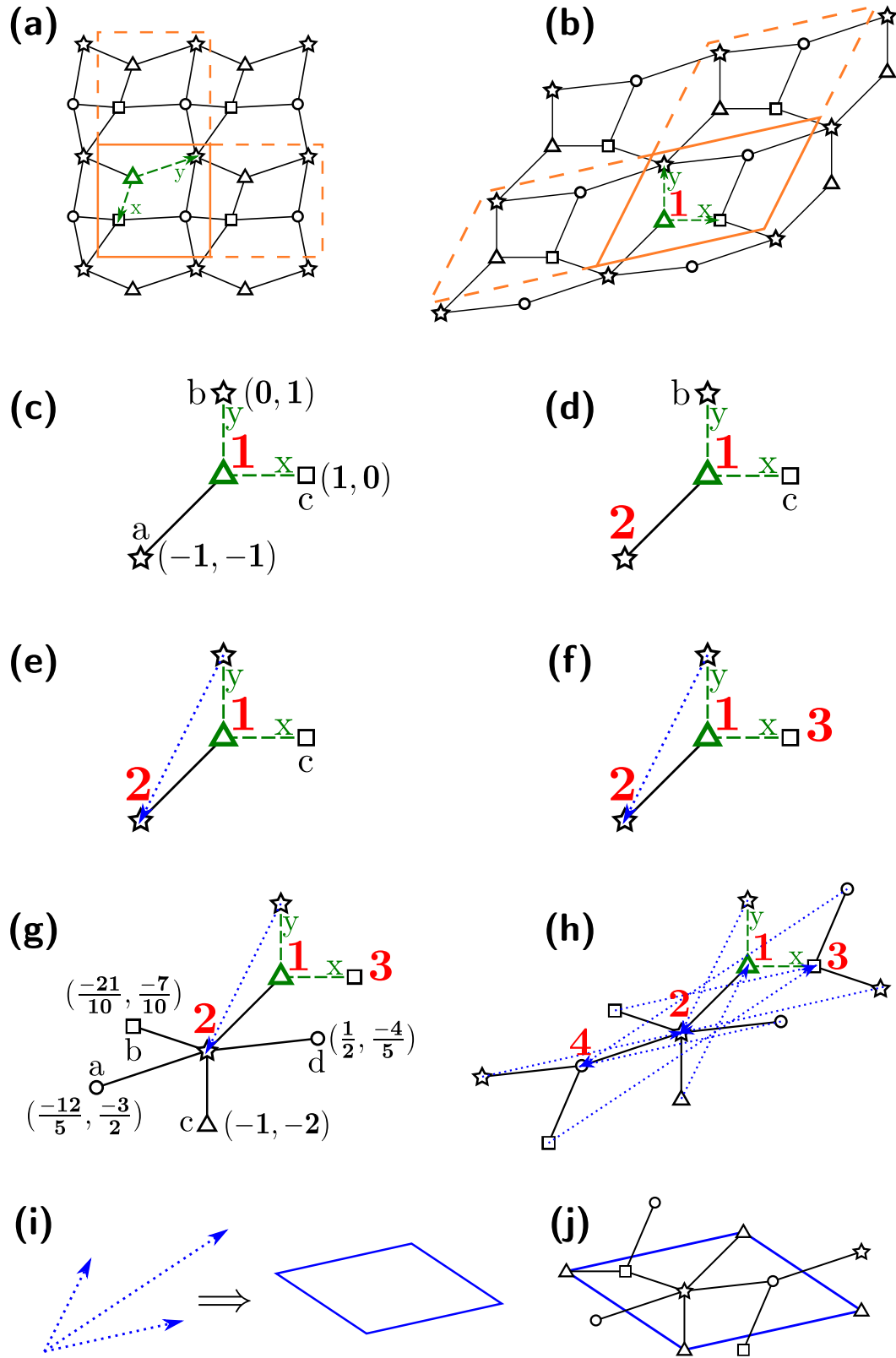


Figure 1.5: Illustration of the algorithm used to extract a key from a candidate on a 2-dimensional graph

- (a) Start from a candidate (in green), whose origin is  $\Delta$  and axes are  $x$  and  $y$ . Initialize an empty queue of vertices.
- (b) Represent the graph in the basis given by the candidate (the former unit cell and two of its neighbours are represented in orange). Note that axes  $x$  and  $y$  are now orthogonal. Assign number 1 to the origin  $\Delta$  and push it to the queue.
- (c) Take the first vertex  $u$  of the queue and sort its neighbours according to the lexicographical order of their position. Here,  $u = 1$  and the sorted neighbours are a, b and c.
- (d) For each neighbour  $v'$ , in order, if it is not the representative of an already encountered vertex, assign it the first available number between 1 and  $n$  and push it to the queue. In this case, neighbour a is assigned number 2.
- (e) Otherwise, store the translation between the newly encountered representative  $v'$  and that which has been recorded  $v$  (the blue arrow). Here,  $v'$  is neighbour b and  $v$  is vertex 2: both are representatives of the same vertex.
- (f) Continue until all the neighbours have been processed. In this case, only neighbour c remains and it is assigned number 3.
- (g) Repeat the steps from (c) until the queue is empty. Here, the neighbours of 2 are being processed.
- (h) When the queue is empty, all numbers between 1 and  $n$  have been assigned and a set of translations has been recorded.
- (i) Triangulate the set of positive translations to obtain a new unit cell (see section 1.2.5).
- (j) Convert the translations to integer offsets using the unit cell to find a new representation of the graph, and extract the key.

*Figure 1.5: Illustration of the algorithm used to extract a key from a candidate on a 2-dimensional graph (continued)*

Given their origin, translations of the set should correspond to integer offsets between vertices and their representatives in the new unit cell to be found. Thus, the matrix  $B \in \mathbb{Q}^{3 \times 3}$  representing the unit cell must be such that each positive translation  $t \in \mathbb{Q}^3$  of the set verifies:

$$B^{-1}t \in \mathbb{Z}^3 \quad (1.5)$$

Not all such basis  $B$  will do, since it should also represent a unit cell, hence the columns of  $B$  must be valid translations. Since all positive translations of the set map some vertex to one of its representatives, they are all valid translations, so it is tempting to look among the integer combinations of these translations to find the columns of  $B$ . However, it remains to be proven that such combinations indeed span the entire group of valid translations.

To show this, let's take the Euclidean space of step (b) and consider a path between the origin and any of its representatives. This path consists in a series of edges  $(u, v, t) \in V \times V \times \mathbb{Q}^3$  where  $t$  is the translation between vertex  $v$  and the vertex  $v'$  which is the actual neighbour of  $u$ . After any number of steps, let's note  $(u, \tau) \in V \times \mathbb{Q}^3$  the pair where  $u$  is identifier of the vertex on which the path has just landed and  $\tau$  is the sum of the translations  $t$  encountered so far. The initial pair thus is  $(1, 0_{\mathbb{Q}^3})$ , since 1 is the number of the origin. An induction on the number of steps shows that the position of the exact vertex on which the

path lands when reaching pair  $(u, \tau)$  is that of vertex  $u$  translated by  $\tau$ . As a consequence, when reaching the final vertex of the path, the pair is  $(u_{\text{end}}, \tau_{\text{end}}) = (1, \tau_{\text{end}})$ . Thus, by construction  $\tau_{\text{end}}$  is the sum of translations  $t$  stored in the edges during the algorithm, so it is an integer combination of the positive translations of the set. But since this reasoning was valid for the translation between the origin and any of its representatives, this proves that any valid translation can be written as an integer combination of positive translations of the set.

Let's now proceed to the algorithm that converts the set of positive translations into a matrix  $B$  satisfying [Equation \(1.5\)](#).

First, note that most positive offsets present in the usual representations of periodic graphs are one of either  $(1, 0, 0)$ ,  $(0, 1, 0)$  or  $(0, 0, 1)$ . As a consequence, in the most common cases, there are only three elements in the set of positive translations, which can simply be mapped to the three canonical offsets. This fact serves as a heuristic optimization for the more general algorithm, by representing all the positive translations in the basis  $A \in \mathbb{Q}^{3 \times 3}$  whose columns are the three first linearly independent positive translations. The reverse transformation will be applied at the end of the algorithm. Overall, this operation is not crucial for the algorithm to work and the input remains a set of translations, but it tends to reduce the denominators of the coefficients of the translations, which is computationally helpful.

Given a set of translations, the goal now is to find three combinations such that they form the columns of a matrix  $B$  satisfying [Equation \(1.5\)](#). In other words, these combinations must span the group of valid translations. This problem on rationals is lifted to integers by storing the least common multiple of the denominators of the coefficients of the translations columnwise, and pointwise multiplying the translations by this triplet of integers in order to obtain a set of integer translations.

From that point, several algorithms exist in order to solve the problem on this integer form.<sup>45–48</sup> The standard procedure is to build the rectangular matrix whose lines are the triplets representing integer translations and put it in Hermite normal form,<sup>55</sup> which is precisely such that it is built from an integer combination of the initial triplets and still spans the same group as that of the triplets.

Determining the exact Hermite normal form is useless in this case however, since there is no need for the complexity brought by its other properties, and the existing solvers are specialized to have their best performance on big square matrices, not thin rectangular matrices one of its dimensions being only 3. Thus, I implemented a custom solver for this particular problem which performs the following steps, for each column  $j$  in a fixed order:

- Find Bézout coefficients of the  $j$ -th element of the integer translations, as well as their greatest common divisor  $d \in \mathbb{N}^*$ . This is done using an efficient algorithm from Havas *et al.*<sup>55</sup>
- Set the  $j$ -th column of  $B$  as the sum of the integer translations weighted by their Bézout coefficient.
- For each integer translation  $t \in \mathbb{Z}^3$ , update it to zero its  $j$ -th element by subtracting the new column of  $B$  times the quotient of the  $j$ -th element of  $t$  by  $d$ . By construction, after this step all translations have at most  $(j - 1)$  non-zero elements.

Finally, columnwise divide  $B$  by the triplet of least common multiples that was found before to get back to rationals, and left-multiply it by  $A$  to go back to the Euclidean space specified by the candidate.

The resulting matrix  $B$  has all the required properties for being a unit cell. Thus, each translation  $t \in \mathbb{Q}^3$  of an edge now corresponds to an offset  $o = B^{-1}t \in \mathbb{Z}^3$  with respect to the unit cell, so the lexicographically ordered set of edges  $(u, v, o) \in V \times V \times \mathbb{Z}^3$  is a representation of the initial graph that does not depend on its initial representation, but only on the candidate.

Let's note that this method transforms a set of translations into a unit cell, and this is precisely the problem encountered when minimising the cell from the set of all valid translations in section 1.2.4. However, in the current case, the procedure cannot rely on a starting cell to minimize, which is why it is more complex.

To conclude, let's observe that this representation might be impossible to embed, in the sense it may be impossible to put all the vertices of the graph, as they were determined by the algorithm, within the same unit cell given the constraints on their edges. This can be circumvented by taking appropriate representatives for each vertex given a fixed unit cell, but even that is unnecessary since the goal is only to extract a key, and it does not matter whether the key itself can be embedded.

## 1.3 REDUCTION OF THE SEARCH SPACE

The only aspect of the algorithm that remains to be explored is the selection of the candidates, which is a crucial point for the overall complexity of the algorithm. After explaining how the implementation of Systre does this, I will present a series of novel reductions of the search space, *i.e.* of the number of candidates, that yield a notable performance gain.

### 1.3.1 The initial search space

Let's recall that a candidate is defined as a triplet of edges, which is used to create a new representation for the graph as explained in Figure 1.5. The topological genome is chosen as the lexicographically smallest key extracted from the candidates, so the set of candidates must be chosen in a fashion that is independent of the initial representation of the graph, lest the selection biases the search space. As a consequence, Delgado-Friedrichs and O'Keeffe [19] proposed the following selection pattern:

- If there exists at least one vertex such that its outgoing edges are not all coplanar, then the set of candidates is the set of triplets of linearly independent edges that all start at the same vertex.
- Otherwise, the candidates are all triplets of linearly independent edges such that the two first start from a common vertex and the third starts from another vertex.

In both cases, the set of valid candidates is not empty (otherwise it would mean that the graph is either not connected or not 3-periodic) and independent of the initial representation of the graph. It can be further reduced by removing duplicate candidates that yield the same key, using symmetry considerations as will be shown in section 1.3.3.

For many graphs, this search space remains rather large compared to the set of all possible triplets of edges. My goal in this project was for this software to be able to tackle very big structures very efficiently, for two different types of applications: high-throughput screening of hypothetical materials, where the topological detection is performed on hundreds of thousands (and sometimes several millions) of structures,<sup>56</sup> and application to very large periodic structures, such as models of amorphous framework materials.<sup>57</sup> Therefore, reducing this search space is crucial for performance since it directly tackles one of the bottlenecks in the original implementation of Systre.

### 1.3.2 Categorization of vertices and edges

Since the search space must remain independent of the representation of the graph, it can only depend on some properties that are common to all its representations. Such a property is called a *topological invariant*. The only invariant used so far is whether there exists a vertex whose outgoing edges are not all coplanar, but many other invariants exist, such as the three used by ToposPro,<sup>17</sup> mentioned in section 1.1.2. These properties can be used to considerably reduce the search space by separating vertices according to them.

The core idea of vertex categorization consists in trying to separate vertices into as many categories as possible, each of these categories being identifiable independently of the representation of the graph. For instance, in this work, vertices are separated according to their coordination sequence (the number of vertices at distance  $k$  from the vertex of interest with  $k = 1, 2, \dots$ , see section 1.1.2), so that two vertices are in the same category if and only if they share the same coordination sequence up to distance 10.

Vertex categories are then sorted by the total number of outgoing edges from vertices in that category and, in case of equality, by the invariant they were defined from. For example, in our case, ties are broken by lexicographically sorting according to the coordination sequences.

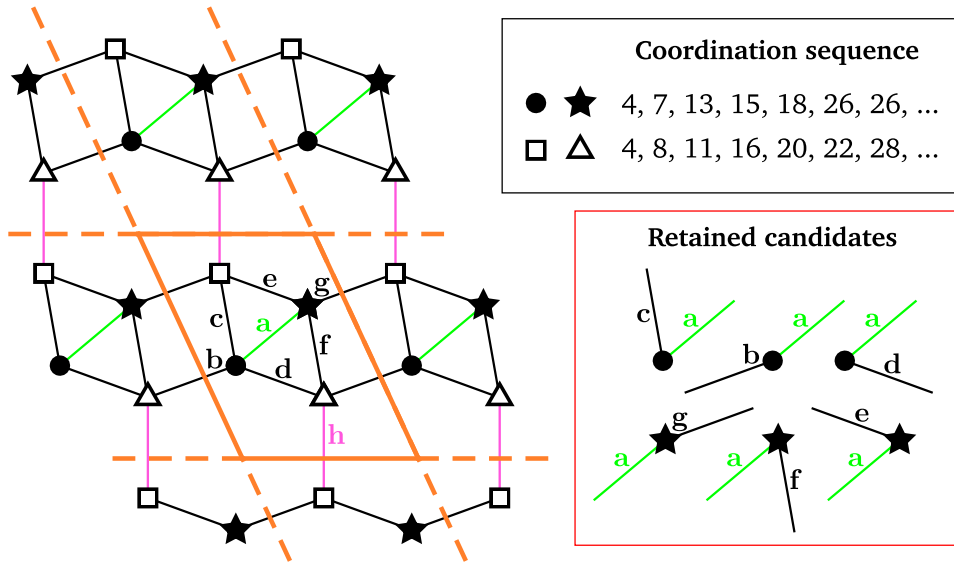
With these sorted categories in mind, let's look for candidates and try to minimize their number. The following strategy is used in the improved algorithm:

- Let  $c$  be the first vertex category such that there is a triplet of non-coplanar edges starting from the same vertex in  $c$  (if no such category exists, skip to the alternative below). Then, for all such triplets, let  $c_1, c_2$  and  $c_3$  be the sorted categories of the vertices to which the initial vertex is bonded with these edges. There are four subsets of such triplets, characterized by whether they satisfy:
  1.  $c_1 = c_2 = c_3$ .
  2.  $c_1 < c_2 = c_3$ .
  3.  $c_1 = c_2 < c_3$ .
  4.  $c_1 < c_2 < c_3$ .

Then the candidates are all the triplets of edges whose categories are in the last non-empty such subset with  $(c_1, c_2, c_3)$  lexicographically minimal.

This strategy illustrated for the 2D case in Figure 1.6.

- Alternatively, if all vertices have only coplanar outgoing edges, let  $c$  be the first category such that there exists another category  $c'$  such that there is a non-coplanar triplet of edges, the two first of which start from a vertex of  $c$  and the last from  $c'$ .  $c'$  is chosen as the first such category. Let  $c_1$  and  $c_2$  be the sorted categories of the destinations of the



1. The coordination sequence of all vertices is computed. In this particular case, there are two vertex categories, one represented with filled symbols (circle and star) and the other with empty symbols (square and triangle). Edges are colored in green when they connect two filled symbols, in magenta for two empty symbols and black otherwise.
2. Both categories have the same number of outgoing edges, so they are sorted in lexicographical order of the coordination sequences: the “filled” category comes first.
3. There exists a filled vertex with two linearly independent outgoing edges (here, all vertices actually match the criterion because no two neighboring edges are aligned). Hence,  $c$  is the “filled” category.
4. Consider all ordered pairs of linearly independent edges starting from a filled symbol  $u$ . There are 24 such pre-candidates, represented as the two first lines of Figure 1.7. Among those, only 6 bond  $u$  to vertices of category  $c_1$  and  $c_2$  respectively, such that  $c_1 < c_2$ . Keep those as candidates.

If there was no such pre-candidate, the candidates would have been all the pre-candidates where  $c_1 = c_2$  with  $c_1$  minimal, i.e. “filled” if possible, “empty” otherwise.

Figure 1.6: Illustration of the candidate selection on the cqe net.

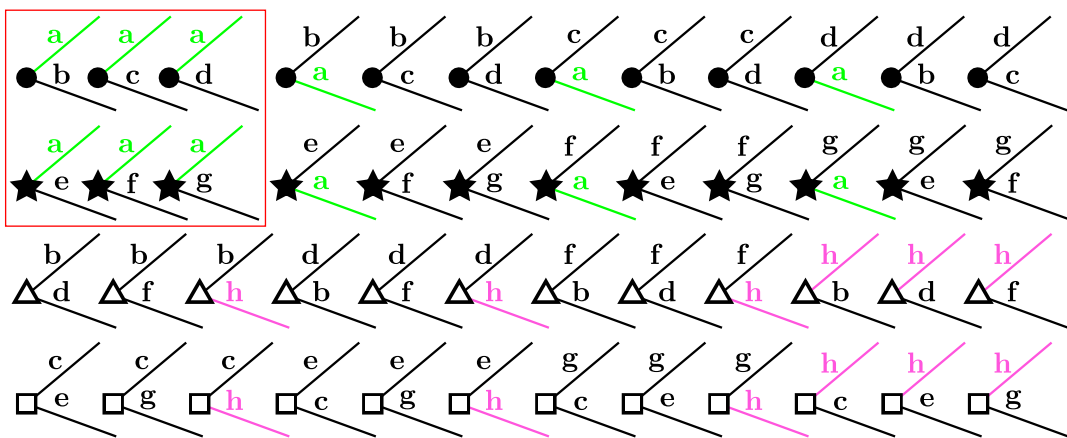


Figure 1.7: The 6 candidates of the cqe net selected by CrystalNets.jl, among the 48 possible candidates.

two first vertices, and  $c_3$  be the destination of the third. Then the candidates are all the triplets of edges, the two first of which start in  $c$  and the last from  $c'$  such that  $(c_1, c_2, c_3)$  is lexicographically minimal.

The main difference with the strategy of Systre is that the categorization of vertices bounds the number of candidates with respect to the maximal size of a category, hence the goal of having as many small categories as possible. However, the two strategies are exactly the same in the worst-case scenario where there is only one category. Note that, although rather complex, the constraints on the retained candidates described above can actually be implemented in an efficient way, which is necessary to prevent the search space reduction from taking more time than the actual search space exploration.

### 1.3.3 Reduction through symmetry

In addition to the individual properties of vertices which are used to separate them into categories, symmetry considerations on the equilibrium placement can be useful in reducing the search space. Indeed, if two candidates are symmetry-related, then the representations extracted from both will be exactly identical. This optimization is already used in Systre, and in the current work, it is useful to perform a symmetry analysis on the equilibrium placement of the unit cell before even categorizing vertices.

Unfortunately, there does not appear to be any available code that can find symmetries for an input given in arbitrary precision; all existing libraries take approximate positions, and thus return only approximate symmetries. I use the *spglib* library<sup>53</sup> to this purpose. *spglib* is a C library, which makes it easy to interface with Julia without sacrificing speed. Since all its inputs and outputs are approximate, the returned symmetries need to be checked against the exact equilibrium placement of the graph to rule out false positives. Because of the imprecision of the input, there might also be some false negatives – that is, some symmetries may be missing – but they do not matter because symmetries can only help to eliminate candidates that are symmetric images of other ones already encountered. Hence, the use of symmetries is purely an optimization, but it has no influence on the result of the algorithm.

Symmetries are useful to avoid needlessly recomputing coordination sequences when dividing the vertices into categories. Indeed, the search space is reduced by singling out one vertex per symmetry orbit, and using the convention that only these can serve as the source of the first edge of a candidate. No such constraint can be placed on the destinations of the edges unfortunately, as that would be unsound.

On the particular example of the **cqe** net shown in Figure 1.6, there is only one symmetry and it maps each symbol of a category on the other of the same category. As a consequence, only one of the two first lines and one of the two last lines of candidates shown in Figure 1.7 need to be kept. Systre thus examines 24 candidates, and only 3 for CrystalNets.jl.

### 1.3.4 Ordering of keys

Finally, the algorithm can be made faster by changing the mode of comparison of the candidates. In Systre, the topological genome was defined as the smallest key extracted from a candidate. However, arrived at step (h) of the algorithm in Figure 1.5, both the embedding of the graph as well as the ordering of its vertices only depend on the candidate, and not on the initial

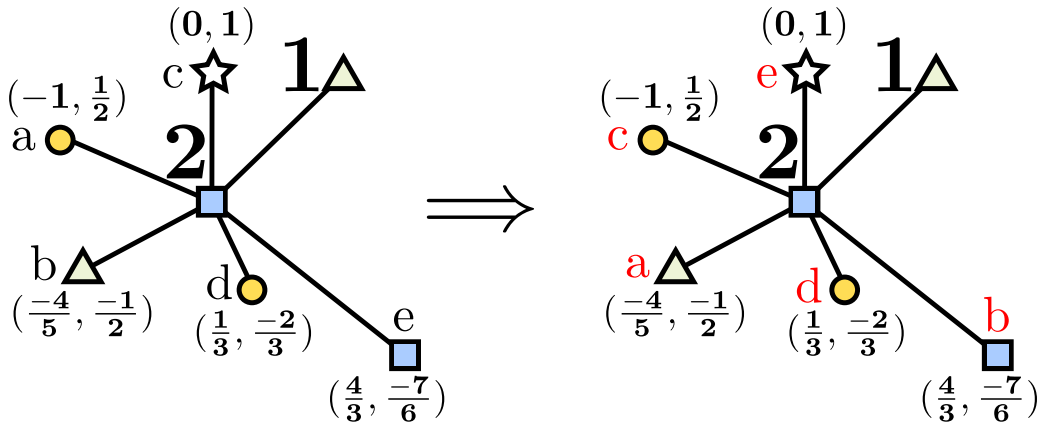


Figure 1.8: Difference between previous and new ordering of neighbours at step (c) on an example. Representatives of the same vertex have the same symbol.

representation. Hence, it is possible to define at that point a pseudo-key consisting in the sorted list of triplets  $(s, d, t) \in V \times V \times \mathbb{Q}^3$  if there is an edge between the vertex defined by its number  $s$  and the representative of vertex number  $d$  which is translated from the latter by  $t$ . This pseudo-key only depends on the intermediate representation of the graph obtained in step (h), which means it is exclusively determined by the candidate, so the genome can be defined as the key extracted from the candidate with the smallest pseudo-key.

Instead of comparing the keys extracted after a costly lifting of the positive translations to a proper representation of the graph, it is thus sufficient to compare the pseudo-keys. Moreover, this pseudo-key can be computed incrementally during the main loop of the algorithm. To do so, at step (c), the neighbours of vertex  $u$  should be sorted in a different manner (represented on Figure 1.8): all representatives of the same vertex should be contiguous and lexicographically sorted according to their position within each category; the categories corresponding to vertices which have a number (assigned in step (d)) are placed first and sorted according to this number, while the others are placed afterwards and sorted according to the position of the first vertex in the category. This makes it so that each edge of the graph is added to the pseudo-key in the order in which it is studied (in steps (d) – (f)), while preserving the invariant that the pseudo-key is lexicographically sorted.

Since the pseudo-key is constructed on-the-fly, it can thus be compared at each step with the previous smallest pseudo-key. If a triplet of the current pseudo-key is lexicographically greater than the triplet at the same position in the previous best pseudo-key, the computation for the candidate is aborted; if it is lower then this comparison can be skipped for the rest of the computation and the pseudo-key will be the new smallest. Finally, once all the candidates have been checked, the minimal pseudo-key is converted to an actual key through steps (i) and (j), yielding the topological genome of the graph.

## 1.4 APPLICATION TO MATERIALS DATABASES

`CrystalNets.jl` is a Julia package which can be intuitively used from an interactive Julia shell or as an executable to determine the structure of single crystallographic files in the variety

of file formats recognized by chemfiles\*. Since chemical bonds are not systematically present in such files, it uses a custom bond detection algorithm inspired from that of chemfiles, and can export both the input with the detected bonds as well as the extracted underlying net to allow visually checking the correspondence with the input. The bonding algorithm reuses available information on the structure to accurately account for the larger bonds surrounding metals in MOFs for instance, but the user can also override the cutoff distance for bonding if necessary.

By combining the bond detection heuristic with topology determination, CrystalNets.jl can also be used to survey large databases of crystalline structures, without the need for user input or relying on other chemical information (such as choice of SBUs) on the structures themselves. In this section, the code is demonstrated on a series of available materials databases.

#### 1.4.1 RCSR, EPINET and IZA-SC database

The Reticular Chemistry Structure Resource (RCSR)<sup>8</sup> † is a repository of 3,132 structures with 2 or 3-periodicity (excluding weaving and 0- and 1-periodic structures), each given a canonical name. It offers a Systre archive containing 2,928 nets that I reprocessed to obtain the 2,928 topological keys corresponding to each structure. These keys are not the same as those of the archive because of the algorithmic differences explained before.

I evaluated the performance of CrystalNets.jl by comparing its time to compute the topological keys of 2053 structures of the RCSR chosen at random, compared to both Java and JavaScript (JS) implementations of Systre<sup>‡</sup>. All three programs were executed 6 times with one input and 6 times with another, each input being a textual file containing a different representation of the same 2053 nets. All ran on a single thread with Intel Xeon Silver 4210R CPUs (2.4 GHz). The average timing over the 12 executions is represented on Figure 1.9. On average, CrystalNets.jl is 56 times faster than the Java version of Systre, and 117 times faster than the its stripped-down JavaScript implementation. Two outliers are marked with a black arrow: these correspond to nets **sas** and **dhe**, the two first nets in the input file of dimension respectively 3 and 2. Since Julia is compiled Just-In-Time,<sup>33</sup> it must compile the entire algorithm the first time the program computes the topological genome of a net, hence a significant overhead. Rerunning the computation on the same two nets after compilation yields an average timing of 3.9 ms for **sas** and 5.9 ms for **dhe**, compared to 63 s and 18 s respectively when including compilation, as represented on the figure.

This performance is consistent across the nets. On the **tep** net, which is the largest of the RCSR (920 vertices and 1840 edges per unit cell), CrystalNets.jl computes a topological genome in 8.6 s, compared to 229 s for the Java implementation of Systre, and 193 s for the JavaScript version. For the smallest net **pcu**, CrystalNets.jl takes 6.5 ms, which is twice as fast as the JavaScript implementation of Systre, and 16 times faster than the Java version. The maximum observed speedup is for the **tsl** net where CrystalNets.jl takes 7.1 ms on average compared to 5.2 s for the Java version of Systre and 16 s for the JavaScript version.

---

\*full list available at <https://chemfiles.org/chemfiles/latest/formats.html#list-of-supported-formats>

†available online at <http://rcsr.anu.edu.au/nets> (3D) and <http://rcsr.anu.edu.au/layers> (2D)

‡available online at <https://github.com/odf/gavrog> and <https://github.com/odf/systreKey> respectively

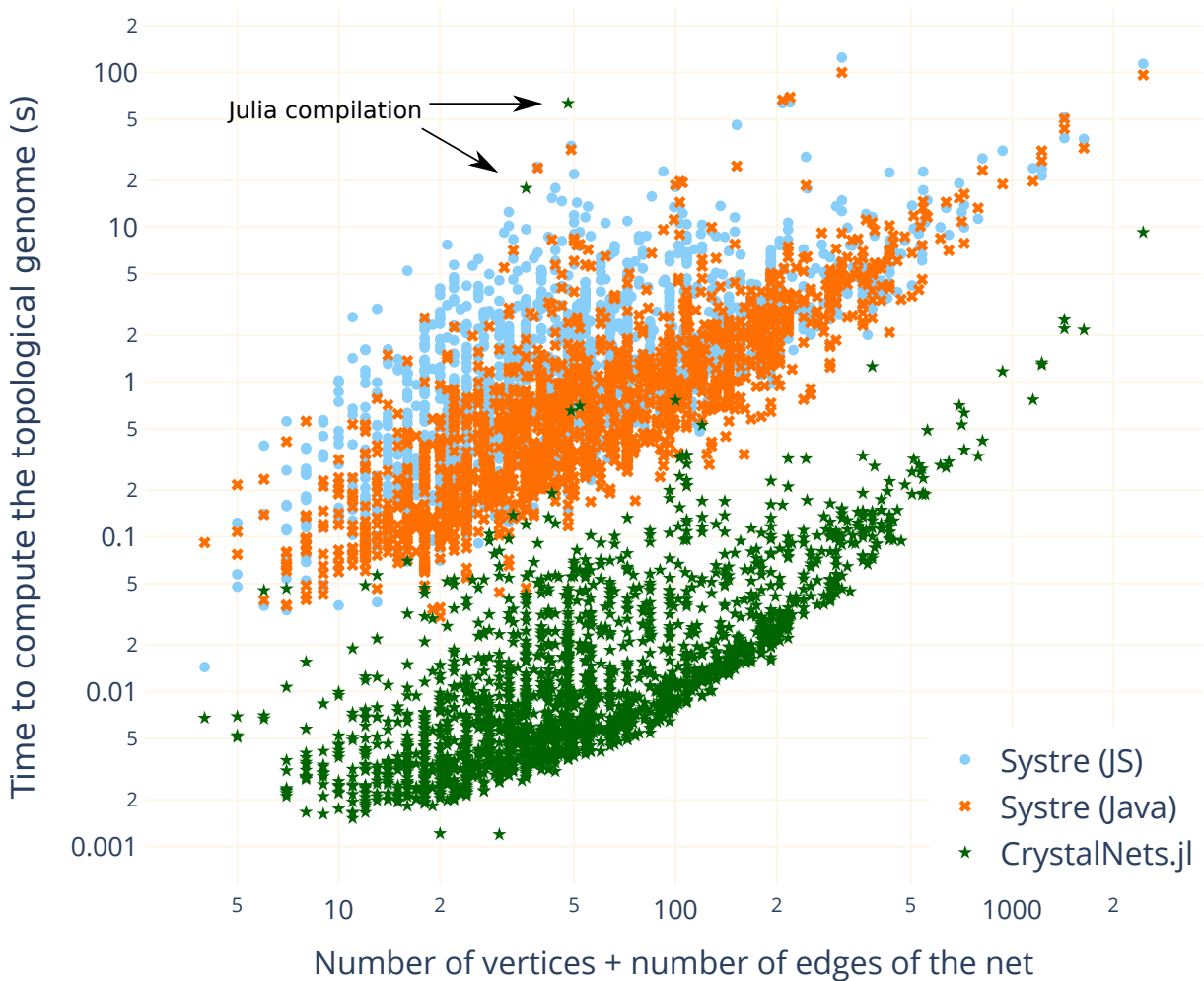


Figure 1.9: Comparison of processing times for 2053 nets with Systre and CrystalNets.jl.

The RCSR partially overlaps with the larger EPINET database<sup>13</sup>\* which contains, among other data, 14 532 stable 3D nets, which were processed similarly. Finally, both databases partially overlap that of Structure Commission of the International Zeolite Association (IZA-SC),<sup>58</sup> which provides names for 255 zeolitic framework structures and corresponding CIF files.<sup>†</sup> These structures have unambiguous vertices, defined by the tetrahedral atoms, and edges between two such atoms bonded by an oxygen, thus a uniquely-defined underlying net.

The results for all three databases are stored within CrystalNets.jl, so that they may be used to recognize the topology of structures processed by the code. In the following, *unknown* nets refer to those that are not part of any of these databases — although it should be noted that other complementary databases of nets do exist (in particular the proprietary databases used by ToposPro).

Finally, this processing of the databases exposed a few mismatches between the names of the structures given in the three databases, which were all reported. Namely, the RCSR nets **ucn**, **rad**, **jst**, **fuv** and **fvb** have as IZA-SC names SBN, ATS, JST, NPT and PTT, which did not appear

\*available online at <http://epinet.anu.edu.au>

<sup>†</sup>available online at <http://www.iza-structure.org/databases/>

on the RCSR. Additionally, 137 structures from EPINET were missing their RCSR name, while 6 RCSR structures mentioned an incorrect EPINET counterpart. This highlights the need for systematic and automated checks of material and topology databases for consistency.

### 1.4.2 MOF structures

#### CoRE MOF 2019

In order to test `CrystalNets.jl` on a realistic workload, I surveyed the CoRE MOF 2019<sup>59</sup> database of metal–organic frameworks (version 1.1.3). For the automatic bonding of the input files, the “MOF” structure option was used, which widens metallic bond radii. Regarding clustering, among the different strategies presented in section 1.2.1, only the results from the “Single Node” option will be discussed to simplify the presentation.

`CrystalNets.jl` recognizes 61% of all 21 692 resulting structures of CoRE MOF 2019 as one of the nets in either the RCSR, the IZA-SC or the EPINET databases (only 33% structures are recognized with “PE&M” and between 45% and 55% with the other clustering options). Among the unrecognized structures, less than 2% correspond to unstable nets which `CrystalNets.jl` does not handle. These proportions are similar for each of the four subcategories of the database, divided whether only free solvent was removed (FSR) or all solvent molecules (ASR), and within each, whether the structure is disordered or not. The closeness of these numbers is expected since most structures from FSR also belong to ASR with only molecules of solvent as difference, which should not affect the topology. This highlights the robustness of the algorithm.

Next, let’s focus on the 11 190 ordered structures of the ASR subset to avoid duplicates. The distribution of the number of structures per corresponding net drops faster for unknown nets than for known ones. This is not surprising since known nets should correspond to the most common occurring in nature, whereas unknown nets should only correspond to at most a few corresponding structures. Indeed, among the latter, 1488 unknown nets only correspond to one MOF structure each, and 302 to two structures. Yet, 5 of them still correspond to thirty MOF structures or more each: I manually checked through the TopCryst interface<sup>20</sup> that these 5 nets were part of the ToposPro database, but I could not do so for all the unknown nets since these databases are not open. In comparison, for known nets, 110 of them only correspond to a single MOF structure, 54 to two and 38 to thirty or more each. These most represented nets are detailed in Figure 1.10: **pcu** (primitive cubic lattice), **dia** (diamond) are by far the most common, together accounting for 27% of known nets, followed by **ths**, **srs** and **pts**. For zeolitic nets, ABW, SOD (sodalite) and BCT are the most commonly encountered.

The high number of nets with known topologies is a good indicator of the quality of the used clustering algorithm. Yet, since it partly relies on heuristics, it should not be considered fail-proof. To assess its validity, `CrystalNets.jl` exports both the input and the detected net in VTF format, which can be superposed in a molecular visualization software like VMD<sup>10</sup> to check the correspondence between the vertices of the nets and the expected clusters. I manually checked this correspondence for hundreds of structures with both known and unknown nets, to assert the validity of my implementation. Comparison with TopCryst on many instances seems to indicate that the vast majority of unknown nets encountered in CoRE MOF are not the result of a wrong clustering by `CrystalNets.jl`, but simply missing from the used databases, probably because they occur on only a handful of actual structures. On the other hand, the proprietary databases of ToposPro appear to include many such nets.

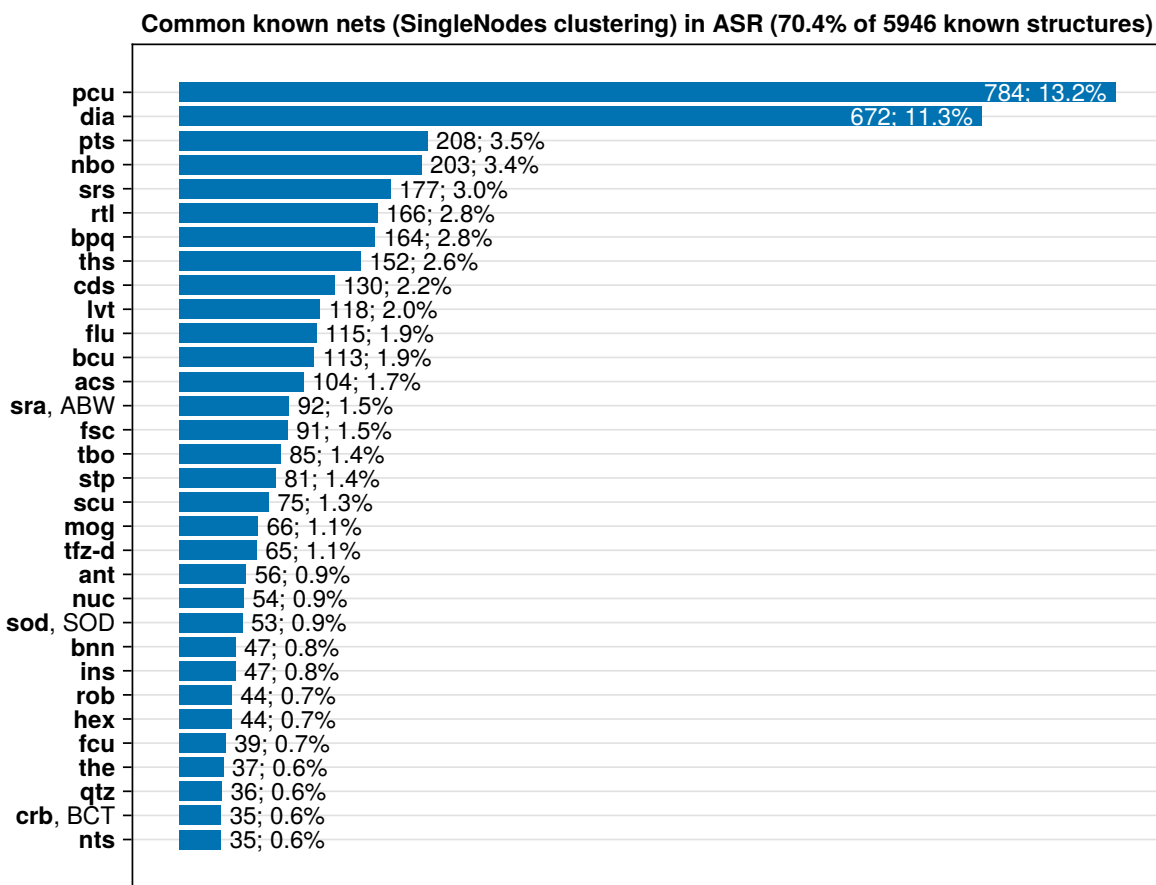


Figure 1.10: Number of structures per known net in the ordered structures of ASR in CoRE MOF 2019.<sup>59</sup>

Since this analysis relies solely on CrystalNets.jl, which is independent from the tools used to build and clean the CoRE MOF database, it enabled the identification of 28 improper structures in the database, which were reported.

#### COMPARISON WITH TOPCRYST

I compared CrystalNets.jl and ToposPro, accessed through its online TopCryst interface, on a selection of MOFs common in the literature. The result, presented on Figure 1.11, shows that both usually return the same topology if it is in the RCSR when using the “Single Node” or the ‘All Nodes’ clustering options. On the other hand, the “Standard” clustering leads to different results in several cases. This comes from the difference in clustering heuristics: my implementation regroups each paddle-wheel into a single SBU and removes SBUs made of a lone oxygen (while bonding their neighbors together) while ToposPro does not systematically do so. These two heuristics can be individually toggled off in CrystalNets.jl by the user if necessary. In practice, keeping these heuristics usually leads to less clusters without loss of chemical meaning, which can in turn help identify relevant underlying topologies, like the **xbi** net for MOF-801 and UiO-66 which contains the information on connectivity between individual metal atoms and with organic linkers. Having access to other clustering options, like “PE” also allows considering alternative topological descriptions of the topology.

Name (CSD identifier)	CrystalNets.jl			ToposPro	
	Single/All Nodes	Standard	PE	Single/All Nodes	Standard (MOF)
HKUST-1 (LUDLED)	<b>tbo</b>	<b>tbo</b>	Unknown	<b>tbo</b>	5,6T2
JXUST-1 (SAXVIEW)	<b>pcu</b>	Unknown	Unknown	<b>pcu</b>	3,5,5,5T11
MIL-53 (MINVUA02)	<b>bpq/rna</b>	<b>bpq</b>	<b>sra</b> , ABW	*	<b>bpq</b>
MIL-100 (BUSPIP)	<b>moo</b>	Unknown	Unknown	<i>Error: timeout</i>	
MIL-101 (OCUNAC)	<b>mtn-e</b>	Unknown	<b>mtn-e-a</b>	<i>Error: timeout</i>	
MOF-5 (FIQCEN)	<b>tbo</b>	<b>tbo</b>	Unknown	<b>tbo</b>	5,6T2
MOF-14 (QOWRAV)	<b>pto</b>	<b>pto</b>	sqc11259	<b>pto</b>	5,6T46
MOF-177 (BABRII)	Unknown	Unknown	Unknown	3,3,5,6T36	4,4,4,4,6,8,8T1
MOF-801 (BOHKAM)	<b>fcu</b>	<b>xbi</b>	<b>ubt</b>	<b>fcu</b>	3,4,8T15
PCN-700 (RUBLAD)	<b>bcu</b>	Unknown	<b>pcb</b> , ACO	<b>bcu</b>	3,3,4,6,8T9
UiO-66 (SURHEU)	<b>fcu</b>	<b>xbi</b>	<b>ubt</b>	<b>fcu</b>	3,4,8T15
ZIF-8 (FAWCEN)	<b>sod</b> , SOD	<b>sod</b> , SOD	<b>sod-e</b>	<b>sod</b> , SOD	<b>sod</b> , SOD
ZIF-67 (GITTOT02)	<b>sod</b> , SOD	<b>sod</b> , SOD	<b>sod-e</b>	<b>sod</b> , SOD	<b>sod</b> , SOD

Figure 1.11: Comparison of CrystalNets.jl and ToposPro<sup>17</sup> (through TopCryst<sup>20</sup>) for the identification of topologies on a selection of MOFs.

Topologies in bold come from the RCSR,<sup>8</sup> in capitals from IZA-SC,<sup>58</sup> sqc11259 comes from EPINET<sup>14</sup> and the rest are part of ToposPro databases.

\*: ToposPro does not provide Single/All Nodes results for MIL-53 but returns **rna** as “Standard representation of covalent and ionic compounds” in addition to **bpq** as “Standard representation of coordination compounds and valence-bonded MOFs”.

ToposPro may fail for big nets because of the 3-minutes timeout of TopCryst: this happens for MIL-100 and MIL-101 among the tested structures. By comparison, CrystalNets.jl takes less than 10 s to handle them, but these timings are not comparable because the performance of the server on which the TopCryst webservice depends is unknown.

Subsequent to the publication of [1], Hoffmann [60] also investigated the difference between TopCryst and the CrystalNets web interface (detailed in section 1.5). He manually selected 100 different MOFs and identified their topology, then compared it with those output by TopCryst and CrystalNets. His results are reproduced in Table 1.1, where the “CSD code” column refers to the name of the structure in the Cambridge Structural Database.<sup>61</sup> On the 100 structures, TopCryst correctly identifies 68 and CrystalNets 80, which indicates that the bonding and clustering algorithms used in CrystalNets.jl are better tailored for the identification of MOF topologies.

## CoRE MOF 2024

The CoRE MOF 2019 database is, at the time of writing, undergoing an update to provide a new CoRE MOF database with more accurate structures, tentatively called CoRE MOF 2024 here. As part of the ongoing effort to build this database, I used CrystalNets.jl to analyze the new distribution of topologies and compare it to the previously obtained one. The 30 known topologies occurring most often are represented on Figure 1.12.

66.2 % of the structures in the ASR subset have a known topology with the “Single Node” clustering, slightly more than for the previous version of the database, which suggests that the

Nº	CSD code	Name	Topology	TopCryst	CrystalNets
1	FAVKAP	MIL - 88	acs	acs	acs
2	JEJWEB	Zn <sub>4</sub> O(D <sub>2</sub> - tcppda) <sub>1.5</sub>	act	act	Unknown/iac
3	HUHVUD	aea - MOF - 1	aea	Unknown	Unknown
4	PIVBEC	UMCM - 150	agw	agw	2-fold kgm
5	NEJJYI	In - alb - MOF - 1	alb	Unknown	Unknown
6	RAZXIA	UTSA - 16	ant	Unknown	Unknown
7	BOHXED	MOF - 802	bct	bct	bct
8	FIJDOS	MOF - 74	bnn	4,8T1	Unknown
9	XICYOZ	DUT - 68	bon	TimeOutError	Unknown
10	ALECEC	NU - 1351	cml	cml	Unknown/cml <sup>†</sup>
11	ICITEU	MOF - 500	crs	crs	crs
12	QEFWUV	MOF - 545	csq	csq	Unknown/csq
13	PEJNOJ	MOAAF - 1	ctn	ctn	ctn
14	LIMNUR	Zn(dmbd)	dmd	dmd	dmd
15	RIDCAJ	soc - MOF	edq	6,9T9	Unknown
16	RUBTAK	UiO - 66	fcu	fcu	fcu
17	OLOPUC	UTSA - 74	fgl	Unknown/fgl	Unknown/fgl
18	BEWCUD	UNLPF - 1	fjh	fjh	Unknown/scu
19	BOHWIG	MOF - 841	flu	flu	flu
20	ANUGEW	UMCM - 151	fmj	fmj	fmj
21	JEHBAC	[Me <sub>2</sub> NH <sub>2</sub> ][Mn <sub>2</sub> (H <sub>5</sub> L) <sub>3</sub> ](H <sub>2</sub> O) <sub>2</sub> ]	fns	3,6T252	Unknown/fns
22	CESFIQ	NOTT - 100	fof	fof	fof
23	RIXPOF	MOF - 519	fon	fon	fon
24	HANWAW	UTSA - 34	frf	frf	frf
25	JIZLEL	PCN - 94	ftw	ftw	Unknown/ftw <sup>‡</sup>
26	VEJZAM	ZIF - 5	gar	gar	gar
27	WONJUG	gea - MOF - 1	gea	Unknown	gea
28	KOZQEX	DUT - 75	gee	gee	gee
29	CAXTUS	DUT - 42	gra	gra	gra
30	SOKXOH	NU - 152	hbk	hbk	hbk
31	SEMMIJ	DUT - 126	hbr	hbr	hbr
32	FIJDEI	MOF - 72	hex	4,4,5,6T3	Unknown
33	ZIJSAO	UTSA - 61	hey	hey	hey
34	OFOJEB	MOF - 893	hfp	hfp	hfp
35	AZAVUU	MOF - 890	htp	3,3,4,6T148	htp
36	IXETEM	pbz - MOF - 1	hxg(-b)	hxg	hxg
37	ACODUT	UTSA - 30	hyb	tsa	tsa
38	KEFBII	IZE - 3	hyx	hyx	hyx
39	UGEMOK	DUT - 109	iab	3,4,6T130	iab
40	BOHWOM	MOF - 812	ith	ith	ith
41	SUKXUS	DUT - 6	ith-d	4,4,4,6T42	pto
42	SUKXUS01	MOF - 205	ith-d	ith-d	ith-d
43	OMULAL	TPMOF - 6	jea	hcb	Unknown
44	BICPUA	UTSA - 62	jjt	jjt	jjt
45	DABQOQ	Y - kce - MOF - 1	kce	Unknown	pcu
46	DABQUW	Y - kex - MOF - 1	kex	Unknown	0-dimensional
47	AZAVII	MOF - 888	kgd	kgd	kgd
48	PACFOP	Cu <sub>2</sub> (py) <sub>2</sub> (1,3 - bdc) <sub>2</sub>	kgm	kgm	kgm
49	XANLOP	UMCM - 3	koh	koh	koh
50	FINMUN	NU - 1400	lim	lim	lim

Table 1.1: Comparison of TopCryst<sup>20</sup> and CrystalNets by Hoffmann [60]<sup>†</sup>: only when using the “MOF” structure option. <sup>‡</sup>: only when using the “input” bonding option.

51	GAZCUI	DUT - 98	llj	llj	llj
52	CUSJAE	FJU - 6-TATB	llz	3,9,12T3	llz
53	XANKOO	CMOF - 1	lqm	pcu	pcu
54	WORREC	UTSA - 60	lvt	lvt	lvt
55	FIBKEI	PCN - 305	mfj	mfj	mfj
56	NAQKUM	USF - 3	mmm	mmm	mmm
57	OCUNAC	MIL - 101	mtn-e	TimeOutError	mtn-e
58	YIXBIQ	MOF - 101	nbo	nso	nbo
59	MAPMOI	[CoCl <sub>4</sub> ] <sub>0.25</sub> [Co <sub>3</sub> (μ <sup>3</sup> -OH)(CPT) <sub>4.5</sub> ]	ncb	ncb	ncb <sup>†</sup>
60	MIJRIJ	MOF - 907	nha	nha	nha
61	TOVKIA	PCN - 280	nht	3,3,6T99	nht
62	QUSBIP	MODF - 1	mod	mod	mod
63	XUDNUH	DUT - 71	nou	nou	Unknown/nou
64	ALECAY	NU - 1350	nuc	3,6T22	Unknown/nuc <sup>†</sup>
65	MAPHET	NU - 1301	nun	TimeOutError	TimeOutError*
66	SEMNIJ	NU - 110	ntt	ntt	ntt
67	BUYBOO	FDM - 3	ott	TimeOutError	ott
68	SAHYOQ	MOF - 5	pcu	pcu	pcu
69	HUHWAK	pek - MOF - 1	pek	Error	pek
70	TEYZAB	MOF - 1210	pfm	pfm	pfm
71	QOWQUO	MOF - 14	pto	pto	pto
72	BIMDIL	MOF - 11	pts	pts	Unknown/bcu
73	UKOLOV	MOF - 150	pyr	pyr	pyr
74	ERIRIG	MOF - 177	qom	qom	qom <sup>†</sup>
75	XICNOO01	DUT - 67	reo	reo	reo
76	CUSQEP	CTH - 6	rtl	rtl	rtl
77	EPISOM	NOTT - 140	scu	mmm/scu	mmm/scu
78	DOGBEI	PCN - 224	she	Error	sqc13549/she
79	TUTWUC	PCN - 223	shp	Error	Unknown/shp
80	LIDDUB	PCN - 250	edq/soc	edq/soc	edq/soc
81	RIDCEN	In - soc - MOF - 1 a	edq/soc	edq/soc	edq/soc
82	UFOROZ	Tb - sph - MOF - 1	sph	TimeOutError	Unknown/sph <sup>†</sup>
83	BOHWUS	MOF - 808	spn	spn	spn <sup>†</sup>
84	DODBUV	PCN - 225	sqc	sqc7923/sqc	sqc7923/sqc
85	GECXUH	MOF - 2	sql	sql	sql
86	KEVWIU	(ZnI <sub>2</sub> ) <sub>3</sub> (tpt) <sub>2</sub>	srs	srs	srs
87	LAYRAH	ZJNU - 74	ssa	ssa	sty/ssa
88	OFOJAX	MOF - 892	stp	stp	stp
89	SOKXIB	NU - 151	sty	sty	sty
90	DAYMAS	Zn(acdc)	sur	sur	sur
91	FIQCEN	HKUST - 1	tbo	tbo	tbo
92	ACOCOM	DUT - 49	tfb	tfb	tfb <sup>†</sup>
93	EBUCOT	[Zn <sub>2</sub> (btc)] <sub>8</sub> [Zn <sub>2</sub> (btc) <sub>4/3</sub> ] <sub>3</sub>	tfe	tbo	tbo
94	UNEJEE	BUT - 12	the	the	the
95	CUSYAR	MOF - 210	toz	Error	toz
96	OVOKOB	MOF - 910	tto	3,4,11T2	Unknown
97	ZECRAC	DUT - 25	ttz	ttz	ttz
98	TAKKIC	UHM - 25	ucp	ucp	ucp
99	TIZQOK	DUT - 32	umt	umt	umt
100	HOGLEV	PCN - 12	zhc	zhc	zhc

Table 1.1: Comparison of TopCryst<sup>20</sup> and CrystalNets by Hoffmann [60] (continued)<sup>†</sup>: only when using the “MOF” structure option. <sup>‡</sup>: only when using the “input” bonding option.\*: CrystalNets.jl correctly yields **nun** but takes 80 s, above the timeout threshold of 60 s.

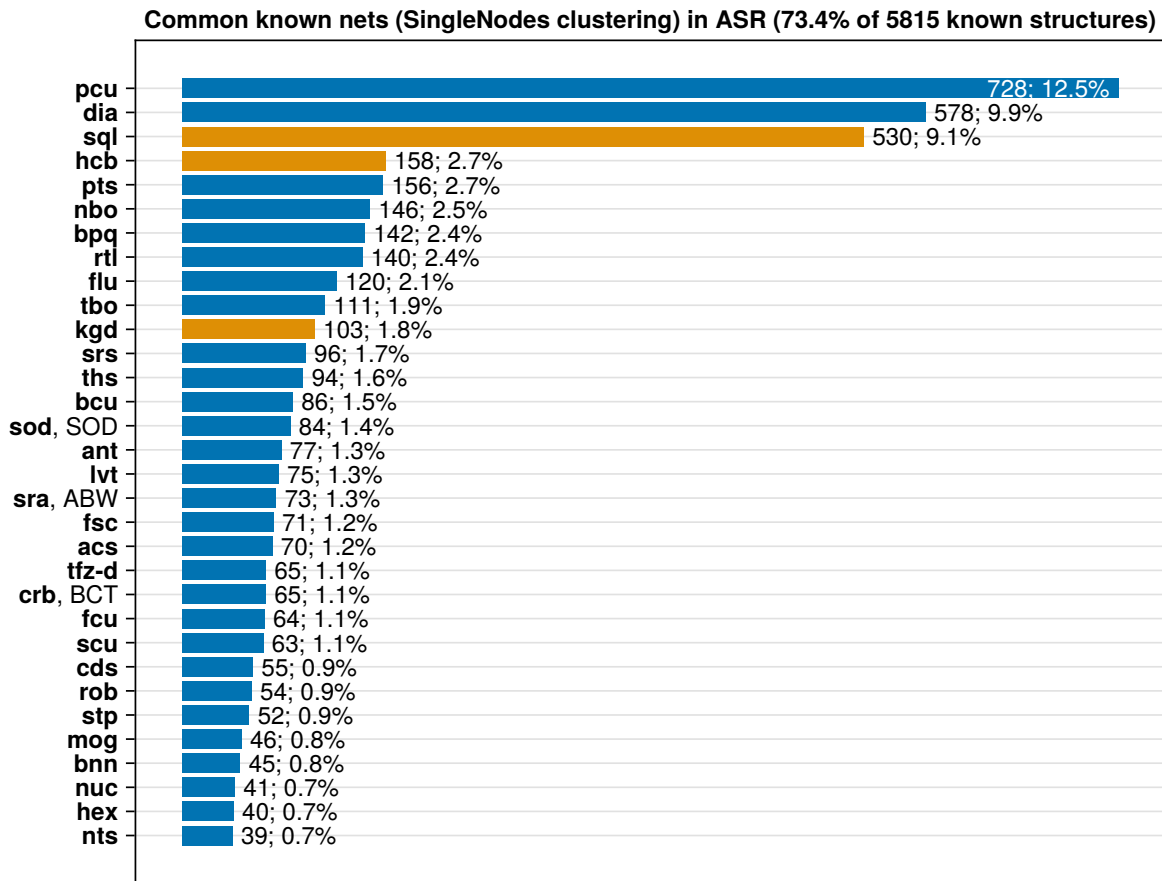


Figure 1.12: Number of structures per known net in the ordered structures of ASR in the CoRE MOF 2024 database (still in construction). 3D topologies are in blue, 2D in orange.

MOFs representations may be more amenable to automatic analysis. The distribution itself shows some similarity, with **pcu** and **dia** largely above all other known 3D topologies again, but the new database includes many more 2D structures such as **hcb** (honeycomb) and **kgd** (kagome dual), and more particularly **sql** (square linear). This indicates a higher diversity of structures.

21.5% of structures are interpenetrated (compared to 13.3% with CoRE MOF 2019), which means that their chemical bond network can be divided into several periodic subsets that have no connection between them. The distribution of interpenetrated nets is represented on Figure 1.13. Similar to the global distribution, nets **dia**, **pcu** and **sql** are the ones that exhibit the highest number of interpenetrated structures with these topologies.

It should be noted that all interpenetrated subgraphs share the same topology in general, so the previous figures count one occurrence for that topology per structure. However, there are a few exceptional cases like the one illustrated on Figure 1.14, where nets corresponding to different topologies interpenetrate. Only five such structures were identified in CoRE MOF 2019 and six in CoRE MOF 2024, and they were discarded from the previous statistics.

Topology **dia** shows the greatest range of interpenetration, from 2- to 8-fold in more than ten structures, but also features cases of 9-fold and 10-fold interpenetration, whereas **pcu** is only

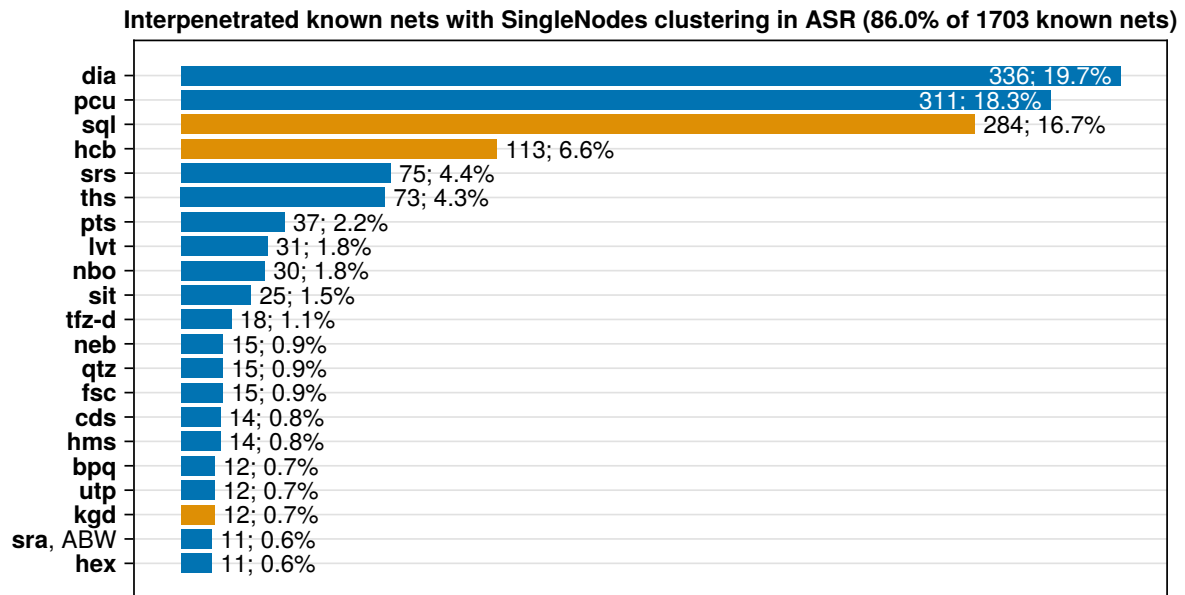


Figure 1.13: Number of structures per known interpenetrated net in the ordered structures of ASR in the CoRE MOF 2024 database (still in construction). 3D topologies are in blue, 2D in orange.

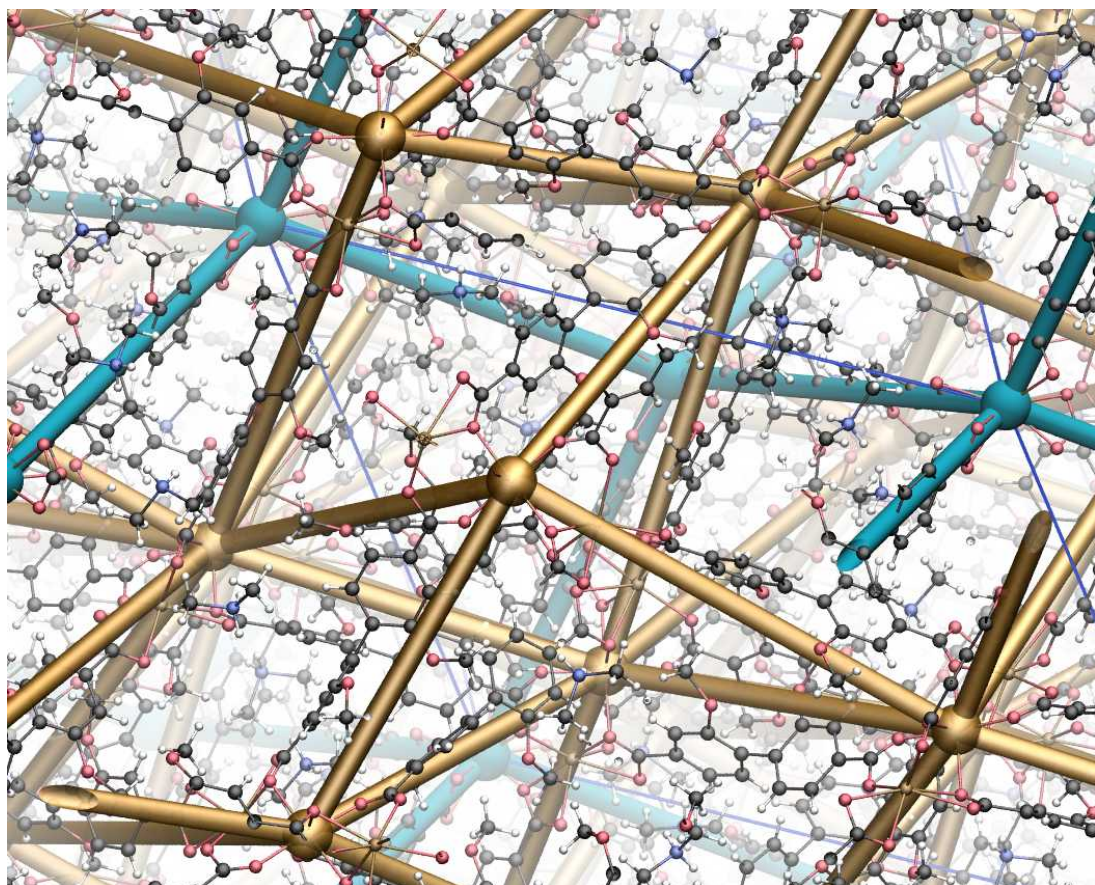


Figure 1.14: Hetero-interpenetration of nets **dia** (blue, matt) and **bcu** (ocre, glossy) in the MOF of Xu et al. [62] (structure WEBZEK in the CSD<sup>61</sup>)

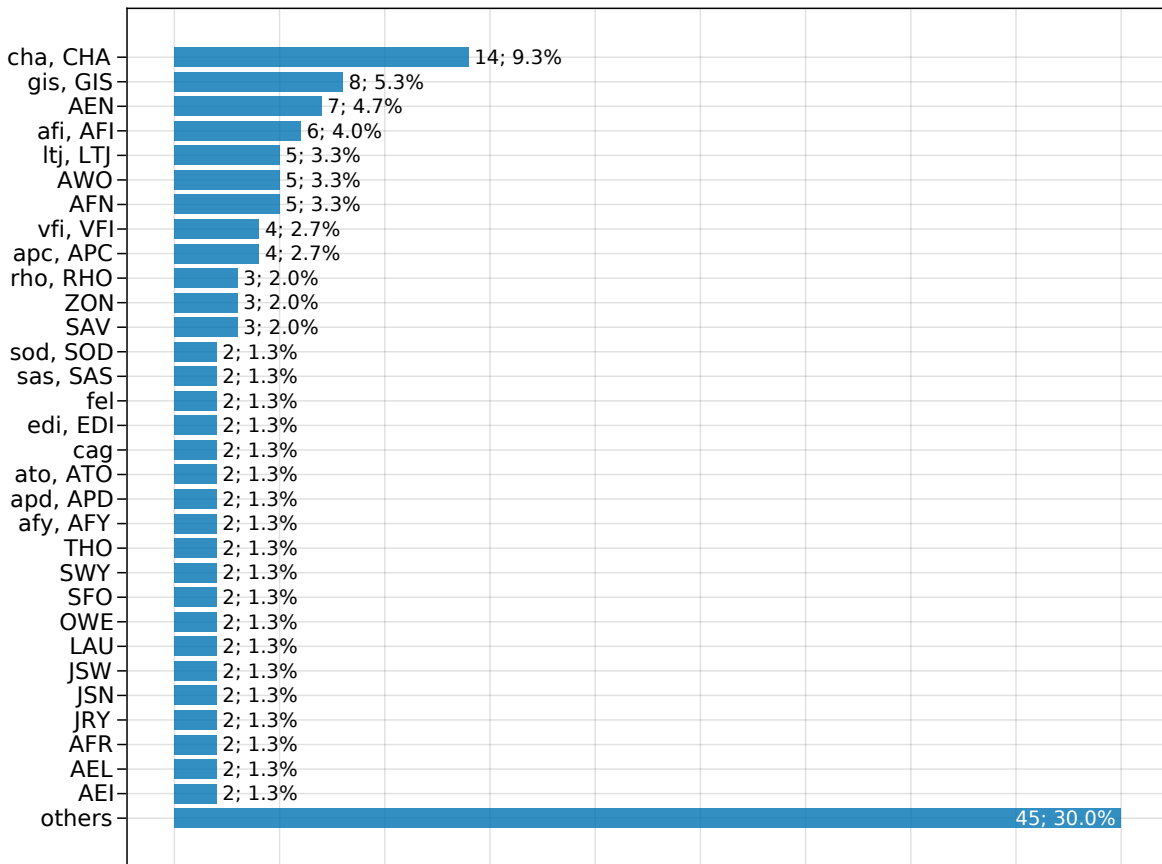


Figure 1.15: Number of structures per known net in the ALPO database.<sup>63</sup>

present up to 4-fold in more than ten structures and 5-fold in one structure, and **sql** is present up to 6-fold in three structures.

### 1.4.3 Database of aluminophosphates

Additionally, I surveyed the topologies of Zheng, Li and Yu's database of aluminophosphates.<sup>63</sup> These 385 experimental structures are given as CIF files with little to no cleaning from the publications they stem from. In particular, solvent is included and the structures can contain multiple overlapping atoms with partial occupancy, while atoms of the main structure are often partially substituted. CrystalNets.jl automatically removes 0-dimensional residues like solvent and keeps for each site only the atom with the highest occupancy. Using the "Zeolite" structure option of CrystalNets.jl, the software recognizes 64% of the 205 3D nets in the database. This number rises to 73% by adding a heuristic to remove P–O–P and Al–O–Al linkages, which are usually not accounted for when computing the topologies of AlPOs.

The 31 known nets represented on more than one structure in the database are represented on Figure 1.15. With the exception of **fel** (originating from feldspars) and **cag** (occurring in variscite), they are all referenced in the database of zeolite frameworks of IZA-SC. This is expected since AlPOs are structurally close to zeolites, with the replacement of Si atoms by Al and P. Conversely, it shows that **fel** and **cag** may be nets underlying the structure of unreported zeolites, especially since both only have 4-coordinates vertices, corresponding to the T-atoms, and can be embedded to exhibit pores.

Most known structures have a net represented only once (45 nets *i.e.* 30%) or twice (19 nets *i.e.* 25%). In comparison, among the unknown nets, 1 occurs on three structures, 5 on two and the 32 others appear only once each. Both distribution tails and comparison of known and unknown nets follow a pattern similar to the CoRE MOF database.

For the structures for which the underlying net has been recognized as one of the IZA-SC, there is little doubt on the validity of the detected net. For the others however, there is no systematic way of determining whether the detected net is indeed that representing the structure or not except from visually checking the adequate superposition of the detected net and the initial framework for each file. This limitation comes from the lack of cleaning of the input CIF files, which can lead CrystalNets.jl to interpret solvent residues as part of the framework for instance, or duplicate atoms as two different atoms instead of one. This issue can be circumvented by either cleaning the CIF inputs, as in the CoRE MOF database, or by manually checking the correspondence if working on individual files. Obviously, this limitation is inherent to the quality of the input files and affects all topology determination codes.

#### 1.4.4 Hypothetical zeolites

The study of framework topology has historically been extensively applied to zeolites.<sup>64</sup> One reason is that the structure of zeolites, made only from tetrahedral (T = Si, Al, ...) atoms bridged by T–O–T linkages, is simple enough to show an almost one-to-one correspondence between each framework and its underlying net. Using this fact, large databases of hypothetical zeolites have been devised: the core idea consists in embedding 4-connected nets in real space, either by enumeration of the nets<sup>65</sup> or by Monte Carlo sampling of vertex positions.<sup>66</sup> The vertices correspond to Si atoms while O atoms are placed along the edges. Each obtained structure is subsequently refined by minimizing its energy through molecular dynamics and with simulated annealing.

Since these structures are built from their underlying net, I tried to perform the opposite operation on the Predicted Crystallography Open Database (PCOD)<sup>66</sup> to assess my implementation. This database contains 331 172 CIF files representing zeolites with energies within 30 kJ/mol (per SiO<sub>2</sub> unit) of  $\alpha$ -quartz, which were analyzed by CrystalNets.jl in 45 minutes using 20 cores (Intel Xeon Silver 4210R CPUs, 2.4 GHz). Bond guessing forced O atoms to have at most 2 neighbours, which is the default heuristic for O atoms not bound to metals: this incidentally ensures that all vertices of the net correspond to Si atoms.

As the SiO<sub>4</sub> tetrahedra are somewhat distorted during the refinement steps, the bonds guessed from the resulting structure do not always correspond to those from which it was built. As a result, there were 11 frameworks whose T-atoms were not all 4-connected, and 75 other frameworks whose coordination sequences did not match that recorded in the database. Two structures were found to have the same underlying net: 8013876 and 8035701, the latter having different detected coordination sequences than indicated. Barring these 86 mismatched structures, 18 nets only have a 2D periodicity and 31 are unstable nets not handled by CrystalNets.jl. All those “problematic” nets represent less than 0.04% of all nets in the database. For the rest, no two structures had the same underlying net.

Indeed, by construction of the database, structures whose topology is already part of the database are removed. The invariants used to identify the topology are the coordination sequences and the ring sizes: this strategy does ensure that no two structures with the same net are present, but it is too restrictive since two distinct nets could share these invariants. In the future, the use of a unique topological identifier through `CrystalNets.jl` could thus potentially lead to the generation of more structures.

## 1.5 WEB INTERFACE

`CrystalNets` is the web interface to the `CrystalNets.jl` Julia library, accessible online at <https://progs.coudert.name/topology>. The focus of this online tool is to provide easier handling than its programmatic back-end, to make it maximally accessible. Its interface, presented on [Figure 1.16a](#) simply consists in an input box where the user can drag-and-drop or browse the input file. The main options are visible below, with pre-selected default values. These main options include the type of material, which may guide the automatic choice of the subsequent options, the bonding algorithm, the clustering strategy, and some visualization export choices. A panel of advanced options, folded by default, can also be accessed to tweak the cutoff radii of the bonding algorithm or toggle the aromatic cycle detection, among other choices.

Once the input and options have been selected, typing Enter or clicking the “Submit” sends the request to a server, which internally calls the `CrystalNets.jl` library, formats the answer and transfers it back to the user. The resulting page, illustrated in [Figure 1.16b](#), contains a green box with the identified topologies, as well as a visualization panel on the right. Visualization files can be downloaded by clicking on the icon next to the required exports: they are in VTF or PDB format, both being accepted by the VMD visualization software.<sup>10</sup> A yellow box, folded by default, may also appear in case `CrystalNets.jl` emitted some warnings or information statements. If an error occurred, or if no net can be extracted (as may happen with a 0-dimensional input), a red box detailing the error appears. In any case, the HTML result page contains all the information; it can thus be saved locally and reopened at a later time if need be.

The visualization panel on the right of the result page relies on the `3Dmol.js` library.<sup>67</sup> This choice was mainly driven by its reactivity when displaying even large crystals, as well as its ease of manipulation. As with any such visualization tool, dragging the canvas rotates the crystal while zooming in or out is done with the mousewheel. The home button on the left resets the viewer position and zoom. Clicking on the right-most button, or double-clicking the canvas, displays it across the entire webpage, which can be convenient to focus on visualization.

The middle buttons control what is currently being displayed. Each button either directly controls a visible element, *e.g.* the button showing the input crystal or its trimmed version, or it reveals a menu with other buttons. For instance, each substructure of an interpenetrated crystal has its own menu. Navigating these menus thus allows interactively choosing the visible elements on the canvas, to enable, for example, focusing on the superposition of the input crystal and the “Single Node” representation of its first substructure only, as illustrated on [Figure 1.17](#).

### Crystallographic file and options

Upload a CIF file, or any other crystallographic file format accepted by [chemfiles](#), here:

No file selected

**Submit**

▼ Main options:

Structure type: [\[?\]](#)

Auto  MOF  Cluster  Zeolite  Guess

Bonding: [\[?\]](#)

Auto  Guess  Input

Clusterings: [\[?\]](#)

Auto  SingleNodes  AllNodes  Standard  PE  PE&M  Input  EachVertex

Exports: [\[?\]](#) (check [the tutorial for visualization](#))

Input  Trimmed  Subnets  Attribution  Clusters

(a) Input prompt with the main options including the structure, bonding and clustering algorithms, and visualization outputs. More advanced options exist below.

### Crystallographic file and options

**Results for MOF-14.cif:**

**Substructure n°1**

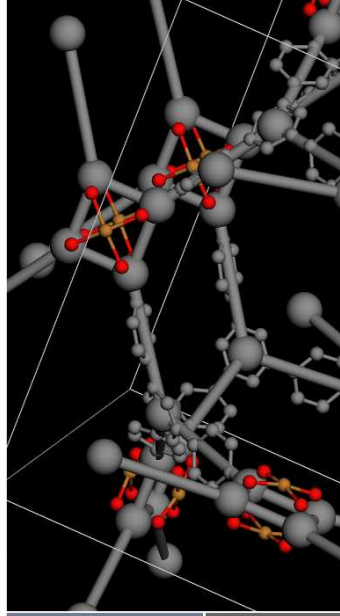
SingleNodes: [pto](#)  
PE: [sqc11259](#)

**Substructure n°2**

SingleNodes: [pto](#)  
PE: [sqc11259](#)

› CrystalNets emitted some warnings (click to reveal):

No file selected



Home

Substruc

(b) Response page, including the results and a visualization panel on the right (truncated here)

Figure 1.16: CrystalNets web interface (<https://progs.coudert.name/topology>)

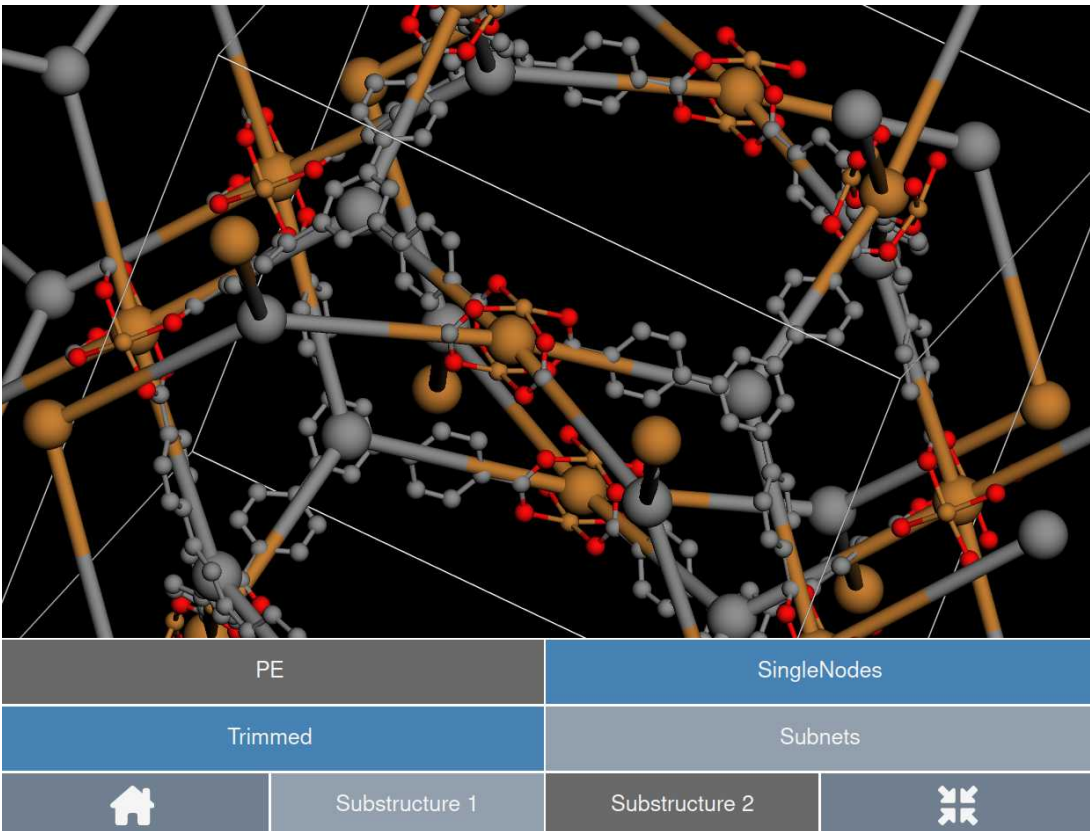


Figure 1.17: Full screen mode of the visualization panel on the CrystalNets web interface

The server handling the requests is written with the Bottle library in Python. Upon receiving a user query for CrystalNets, it calls a custom code written in Julia, passing on the input and related options. This code relies on the `DaemonMode.jl` Julia library to minimize the experienced latency. Indeed, Julia works with a Just-In-Time (JIT) compilation paradigm, which enables highly specialized compilation of code leading to very fast execution.<sup>33</sup> The counterpart of this strategy is the compilation time incurred each time a function is called with a new set of argument types, which causes some initial latency.

Although several mitigation strategies have been implemented to relieve this issue in most cases, the latency requirements of a web server are particularly stringent, since this waiting time is immediately felt by the user. `DaemonMode.jl` is a Julia library offering an a latency-reduction scheme well adapted to this use-case. Instead of launching a new Julia process with each request, it forwards each query to a single Julia process that operates all of them. JIT compilation can then be performed on the unique process at startup, and any subsequent Julia call will simply be executed by the same process, without the need to compile anything at all, effectively resulting in an ahead-of-time compilation of the necessary codebase.

Depending on the load state of the server, it appears that most requests can be served within a few seconds at most. The only cases exceeding ten seconds occur with very large nets, for which the latency time is negligible with respect to the actual processing time of the topology identification algorithm. A timeout is set to one minute, after which the computation is aborted: in such a case, which requires a particularly large and complex net, the topology identification should be operated on a local installation of `CrystalNets.jl` instead.

## 1.6 SUMMARY AND PERSPECTIVES

`CrystalNets.jl` is a Julia library that implements topology identification on crystalline materials. The core algorithm for topology detection is strongly inspired from that used in `Systre`<sup>19</sup> which computes a topological genome, that is a sequence of numbers uniquely identifying the net underlying the given structure. The algorithmic and implementation improvements of `CrystalNets.jl` still preserve the soundness and polynomial time complexity of the initial algorithm, while offering a much better performance across all kinds of nets: it is on average 56 times faster than `Systre` and up to thousands of times faster in some cases. Moreover, the software directly takes crystallographic files as input and can automatically detect bonds if they are absent; it also includes a general clustering algorithm with different target options for framework materials, and heuristics adapted to metal–organic frameworks specifically.

Overall, `CrystalNets.jl` was successfully tested against a large diversity of crystalline structures: MOFs, aluminophosphates, zeolites and many other crystals. Even on large databases, the program shows great performance and can reliably recognize any structure in the `Systre` archive of the RCSR, in the IZA-SC database of zeolite structures and in EPINET. It successfully attributes known topologies to 60% of the structures in CoRE MOF 2019 after automatically clustering the vertices according to the “Single Node” policy. It was also able to recognize 73% aluminophosphate structures from Zheng et al. [63]’s database, automatically removing solvent residues and colliding atoms when possible.

`CrystalNets.jl` can be used as a faster and more convenient alternative to `Systre` and `ToposPro` for the identification of nets underlying crystalline structures. Its programmatic interface can be integrated to any computational pipeline written in Julia, as well as some other languages like Python through bindings. Its web interface makes it ideally accessible to anyone without having to learn a programming language, and still contains most of the features of the underlying software. Moreover, the included visualization panel allows immediately checking the accuracy of the detected topology, which is critical to ensure reliability.

The topology of a framework can also be useful apart from its bare identity, which mostly serves for classification and comparison purposes. While `PeriodicGraphs.jl`, another library I developed underlying `CrystalNets.jl`, already contains some tools to study the properties of topologies, more work is required to be able to automatically compute the natural tiling<sup>27</sup> of a crystal structure, which would be of special interest to study the porosity of frameworks, directly linked to their adsorption properties.





# 2

---

## CATION PLACEMENT IN ZEOLITES

---



2.1	Cationic zeolites . . . . .	48
2.1.1	Structure and properties . . . . .	48
2.1.2	Aluminium placement . . . . .	50
2.1.3	Cations . . . . .	54
2.2	Methodology for the prediction of cation placement . . . . .	54
2.2.1	Underlying algorithms . . . . .	56
2.2.2	Meta-algorithms . . . . .	62
2.2.3	Extraction of sites and population from simulation . . . . .	66
2.3	Results . . . . .	68
2.3.1	Case study: FAU . . . . .	68
2.3.2	Other zeolites . . . . .	75
2.4	Energy computation . . . . .	79
2.4.1	Force fields . . . . .	79
2.4.2	Short-term interactions . . . . .	80
2.4.3	Ewald summation . . . . .	81
2.4.4	Precomputation . . . . .	83
2.5	Possible alternatives . . . . .	87



Among the many possible kinds of adsorbents, zeolites form a family which is particularly popular in the industry. Small gases tend to adsorb preferentially near cations when they are present, which makes the study of cationic zeolites primarily relevant to the understanding of industrial adsorption processes. This chapter presents the chemical nature of cationic zeolites and explains the challenges and methods used to obtain representative atomistic models of them for subsequent adsorption simulations.

## 2.1 CATIONIC ZEOLITES

In this section, I detail the general structure of cationic zeolites and highlight the challenges associated with the molecular simulation of these systems.

### 2.1.1 Structure and properties

Zeolites are a family of aluminosilicates, first discovered by Axel Fredrik Cronstedt in 1756. Similar to glass, their atomic structure is made of tetrahedra  $\text{TO}_4$  where the central 4-connected T-atoms, usually Si but sometimes substituted by other atoms, are thus bridged together by bivalent O. They are crystalline however, with typical unit cell lengths varying between 6 Å and 25 Å, and have nanopores, usually below 2 nm in size. This general structure is illustrated in Figure 2.1

The different kinds of zeolites are separated by topology: each known zeolite topology is given a capital three-letter code by the International Zeolite Association Structure Committee (IZA-SC). As explained in section 1.1.1, the topology designates the information extracted from the network of chemical bonds: in the case of zeolites, this network can be simplified by taking one vertex per T-atom, and abstracting each oxygen bridge as a simple edge between the two corresponding T-atoms. The simplicity of this protocol makes it clear that the net of a zeolite is very close to the structure it represents – in other words, simplifying the crystal into its net does not lose much information on the initial structure – which explains why a classification by topology is the primary way to distinguish different zeolite structures. It is noteworthy that such a classification is vastly insufficient in the case of MOFs, where the chemistry of metal nodes and the nature of the ligands is thus used first; while for other kinds of materials such as glasses, it is downright impossible to establish because of the absence of cell periodicity.

While millions of hypothetical zeolite topologies have been identified by numerical methods,<sup>66</sup> only 256 have been experimentally observed as of 2024 (plus 9 intergrowth families, which are not strictly crystalline). This discrepancy may stem from the metastability of zeolites, whose porosity makes them thermodynamically less favourable than glass or other dense phases.<sup>68</sup> On the other hand, new experimental zeolite topologies have been discovered each year in the last twenty years, which indicates that the access to new structures is also limited by the current synthetic methods used. Moreover, new synthetic routes can allow new chemistry on existing topologies.<sup>69,70</sup>

Indeed, each given topology may give rise to several zeolites that differ by their exact chemical composition. A very common kind of substitution consists in replacing some Si by Al, or, more anecdotally, B<sup>71</sup> or Ga.<sup>72</sup> Each such substitution introduces one extra electron in the system because of the difference in oxidation state of the T-atom, hence these zeolites contain cations to balance the additional charge. Those are called “extra-framework” cations because they

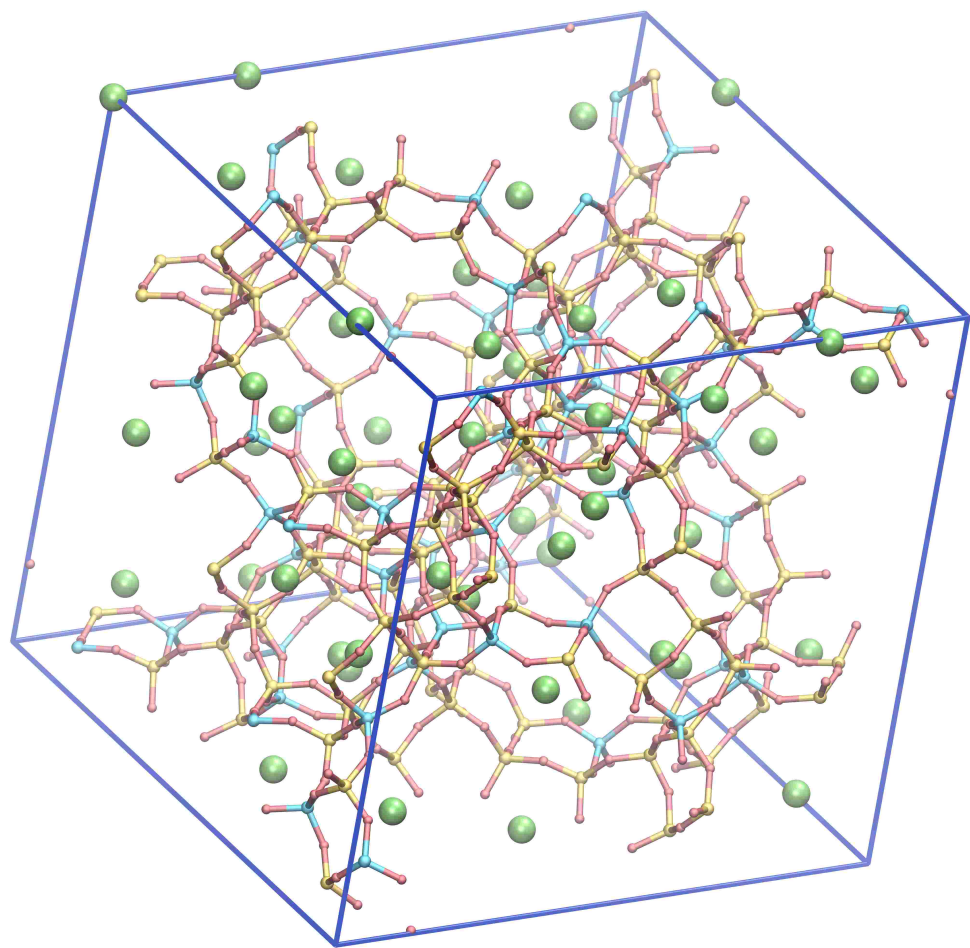


*Figure 2.1: Unit cell of a zeolite, in this case a faujasite. The T-atoms are usually Si (in yellow), sometimes substituted by Al (in blue), and bridged together by O (in red). Na<sup>+</sup> cations (green spheres), not bonded to the previous framework atoms, ensure the electroneutrality of the material.*

are not covalently bonded to the framework. The nature of the cation itself leads to some more variability: sodium cations are usually the ones used during synthesis, and can then be exchanged with other cations.<sup>73,74</sup> Some other T-atom substitutions include Ge,<sup>75</sup> Sn,<sup>76</sup> or transition metals such as Ti, Fe or V.<sup>76,77</sup>

Ion exchange is currently the most prevalent industrial use case for cationic zeolites, especially as water softener for laundry agents.<sup>70</sup> Their considerable internal surface and the accessibility of active sites such as the cations or the substituted metals make them also useful for catalysis.<sup>77</sup> Other applications include nuclear waste storage,<sup>78</sup> building material additives,<sup>79</sup> water absorbents,<sup>80</sup> soil treatment,<sup>81</sup> oxygen and contrast agent carrier for cancer treatment<sup>82</sup> and others. Finally, they can be used as adsorbents for gas separation or storage, which is also of capital industrial interest.

Zeolite structures are mostly considered rigid structures in simulations, although some notable exceptions exist,<sup>83,84</sup> and most actually possess a flexibility window<sup>85</sup> which can be exploited in specific cases of adsorption.<sup>86</sup> In addition, T-atom substitution tends to modify only slightly the T-O bond length (on average, Si-O: 1.603 Å while Al-O: 1.736 Å) and does not affect the O-T-O angles much, averaging at 109.5°.<sup>87</sup> As a consequence, the structure of a substituted

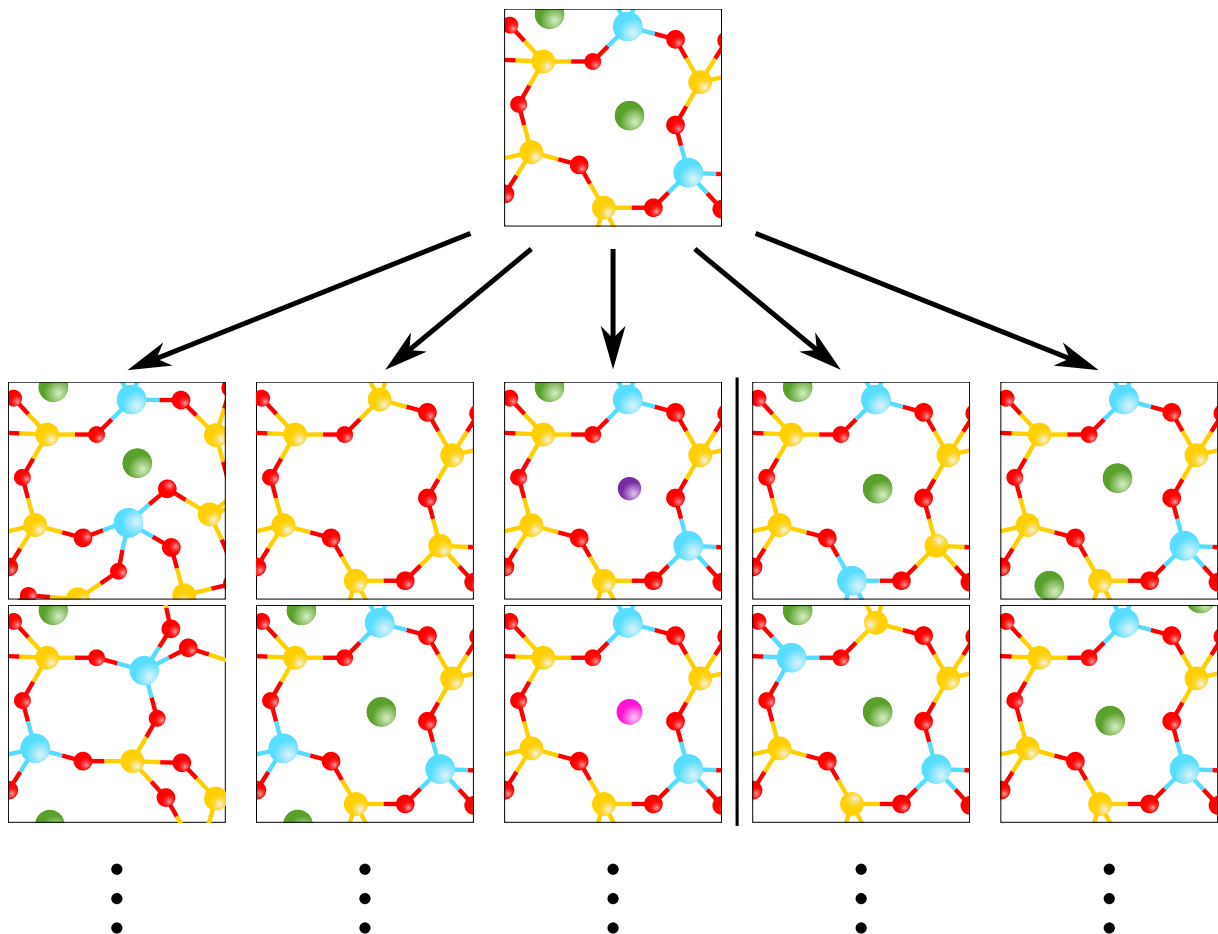


*Figure 2.2: Schematic representation of the five defining characteristics of a cationic zeolite model. From left to right: topology, Si/Al ratio, nature of the extra-framework cations, Al placement, cation placement. The first three are properties of the material that can be experimentally controlled; the last two are additionally necessary for molecular simulations.*

zeolite can usually be well approximated by taking the reference structure of the topology (provided as a pure silicate by the IZA-SC) and replacing the relevant silicon atoms by their substituent.

The five properties characterizing a unique zeolite model are represented on Figure 2.2. The topology, Si / Al ratio and nature of the cations define a zeolite used experimentally: for example, the name “Li-LSX” refers to the zeolite of topology FAU with Si / Al = 1 and cation Li<sup>+</sup>. However, two additional parameters are required in order to know the exact position of all atoms in a unit cell of the material, which is necessary for molecular simulations: they are the repartition of the substituents among the T-atoms and the placement of the cations in the zeolite. Both will now be studied in detail.

### 2.1.2 Aluminium placement

For simplicity, all zeolites discussed henceforth will be considered having only either Si or Al as T-atoms. The question of the repartition of the substituents thus become that of determining which T-atom should be occupied by Al instead of Si. This turns out to be a difficult experimental issue to solve.

## RULES

The first experimental rule, which is obeyed by almost all known zeolites, was discovered by Walter Löwenstein [88]. It states that no two aluminium atoms may be neighbours, in the topological sense of being bridged by an oxygen. This hard rule limits the maximum number of aluminium atoms to half the number of T-atoms in general, and less for topologies that contain odd cycles: for instance, if there is a cycle of 5 T-atoms, only two among them can be aluminium.

The amount of aluminium atoms in an aluminosilicate is usually discussed in terms of Si/Al ratio. Löwenstein's rule thus limits the minimal Si/Al ratio to 1, which corresponds to the maximum number of aluminium atoms and thus of cations. Zeolites with high Si/Al ratios, usually called high-silica zeolites, contain few cations and tend to be hydrophobic; they also tend to adsorb fewer molecules per unit cell since cations are privileged adsorption sites.

While Löwenstein's rule is widely accepted as an axiom, and is mainly sustained by the absence of experimental synthesis of any zeolite with Si/Al ratio lower than 1, it is not currently proven. This comes from the cost of the few spectroscopic methods that allow identifying the precise locations of Al atoms:  $^{27}\text{Al}$  and  $^{29}\text{Si}$  magic-angle spinning NMR can be used to provide some limited information,<sup>89</sup> while Dedeček et al. [90, 91] used UV-Visible-NIR spectroscopy on  $\text{Co}^{2+}$ -exchanged ZSM-5 with high Si/Al ratio to retrieve their Al distribution. Yet, this method cannot be generalized to low-silica zeolites. Density Functional Theory (DFT) computation confirms the rule in general, but also shows that potential violations could exist for some zeolite topologies such as HEU.<sup>92</sup>

The second rule, proposed by Dempsey et al. [93] on the basis of FAU zeolites with varying Si/Al ratios, states that when possible, the number of next-neighbours Al atoms should be minimized to decrease the number of unfavourable interactions between close aluminium atoms. This rule is actually known to be violated in many real zeolites, including dealuminated FAU. Speculatively, this may come from the fact that Dempsey et al. [93] made their observations on zeolites whose synthesis lead them to reach their global energy minimum, while many other synthetic routes can create structures trapped in a local energy minimum with respect to their Si/Al ordering.

## SIMULATION METHODOLOGIES

Overall, the lack of experimental evidence attesting to the precise position of aluminium atoms in zeolites makes the theoretical prediction of such placement delicate, because of the need for verifiable comparison points. In particular, a crucial question is whether the actual Si/Al ordering is the thermodynamically most stable one.<sup>94</sup> If not, it means that the structure is in a metastable state, which is likely to be the case for many real zeolites as evidenced by Gábová et al. [91] in one of the few experimental studies tackling that very issue.

Even if the aluminium placement can be obtained as that which minimizes the global energy of the structure, this does not necessarily mean that the placement itself is periodic, nor that it should follow the same periodicity as the unit cell. Yet, as it is difficult to provide a concrete result on the localization of aluminium atoms without making such hypotheses, the studies in the literature only focus on the study of their placement in a single unit cell, supposing that the rest is periodic.

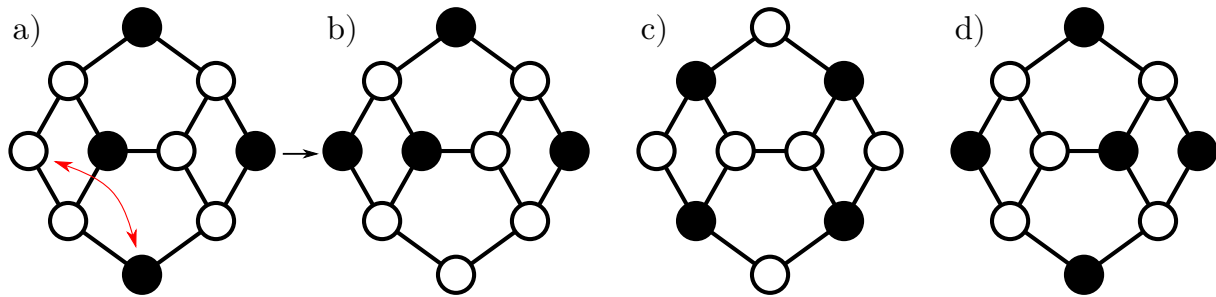


*Figure 2.3: Schematic representation of aluminium placement in a zeolite fragment. Empty circles represent silicon, filled circles represent aluminium. Black edges represent T-O-T bridges. Löwenstein's rule forbids two aluminium atoms from being neighbors.*

a) An exchange move between a silicon and an aluminium, used in Marie Jeffroy's scheme.<sup>96</sup>

b) The result of the exchange.

c) A blocked configuration where no move is possible.

d) A configuration with one more aluminium, which cannot be reached from c).

In these conditions, the last remaining question is the simulation methodology to use to find the global energy minimum of the structure. The most basic method consists in generating all possible configurations, computing their energy, and choosing that which minimizes the energy. This approach has actually been widely followed to find the preferred location of aluminium atoms when there are only one or two Al per unit cell, using DFT to compute the energy.<sup>94,95</sup> The involved computational cost makes it impractical for lower Si/Al ratios however, which are of major interest for adsorption purposes.

Marie Jeffroy [96] proposed a more refined Monte Carlo (MC) protocol for this problem, based on classical force fields for energy computation. Starting from a configuration with the target Si/Al ratio under Löwenstein's rule, each MC step consists in exchanging the positions of a Si and an Al while maintaining Löwenstein's rule, and accepting or rejecting the step according to the Metropolis-Hastings criterion (explained in section 2.2.1). For low Si/Al ratios, this algorithm requires adding a “restart” option that entirely repopulates the aluminium atoms at random under Löwenstein's rule, because that very rule can lead to blocked situation where no single Si/Al exchange is possible, as illustrated on Figure 2.3.

García-Pérez et al. [97] proposed an innovative method to assess the validity of theoretically-obtained aluminium placements, by studying alkane adsorption isotherms (defined in section 4.2.1). They found that different Si/Al orderings can lead to different isotherms, which, conversely, means that obtaining a precise experimental isotherm can allow retrieving the aluminium ordering. Their subsequent study [98] determined that topologies LTL, FER, TON, and MOR exhibited isotherms sensitive to the aluminium placement, which could thus be retrieved from experimental adsorption isotherms, while FAU, LTA, MEL, and MFI were not sensitive enough. Findley et al. [99] reused a similar method with CO<sub>2</sub> isotherms instead, combined with reverse Monte Carlo method to tackle lower Si/Al ratios: they conclude that topologies LTA, CHA are more likely to have their aluminium atoms placed at random compared to FER.

Hence, given the uncertainty that any aluminium placements obtained by thermodynamical simulation actually reflects those observed in real zeolites, I chose to consider that the aluminium placement in the zeolites is taken at random. In practice, each zeolite with a given Si/Al ratio is

modeled as the average of six zeolites of that topology with the same Si/Al ratio, all following Löwenstein's rule but having different Al repartitions (taking symmetry into account as well). The results are computed on each of these six models, and averaged to obtain the result for the zeolite.

To obtain the zeolite structures with random aluminium placements obeying Löwenstein's rule and the target Si/Al ratio, I implemented the following algorithm:

- The starting point is either the zeolite filled with Si if the required Si/Al ratio is above 3, else a zeolite filled with as many Al as possible using a greedy algorithm. That greedy technique consists in doing a graph traversal of the T-atoms, transforming each atom into an Al if it is not the neighbour of an Al, or making it a Si otherwise: if all cycles in the graph are even, this is guaranteed to provide an aluminium placement with the minimal Si/Al of 1. The main interest of such a starting point is for the lowest Si/Al ratios, where a stochastic filling approach from a silicic zeolite would likely miss the few desired structures, whereas the greedy algorithm reaches them.
- The main algorithm then alternates between adjusting the number of Al and changing their positions, back and forth.
  - The position update follows the principle of Marie Jeffroy's MC scheme but disregarding the energy change: one Al is picked at random, then one Si is chosen at random among those that have either no Al neighbor or only one which is the picked Al, and both are exchanged. This guarantees that the resulting structure still follows Löwenstein's rule.
  - The number of Al atoms is modified if the current Si/Al ratio does not correspond to the target: if it is too high, an Al is converted into a Si, and otherwise a Si that has no Al neighbour is converted into an Al.
- Since the situation can be blocked (see [Figure 2.3](#)), the algorithm sometimes does a partial restart by converting multiple Al atoms into Si (once every 2000 previous steps), and sometimes restarts from scratch (once every 1000 partial restarts) up to 30 times.
- Configurations with the closest Si/Al ratio to the target are kept in a set. Each configuration is assigned a hash, which is simply a sequence of 0 if the T-atom is a Si or 1 otherwise, in a fixed order of the T-atoms. To avoid considering symmetry-equivalent configurations as different, a unique signature of each configuration is computed as the lexicographically minimum of all such hashes corresponding to the application of a symmetry operation on the configuration. For each unique signature, a corresponding unique configuration is then retained, and the six final models are taken at random among these unique configurations.

One last consideration is the choice of the supercell. It appears that, for a large number of zeolites topologies, the smallest unit cell cannot be filled with aluminium atoms so that it both obeys Löwenstein's rule and reaches the minimal Si/Al ratio for that topology. In the case of LTA for instance, the smallest compatible cell is a  $2 \times 2 \times 2$  supercell, expressed in terms of the smallest unit cell. As a consequence, the greedy algorithm used before is launched on several

supercells in an initial pass, and the one leading to the smallest Si/Al ratio is retained. This supercell is then used for all aluminium placement attempts on the same topology.

The full list of minimum Si/Al ratio found for each zeolite topology (except interrupted ones) and the respective supercell is presented in [Table 2.1](#). The supercell is considered with respect to the idealized framework available for each topology on the IZA-SC database\*. This table presents the lowest Si/Al ratio found, but apart for the cases where it is 1, the values here are not proven to be minimal, since the algorithm relies on random attempts. Similarly, the supercell used could be not minimal.

It is worth mentioning that a previous study of adsorption in zeolite by Erdős et al. [100] claimed to use the lowest possible Si/Al ratios to screen through zeolites, but failed to reach the ones presented here, systematically in the case where a supercell needed to be used. Another by Daou, Fang, et al. [101, 102] alluded to that issue in the case of LTA, yet failed to identify some other topologies (ATT, JBY, LEV, LTL, MRT, OFF) which could reach an Si/Al ratio of 1. The choice of the supercell during aluminium placement is thus an easily overlooked, yet critical, point to consider.

### 2.1.3 Cations

The electroneutrality of the zeolitic materials requires that each negative charge introduced by an Al substitution be compensated by the introduction of a cation in the pores of the framework. In many cases,  $\text{Na}^+$  or  $\text{H}^+$  are used during synthesis; they are sometimes replaced by other cations in later steps.

These cations have a primordial role for adsorption processes, because they constitute privileged adsorption sites for many small gases. The precise mechanism by which they contribute to the overall adsorption capacity of a material depends on their nature, their location, and the nature of the guest molecule however. Moreover, in addition to simple one-to-one adsorption cases of a small molecule on a cation, X-ray spectroscopy evidences the presence of adsorption complexes involving several cations and guest molecules at the same time.<sup>103</sup> Finally, the very nature of the cations present in the structure can be quite diverse, ranging from monovalent alkali to polyvalent metal ions, and even molecular ions such as many of the organic structure directing agents (OSDAs) used during zeolite synthesis.

In order to perform numerical simulation of the adsorption process, it is thus necessary to have a microscopic model of the zeolite that places its cations in the correct positions. Fortunately, and opposite to the previous case of aluminium atoms, X-ray diffraction is a convenient technique which can be used to obtain the crystallographic sites in which the cations are located, as well as the respective occupancy of each such site. Let's now detail a methodology for numerically obtaining cation placements compatible with such experimental results.

## 2.2 METHODOLOGY FOR THE PREDICTION OF CATION PLACEMENT

While experimental cation maps are available for some zeolite structures, two seminal problems remain. First, when screening through a large amount of zeolite topologies and Si/Al ratios,

---

\*accessible at [https://europe.iza-structure.org/IZA-SC/ftc\\_table.php](https://europe.iza-structure.org/IZA-SC/ftc_table.php)

## 2.2 METHODOLOGY FOR THE PREDICTION OF CATION PLACEMENT

Topology	Si/Al	Supercell	CHA	1	$1 \times 1 \times 1$	ITH	1.33	$1 \times 2 \times 1$	MVY	1	$1 \times 1 \times 1$	SBT	1	$1 \times 1 \times 1$
ABW	1	$1 \times 1 \times 1$	CON	1.33	$1 \times 1 \times 1$	ITR	1.33	$1 \times 1 \times 1$	MWF	1	$1 \times 1 \times 1$	SEW	1.36	$1 \times 2 \times 1$
ACO	1	$1 \times 1 \times 1$	CSV	1.22	$1 \times 2 \times 1$	ITT	1.56	$2 \times 2 \times 3$	MWW	1.53	$2 \times 2 \times 1$	SFE	1.33	$1 \times 1 \times 1$
AEI	1	$1 \times 1 \times 1$	CZP	1	$1 \times 1 \times 1$	ITW	1.4	$1 \times 1 \times 1$	NAB	1.5	$2 \times 2 \times 1$	SFF	1.46	$2 \times 1 \times 2$
AEL	1	$1 \times 1 \times 1$	DAC	1.57	$1 \times 3 \times 2$	IWR	1.33	$2 \times 2 \times 2$	NAT	1.22	$2 \times 2 \times 4$	SFG	1.47	$1 \times 2 \times 2$
AEN	1	$1 \times 1 \times 1$	DDR	1.73	$1 \times 2 \times 1$	IWS	1.27	$1 \times 1 \times 2$	NES	1.52	$1 \times 1 \times 1$	SFH	1.29	$5 \times 1 \times 2$
AET	1	$1 \times 1 \times 1$	DFO	1	$2 \times 2 \times 2$	IWW	1.62	$1 \times 1 \times 2$	NON	1.44	$1 \times 1 \times 1$	SFN	1.29	$1 \times 5 \times 2$
AFG	1	$1 \times 1 \times 1$	DFT	1	$4 \times 4 \times 3$	JBW	1	$5 \times 4 \times 3$	NPO	2	$4 \times 4 \times 5$	SFO	1	$2 \times 2 \times 4$
AFI	1	$1 \times 1 \times 1$	DOH	1.62	$1 \times 2 \times 1$	JNT	1	$1 \times 1 \times 1$	NPT	2	$2 \times 2 \times 2$	SFS	1.67	$1 \times 1 \times 1$
AFN	1	$1 \times 1 \times 1$	DON	1.29	$1 \times 1 \times 1$	JOZ	1.5	$2 \times 1 \times 1$	NSI	1.4	$2 \times 5 \times 3$	SFW	1	$1 \times 1 \times 1$
AFO	1	$1 \times 1 \times 1$	EAB	1	$1 \times 1 \times 1$	JRY	1	$1 \times 1 \times 1$	OBW	1.92	$1 \times 1 \times 1$	SGT	1.49	$2 \times 2 \times 1$
AFR	1	$2 \times 2 \times 4$	EDI	1	$4 \times 4 \times 4$	JSN	1	$3 \times 4 \times 2$	OFF	1	$3 \times 3 \times 4$	SIV	1	$1 \times 1 \times 1$
AFS	1	$1 \times 1 \times 1$	EEI	1.44	$1 \times 1 \times 1$	JSR	1.67	$1 \times 1 \times 1$	OKO	1.62	$1 \times 1 \times 1$	SOD	1	$1 \times 1 \times 1$
AFT	1	$1 \times 1 \times 1$	EMT	1	$1 \times 1 \times 1$	JST	2	$1 \times 1 \times 1$	OSI	1	$1 \times 1 \times 1$	SOF	1.5	$1 \times 1 \times 1$
AFV	1	$3 \times 3 \times 2$	EON	1.4	$2 \times 1 \times 1$	JSW	1	$1 \times 1 \times 1$	OSO	2	$1 \times 1 \times 1$	SOR	1.18	$1 \times 1 \times 2$
AFX	1	$1 \times 1 \times 1$	EOS	1.18	$1 \times 2 \times 2$	JSY	1	$1 \times 1 \times 1$	OWE	1	$2 \times 4 \times 3$	SOS	1.4	$2 \times 4 \times 3$
AFY	1	$1 \times 1 \times 1$	EPI	1.74	$4 \times 2 \times 3$	JZO	1.37	$1 \times 1 \times 1$	PAU	1	$1 \times 1 \times 1$	SOV	1.29	$1 \times 1 \times 1$
AHT	1	$1 \times 1 \times 1$	ERI	1	$1 \times 1 \times 1$	JZT	1.35	$1 \times 1 \times 1$	PCR	1.5	$1 \times 1 \times 1$	SSF	1.25	$2 \times 2 \times 2$
ANA	1	$1 \times 1 \times 1$	ESV	1.4	$1 \times 1 \times 1$	KFI	1	$1 \times 1 \times 1$	PHI	1	$1 \times 1 \times 1$	SSY	1.33	$1 \times 1 \times 1$
ANO	1	$1 \times 1 \times 1$	ETL	1.48	$2 \times 1 \times 1$	LAU	1	$2 \times 2 \times 4$	PON	1	$1 \times 1 \times 1$	STF	1.46	$1 \times 1 \times 2$
APC	1	$1 \times 1 \times 1$	ETR	1	$1 \times 1 \times 1$	LEV	1	$3 \times 3 \times 2$	POR	1	$1 \times 1 \times 1$	STI	1.25	$1 \times 1 \times 1$
APD	1	$1 \times 1 \times 1$	ETV	1.33	$1 \times 1 \times 1$	LIO	1	$1 \times 1 \times 1$	POS	1.29	$1 \times 1 \times 1$	STT	1.46	$1 \times 1 \times 1$
AST	1	$1 \times 1 \times 1$	EUO	1.49	$1 \times 1 \times 1$	LOS	1	$1 \times 1 \times 1$	PSI	1	$1 \times 1 \times 1$	STW	1.5	$1 \times 1 \times 1$
ASV	1	$1 \times 1 \times 1$	EWF	1.49	$2 \times 1 \times 1$	LOV	1.25	$2 \times 2 \times 1$	PTF	1.5	$1 \times 1 \times 1$	SVV	1.33	$1 \times 1 \times 1$
ATN	1	$1 \times 1 \times 1$	EWG	1.4	$2 \times 2 \times 5$	LTA	1	$2 \times 2 \times 2$	PTO	1.4	$1 \times 1 \times 1$	SWY	1	$1 \times 1 \times 1$
ATO	1	$1 \times 1 \times 1$	EWS	1.53	$1 \times 1 \times 1$	LTF	1.27	$1 \times 1 \times 4$	PTT	1	$1 \times 1 \times 1$	SZR	1.25	$1 \times 1 \times 2$
ATS	1	$1 \times 1 \times 1$	EZT	1	$1 \times 1 \times 1$	LTJ	1	$1 \times 1 \times 1$	PTY	1.5	$1 \times 1 \times 1$	TER	1.35	$1 \times 1 \times 1$
ATT	1	$3 \times 4 \times 3$	FAR	1	$1 \times 1 \times 1$	LTL	1	$2 \times 2 \times 4$	PUN	1.25	$1 \times 1 \times 1$	THO	1	$2 \times 4 \times 4$
ATV	1	$1 \times 1 \times 1$	FAU	1	$1 \times 1 \times 1$	LTN	1	$1 \times 1 \times 1$	PWN	1	$1 \times 1 \times 1$	TOL	1	$1 \times 1 \times 1$
AVE	1	$1 \times 1 \times 1$	FER	1.57	$1 \times 1 \times 3$	MAR	1	$1 \times 1 \times 1$	PWO	1.5	$1 \times 1 \times 1$	TON	1.4	$2 \times 2 \times 5$
AVL	1	$3 \times 3 \times 2$	FRA	1	$1 \times 1 \times 1$	MAZ	1.4	$1 \times 1 \times 2$	PWW	1.5	$1 \times 1 \times 1$	TSC	1	$1 \times 1 \times 1$
AWO	1	$1 \times 1 \times 1$	GIS	1	$1 \times 1 \times 1$	MEI	1.43	$1 \times 1 \times 1$	RFE	1.4	$1 \times 1 \times 1$	TUN	1.53	$1 \times 1 \times 1$
AWW	1	$2 \times 2 \times 4$	GIU	1	$1 \times 1 \times 1$	MEL	1.67	$1 \times 1 \times 1$	RHO	1	$1 \times 1 \times 1$	UEI	1	$1 \times 1 \times 1$
BCT	1	$1 \times 1 \times 1$	GME	1	$1 \times 1 \times 1$	MEP	1.71	$1 \times 1 \times 1$	RRO	1.25	$2 \times 1 \times 1$	UFI	1.29	$2 \times 2 \times 1$
BEC	1.29	$2 \times 2 \times 2$	GON	1.29	$1 \times 1 \times 1$	MER	1	$1 \times 1 \times 1$	RSN	1.59	$4 \times 1 \times 4$	UOS	1.18	$2 \times 4 \times 3$
BIK	1.4	$4 \times 2 \times 5$	GOO	1	$1 \times 1 \times 1$	MFI	1.67	$1 \times 1 \times 1$	RTE	1.4	$1 \times 1 \times 2$	UOV	1.38	$1 \times 1 \times 1$
BOF	1.4	$2 \times 1 \times 1$	HEU	1.25	$1 \times 1 \times 2$	MFS	1.45	$3 \times 1 \times 1$	RTH	1.53	$2 \times 1 \times 3$	UOZ	1	$1 \times 1 \times 1$
BOG	1.4	$1 \times 1 \times 1$	IFO	1	$1 \times 1 \times 1$	MON	1.67	$2 \times 2 \times 1$	RUT	1.57	$2 \times 2 \times 3$	USI	1	$1 \times 1 \times 1$
BOZ	1.88	$1 \times 1 \times 1$	IFR	1.29	$1 \times 1 \times 2$	MOR	1.67	$1 \times 1 \times 2$	RWR	1.6	$4 \times 4 \times 1$	UTL	1.62	$1 \times 2 \times 2$
BPH	1	$1 \times 1 \times 1$	IFW	1.29	$1 \times 1 \times 1$	MOZ	1	$1 \times 1 \times 4$	RWY	3	$1 \times 1 \times 1$	UWY	1.37	$1 \times 2 \times 3$
BRE	1.29	$4 \times 2 \times 4$	IFY	1	$1 \times 1 \times 2$	MRT	1	$2 \times 4 \times 2$	SAF	1	$1 \times 1 \times 1$	VET	1.43	$1 \times 1 \times 1$
BSV	1	$1 \times 1 \times 1$	IHW	1.55	$1 \times 1 \times 1$	MSE	1.55	$1 \times 1 \times 1$	SAO	1	$1 \times 1 \times 1$	VFI	1	$1 \times 1 \times 1$
CAN	1	$1 \times 1 \times 1$	IMF	1.55	$1 \times 1 \times 1$	MSO	1	$2 \times 2 \times 2$	SAS	1	$1 \times 1 \times 1$	VNI	1.73	$3 \times 3 \times 1$
CAS	1.4	$1 \times 1 \times 1$	IRN	1.19	$1 \times 1 \times 1$	MTF	1.44	$1 \times 1 \times 2$	SAT	1	$1 \times 1 \times 1$	VSV	1.78	$4 \times 4 \times 1$
CDO	1.62	$4 \times 2 \times 2$	IRR	1.6	$2 \times 2 \times 2$	MTN	1.72	$1 \times 1 \times 1$	SAV	1	$1 \times 1 \times 1$	WEI	1.5	$1 \times 1 \times 1$
CFI	1.46	$2 \times 5 \times 1$	ISV	1.31	$2 \times 2 \times 1$	MTT	1.4	$1 \times 1 \times 1$	SBE	1	$1 \times 1 \times 1$	YFI	1.4	$1 \times 1 \times 1$
CGF	1	$2 \times 2 \times 4$	ITE	1.56	$1 \times 2 \times 1$	MTW	1.33	$1 \times 5 \times 3$	SBN	1.5	$1 \times 2 \times 1$	YUG	1.56	$3 \times 2 \times 4$
CGS	1	$1 \times 1 \times 1$	ITG	1.33	$1 \times 1 \times 2$	SBS	1	$1 \times 1 \times 1$	ZON	1	$4 \times 2 \times 2$			

Table 2.1: Minimal Si/Al and corresponding supercell obtained for all 239 non-interrupted topologies

only a small fraction of structures have their experimental cation map available. Second, even with the crystallographic sites, not all cation repartitions that obey the given occupancies have the same energy. For example, the site I and I' of FAU being very close to one another, the occupation of a site I prevents either of the neighbouring sites I' from being occupied at the same time. Deciding on the exact location of cations in a zeolite model is thus no trivial matter.

### 2.2.1 Underlying algorithms

To obtain equilibrium data, such as average positions, on molecular systems, there are two general simulation frameworks which can be used: molecular dynamics and Monte Carlo simulation. In my work, I only used Monte Carlo and its variations because of the possibility to include non-local move, of particular interest for cation placement. Additionally, Monte Carlo is the only strategy available to handle a variable number of molecules, which is necessary for the simulation of adsorption as I will explain in more details in section 3.2. The possible use of molecular dynamics and its variants will be discussed later in section 2.5.

#### CANONICAL MONTE CARLO DIRECT SIMULATION

The Monte Carlo (MC) method designates a large variety of algorithms which all converge towards their result by performing multiple random samplings. A wide subset of these form the Markov Chain Monte Carlo (MCMC) schemes, which are a class of algorithms that aim at sampling a target probability distribution. In the context of statistical physics, such methods provide practical ways of obtaining macroscopic observable values from the simulation of the microscopic behaviour of particles. Indeed, an observable  $\mathcal{O}$  can be computed as the ensemble average of its microscopic counterpart  $\langle o \rangle$ , which can be obtained from an integral over the configuration space. For example, in the canonical ensemble where the number of particles, the external temperature T and the volume of the system is fixed,

$$\mathcal{O} = \langle o \rangle = \frac{1}{Z} \int d\mathbf{p} o(\mathbf{p}) \exp(-\beta U(\mathbf{p})) \quad (2.1)$$

where  $\beta = 1/k_B T$ ,  $U(\mathbf{p})$  is the energy of configuration  $\mathbf{p}$  and  $Z$  is the partition function. In other words,  $\mathcal{O}$  can be computed as an integral of the values of  $o$  on a probability distribution of  $\mathbf{p}$  given by  $\mathbf{p} \mapsto \frac{1}{Z} \exp(-\beta U(\mathbf{p}))$ .

The direct evaluation of this probability distribution is impossible in general, because of the partition function  $Z$  whose value cannot be computed. Instead, the MCMC method gives a way to directly evaluate the observable  $\mathcal{O}$  by providing a sequence of configurations  $\{\mathbf{p}\}$  that follows the same probability distribution as the target. The integral can then simply be computed as the average value of  $o$  on this specific set of configurations  $\{\mathbf{p}\}$ .

The Metropolis-Hastings algorithm is the most common MCMC scheme used to provide such a sequence of configurations. It consists in starting from an initial state, *i.e.* an initial position for all the mobile particles of the system, and making it evolve through a sequence of steps. At each step, a trial move, *i.e.*, a modification of the state, is attempted and may, or may not, be accepted with a certain probability. In the case of a simulation in the canonical ensemble, the difference of energy  $\Delta E$  between after and before the move gives the probability

$$P_{\text{accept}}(\Delta E) = \min(1, \exp(-\beta \Delta E)) \quad (2.2)$$

that the move be accepted. Intuitively, this means that any move that decreases the energy of the system is accepted, while the others are accepted with a probability that decreases as the energy difference increases, sharply at low temperature and more slowly at high temperature. In the limit of infinite temperature, all the moves are accepted; at zero temperature, only the moves that decrease the energy are. The details on how to compute energy based on interatomic interactions are deferred to [section 2.4](#).

To ensure that the algorithm samples the correct distribution, it is usually implemented to obey detailed balance which, conceptually, represents the microreversibility of the simulated physical processes. In practice, this means that, for each MC move that brings the system from configuration  $\mathbf{p}_A$  to  $\mathbf{p}_B$ , there must exist a “converse” MC moves that can bring the system from  $B$  to  $A$  such that  $\pi_A P_{A \rightarrow B} = \pi_B P_{B \rightarrow A}$  where  $\pi_X$  is the stationary probability of state  $\mathbf{p}_X$  and  $P_{X \rightarrow Y}$  is the probability of the move from  $\mathbf{p}_X$  to  $\mathbf{p}_Y$ . In the canonical ensemble,  $\pi_X$  is equal to  $\frac{1}{Z} \exp(-\beta U(\mathbf{p}_X))$ , while the probability of transition is  $\min(1, \exp(-\beta \Delta E))$ . Hence, detailed balance simply translates to the algorithmic condition that the probability of choosing the trial move  $A \rightarrow B$  must be equal to that of choosing the trial move  $B \rightarrow A$ , irrespective of the probability of accepting these moves.

The MC moves which are used for simulations of small rigid species in the canonical ensemble are usually the following:

- translation: displace each atom of a mobile molecule by the same vector. By default, the translation move is local, by taking the translation vector uniformly at random in a sphere, but it is also useful in some cases to add unbounded translations.
- rotation: rotate the molecule around one of its atoms (called the “bead”) along three uniformly random Euler angles, possibly constrained to some values only, most often all values under a maximum angle.
- reinsertion: remove and reintroduce the molecule uniformly at random in the system.

They are represented on [Figure 2.4](#), along the two swap moves which will be discussed in [section 3.2.2](#)

Overall, the algorithm thus consists in a sequence of steps, each of which is an attempt to displace a species, in our case a cation, either locally (translation) or not (reinsertion) and is accepted or not depending on the difference of energy the move generates. Configurations corresponding to neighbour steps are thus either identical if the move was rejected, or only separated by one MC move, so they are strongly correlated. To reduce computational cost, the computation of the microscopic state function  $o$  is thus only realized once every cycle, each cycle corresponding to a number of steps. I fix the number of steps per cycle to the number of mobile particles in the system in the case of canonical ensemble simulations.

To satisfy detailed balance, the sphere in which the translation vector is taken must have a fixed radius, the bead must be fixed and the angle constraints must be symmetric. However, the best maximum translation length  $d_{\max}$  and maximum angle  $\theta_{\max}$  are those that yield a simulation that converges in the smallest number of cycles. Frenkel and Smit [104] indicate that this usually translates to a MC move acceptance rate close to 20 % for translation moves (and not 50 % as widely expected). All of this depends on the precise simulation, but it is customary

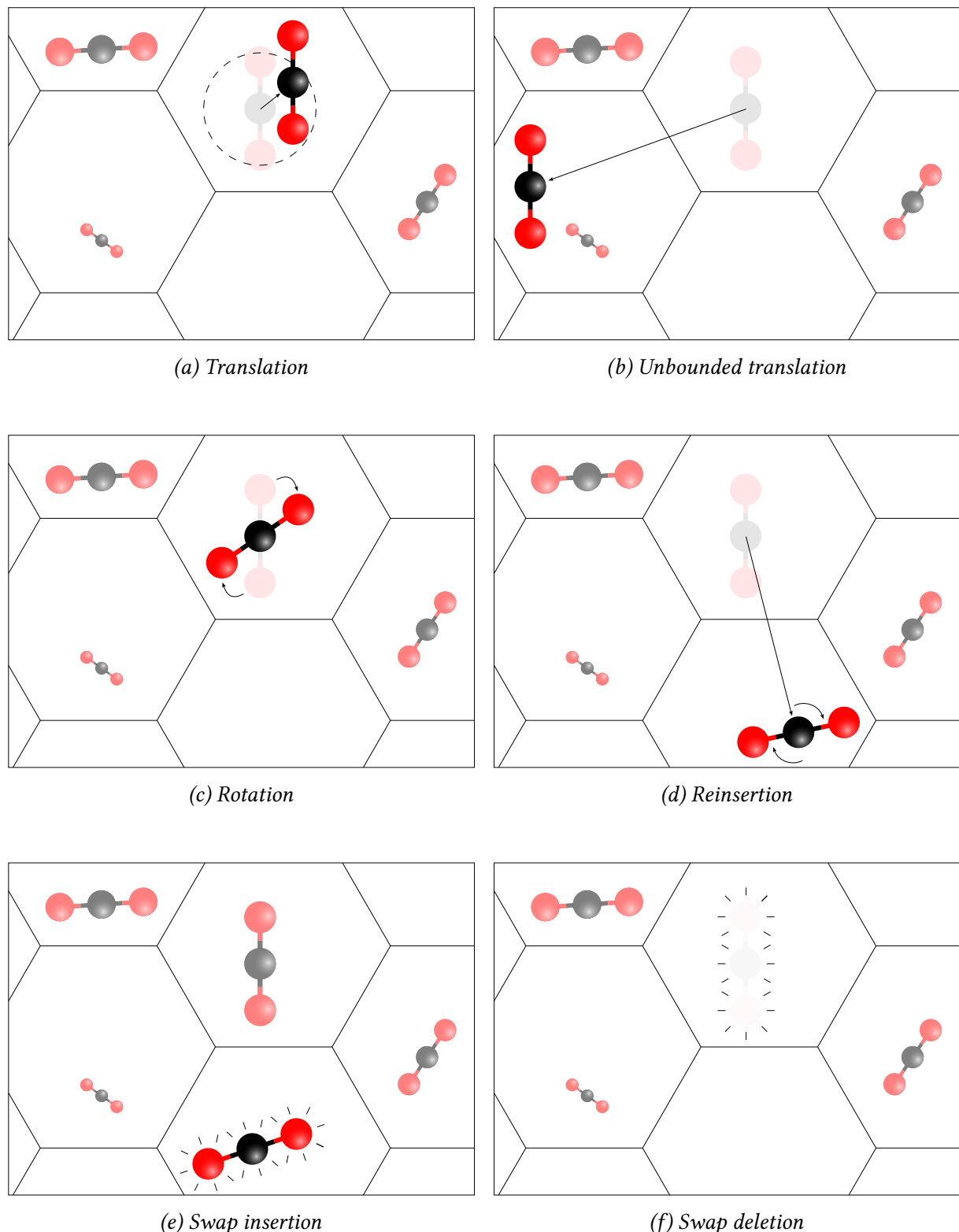
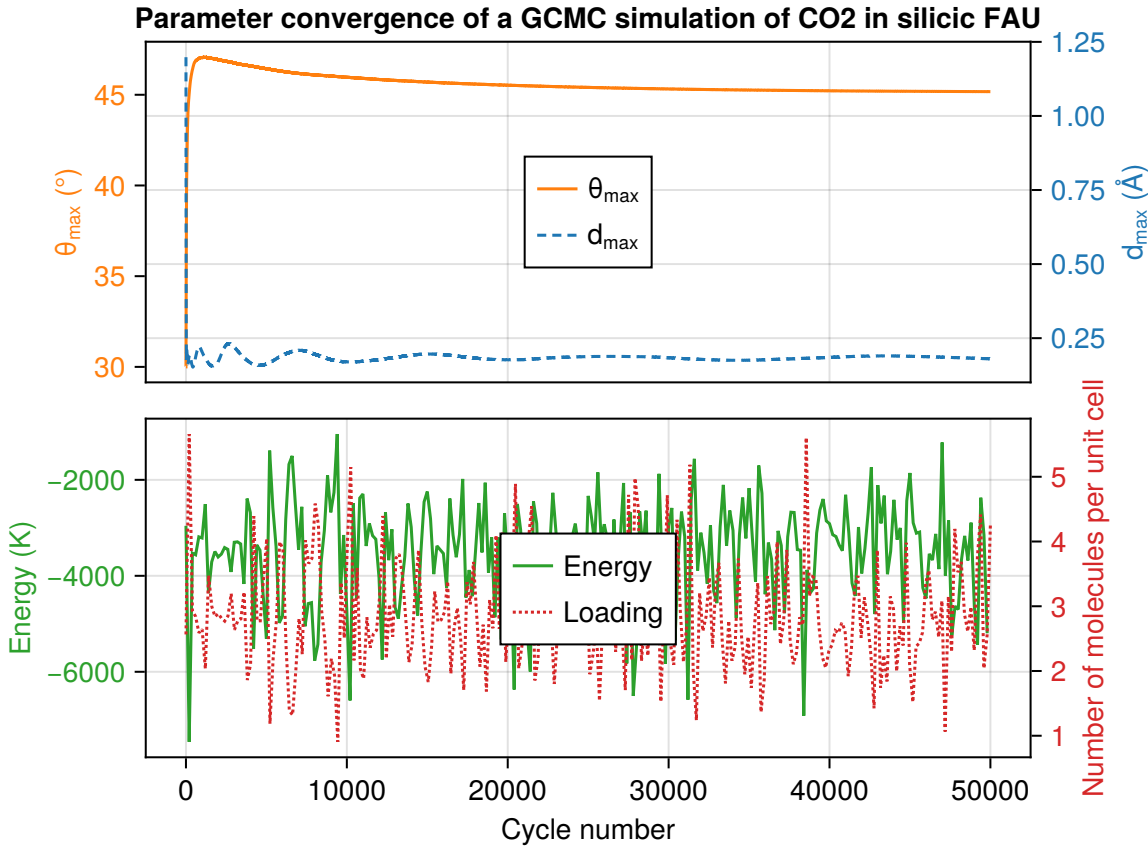


Figure 2.4: Schematic representation of typical MC moves



*Figure 2.5: Evolution of  $d_{\max}$ ,  $\theta_{\max}$ , the energy and the number of molecules during a Grand Canonical Monte Carlo simulation of  $\text{CO}_2$  in silicic FAU at 300 K and 50 MPa. The values for the energy and the loading are represented with one point per 200 cycles, averaging the corresponding values.*

to make the two constraints  $d_{\max}$  and  $\theta_{\max}$  evolve along the simulation until reaching a target acceptance rate, for example 25 % for translations and 50 % for rotations. To do so, at the end of each cycle, they are updated with the following empirical formulas:

$$\begin{aligned} d_{\max} &\leftarrow \text{clamp} \left( d_{\max} \times \left( 1 + (\text{T}_{\text{ratio}} - 1/4) \times \sqrt{\frac{10}{99+i}} \right), 0.1 \text{\AA}, 3 \text{\AA} \right) \\ \theta_{\max} &\leftarrow \text{clamp} \left( \theta_{\max} + \frac{(\text{R}_{\text{ratio}} - 1/2) \times 120^\circ}{i}, 10^\circ, 180^\circ \right) \end{aligned} \quad (2.3)$$

where  $i$  is the number of the current cycle (starting at 1),  $\text{T}_{\text{ratio}}$  (respectively  $\text{R}_{\text{ratio}}$ ) is the ratio of accepted over attempted local translations (respectively rotations) in the entire simulation, and  $\text{clamp}(x, m, M)$  is  $x$  if  $m \leq x \leq M$ , otherwise  $m$  if  $x \leq m$ , otherwise  $M$  (if  $x \geq M$ ). Having  $d_{\max}$  and  $\theta_{\max}$  change across the simulation breaks detailed balance, which is theoretically forbidden; yet it does not actually pose a problem in reality because the formulas used ensure that the two values evolve smoothly towards the optimum, and become almost constant once the simulation has been running for enough cycles.

Figure 2.5 illustrates the evolution of  $d_{\max}$  and  $\theta_{\max}$ , as well as the corresponding evolution of the energy and the number of molecules, which indicate the global convergence of the

simulation. Both parameters  $d_{\max}$  and  $\theta_{\max}$  converge smoothly towards their optimum. In this particular simulation, the final translation move acceptance rate was 24.93% and for rotation 49.87%, very close to the targets of respectively 25% and 50%.

At the beginning of each step, an MC move is chosen at random. In my simulations, all three moves (translation, rotation and reinsertion) are chosen equiprobably. For the particular case of the movement of monoatomic species, such as most cations in zeolites, the rotation MC move is useless and thus not used, while the reinsertion move collapses to a simple unbounded translation, hence all the moves are translations, local or not at equiprobability.

The Metropolis-Hastings algorithm thus provides a way to walk through the configuration space. By privileging moves that decrease energy, the system spends more steps in low energy regions; by yet allowing opposite moves sometimes, the scheme ensures that all the configuration space is eventually visited. Hence, the algorithm guarantees ergodicity: in an infinitely long simulation, the fraction of steps spent in a part of the configuration space is proportional to its volume.

#### COMBINED ALUMINIUM AND CATION PLACEMENT

Specifically in the case cationic zeolites, Marie Jeffroy [96] proposed a simulation method to obtain both the placement of cations in the structure and the location of aluminium atoms across the T-sites. This consists in running an MC simulation where the cations are allowed all previously mentioned MC steps, while the aluminium atoms are only allowed exchanging positions with silicon atoms, or a restart step that randomly places aluminium and silicon atoms, both while obeying Löwenstein's rule as explained in [section 2.1.2](#).

The statistical ensemble simulated in this setting includes both aluminium and cations, which means that the distribution sampled through such a simulation method represents the thermodynamic equilibrium for both species. From a chemical point of view, this situation is representative of a framework whose synthesis was done with that very cation, and was thermodynamically-driven. While this does correspond to reality in some cases, there is also evidence that the synthesis is kinetically-driven in many other occurrences: for such situation, obtaining the aluminium positions from statistical equilibrium is not representative of the actual framework. And in yet other situations, the cation is exchanged post-synthesis, which decorrelates the aluminium placement in the framework from the cation used for adsorption purposes.

Nonetheless, even in those cases, there is no less value in the aluminium placement obtained from such a hybrid strategy than from random sampling of the T-atoms. In fact, by virtue of the added dimensions of the free energy landscape, a kinetically trapped cation may move more freely following the rearrangement of the aluminium atoms in the structure, which can make the entire simulation converge more efficiently. If not for the hope of obtaining more relevant aluminium placements, this combined strategy remains valuable for its diminished computational cost compared to parallel tempering, explained later in [section 2.2.2](#).

Unfortunately, the fact that the framework is not strictly fixed as before prevents the use of precomputed energy grids, later discussed in [section 2.4.4](#). This was not a problem in the context of Marie Jeffroy [96]'s study because the force field they used was such that a silicon-aluminium swap would not change the van der Waals interactions, but this is not the case of most force fields, including the one, by Boulfelfel et al. [105], which I used my study. Being

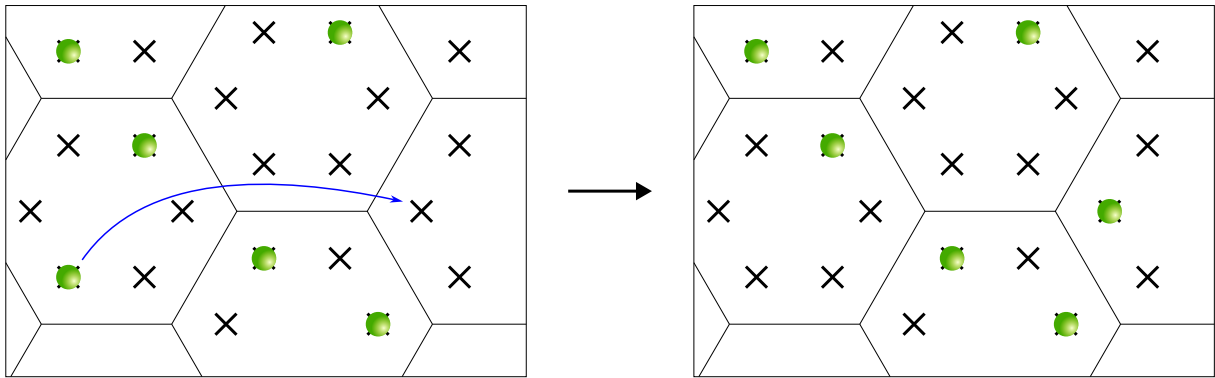


*Figure 2.6: Schematic representation of a hop, the only MC move used in site hopping. Crosses mark the possible sites, spheres indicate whether they are occupied.*

unable to precompute the short-term energy contribution of the framework would thus make the simulations significantly slower, tipping the balance against the use of this method.

### SITE HOPPING

Cations are free to move in a canonical MC simulation with translation moves, but some reconfigurations can be problematic. In particular, the cations may not have enough energy to overcome the barriers inherent to the structure of the zeolitic framework in any reasonable simulation time. For example, a cation trapped in the site I of a FAU zeolite will never manage to escape into a site III in a room-temperature simulation of reasonable length without a reinsertion move: this simply comes from the high energy barrier it needs to overcome while physically moving out of the sodalite cage. Reinsertion moves are thus useful to allow large configuration movements to occur without having to pass through physical energy barriers.

However, reinsertion consists in attempting to displace a cation to a random position in the framework, which, in the vast majority of cases, ends up rejected because it is too energetically unfavourable. A better move would consist in displacing the cation towards a favourable position, to increase the likelihood of the move being accepted: this is called biasing, which requires unbiased the acceptance rate to maintain micro-reversibility.

Taking this idea to the extreme, all cations can be forced to sit on one of a fixed set of possible positions, the “sites”, and to only move by hopping onto another of these positions, irrespective of the distance with the previous position, as illustrated in [Figure 2.6](#). One hop is then accepted or rejected based on the Metropolis-Hastings criterion, like any other MC simulation. This “site hopping” approach entirely bypasses the issue of spatial energy barrier since the cations directly hop onto a site, without having to move through an unfavourable region to access it. Hence, it makes this kind of simulation particularly well adapted to sharp energy landscapes, like that of cations in zeolites.

A major constraint of this simulation method however, is that it requires knowing the cationic sites, which is precisely the purpose of the current development. One could weaken this constraint by allowing many pseudo-sites, for instance taking all the points of a regular grid, but this basically amounts to reverting to reinsertion moves without sites, which defeats the purpose of this protocol. Site hopping is thus useful in the later stages of cation placement, once the positions of the sites have already been identified, in order to evaluate their population.

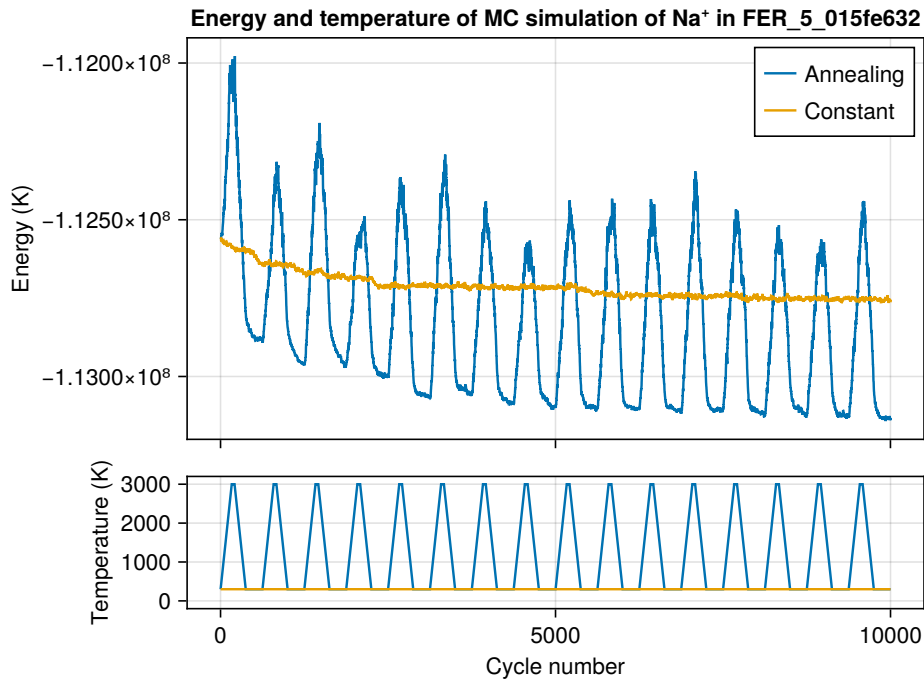


*Figure 2.7: Comparison of energy convergence with simulated annealing (16 times between 300 K and 3000 K) and without, for  $\text{Na}^+$  placement in FER with  $\text{Si}/\text{Al} = 5$*

### 2.2.2 Meta-algorithms

The previous algorithms allow sampling the configuration space at a fixed temperature. However, even with reinsertion or site hopping, only one particle can move at a time, which is sometimes not enough. For instance, in FAU zeolites, filling both sites I' when starting from an initial configuration where only the central site I is occupied requires that both the central cation move to the edge of the cage and that an external cation be set in the opposite window. Since both movements require passing through an activation barrier, the probability of it happening naturally is low, and thus requires particularly long simulation times to be observed. More generally, collective movements can remain difficult unless custom MC moves are specifically introduced.

To circumvent this issue, the temperature of the simulation can be raised: this makes all MC steps more likely to be accepted, so higher-energy regions become more reachable. At the same time, a simulation at a hot temperature is much less likely to explore the details of the energy landscape enough to fall into the energy minima of interest, since the accessible configuration space became so much larger. Several meta-algorithms rely on the previously explained algorithms but use different temperatures in different settings, to attempt finding the optimal compromise between broad and detailed explorations.

#### SIMULATED ANNEALING

The simplest idea consists in running the simulation while smoothly varying the temperature between cold and hot, alternating between increasing and decreasing phases, possibly interspersed with plateaus. This is called simulated annealing, because of the similarity with the recrystallization method used in metallurgy.

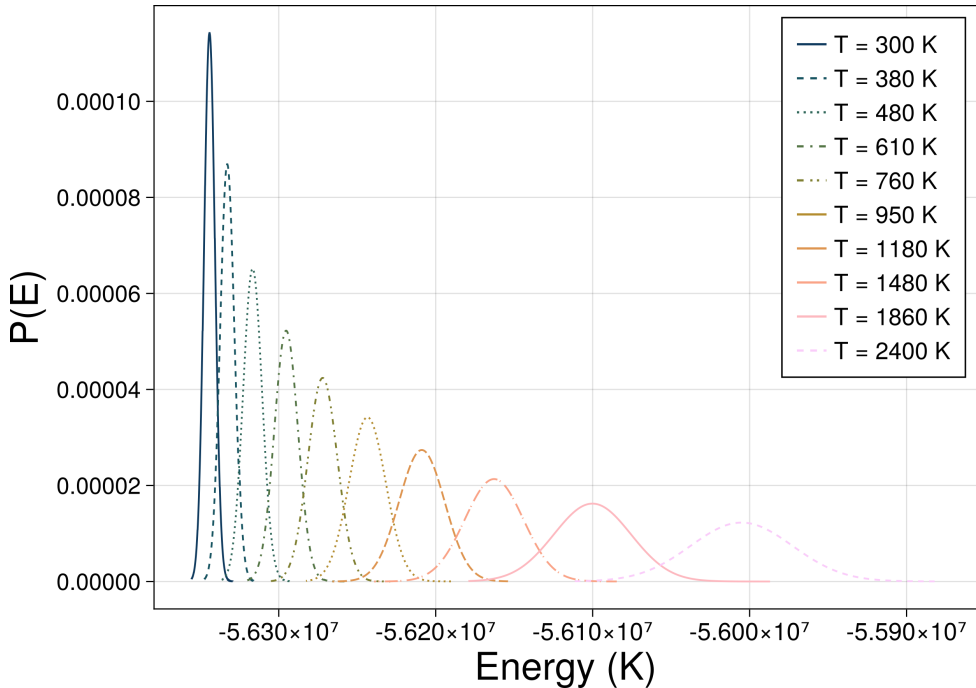


*Figure 2.8: Parallel tempering energy distribution in a canonical MC simulation of  $\text{Na}^+$  in FAU with  $\text{Si}/\text{Al} = 1.4$*

[Figure 2.7](#) compares MC with simulated annealing to a simulation with constant temperature, starting from the same initial configuration on an example system,  $\text{Na}^+$  in a FER zeolite with  $\text{Si}/\text{Al} = 5$ . As the lower final energy demonstrates, this strategy usually allows faster convergence of the system towards the minimum energy. Finding the best high temperature and slope can be a difficult optimization task however.

#### PARALLEL TEMPERING

Simulated annealing explores the configuration space by alternating between cold phases, where the exploration is detailed but localized, and hot phases, where the exploration is fast but superficial. Parallel tempering, also called “replica exchange”, proposes doing both phases at the same time.

In more detail, a parallel tempering simulation consists in running several MC simulations, the “replicas”, in parallel, each at a different temperature. The temperatures are taken between room temperature and a hot temperature. An extra MC step is introduced, called the “exchange” step, which consists in exchanging the configurations of two replicas with neighbour temperatures. As with any MC step, the Metropolis-Hastings algorithm ensures that the exchange is accepted only if the difference of energy resulting from this exchange is not too high: as a consequence, for the exchange step to be accepted regularly, the temperatures must be taken so that the typical energies of the system between neighbour temperatures overlap, as shown on an example in [Figure 2.8](#).

In this strategy, the coldest simulation is constantly exploring a local free energy minimum, while the hottest simulation easily accepts MC moves and thus walks through the entire configuration space. By virtue of the exchange MC move, new configurations regularly trickle down from the hot simulations to the colder ones, as represented schematically in [Figure 2.9](#), while the general Metropolis-Hastings strategy ensures convergence towards a global minimum.

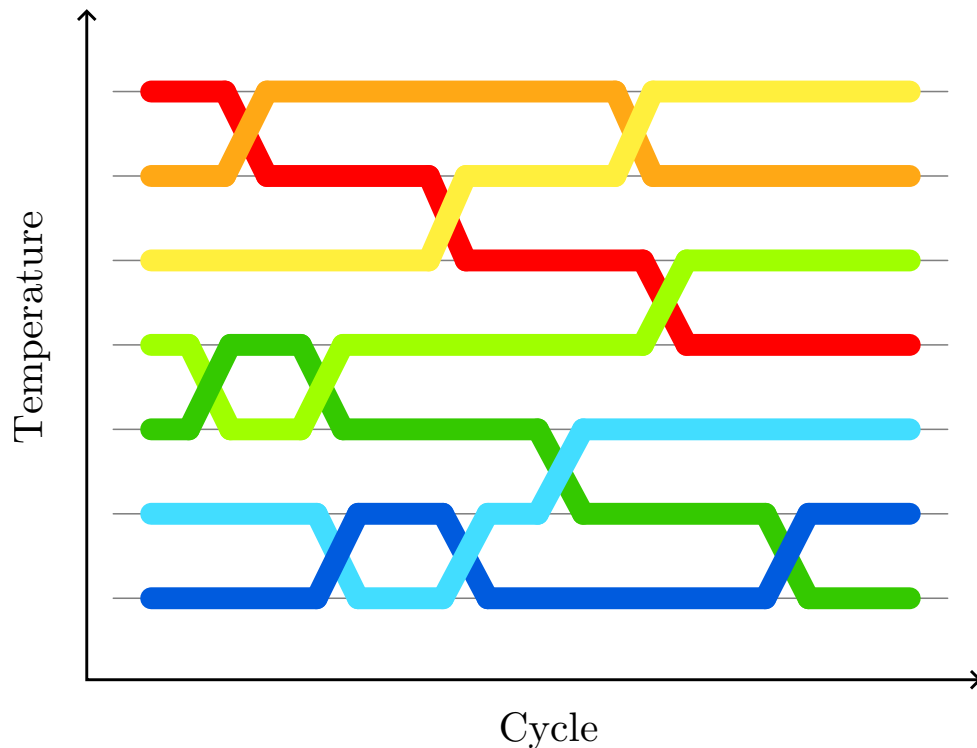


*Figure 2.9: Principle of parallel tempering: multiple replicas of the system are simulated at the same time. An exchange MC move swaps the temperature of two neighbouring systems.*

It is also more efficient than simulated annealing since the exploration of the configuration space is not constrained by the small duration of the hot phase. Parallel tempering is therefore the method of choice used to obtain convergence when facing difficult energy landscapes such as the one encountered for cation placement.<sup>106</sup>

Naturally, its main downside is its computational cost, proportional to the number of replicas and thus effectively related to the difference between the highest and the lowest temperatures. The choice of intermediate temperatures must be guided by an initial discovery of the typical energies encountered by system at each temperature, which requires a few dedicated simulations prior to the parallel tempering. Finding the optimal number of simulations requires striking a balance with the proportion of accepted MC exchange steps, whose impact on the overall simulation convergence can be difficult to measure. Additionally, simulations with neighbour temperatures must regularly synchronize to attempt an exchange, which strongly limits the amount of parallelization usable in the implementation of parallel tempering.

#### “SHOOTING STAR” METHODOLOGY

Previously exposed methods such as simple canonical MC, simulated annealing or parallel tempering focus on making the system (or at least, one of its replicas) reach equilibrium after a certain number of initial steps, so that the rest of the simulation occurs at equilibrium. This is crucial for the problem of sampling the equilibrium distribution of states in general. For the case of cation placement in zeolites however, the observed crystallographic positioning of the cations indicates that this distribution is sharply peaked: only a discrete number of sites can be occupied, and the question is to find their positions and occupancy. As a consequence, I am proposing to use another, simpler, strategy, which is potentially less efficient for the actual sampling of the distribution, but can uncover relevant local minima faster.

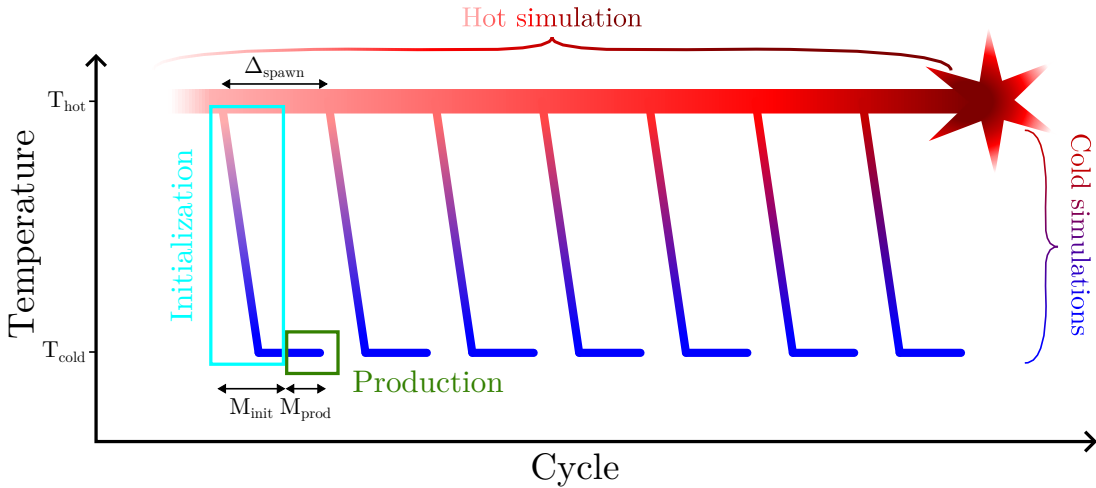


Figure 2.10: Schematic representation of the “shooting star” methodology

This new methodology takes the same simulation elements as the ones previously detailed, but arranges them in a different fashion. I call it “shooting star” because it can be decomposed into one hot simulation, like the bright head of a meteor, and a series of cold simulations that stem from it, like the cooling incandescent debris left in its wake.

The first element is the exploration of the phase space. In order to fully explore it, a naive approach consists in doing steps, each of which randomly reinserts a particle in the system. Without the possibility for step rejection, this leads to sampling extremely unlikely states almost all the time however. Therefore, I propose to perform global exploration by simply running a canonical MC simulation at a very high temperature, for instance 2000 K. Such an approach makes most kinetic obstacles irrelevant, but still prevents absurd configurations like when two atoms collide. This MC simulation is simply called the hot simulation.

The second element is the local minima exploration, which is grafted onto the previous one: every  $\Delta_{\text{spawn}}$  cycles of the hot simulation, a snapshot of its current configuration is taken and used as the starting point for a cold simulation, *i.e.* another canonical MC simulation that runs at room temperature.  $\Delta_{\text{spawn}}$  is chosen so that two consecutive starting points should be uncorrelated. The higher the temperature of the hot simulation, the less correlated its consecutive steps are, so  $\Delta_{\text{spawn}}$  can actually be low. Each cold simulation runs for  $M_{\text{init}}$  initial steps, that allow the system to cool down, and  $M_{\text{prod}}$  production steps at the target room temperature. Figure 2.10 provides an illustration of the methodology.

Similar to the previous accelerated methodologies, only a fraction of the explored states can actually be used to perform statistics. In the case of simulated annealing, it corresponds to the cold regions of the simulation; for parallel tempering, only the coldest replica is useful to obtain statistics at that temperature; for the current methodology, the relevant steps are the production of the cold simulation. The main advantage of the “shooting star” protocol resides in the efficient exploration of the configuration space, rooted in the hot simulation that is independent from the cold ones. Conversely, it lacks the physical meaning of simulated annealing – which is the numerical counterpart to the annealing process used in metallurgy – or the time-reversibility of parallel tempering and bare canonical MC.

In terms of parameters, the “shooting star” method requires choosing  $T_{\text{hot}}$  the hot temperature,  $T_{\text{cold}}$  the cold one,  $N_{\text{cold}}$  the total number of cold simulations to launch, the previously mentioned  $M_{\text{init}}$ ,  $M_{\text{prod}}$  and  $\Delta_{\text{spawn}}$ , as well as the number  $N_{\text{init}}$  of initial steps of the hot simulation before launching the first cold simulation. Of all these parameters,  $T_{\text{cold}}$ ,  $N_{\text{init}}$  and  $N_{\text{prod}} = M_{\text{prod}} \times N_{\text{cold}}$  must also be chosen for a single canonical MC simulation and  $\Delta_{\text{spawn}}$  can always be taken around 100 (its value has little effect on overall performance and quality as long as it is not too low nor too high). The extra parameters  $T_{\text{hot}}$  is equivalent to the hottest temperature used in simulated annealing and parallel tempering. Finally,  $M_{\text{init}}$  must be evaluated by an initial run, similar to how the intermediate temperatures used in parallel tempering are obtained or the slope and plateau lengths of simulated annealing are usually chosen.

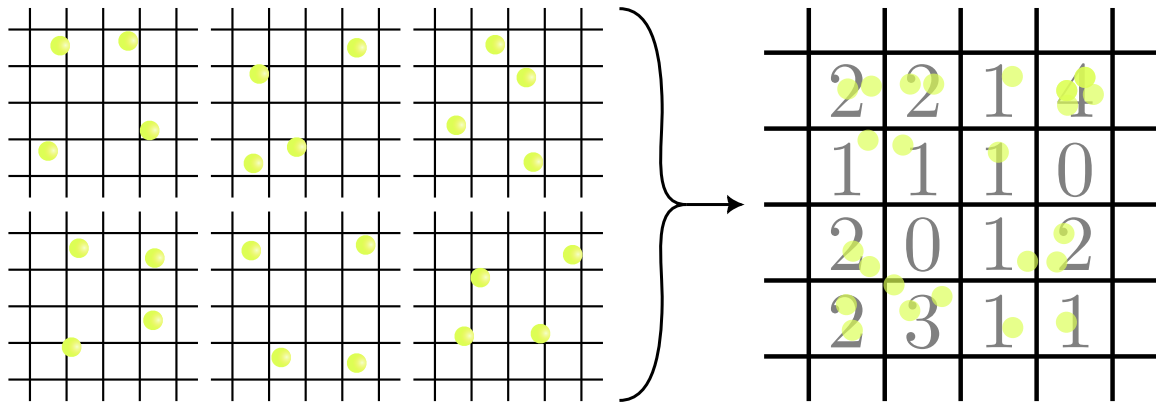
The complexity of the overall setup is thus similar to that of simulated annealing. Contrary to the latter however, this simulation strategy lets the cold simulations run for as long as necessary without restarting the simulation, which is desirable to assert convergence. Compared to parallel tempering, comparatively less simulation time is spent on the hot simulations, which allows doing more statistics on the cold runs. The particular mixing strategy of parallel tempering gives it better overall convergence properties, but a key feature of “shooting star” is the possibility to evaluate its global convergence, as will be later explained on an example in [section 2.3.1](#).

### 2.2.3 Extraction of sites and population from simulation

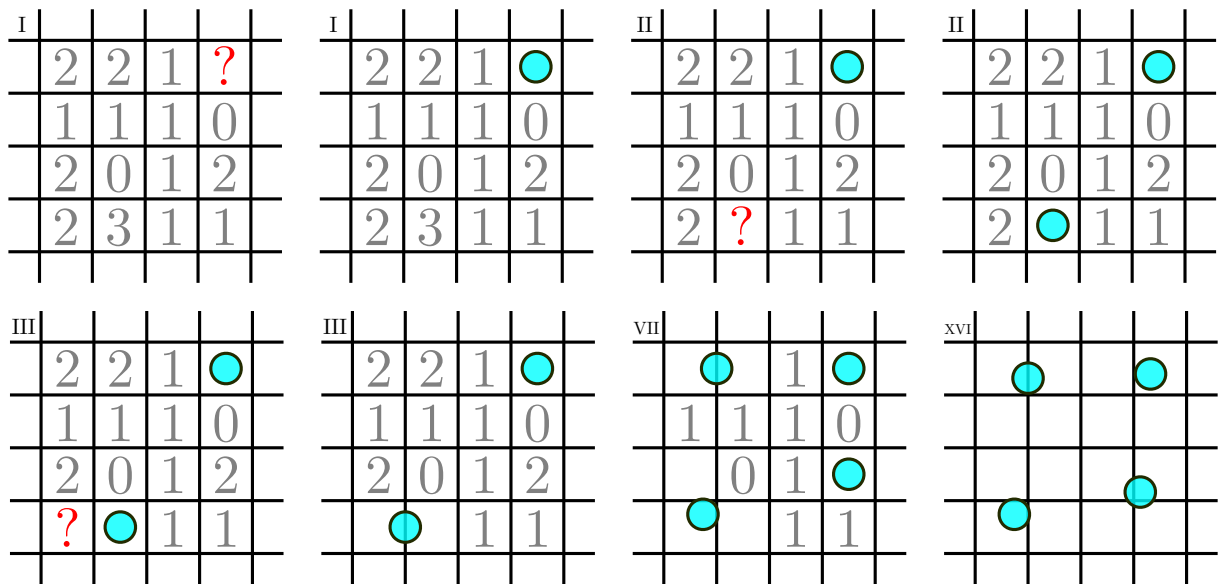
Assuming we do not know the position of the cation sites, a canonical MC simulation (possibly with “shooting star” or another meta-algorithm) yields a sequence of cation configurations sampled at room temperature. This sequence can be flattened into a map of the zeolite framework, with one additional point at each position occupied by a cation in one of the steps. Looking at this map allows qualitatively identifying the crystallographic sites as the zones where the density of points is the highest. In order to get quantitative information on the site localization and population, I devised a clustering algorithm that extracts the sites from the previous density map, represented in [Figure 2.11](#).

The first step ([Figure 2.11a](#)) consists in dividing the space by a regular grid, whose voxels have the same shape as the unit cell (same angles but possibly different lengths, taken to be closest to a target value around 0.15 Å). To each voxel is then attributed the number of cations encountered within, across the recorded simulation cycles. This first step thus bins the density onto a regular grid.

In the second step ([Figure 2.11b](#)), the bins are sorted by decreasing order of their value. Each voxel is then taken in that order: if it is closer than a set distance to a previously recorded site (case III in [Figure 2.11b](#)), then the location of the site is updated as the average of its current position and that of the voxel, weighted by the respective density of both; the density of the voxel is then added to that of the site. Otherwise, if it is far enough from all existing sites – the minimum distance is set to 1.6 Å –, it is added to the (initially empty) list of recorded sites, along with its density (case I and II in [Figure 2.11b](#)). This yields a series of sites and their respective occupancy. To be more efficient, the main loop stops early when the density of the inquired voxels goes below a threshold value, taken as the maximum density of all bins divided by 100: as a consequence, the occupancies are corrected by a multiplicative factor so that the sum of the occupancies of all sites correspond to the number of cations. This should not be

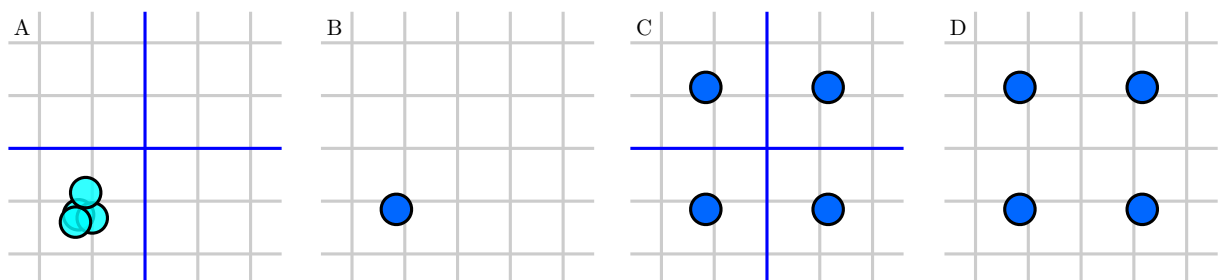


(a) Flattening of the cation locations onto a density grid. Numbers count how many cations were recorded on the corresponding voxel.



(b) Main loop: clustering of densities into sites. The top left roman numeral indicates is the loop iteration number which iterates by decreasing order of voxel population, starting at I with the most populated voxel (in position (1, 4)), until XVI for the least populated voxel (either (2, 4) or (3, 2) here).

In represented iterations I and II, new sites are created because they are far enough from all other sites. In iteration III, the density is merged with the neighbouring site, which is displaced to the barycentre of its densities.



(c) Resymmetrization of sites. Blue lines indicate the mirror symmetries of the framework.

A: each site is mapped to a unique symmetric image during “folding”. B: sites that are too close from one another are merged together. C: the obtained sites are “unfolded”, i.e. one new site is created per symmetric image of the previous sites. D: final sites.

Figure 2.11: Schematic representation of the site extraction algorithm

required in theory, but it is the necessary fix to a double discretization artifact, once inherent to the MC scheme, and one due to the binning.

The results are slightly better if the density grid is smoothed into a temporary grid, which is then used to obtain the order of the voxels, by sorting them in decreasing order of density, instead of using the order directly from the initial density grid. Indeed, this erases some small statistical fluctuations that may change the precise order of the voxels. Smoothing is done by convolving the density map by a small Gaussian, of standard deviation the size of the diagonal of a voxel.

This initial list of sites is then symmetrized ([Figure 2.11c](#)), to obtain a common list of sites irrespective of the aluminium placements. To do so, a strategy similar to the hashing of aluminium placements (explained in [section 2.1.2](#)) is used: for each site, its image is computed for each symmetry of the framework. If one of the images is too close (I use a minimum distance of 1 Å) to one of the previously recorded sites, they are merged; otherwise, the one closest to a fixed arbitrary reference is recorded. Hence, the initial sites are “folded” to yield a list of symmetrically unique sites. Those are then “unfolded” again by applying all symmetries to obtain the final list of all sites in the framework.

An alternative strategy could consist in symmetrizing the initial density map itself, by applying all the symmetries to the cations before counting them in the density grid. However, this is computationally more costly than the last option, and it does not yields better results in practice, probably due to the additional discretization artifact incurred by this strategy.

The final list of sites is such that for any site, all its symmetric images are also sites, and two sites cannot be closer than 1 Å. Note that the minimum distance of 1.6 Å used as a minimum between two starting points of initial sites does not necessarily transfer to the final sites, because of both the growing of the initial sites, and because of the merging operated during the “folding” part of resymmetrization. The result of each step of the algorithm is represented in the case of FAU in [Figure 2.12](#), where the final cationic site colors and sizes differentiate the different kinds of site.

## 2.3 RESULTS

This section presents the cation location and population results in the studied zeolites. FAU (faujasite) zeolite will be presented first, because it is an already well-studied case<sup>74,107–110</sup> that highlights the main difficulties encountered when attempting to locate cations, followed by a generalization.

### 2.3.1 Case study: FAU

The FAU zeolite is one of the most well-known zeolites used in the industry. It is composed of large cages, of 12 Å in diameter, separated by 12-membered rings, and small sodalite cages separated by hexagonal prisms. A detail of FAU with Si/Al = 1 is illustrated on [Figure 2.12a](#).

#### SITE LOCALIZATION

As previously explained, the sites are located by running “shooting star” simulations. I used the force field of Boulfelfel et al. [105] with the hot simulation running at 2000 K for 20 000 cycles after 2000 initialization cycles, using both local and unbounded translations equiprobably,

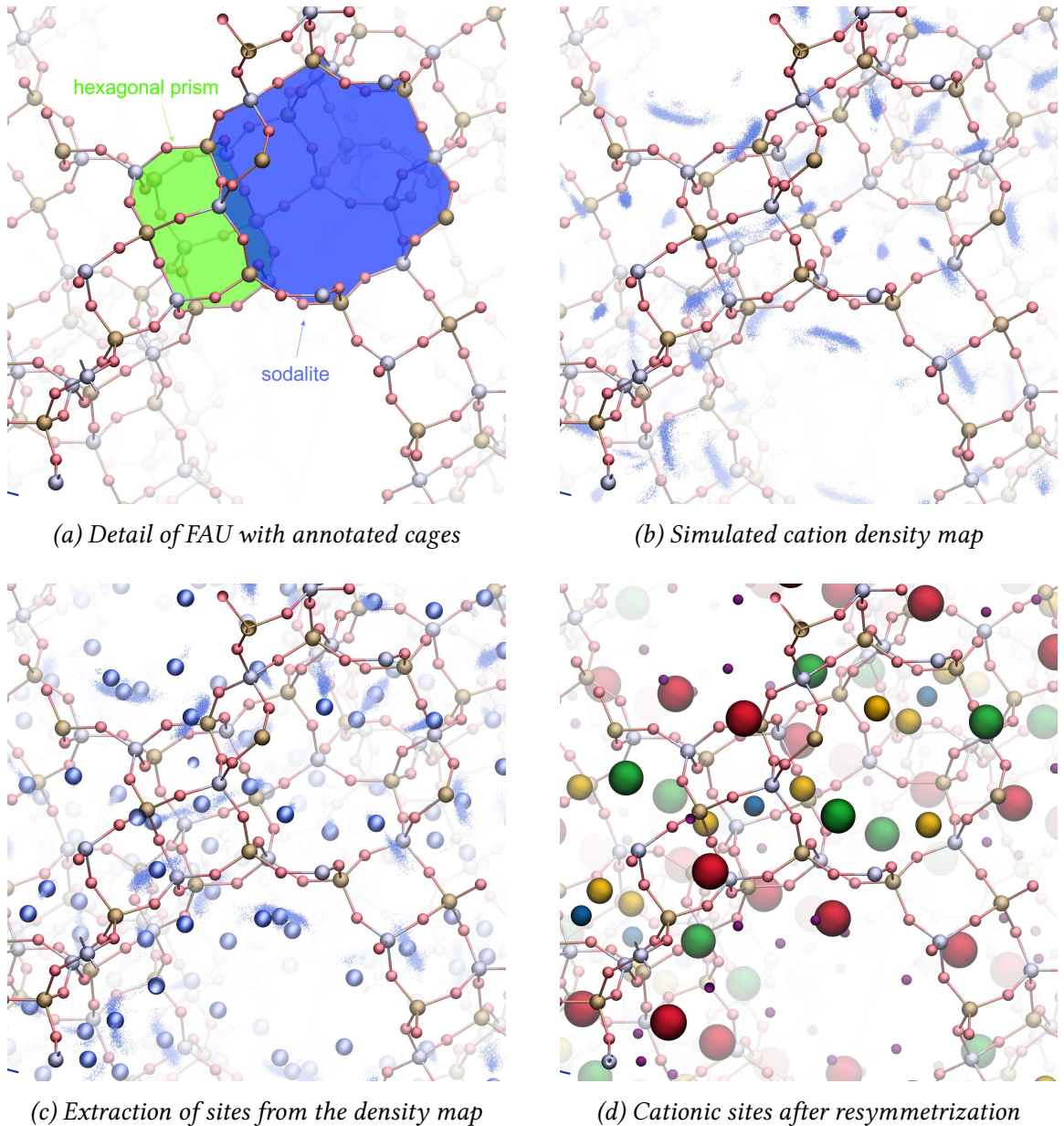
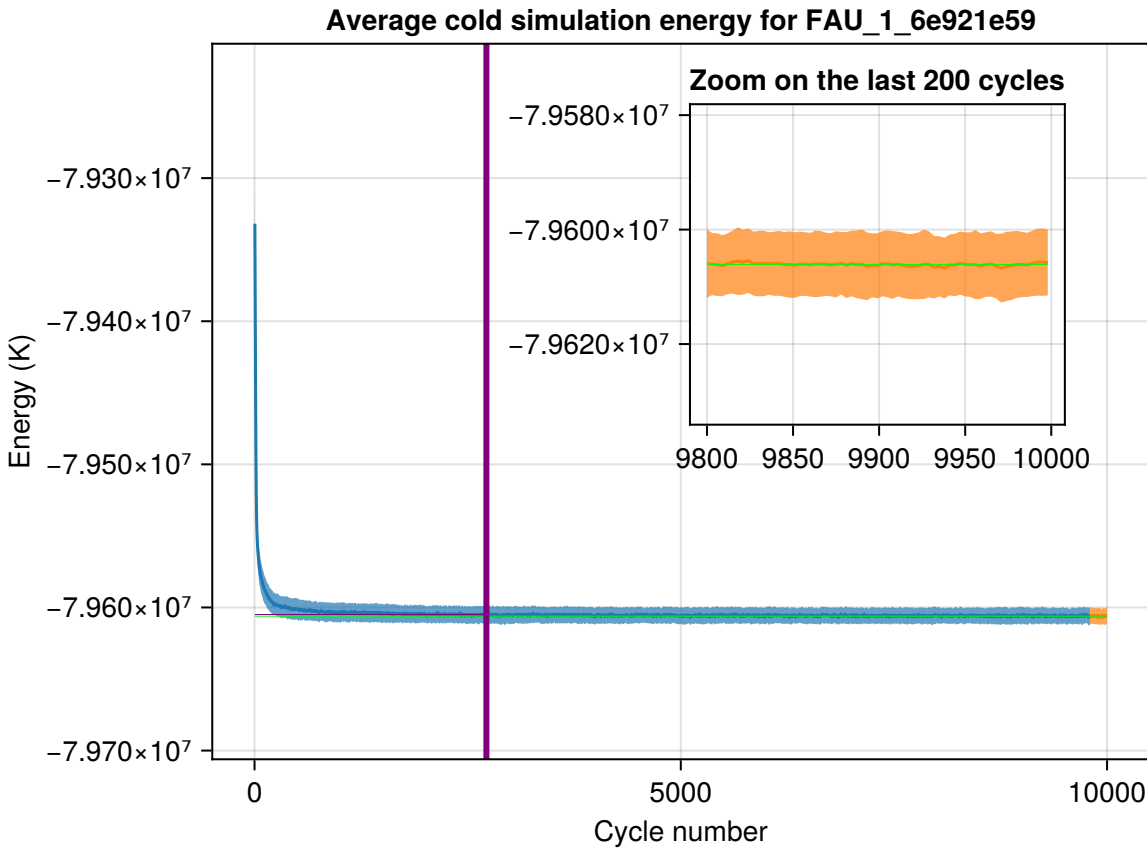


Figure 2.12: Cation localization for FAU

without the need for other MC moves since the cation studied here,  $\text{Na}^+$ , is monoatomic. 200 cold simulations spawn, once every 100 hot cycles, running for 200 production cycles after 9800 initialization cycles. Only the production cycles are used to record the density map.

The convergence of the “shooting star” simulation can be analyzed on [Figure 2.13](#) in the particular case of FAU\_1\_6e921e59, which is simply the faujasite framework with  $\text{Si}/\text{Al} = 1$  (6e921e59 is the hash of the only possible aluminium placement compatible with Löwenstein’s rule, as explained in [section 2.1.2](#)). This figure mostly focuses on the initialization cycles of the cold simulations, to study the global convergence of the simulation.

Assuming that the different cold simulations are uncorrelated, the standard deviation of their energy at a fixed cycle number gives an information on the statistical noise of the system, which appears to be approximately constant on the figure. Convergence is assessed based on



*Figure 2.13: Convergence of the “shooting star” simulation of  $\text{Na}^+$  in FAU with  $\text{Si}/\text{Al} = 1$*

The dark blue line represents the average energy of the cold simulations for each cycle number. The light blue halo around it represents plus or minus its standard deviation across the cold simulations. The inset focuses on the production cycles using dark and light orange for the same purpose. The vertical purple line identifies the cycle at which the simulation is estimated to have converged. The thin horizontal green line is the average of the energy of the cold simulations during the production cycles. The thin horizontal purple line is the average energy of the cold simulations at the estimated convergence cycle.

the lack of evolution of the energy averaged across the cold simulations: the vertical purple line marks the first cycle from which the slope of this average energy (smoothed on a few cycles to avoid artifacts) remains below a target bound. That mark is found automatically and all simulations are checked for convergence, determined by the presence of this mark before the production cycles.

The vertical separation between the green (final energy) and the purple (convergence energy) horizontal lines is another way to quantify the error on the estimation of the convergence of the simulation. In the current case, the difference is well below the statistical noise, which is a further sign of convergence.

Such a simulation runs for all structures corresponding to the reference topology: in the case of FAU, and for all other topologies that can reach  $\text{Si}/\text{Al} = 1$ , this means one simulation for  $\text{Si}/\text{Al} = 1$  and six (with six different aluminium placements) for  $\text{Si}/\text{Al}$  equal or approximately

Cationic site name	Number of sites per unit cell	Location	Color in figure 2.12d
I	16	At the centre of the hexagonal prism.	Blue
I'	32	In the middle of the 6-membered window between the hexagonal prism and the sodalite cage, slightly displaced toward the sodalite cage.	Yellow
II	32	In the middle of the 6-membered window between the sodalite cage and the supercage.	Green
III	48	In the supercage, atop the 4-membered window between the sodalite and the supercage.	Red
III'	96	In the supercage, atop the 4-membered window between the hexagonal prism and the supercage.	None
J	96	In the 12-membered window between two supercages, atop the oxygen of the 4-membered window between the sodalite and the supercage.	Purple

Table 2.2: Description of cationic sites of FAU

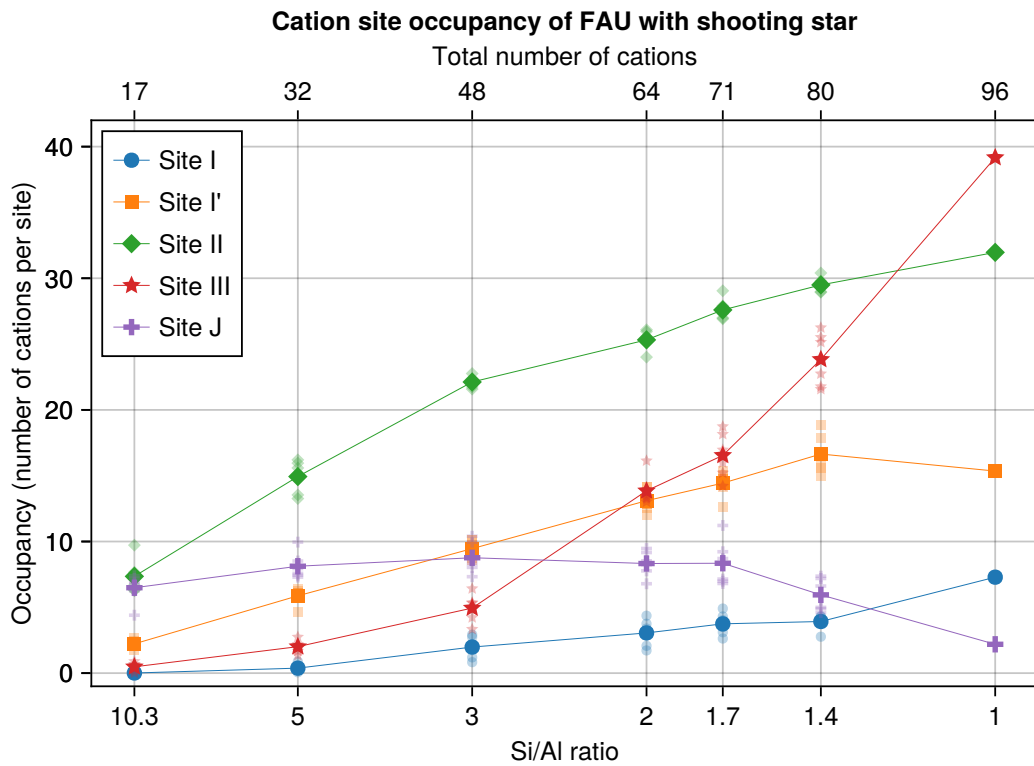
equal to 1.23, 1.4, 1.7, 2, 3, 5 and 10, hence 43 different “shooting star” simulations. The positions of each cation on each recorded cold production cycle across these simulations are flattened into a single density map of the framework, which serves as the basis for the location of cationic sites as explained in section 2.2.3.

#### DIRECT SITE POPULATION

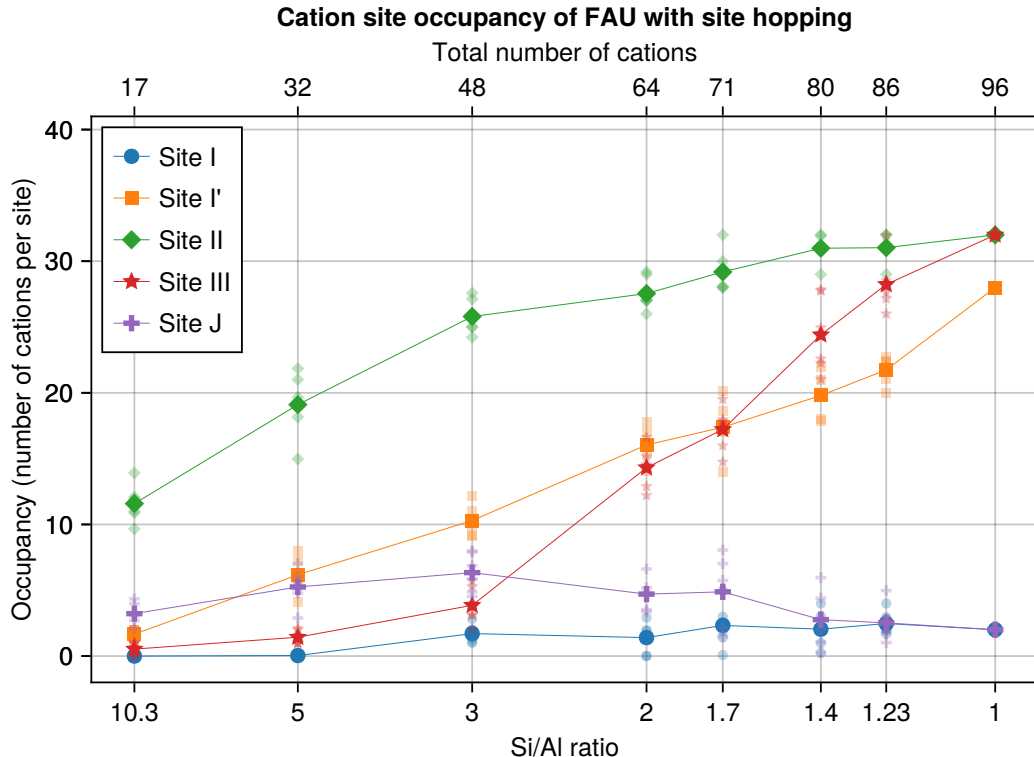
The site locations are obtained from the flattened density map across different Si/Al ratios, but the resulting occupancies are meaningless. To retrieve the actual site population, the unit cell of the zeolite is divided into volumes centered around each site, such that each point in a volume is closest to the corresponding site than to any other site. This operation is actually the Voronoi decomposition of the crystal space around the sites.

To assert their physical meaning, the Voronoi cells are intersected with solid spheres centered on the corresponding site and of radius 2 Å. Hence, any point in space is either in one of the truncated cells, in which case it is associated with a site closer than 2 Å, or it is not associated with any site. Once established for a given topology, this map is used for all its corresponding structures (with different Si/Al ratios and aluminium placements). Finding the population of each site from a simulation thus becomes a matter of averaging, across all recorded cycles, the number of cations in the truncated cells associated with each site.

In the literature, the different sites of FAU are well-known and have been given names. Those detected by the previous algorithm are listed in Table 2.2 along their usual names and represented in Figure 2.12d, using one color per kind of site and with size proportional to their occupancy. Site III' is also mentioned because it is present in other studies, although it was not detected by the algorithm. By contrast, site J is not usually mentioned in studies of faujasite, presumably because it is unoccupied except in the presence of water,<sup>111,112</sup> so its apparition here is possibly an artifact of the force field I use, from Boulfelfel et al. [105].



(a) Data from “shooting star” simulation



(b) Data from site hopping

Figure 2.14: Population of each site of FAU with force field from Boulfelfel et al. [105]  
Transparent symbols indicate the values for each of the 6 explicit aluminium placements.

With this information, the attribution of the cations to their site can be operated for each cold production cycle of the “shooting star” simulation. The average result is presented in [Figure 2.14a](#).

#### POPULATION COMBINED WITH SITE HOPPING

Alternatively to using the “shooting star” simulation results to establish the site population, the resulting site positions can be used to launch a site hopping simulation. Using 1 million production cycles (after 2 million initialization cycles) at 300 K with an output every 1000 production cycles takes up to three minutes per structure and yields a slightly different site population presented in [Figure 2.14b](#).

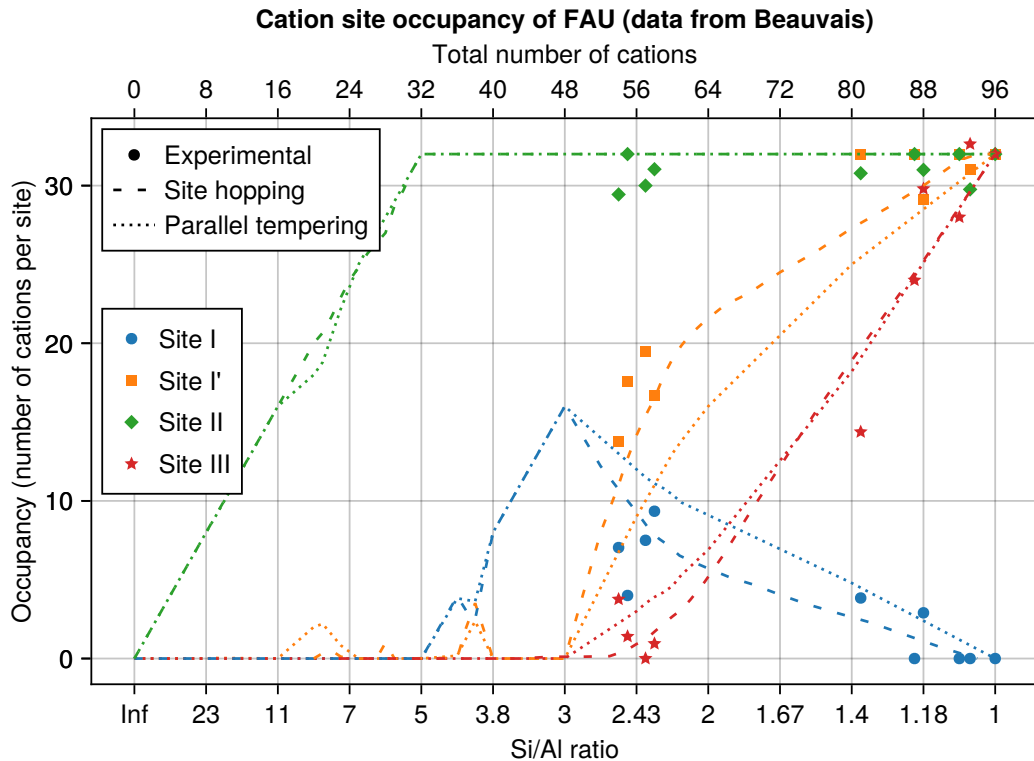
The main difference comes from the occupation of the sites I' at low Si/Al, which becomes almost maximal for the lowest ratio since there are 32 sites I'. It appears that the “shooting star” simulation alone does not correctly reproduces this trends, while site hopping manages to explore more combinatorial configurations of site occupancy, thus yielding more faithful site populations.

To compare those results with the literature, [Figure 2.15a](#) reproduces the site population of FAU obtained by Christèle Beauvais in her Ph.D. thesis [108], superposing experimental previous works as well as simulation data obtained from both parallel tempering and site hopping, using the force field from Di Lella et al. [111]. Site J is not used in that work. Nonetheless, while the general trend of site occupations bears some similarity, the evolution also has some marked differences, notably for site I around Si/Al = 3.

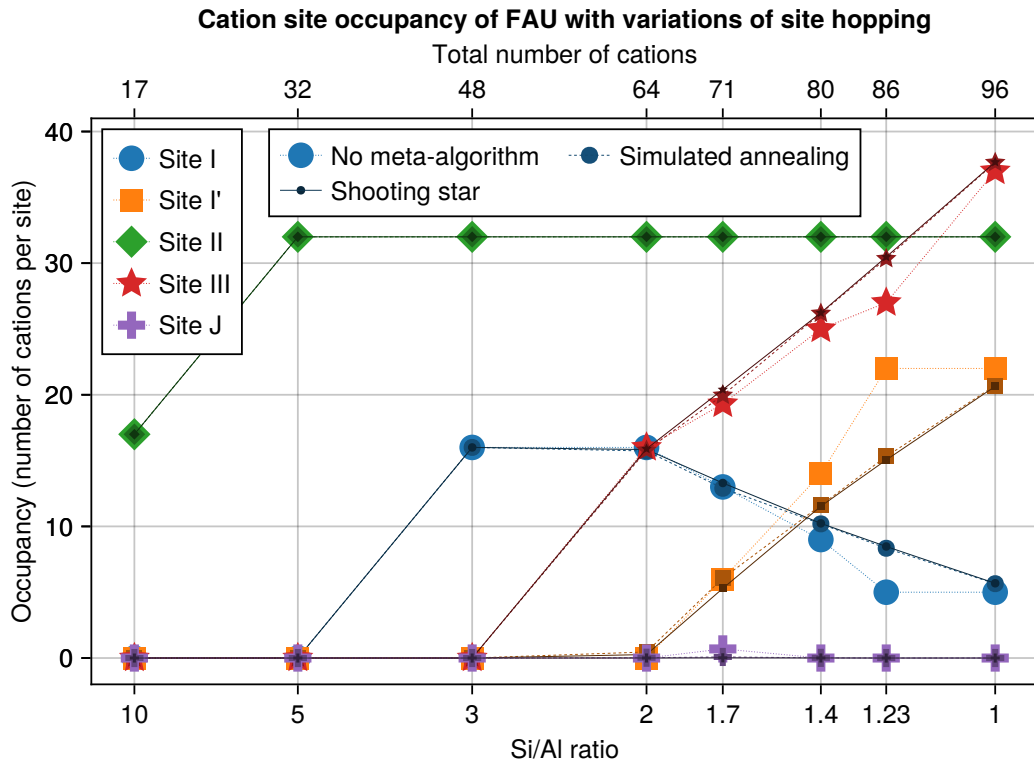
I investigated this discrepancy by running a new site hopping simulation, using the same force field by Di Lella et al. [111]. The resulting site population, shown in [Figure 2.15b](#) (big light symbols), is indeed more faithful to the original, but still bears a notable population difference for the lowest Si/Al ratios, where site I' fails to reach its expected occupancy of 32. In this force field, the aluminium and silicon atoms of the framework are represented by an identical T-atom, whose charge depend on the Si/Al ratio, hence there the absence of the transparent symbols indicating the result of each explicit aluminium placement.

Much like any base MC scheme, the site hopping algorithm can be combined with a meta-algorithm to improve its convergence. It is thus possible to run a simulated annealing version, by varying the temperature during the simulation, or even a “shooting star” simulation of site hopping. For simulated annealing, the temperatures ramped down 400 times, each time starting from 3000 K to 2000 K, then 1000 K, 300 K and finally 300 K again, equally spaced by 1000 cycles for each sub-ramp, and recording the site repartition at the end of the last 1000 cycles. For the “shooting star” variant, this hybrid simulation ran for 2 million hot cycles at 2000 K, spawning a cold simulation every 1000 cycles, each running for 20 000 cycles following 1 500 000 initialization cycles at 300 K.

The results are superposed to the simple site hopping computation on [Figure 2.15b](#) (medium symbols for simulated annealing, small dark symbols for “shooting star”). The two evolutions with meta-algorithm superpose almost exactly, which shows that simulated annealing is complex enough to ensure convergence of site hopping simulations. These evolutions are smoother compared to the bare simulation without meta-algorithm, and show a consistent and marked difference around Si/Al = 1.23 in particular: this highlights the interest of using meta-algorithms to ensure proper convergence of even site hopping simulations. It is worth



(a) Data from Christèle Beauvais's Ph.D. thesis [108]



(b) Data from site hopping with and without meta-algorithms

Figure 2.15: Population of each site of FAU with force field from Di Lella et al. [111]

mentioning that the simulated annealing simulation ran to create Figure 2.15b only takes a few minutes per point, and can be realized in parallel, so the main computational cost of finding the site populations is incurred earlier, when attempting to locate these sites.

These results still differ from those of Christèle Beauvais [108] at low Si / Al, which is unexpected; it might be due to a difference in the exact positions used for the site, or even in the faujasite model used.

#### **“SHOOTING STAR” SIMULATION CALIBRATION**

The temperature of the hot simulation, as well as the inclusion of unbounded translations, was determined by running “shooting star” simulations at other temperatures with and without MC moves. Two starting positions of the cations were used, using a single structure with Si/Al = 2 hence needing 64 cations: both configurations start by filling the 32 sites II, then the first configuration fills the 32 sites I’ (configuration I’) while the second fills the 16 sites I and then selects 16 sites III at random (configuration I). As shown on Figure 2.12d, every site I is sandwiched between two very close sites I’, so a site I’ and its neighbor site I cannot be occupied by cations at the same time. These two starting configurations are thus extremes, in the sense that crossing from one to the other requires transitioning through a state where one cation is in a site I’ and another in either III or J, which is kinetically costly.

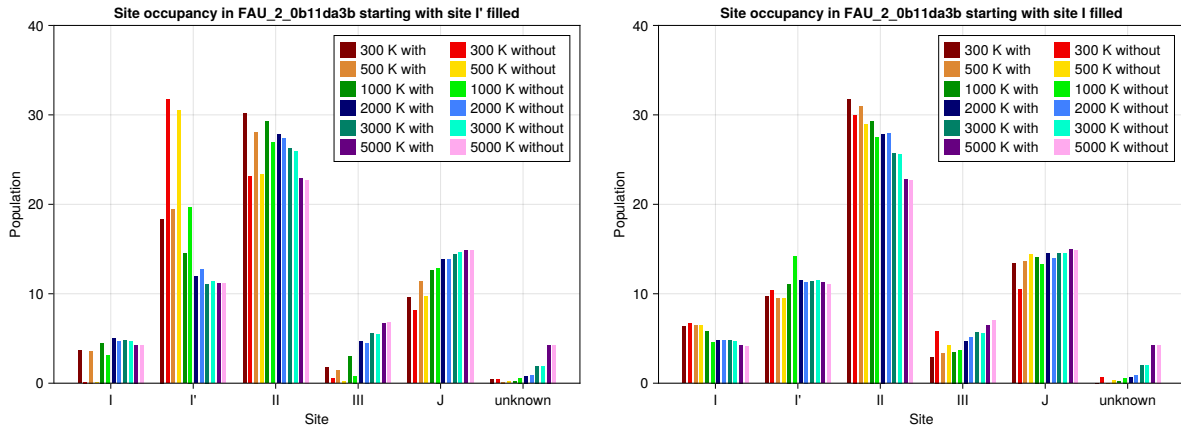
The average repartition of cations across the different sites corresponding to these two starting positions are represented on Figure 2.16, using two different force fields. The first one, from Boulfelfel et al. [105], requires having explicit aluminium atoms so a specific fixed placement was chosen, while the second one, from Di Lella et al. [111], is designed for uniform T-atoms whose properties were set to correspond to the target Si / Al = 2.

In both cases, sites I’ remain strongly populated for starting configuration I’ up to 1000 K with only local translations, much less so with unbounded translations, hence the inclusion of these MC moves appears to significantly increase the convergence of the MC simulations.

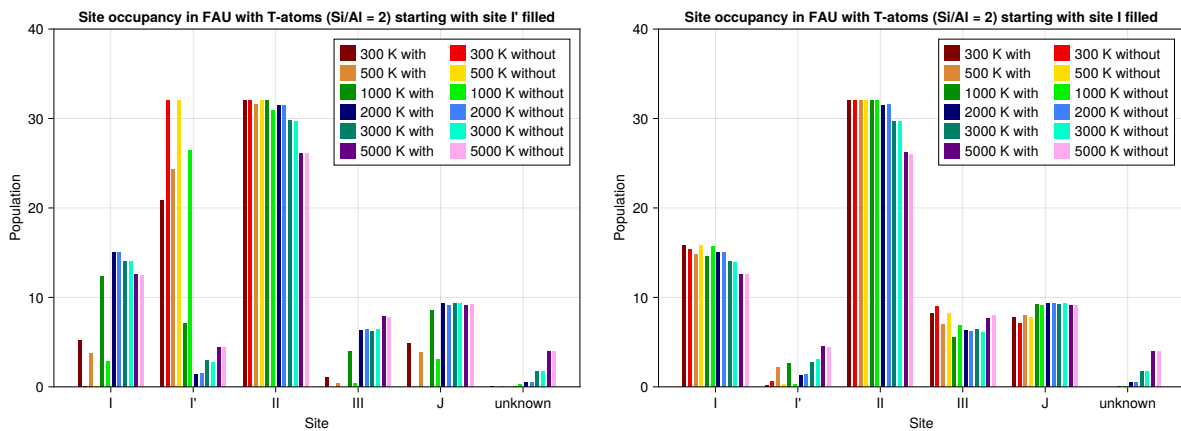
The temperature of the hot simulation plays a critical role: at low temperatures, the repartition remains close to the starting position, while at high temperatures the repartition becomes independent of the starting position. This effect is more pronounced on the simulations starting from configuration I’, in particular when using the force field by Di Lella et al. [111]. The hot temperature of 2000 K was thus chosen because it is the first temperature that shows an identical repartition independent of the starting configuration, while still avoiding having cations out of site (the right-most “unknown” bucket in the figure). At that temperature, the influence of the unbounded translation MC moves is very small, but I kept them for the expected improved convergence overall. The residual cations out of a site have been discarded from the other figures in this section because of their negligible number.

#### **2.3.2 Other zeolites**

The methodology developed before is not specific to the FAU zeolite, and can be used on any other structure. At the time of writing, 64 zeolite topologies were automatically investigated by running “shooting star” simulations on them at different Si / Al ratios, in order to identify their cationic sites. Table 2.3 lists these topologies, along the number of symmetry-wise unique sites identified for each: for example, zeolite FAU has 5 detected unique sites, which are I, I’, II, III and J.



(a) Sites population with force field from Boulfelfel et al. [105]



(b) Sites population with force field from Di Lella et al. [11]

*Figure 2.16: Hot temperature calibration results for “shooting star” simulations. “with” (resp. “without”) in the legends refers to the presence (resp. absence) of unbounded translations.*

These numbers exhibit quite large disparities, between only 1 for AST and SOD to 32 different unique sites for MFI. This can be explained by correlating them with the volume of the asymmetric unit of the framework, that is the volume of its unit cell divided by the number of symmetries of the topology, as illustrated on Figure 2.17. This correlation is mathematically founded by the nature of the cationic sites the algorithm finds, since they must obey the symmetries of the framework.

Nonetheless, like for the case of FAU, the repartition of the cations across these sites is far from uniform, making the less populated sites less relevant for analysis. For example, the ANO topology whose site population is represented on Figure 2.18 has 12 identified sites, of which 4 are never populated by more than one cation across all Si/Al ratios.

For this topology, the raw “shooting star” results are quite close to those obtained from the refined site hopping methodology augmented with simulated annealing, using the same conditions as in section 2.3.1. Similar to the results for FAU represented on Figure 2.15b, the trends are very similar, but the exact site occupancies sometimes differ, in particular here for

ABW	3
AEL	7
AFG	6
AFO	6
AHT	4
ANA	2
ANO	12
AST	1
ASV	3
ATN	3
ATS	7
ATV	5
AWW	5
BOZ	15
CAN	2
CAS	5
CFI	8
CHA	4
DOH	6
DON	12
EMT	14
EWO	7
FAR	8
FAU	5
FER	8
FRA	13
GIU	10
IFO	8
IHW	11
IRN	14
JRY	6
LIO	11
LOS	4
LTA	2
LTJ	2
LTL	6
MAR	11
MEL	19
MFI	32
MSO	5
MTW	8
NPT	2
NSI	7
OBW	6
PTT	5
RFE	10
RTE	5
RWY	3
SAF	7
SAS	3
SAT	6
SFE	12
SFG	22
SFN	11
SGT	5
SOD	1
SSF	11
TOL	17
TON	6
TSC	8
UFI	8
UOZ	4
VET	6
VFI	4

Table 2.3: Number of cationic sites identified per investigated zeolite topology

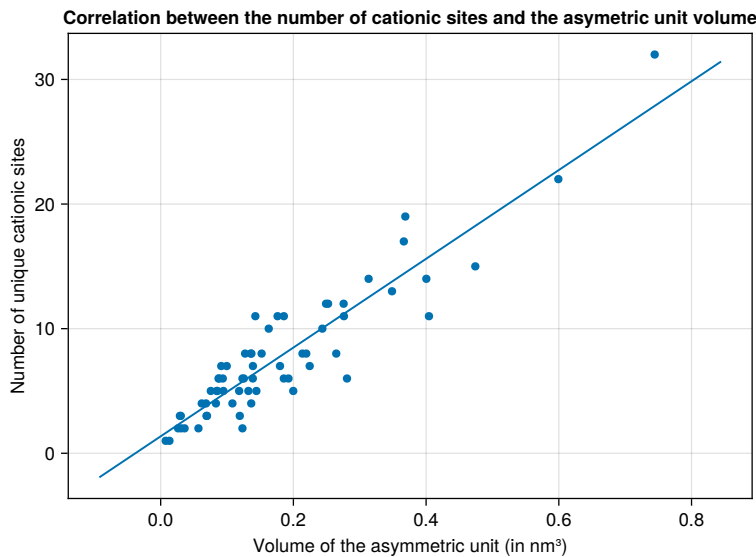
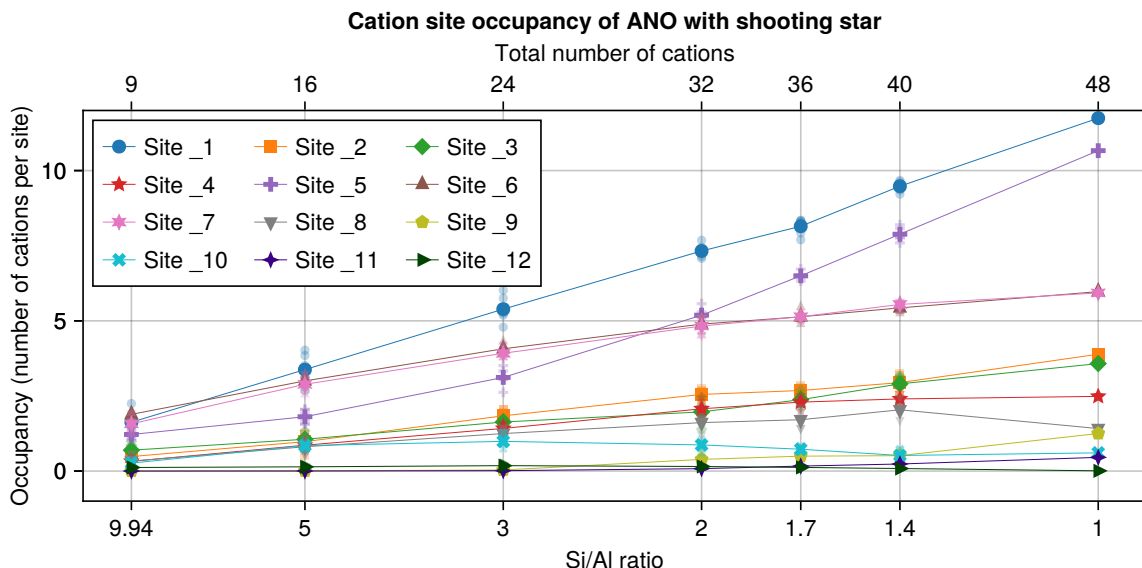


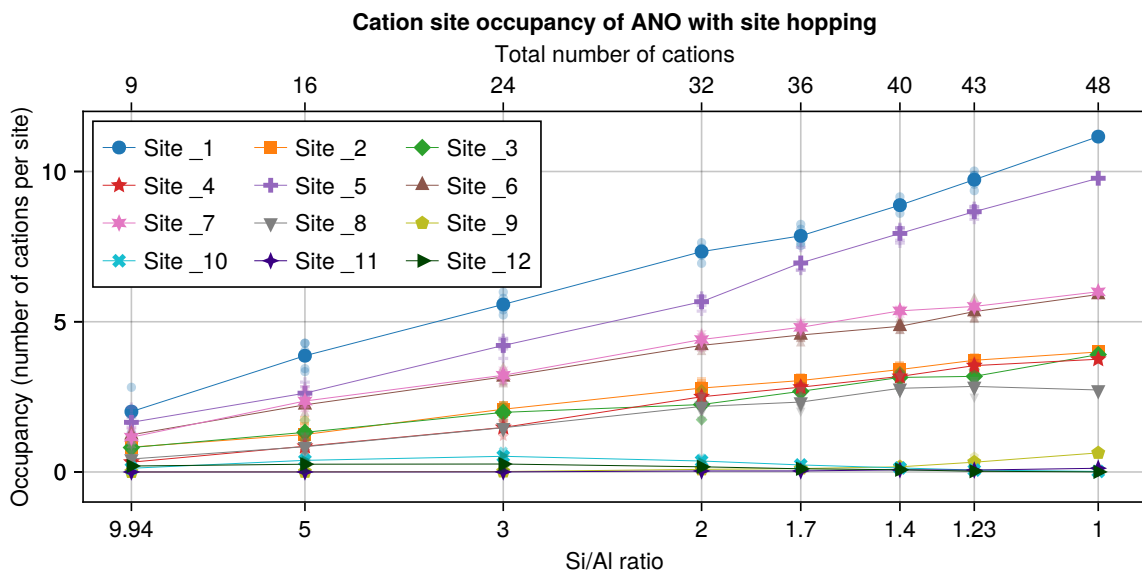
Figure 2.17: Correlation between the volume of the asymmetric unit and the number of unique site per zeolite. Coefficient of determination:  $R^2 = 0.848$

site “\_5”. Once again, this highlights the added value of site hopping simulations in order to obtain precise site population results.

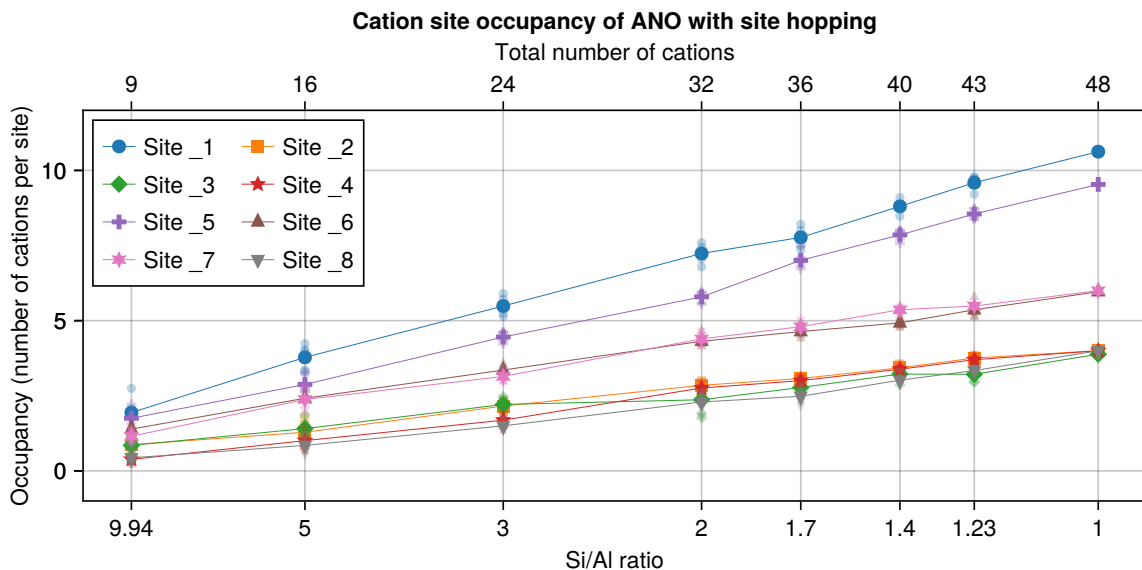
Figure 2.18c shows the result of site hopping (still with simulated annealing) on ANO, but using only the 8 most occupied unique sites. With all their symmetric images, these account for 576 site positions per cell (using a  $3 \times 3 \times 1$  supercell), compared to 828 positions when taking into account all 12 unique sites. These results are almost identical to those represented on Figure 2.18b for all 12 sites. The influence of possibly spurious sites is thus negligible for the overall repartition of cations with this methodology, which indicates its robustness.



(a) Results directly from “shooting star” simulations



(b) Refined results from site hopping with simulated annealing



(c) Refined results from site hopping with simulated annealing on only the first 8 sites

Figure 2.18: Population of each site of ANO

Overall, the proposed methodology for identifying the cationic sites of a zeolite consists in running “shooting star” simulations of the target topology across different Si/Al ratios, flattening the cation density maps resulting from all the different cold simulations into a single map, from which the location of the sites are extracted. Their population is then found by running site hopping simulations augmented with simulated annealing. This method shows robust results even for zeolites with many sites, and convergence of the intermediate simulations can be controlled systematically.

## 2.4 ENERGY COMPUTATION

All of the previously exposed methods rely on Monte Carlo moves which may, or may not, be accepted, depending on the difference of energy between the configuration before and after. By far, the greatest computational cost of any of these methods lies in these energy computations; it is therefore crucial to be able to compute it efficiently.

### THE RASPA2 SOFTWARE

RASPA2 is an open-source software developed by Dubbeldam et al. [113] for classical simulations of molecular systems. Although general purpose, it is mainly used with nanoporous materials and in particular for the study of adsorption and diffusion within. RASPA2 implements Monte Carlo schemes with the Metropolis-Hastings algorithm to perform canonical simulations, but also grand canonical for adsorption (see chapter 3), as well as parallel tempering. Furthermore, it also includes the Gibbs ensemble simulation, it can handle flexible guest species and frameworks, and has many other functionalities which were not needed here.

RASPA2 is written in C, a low-level programming language which allows reaching optimal performance, but is tedious to program in. It cannot be used on GPU and is single-threaded. In order to develop new simulation strategies in an easier setting, I re-implemented the algorithms used for both canonical and grand-canonical simulation of rigid species in rigid frameworks using the Julia programming language.<sup>32,33</sup>

The energy computation algorithms detailed below are those which were implemented in this new code. Most of them follow the implementation in RASPA2, with some improvements explained herein. Moreover, RASPA2 was used to validate the new code, by checking that the simulations yielded the correct physical values (energies, adsorption capacities, and such). By contrast, the “shooting star” meta-algorithm presented before does not exist in RASPA2.

### 2.4.1 Force fields

The energy of a molecular structure results from the interaction of its constituent atoms, which are intrinsically quantum. At the molecular level, a popular method used to compute it is the quantum Density Functional Theory (DFT), which includes a variety of particular methods, each presenting its own compromise between precision and performance. Some alternatives include methods derived from molecular orbital theory. The number of energy computations for a single molecular simulation can be of the order of  $10^4$  to  $10^7$  however, which would be much too costly with such methods for large scale screening.

What is commonly used instead are classical force fields, which approximate quantum interactions as a sum of classical interactions between each pair of atoms. These pairwise interactions

are defined by one formula per pair of natures of atoms; in the case of non-bonded interactions, each formula is simply a function of the distance between the two atoms. Zeolites are mostly rigid materials, which means that their deformation due to their vibration modes, or subsequent to the organization of cations or adsorbed gas inside, is negligible for the purpose of the molecular simulation. As a consequence, the interactions between framework atoms can be skipped, the only ones to consider for cation placement are those between the cation and the different atoms of the zeolites, which are not bonded.

The pairwise interaction formula is usually divided between the coulombic contribution due the charges of the atoms, and a short-range van der Waals term. Designing a force fields thus customarily consists in choosing the atomic charges and the formula for the van der Waals term. Several options have been used in the literature for the latter: a very common option is the Lennard-Jones potential

$$r \mapsto 4\epsilon \left( \left( \frac{\sigma}{r} \right)^{12} - \left( \frac{\sigma}{r} \right)^6 \right) \quad (2.4)$$

where  $r$  is the distance between atoms. One alternative is the Buckingham potential

$$r \mapsto A \exp(-B \times r) - \frac{C}{r^6} \quad (2.5)$$

The potential parameter  $\epsilon$ ,  $\sigma$ ,  $A$ ,  $B$  or  $C$  are part of the design of the force field and depend on the chemical nature of the atoms involved.

#### 2.4.2 Short-term interactions

Since the van der Waals term decays quickly towards zero, it is computationally useful to set it to exactly zero beyond a cutoff distance. To do so while avoiding the introduction of unphysical forces, one possibility consists in shifting the formula by a constant, so that the function remains continuous at the cutoff. If no force is required, such as in the MC methods, it is possible to leave the potential unshifted and discontinuous at the cutoff; a tail correction is then added to the total energy to account for the missing interactions (this will be detailed in section 3.2.3). In any case, knowing that the interaction becomes zero after the cutoff allows some computational optimizations, such as using cell lists in order to iterate over the relevant atom pairs only, instead of all atom pairs.

For simplicity of the implementation, the dimensions of the simulated unit cell must be taken so that for any atoms A and B, there is at most one periodic image of B which is closer to atom A than the cutoff distance. This translates to the constraint that the orthogonal lengths of the unit cell must be as long as at least twice the cutoff. We typically take this cutoff as 12 Å, as is common in the literature and is the default in RASPA2.

Given this constraint, the total energy of a configuration due to the van der Waals interaction can be computed by summing the contribution of each the pair of atoms which are closer than the cutoff distance. This can be done naively with a double loop over all atoms, computing the distance of each pair and rejecting those above the threshold. Here, the distance considered is the periodic distance, *i.e.* the smallest distance between periodic images of the two atoms, respective to the periodicity of the crystal. Computing it is up to 6 times more costly than without periodicity, and the application of the minimal image convention can become a computational bottleneck for simple enough force fields.

To avoid unnecessary distance computations, a possibility consists in binning the space of the unit cell, and skipping the pairs of atoms that belong to bins further than the cutoff distance. This idea underlies the principle of neighbour list which can be used to obtain the list of relevant pairs of atoms efficiently. I use the `CellListMap.jl`<sup>114</sup> Julia package for this purpose, although it is only enabled when the cell is large enough. Indeed, the naive approach can actually be more efficient in many cases where the orthogonal lengths of the cell are close to twice the cutoff distance.

### 2.4.3 Ewald summation

#### ENERGY DECOMPOSITION

In opposition to the van der Waals term, charge interactions do not have a fixed cutoff, because Coulomb's law does not decay fast enough towards zero. The interaction between atoms A and B, of respective charge  $q_A$  and  $q_B$ , is:

$$E_{A,B}^{\text{Coulomb}} = \frac{q_A q_B}{4\pi\epsilon_0 \times \|r_B - r_A\|} = \frac{q_n q_m}{4\pi\epsilon_0 \times \|r_m - r_n + l\|} \quad (2.6)$$

where  $n$  and  $m$  are the unique atom numbers in a reference unit cell of respectively A and B, and  $l$  is the lattice vector between the origin of the unit cell of A and that of B. Therefore the total contribution of charge interactions in a crystal with N atoms per unit cell is:

$$E^{\text{Coulomb}} = \frac{1}{2} \sum_{A \neq B} E_{A,B}^{\text{Coulomb}} = \frac{1}{8\pi\epsilon_0} \sum_l \sum_{n=1}^N \sum_{\substack{m=1 \\ n \neq m \text{ if } l=0}}^N \frac{q_n q_m}{\|r_n - r_m + l\|} \quad (2.7)$$

where  $l$  iterates over the lattice vectors.

The semi-convergence of the sum over  $l$  makes it impossible to compute directly. Hence, several methods have been developed to obtain the result such as particle mesh Ewald (PME) and particle-particle-particle-mesh ( $P^3M$ ). Let's focus on the initial Ewald summation technique underlying them, which is used in RASPA2 and which I also implemented.

Since the crystal is a periodic system, any function of the system that depends on a position in space can be decomposed into a simple sum by Fourier transform. This is in particular true of the electric potential, hence the problematic sum above could be computed in Fourier space. However, the charges are located on the atoms, and are thus discrete, which causes singularities that prevent the computation. The idea behind Ewald summation consists in fictitiously smoothing the point charges into Gaussians: these smooth charges yield a potential computable in Fourier space, while the potential resulting from the real point charge minus their Gaussian counterpart is computed in real space. Electric potential is additive, so the total electric potential  $\Phi(\mathbf{r})$  is then obtained by adding the real space term  $\Phi^{\text{direct}}(\mathbf{r})$  and the Fourier term  $\Phi^{\text{reciprocal}}(\mathbf{r})$ . Finally, the resulting energy is simply the action of the point charges on the potential:

$$E^{\text{Coulomb}} = \frac{1}{2} \sum_{n=1}^N q_n \left( \Phi^{\text{direct}}(\mathbf{r}_n) + \Phi^{\text{reciprocal}}(\mathbf{r}_n) \right) - E^{\text{self}} \quad (2.8)$$

$E^{\text{self}}$  designates a spurious self-interaction energy term which must be subtracted.

**DIRECT TERM**

To each atom A of the crystal is associated a Gaussian charge density

$$\mathbf{r} \mapsto q_A \left( \frac{\alpha}{\sqrt{\pi}} \right)^3 \exp \left( -\alpha^2 \|\mathbf{r}_A - \mathbf{r}\|^2 \right) \quad (2.9)$$

Thus, the direct term is the potential resulting from the point charge minus this Gaussian. This can be obtained by solving Poisson's law:

$$-\nabla \Phi(\mathbf{r}) = 4\pi\rho(\mathbf{r}) \quad (2.10)$$

which yields, after some simplification steps not detailed here:

$$\Phi_A^{\text{direct}}(r) = q_A \frac{\text{erfc}(\alpha r)}{r} \quad (2.11)$$

where  $r$  is the distance to atom A and erfc is the complementary error function  $\text{erfc} = 1 - \text{erf}$ , with  $\text{erf} : x \mapsto \frac{2}{\sqrt{\pi}} \int_0^x e^{-t^2} dt$ . Since erfc quickly decays towards 0, the total direct potential at a given point can be computed by only considering the contribution of the closest charges around, so

$$\Phi^{\text{direct}}(\mathbf{r}) \approx \sum_{n=1}^N \frac{q_n}{\|\mathbf{r} - \mathbf{r}_n\|_p} \left( \text{erfc} \left( \alpha \|\mathbf{r} - \mathbf{r}_n\|_p \right) \right) \quad (2.12)$$

where  $\|\mathbf{x}\|_p$  designates the distance to the origin of the closest periodic image of  $\mathbf{x}$ .

**RECIPROCAL TERM**

For the reciprocal term, we start by writing the total charge density coming from the Gaussians given in Equation (2.9):

$$\rho^{\text{reciprocal}}(\mathbf{r}) = \sum_{\mathbf{l}} \sum_{n=1}^N \frac{q_n}{4\pi\epsilon_0} \left( \frac{\alpha}{\sqrt{\pi}} \right)^3 \exp \left( -\alpha^2 \|\mathbf{r}_n + \mathbf{l} - \mathbf{r}\|^2 \right) \quad (2.13)$$

Its Fourier decomposition over the periodic unit cell of volume V is:

$$\begin{aligned} \hat{\rho}^{\text{reciprocal}}(\mathbf{k}) &= \frac{1}{V} \int_V e^{-i\mathbf{k} \cdot \mathbf{r}} \rho^{\text{reciprocal}}(\mathbf{r}) d\mathbf{r} \\ &= \frac{1}{V} \int_{\Omega} e^{-i\mathbf{k} \cdot \mathbf{r}} \sum_{n=1}^N \frac{q_n}{4\pi\epsilon_0} \left( \frac{\alpha}{\sqrt{\pi}} \right)^3 \exp \left( -\alpha^2 \|\mathbf{r}_n + \mathbf{r}\|^2 \right) d\mathbf{r} \\ &= \frac{2\pi\alpha^3}{V\pi^{3/2}} \sum_{n=1}^N \frac{q_n}{4\pi\epsilon_0} e^{-i\mathbf{k} \cdot \mathbf{r}_n} \int_0^{\infty} \|\mathbf{r}'\|^2 \exp \left( -\alpha^2 \|\mathbf{r}'\|^2 \right) \int_0^{\pi} e^{-i\mathbf{k} \cdot \mathbf{r}'} \sin(\theta) d\theta d\mathbf{r}' \\ &= \frac{1}{4\pi\epsilon_0 V} \exp \left( \frac{-k^2}{4\alpha^2} \right) \sum_{n=1}^N q_n e^{-i\mathbf{k} \cdot \mathbf{r}_n} \end{aligned} \quad (2.14)$$

after several simplification steps not detailed here. Using Poisson's law (Equation (2.10)), the electric potential due to the Gaussians can then finally be expressed as:

$$\Phi^{\text{reciprocal}}(\mathbf{r}) = \frac{1}{\epsilon_0 V} \sum_{\mathbf{k} \neq 0} \sum_{n=1}^N \frac{q_n}{k^2} e^{i\mathbf{k} \cdot (\mathbf{r} - \mathbf{r}_n)} \exp \left( \frac{-k^2}{4\alpha^2} \right) \quad (2.15)$$

The term  $\kappa_{\mathbf{k}} = \frac{1}{k^2} \exp(-k^2/(4\alpha^2))$  decays fast, so the sum over  $\mathbf{k} \neq \mathbf{0}$  is actually computed as a sum over a finite number of values of  $\mathbf{k}$  close to  $\mathbf{0}$ . These values are chosen so that the remaining sum of  $\kappa_{\mathbf{k}}$  for any  $\mathbf{k}$  not retained is below the target precision of the computation.

### SELF-INTERACTION TERM

The last remaining term is the self-interaction, which must be removed. Its existence comes from the way the reciprocal term is computed:  $\Phi^{\text{reciprocal}}(\mathbf{r})$  includes the contribution of all charges on point  $\mathbf{r}$ , but there should not be any contribution of atom A at position  $\mathbf{r}_A$ .

Moreover, in the case of rigid polyatomic molecules, like the small gases that will be discussed in chapter 3, there should not be any contribution of atom A at the positions  $\mathbf{r}_B$  of other atoms B part of the same molecule.

Each atom  $1 \leq n \leq N$  thus contributes a spurious potential term:

$$\Phi_n^{\text{self}} = \frac{2\alpha q_n}{\sqrt{\pi}} + \frac{1}{2} \sum_{\substack{m \\ m \sim n, m \neq n}} \frac{q_m \text{erf}\left(\|\mathbf{r}_n - \mathbf{r}_m\|_p\right)}{4\pi\epsilon_0 \|\mathbf{r}_n - \mathbf{r}_m\|_p} \quad (2.16)$$

where  $m \sim n$  is true when both atoms  $m$  and  $n$  belong to the same molecule.

### TOTAL CHARGE ENERGY

Combining the last three terms, we obtain the overall Coulomb energy:

$$\begin{aligned} E^{\text{Coulomb}} = & \sum_l \sum_{n=1}^N \sum_{\substack{m=1 \\ m \neq n}}^n \frac{q_n q_m}{8\pi\epsilon_0} \frac{\text{erfc}\left(\alpha \|\mathbf{r}_n - \mathbf{r}_m + \mathbf{l}\|\right)}{\|\mathbf{r}_n - \mathbf{r}_m + \mathbf{l}\|} \\ & + \frac{1}{2\epsilon_0 V} \sum_{\mathbf{k} \neq \mathbf{0}} \sum_{n=1}^N \sum_{m=1}^N \frac{q_n q_m}{k^2} e^{i\mathbf{k} \cdot (\mathbf{r}_m - \mathbf{r}_n)} \exp\left(\frac{-k^2}{4\alpha^2}\right) \\ & - \cancel{\sum_{n=1}^N \frac{2\alpha q_n}{\sqrt{\pi}}} - \frac{1}{2} \sum_{n=1}^N \sum_{\substack{m=1 \\ m \sim n, m \neq n}}^N \frac{q_n q_m}{4\pi\epsilon_0} \frac{\text{erf}\left(\|\mathbf{r}_n - \mathbf{r}_m\|_p\right)}{\|\mathbf{r}_n - \mathbf{r}_m\|_p} \end{aligned} \quad (2.17)$$

The term summing the  $2\alpha q_n / \sqrt{\pi}$  cancels out because the overall system needs to be electrically neutral to carry a physical meaning, so the sum of all  $q_n$  is 0. This invariant is checked in the code to avoid any error.

### 2.4.4 Precomputation

Different algorithms that solve a particular computational problem generally differ in the specific space-time trade-off they choose. Obtaining the energy of an atomic configuration presents the same possibility: while entirely computing the energy from scratch requires a set amount of computation, it is possible to make subsequent computations faster at the cost of a greater memory footprint of the algorithm, by storing some intermediate results which can be reused afterwards.

### ENERGY GRID

In the case of simulations involving a rigid framework, the most obvious precomputation that can be done is that of the short-term interactions of the guest species with the framework

atoms. Indeed, such interactions only depend on the nature and the position of the guest atom, so it is possible to store them on an energy grid.

More precisely, for each possible guest atom, the unit cell of the framework is divided into a regular grid, with a set spacing between consecutive points. I use 0.15 Å, which is fine enough to be accurate but not too fine to avoid using too much memory. For each grid point, the sum of the interactions of all framework atoms with a guest atom in that position is stored at that point. The grid is then written to disk.

During the simulation, in order to compute the short-term interactions between the framework atoms and a guest atom at a given position, the value is interpolated from the surrounding grid points. Using a simple linear interpolation of the values does not yield very satisfactory results however, since derivative discontinuity would push the atoms towards the grid points, which would result in simulation artifacts. To prevent this, RASPA2 stores not only the value of the energy, but also the three first derivatives, three values of the second derivatives and one of the third, following a scheme by Lekien and Marsden [115]. Moreover, the grid is forced to be orthorombic: this means that it may not be aligned with the unit cell of the framework, but it does not matter as long as each point in the unit cell can be surrounded by recorded grid points. I implemented the same grid algorithm in Julia, which ensures a smooth interpolation everywhere in space.

### EWALD PRECOMPUTATION

Short-term interactions that can be stored in grids include the short-term direct part of the Ewald summation. The reciprocal term cannot however be simply stored as such.

Yet, it is still possible to precompute a large part of the reciprocal interaction which is due to the framework. To take the potential given by Equation (2.15) back to the energy, it is useful to introduce the sums:

$$S_{\mathbf{k}} = \sum_{n=1}^N q_n e^{-i\mathbf{k} \cdot \mathbf{r}_n} \quad (2.18)$$

for each  $\mathbf{k}$ . With this notation, the contribution of the reciprocal term to the energy is

$$\begin{aligned} E^{\text{reciprocal}} &= \frac{1}{2} \sum_{m=1}^N q_m \Phi^{\text{reciprocal}}(\mathbf{r}_m) \\ &= \frac{1}{2\epsilon_0 V} \sum_{m=1}^N q_m \sum_{\mathbf{k}} \kappa_{\mathbf{k}} e^{i\mathbf{k} \cdot \mathbf{r}_m} S_{\mathbf{k}} \quad \text{then using } \overline{S_{\mathbf{k}}} = \sum_{m=1}^N q_m e^{i\mathbf{k} \cdot \mathbf{r}_m} \\ &= \frac{1}{2\epsilon_0 V} \sum_{\mathbf{k}} \kappa_{\mathbf{k}} \overline{S_{\mathbf{k}}} \times S_{\mathbf{k}} = \frac{1}{\epsilon_0 V} \sum_{\mathbf{k}} \kappa_{\mathbf{k}} \|S_{\mathbf{k}}\|^2 \end{aligned} \quad (2.19)$$

Hence, to avoid redundant computations, the list of relevant  $\mathbf{k}$ , associated to their factor  $\kappa_{\mathbf{k}} = \exp(-k^2/(4\alpha^2))/k^2$ , is computed once and for all. For each atom  $n$  of the framework, the factors  $q_n \exp(i\mathbf{k} \cdot \mathbf{r}_n)$  are also computed once. Distinguishing between the atoms of the framework and the guests allows separating  $S_{\mathbf{k}}$  into  $S_{\mathbf{k}}^{\text{framework}} + S_{\mathbf{k}}^{\text{guest}}$ , so that finally, the energy can be computed as

$$E^{\text{reciprocal}} = \underbrace{\frac{1}{2\epsilon_0 V} \sum_{\mathbf{k}} \kappa_{\mathbf{k}} \|S_{\mathbf{k}}^{\text{framework}}\|^2}_{\text{precomputed part}} + \frac{1}{2\epsilon_0 V} \sum_{\mathbf{k}} \kappa_{\mathbf{k}} (\overline{S_{\mathbf{k}}^{\text{framework}}} + \overline{S_{\mathbf{k}}^{\text{guest}}}) \times S_{\mathbf{k}}^{\text{guest}} \quad (2.20)$$

Finally, the entire self-interaction term can be computed once for all, since it does not depend on the configuration. This is only the case here because the simulated molecules are rigid bodies; for deformable structures, the self-interaction term depends on the actual conformation of the guests, which may depend on the state.

### OPTIMIZATIONS FOR COMPUTING THE DIFFERENCE OF ENERGIES

A simulation that follows the Metropolis-Hastings algorithm walks across configurations, each pair of contiguous states being separated by a single MC move. In this context, computing the energy of each trial configuration to compare it to the previous one is wasteful: the only part of the energy impacted by the MC move is that which stems from the moved species. Instead of computing the energy of the trial configuration, it is thus better to directly compute the energy difference due to the move.

For the short-term interactions, this is straightforward: the energy difference is simply the sum of the interactions of the species at the new position minus that at its previous position. If there are  $N$  species, moving one thus costs  $O(N)$  computations for these terms, instead of  $O(N^2)$  required to compute this energy the first time. The direct part of the Ewald summation follows the same principle.

For the reciprocal part, the difference in energy is derived from [Equation \(2.20\)](#) by removing the first constant term and computing:

$$\Delta E^{\text{reciprocal}} = \frac{1}{2\varepsilon_0 V} \sum_{\mathbf{k}} \kappa_{\mathbf{k}} \left( \overline{S_{\mathbf{k}}^{\text{framework}}} \times \Delta S_{\mathbf{k}}^{\text{guest}} + \Delta \|S_{\mathbf{k}}^{\text{guest}}\|^2 \right) \quad (2.21)$$

Since both values of  $S_{\mathbf{k}}^{\text{guest}}$  need to be computed before and after the move to take the difference of their norm, it is actually equally efficient to directly compute both values of  $E^{\text{reciprocal}}$  before and after the move, directly following [Equation \(2.20\)](#), and taking the difference, instead of the previous formulation.

In order to allow computing this efficiently, each term  $q_n e^{-i\mathbf{k} \cdot \mathbf{r}_n}$  is thus stored in memory (instead of recomputing it each time). The new values  $q_n e^{-i\mathbf{k} \cdot \mathbf{r}'_n}$  computed for the trial move are also temporarily kept in memory, so they can be used to replace the previous ones if the trial move is accepted. Finally, the value of each  $S_{\mathbf{k}}^{\text{guest}}$  is also kept in memory, so that it can be updated by reusing the previous computation.

RASPA2 does not implement this optimization, and simply recomputes the  $e^{-i\mathbf{k} \cdot \mathbf{r}_n}$  terms each time, which is slower but requires less memory.

### BLOCKING POCKETS

Some MC trial moves attempt to displace an atom to a location that would lead to unphysically high energies – typically, too close to a framework atom. Such positions can be determined once and for all, and the relevant MC moves automatically rejected without the need for any energy computation.

The simplest strategy to do so consists in making a boolean grid, aligned with the energy grids used for short-term interactions, which stores a 1 when the voxel is blocked or 0 if it is allowed. The first step of any MC trial move then consists in checking whether each atom is in an allowed voxel, or rejecting the move otherwise. In practice, the simplest implementation consists in making one such boolean grid per atom kind (since the value of the framework-atom

interaction energy depends on the atom), and for each actual atom position, checking the closest grid point of its kind.

In addition to its use as computational optimization, such boolean grids can also be used to mark some parts of the framework as inaccessible, irrespective of the corresponding energy. This is useful when small window size prevents a species – for instance a gas molecule – from entering a pore – for instance the sodalite cages in LTA zeolites.<sup>116</sup> Indeed, without explicitly blocking the pocket, an MC move could make a species appear in the pore, whereas it should be kinetically impossible to enter. This strategy will thus be used when studying the adsorption of gases in zeolites (see [chapter 3](#)), but for the small cations under study here, there is no need to additionally block any part of the frameworks.

RASPA2 only implements blocking for the latter case – *i.e.* explicit pocket removal. It does not use a boolean grid: instead, the blocked space is described as a combination of blocking spheres. For each trial move, the distance between the atoms of the moved guest and the centre of each sphere is computed: if one is below its radius, the move is rejected. This approach requires less precomputation and thus less memory than storing the boolean grids, but its runtime cost is much greater, and increases with the number of blocking spheres, preventing it from being used as an optimization like before. It is thus less efficient than the approach I implemented.

These boolean grids are also useful to improve the acceptance rate of reinsertions and unbounded translations. When a reinsertion move is attempted, a new position for the species is chosen at random in the unit cell, but it is then immediately checked against the blocking pocket grids. If the attempted position is forbidden, a new random position is chosen, and so iteratively until finding a position compatible with the boolean grid constraints. This trial position is then used as any other trial moves, and can be accepted or rejected based on the energy criterion. Crucially, biasing the choice of the reinsertion trial move in this fashion improves its acceptance rate while still maintaining the detailed balance of the simulation, because a reinserted species was necessarily located in a position that was not blocked by the boolean grids either. Note that this bias cannot be used for local translations or rotation however: if a trial local translation moves a species in a blocked pocket, the move must be rejected.

### SITE HOPPING PRECOMPUTATIONS

The main computational advantage of site hopping simulations, defined in [section 2.2.1](#), is that the number of sites is fixed in advance, which allows precomputing all framework-site and site-site interactions.

To do so, the value of the framework-site interaction energy is computed and stored for each site by computing the energy associated with putting only one cation in the framework at the position of the site. However, this energy is actually ill-defined, since placing only one cation in the framework means that the unit cell has a net charge, and thus the (infinite periodic) material has an infinite charge. Moreover, even disregarding the physical absurdity of this scenario, a net charge would lead to a non-zero  $\sum_{n=1}^N 2\alpha q_n / \sqrt{\pi}$  term, even though it was removed in [Equation \(2.17\)](#). Still, the computations can be carried to yield a numerical value, which is thus stored in a list `framework[i]` where  $i$  designates the index of a particular site  $s_i$ . The reciprocal Ewald contribution of this energy is also temporarily stored in a separate list as  $r_i$ .

Likewise, for each pair  $(s_i, s_j)$  of sites, the energy of the framework containing only two cations, one in  $s_i$  and one in  $s_j$ , is computed as  $e_{i,j}$ , although it also does not carry physical sense either. What is stored in a matrix is  $\text{interaction}[i, j] = e_{i,j} - r_i - r_j$ . This is only possible if the number of sites is not too high, since the number of interactions to store grows quadratically with the number of sites and would become prohibitively high otherwise.

Finally, the tail correction  $\text{tc}_n$  associated with the framework filled with  $n$  cations is computed once, where  $n$  is constrained by the number of aluminium atoms in the structure.

Using these unphysical values, the actual physical energy of a real configuration with  $n$  cations on sites  $s_{k_1}, s_{k_2}, \dots, s_{k_n}$  can then be computed as

$$E(s_{k_1}, s_{k_2}, \dots, s_{k_n}) = \text{tc}_n + \sum_{i=1}^n \text{framework}[k_i] + \sum_{1 \leq i < j \leq n} \text{interaction}[k_i, k_j] \quad (2.22)$$

and the energy associated with a trial move of one cation can thus be computed with only  $n$  array reads, which is optimally efficient.

As previously emphasized, the components  $\text{framework}[i]$  and  $\text{interaction}[i, j]$  should not be considered individually to assess the stability of a particular site. Indeed,  $\text{framework}[i] < \text{framework}[j]$  does not necessarily mean that site  $s_i$  is more populated than  $s_j$ , because the site-site interaction energies could make the total energy  $E$  systematically higher when  $s_i$  is populated rather than  $s_j$ , which is the true measure of a site stability.

## 2.5 POSSIBLE ALTERNATIVES

Although I only used Monte Carlo schemes during this study, it is worth explaining why molecular dynamics (MD) schemes, which could also in principle be used, seem less relevant for the purpose of placing cations in zeolites.

Generally speaking, the principle of MD consists in running a simulation where the particles follow Newton's laws of motion, with forces based on force fields like for MC schemes. The simulation is divided in time steps, between which the forces are computed on each particle to derive their position at the next time step. Hence, the trajectories of the particles in MD follow a physical path.

Temperature can be included in different ways in MD, all of which use an element of randomness that eventually impacts the velocities of particles, in order to ensure that the average values extracted from the simulation correspond to those which would be obtained at that temperature. This means that the precedent discussion on the inaccessibility of high-energy regions to the system at room temperature still applies in MD. A simple MD simulation is thus doomed to only explore local energy minima, failing to reach ergodicity like with the simple canonical MC scheme.

To circumvent this issue, it is necessary to bias the simulation in order to force the system to explore regions of high energy. One such strategy consists in doing metadynamics,<sup>117</sup> which is a variation of MD in which the potential energy landscapes is modified during the simulation. The effective free energy of a point in configuration space is computed as the sum of the real free energy of that point without bias, added to the sum of some Gaussian functions centred on

previously explored points. Every few steps, another Gaussian function centred on the current configuration point is added to the bias, so that the effective free energy of explored regions increases through the simulation, which allows the system to eventually escape local minima and explore other regions.

A Gaussian is a function of the form  $f : \mathbf{x} \mapsto Ae^{-(\mathbf{x}-\boldsymbol{\mu})^\top \Sigma(\mathbf{x}-\boldsymbol{\mu})}$ . In practice, the variable  $\mathbf{x}$  of the Gaussians used in metadynamics are not directly the  $3N$  coordinates of the  $N$  particles, but a small-dimensional vector whose coordinates are called “collective variables”. These collective variables are themselves function of the  $3N$  initial coordinates. The parameter  $A$  and  $\Sigma$  of the Gaussians being usually fixed, each Gaussian is stored by its centre  $\boldsymbol{\mu}$ , whose coordinates are thus the collective variables of the current configuration point. Therefore, compared to regular MD, running a metadynamics simulation incurs the additional cost of computing the collective variables  $\mathbf{x}$  of each visited configuration point, storing the Gaussians’ centres, and computing their value at each step.

For cation placement the main issue is to find a small set of relevant collective variables, since the cost of metadynamics grows with their number. I did not explore this venue because I expected it to be similar in difficulty to the MC alternatives, with no clear reason why it should be more efficient. MD in general is also known to converge more slowly than MC, because large configuration change made possible by MC steps are prohibited by the physics-driven approach of MD, and the same argument could be made of metadynamics compared to other accelerated MC schemes. Exploring metadynamics or its variants could nonetheless be of interest in the search for more alternative, and potentially more efficient, algorithms.





# 3

---

## MOLECULAR SIMULATION OF ADSORPTION

---

3.1	Molecular description . . . . .	92
3.1.1	Physisorption and chemisorption . . . . .	92
3.1.2	Adsorption sites in crystalline materials . . . . .	92
3.1.3	Small gases in zeolites . . . . .	93
3.2	Grand Canonical Monte Carlo . . . . .	94
3.2.1	Principle . . . . .	94
3.2.2	Implementation . . . . .	95
3.2.3	Computational aspects . . . . .	97
3.3	GCMC on a grid . . . . .	99
3.3.1	Principle . . . . .	99
3.3.2	Validation . . . . .	102
3.3.3	Computational aspects . . . . .	103

---

Adsorption is the physical phenomenon by which a molecule, the adsorbate, attaches to a surface, the adsorbent. One particular application of adsorption in the industry is for gas separation, by using an adsorbent that specifically binds one constituent of the target gas mixture more than the other.

In this chapter, I will detail the nature of this phenomenon in the case of small gases in zeolites. I will then explain the usual techniques which are used for its numerical simulation, as well as a possible alternative.

## 3.1 MOLECULAR DESCRIPTION

### 3.1.1 Physisorption and chemisorption

The atomic nature of adsorption depends on the kind of chemical interaction that supports it. On the one hand, if the adsorbate forms a strong (*i.e.* covalent, sometimes ionic) bond with the adsorbent, then the adsorption is called a chemisorption, because it involves a chemical reaction. In that case, the surface is modified. On the other hand, if the adsorbate and adsorbent are only bonded by a weak interaction, the adsorption is called a physisorption and the surface is left intact.

Chemisorption involves a stronger bond than physisorption, and is thus less reversible. Since it changes the surface of the adsorbent, it cannot be used industrially to separate large amounts of gas, as the adsorbent would need to be provided in equivalently large amount. It can still be used as an intermediate step of a catalytic cycle that ends up regenerating the surface. In this thesis however, adsorption will implicitly refer to physisorption.

### 3.1.2 Adsorption sites in crystalline materials

An adsorption site designates a particular space where the adsorbate is likely to remain trapped on the surface of the adsorbent. In other words, the interaction between the adsorbate and the adsorbent is maximally attractive when the adsorbate is located in one of the adsorption sites.

The position of the adsorption site depends on the adsorbent, but also the adsorbate. At very low density for example, a small polar molecule like H<sub>2</sub>O will preferentially adsorb in locations where it can orient itself to maximize the stabilizing Coulomb interaction of the framework. A large apolar molecule like a xylene on the other hand, will adsorb in locations that maximize its Van der Waals interactions with the adsorbent. Such sites are not necessarily related.

Moreover, the location of the adsorption sites becomes less relevant when the density of the adsorbate becomes high. Indeed, the adsorbate-adsorbate interactions can play a key role in the global adsorption capacity of a material, and the stronger these interactions, the more the internal structure of the adsorbate will reorganize to accommodate these interactions, which may displace some molecules from the ideal adsorption site.

In the case of crystalline materials, adsorption sites can be identified through XRD spectroscopy. For example, Marqueño et al. [118] identify the preferred adsorption sites for CO<sub>2</sub> in silica MFI zeolite (silicalite) in a context of very high mechanical pressure, compatible with DFT

computations. Yet, the obtained positions for CO<sub>2</sub> molecules is not guaranteed to carry to another gas pressure than the one used in the study.

Overall, the situation is quite different from the cationic sites, discussed in section 2.2.1, mostly because the cations cannot reach a “high-density” regime, given that their number is constrained by the number of aluminium atoms. In turn, this makes the use of site hopping or other site-derived algorithms less relevant in the context of adsorption simulation, except in the low-pressure regime.

### 3.1.3 Small gases in zeolites

Small gases such as CO<sub>2</sub>, N<sub>2</sub>, O<sub>2</sub>, CH<sub>4</sub> or Ar, among others, are typical adsorbates that need to be separated for industrial purposes, be it for carbon capture, medical O<sub>2</sub> packaging, cold generation with N<sub>2</sub> or He, and many other applications. In general, molecular sieves like zeolites can be used for this purpose

To separate molecules with significant size disparities, a simple approach consists in using a framework whose pore size allows one of the molecule to enter and adsorb, but not the other. Given the proximate sizes of the previous species however, this method cannot be used to separate these gases. Instead, what plays a key role is the adsorption capacity of the material with respect to each of these gases: if there is a material that adsorbs CO<sub>2</sub> easily but not N<sub>2</sub> for instance, then it can be used to separate the two.

In that regard, both van der Waals and Coulomb components of the framework-guest interaction energy need to be taken into account, as Figure 3.1 illustrates in the case of CO<sub>2</sub> adsorption in zeolite CHA. The adsorption isotherms (see section 4.2.1 for the definition) were computed for CO<sub>2</sub> in CHA with two Si/Al ratios:  $\infty$  (*i.e.* fully silicic) and 1.4, using a fixed placement of both aluminiums and cations. In both cases, one isotherm was computed using the full force field from Boulfelfel et al. [105], while on the other, all the atoms of the framework (and the cations) were set to be neutral.

In the silicic case, the loading is  $2.8 \pm 0.2$  times higher with than without charges for the low/medium pressures (lower than 0.5 MPa), then the difference starts to decrease. Therefore, while the porous volume, which roughly defines the van der Waals interaction, is the most important parameter for the global adsorption capacity in that case, the electrostatic interactions also plays a critical role.

That role becomes considerably more important for the cationic zeolite however, where the difference of loading with and without charges is of multiple orders of magnitude, and the absolute loading is much higher than in the silicic case for the low/medium pressures. At high pressure, the pores are already filled with gas so the trend becomes different: since the cation occupy some space, they leave less room for CO<sub>2</sub>, which explains why the loading becomes higher in the silicic zeolite.

Hence, the electrostatic interactions are the main adsorption drive in cationic zeolites at low/medium pressures. Otherwise, *i.e.* for silicic zeolites or at high pressure, the van der Waals interactions are the most important parameter, although the coulombic interactions continue to play a key role.

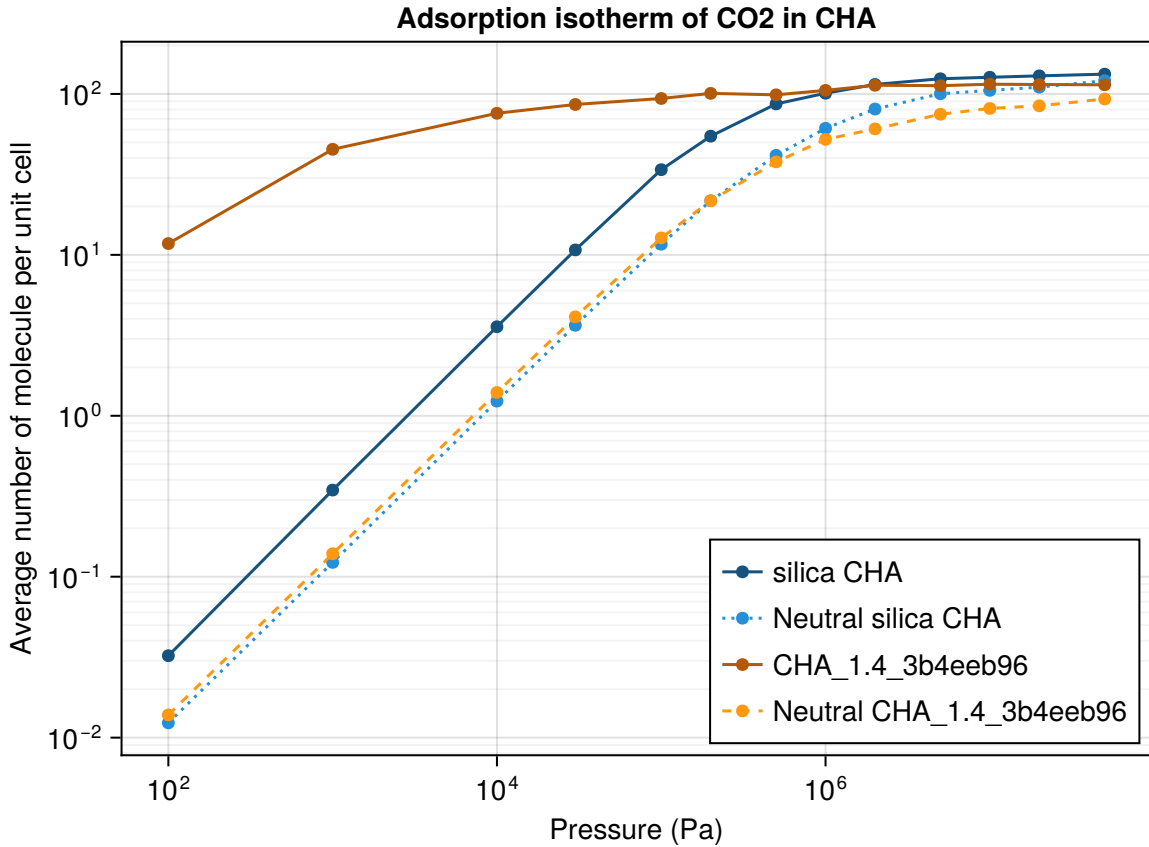


Figure 3.1: Adsorption isotherms of CO<sub>2</sub> on CHA at Si / Al =  $\infty$  or 1.4, with and without charges

## 3.2 GRAND CANONICAL MONTE CARLO

### 3.2.1 Principle

The adsorption capacity of a gas in a material at a fixed temperature and pressure is the number of molecules of gas that are retained by the material when in contact with a gas in these conditions, at equilibrium. Since it is a macroscopic observable  $\mathcal{O}$ , which can be experimentally measured, it can also be expressed as the statistical average of its microscopic counterpart  $o$  in a well-chosen statistical ensemble. For the current case, the adsorption capacity results from a chemical equilibrium between the gas out of the material, at its given temperature T and pressure P, and the gas in the pores of the material, at the same temperature T. The pressure of the gas in the material is an ill-defined concept, because it depends on the density of the gas, which itself is not uniform at any mesoscopic scale in a porous material. Instead, the chemical equilibrium translates to the equality of the chemical potentials  $\mu$  of the gas in both conditions, hence  $\mu$  is the relevant statistical variable to describe the system in the material, which accounts for the fixed gas pressure P out of the material. Finally, this study focuses on rigid crystalline materials, hence the volume V of a unit cell can be used as an extensive variable to limit the size of the system.

The statistical ensemble resulting from the constraints of fixing the chemical potential  $\mu$ , the temperature T, and the volume V is called the grand canonical ensemble. Similar to

Equation (2.1) used for the canonical ensemble (where the number of particles  $N$  is fixed instead of their chemical potential  $\mu$ ),  $\mathcal{O}$  can be expressed using an integral over the microstates  $(N, \mathbf{p}_N)$ :

$$\mathcal{O} = \langle o \rangle = \frac{1}{\Xi} \sum_N \int d\mathbf{p}_N o(\mathbf{p}_N) \exp(-\beta U(\mathbf{p}) + \mu N) \quad (3.1)$$

where  $\beta = 1/k_B T$ ,  $N$  is the number of gas particles,  $\mathbf{p}_N$  is their configuration, and  $\Xi$  is the grand canonical partition function.

Likewise, this integral can be numerically evaluated by relying on a Monte Carlo Markov Chain to provide a sequence of configurations  $(N, \mathbf{p}_N)$  such that the statistical average  $\langle o \rangle$  can be retrieved by computing the arithmetic average of  $o(\mathbf{p}_N)$  over these configurations: this particular kind of simulation is naturally called a grand canonical Monte Carlo (GCMC) simulation. In the specific case of the adsorption capacity, the microscopic function is simply  $o(\mathbf{p}_N) = N$ , thus it is computed by running a GCMC simulation and simply averaging the number of particles in the system across the simulation.

### 3.2.2 Implementation

In practice, GCMC is implemented like a canonical MC simulation with one additional element: a swap MC move that can either insert or delete a particle. The insertion move simply consists in adding one additional gas particle to the system, while the deletion move removes one. If there are no particle in the systems anymore, the deletion move systematically fails; yet, it is crucial that the probability of trying an insertion or a deletion remains equal independently of the number of particles in the system, to ensure micro-reversibility. For this reason, only the probability of trying a swap move is specified as a simulation parameter, while the probabilities of trying either an insertion or a deletion cannot be individually chosen and are necessarily equal to half the probability of a swap move.

The acceptance probability of a swap move is not decided purely on the basis of the difference of energy in the system, as is the case in Equation (2.2) for the canonical ensemble, because it also depends on the chemical potential  $\mu$  of the system. With  $N$ , the number of particles in the system before the trial swap move, and  $\Delta E$  the energy difference between before and after the move, the acceptance probabilities for insertion and deletion are:

$$\begin{aligned} P_{\text{accept}}(\Delta E, N \rightarrow N + 1) &= \min \left( 1, \frac{\beta \varphi P V}{N + 1} \exp(-\beta \Delta E) \right) \\ P_{\text{accept}}(\Delta E, N \rightarrow N - 1) &= \min \left( 1, \frac{N}{\beta \varphi P V} \exp(-\beta \Delta E) \right) \end{aligned} \quad (3.2)$$

The dependency to the chemical potential  $\mu$  is conveyed by the pressure  $P$  of the gas exterior to the zeolite. This value is corrected by the fugacity coefficient  $\varphi$ , which accounts for the difference between the real gas and the ideal gas model.

While the pressure  $P$  and volume  $V$  of the systems are simulation inputs, the fugacity coefficient  $\varphi$  of the gas needs to be computed prior to the simulation. To do so, RASPA uses the Peng-Robinson equation of state,<sup>119</sup> which is adequate for many common fluids. Since the range of gas applications I study is more restricted than the general-purpose RASPA software, I decided to use the GERG-2008<sup>120</sup> equation of state, which is the ISO standard for natural gases due to

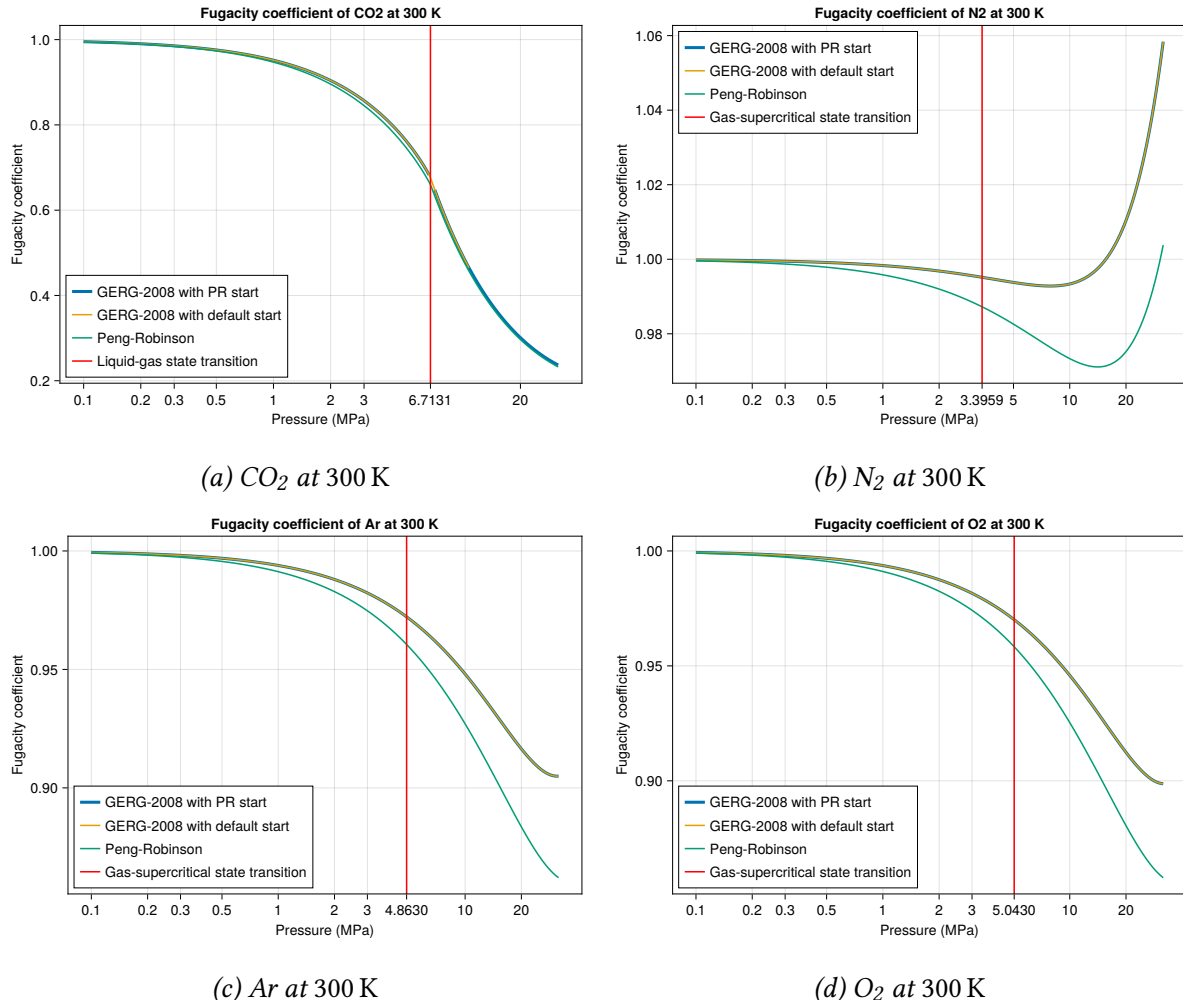


*Figure 3.2: Fugacity coefficients of small gases computed with different Clapeyron.jl models*

its accuracy compared to experimental measurements, with an extended validity range up to 700 K and 70 MPa, in the scope of this study.

In terms of programming, the fugacity coefficient can directly be obtained from the Julia package `Clapeyron.jl`,<sup>121</sup> which provides a convenient unified access to many useful thermodynamic tools. Due to the way it is implemented, `Clapeyron.jl` fails at finding the fugacity coefficient for  $\text{CO}_2$  at high pressures with the GERG-2008 model: this issue can be solved by computing an initial volume for the gas in the target conditions using the Peng-Robinson model, and using the result as the starting point to compute the coefficient with the GERG-2008 model in `Clapeyron.jl`. Figure 3.2a illustrates the differences between these approaches: the latter allows to compute fugacities at any pressure except those very close to the critical point (304.13 K and 7.3773 MPa for  $\text{CO}_2$ ), while the former simply fails at high pressures (above 1 MPa). The other gases illustrated on Figure 3.2 show that the Peng-Robinson fugacity is usually very close (less than 5 % difference) but systematically slightly lower than that obtained with GERG-2008, which would result in an equally slight shift of the isotherm. The difference between the two equations of state remains in the uncertainty margin of the GCMC simulation however, so it should not lead to a visible difference in the measured adsorption capacity.

Finally, the number of MC steps per simulation cycle can no longer be taken as the number of mobile species in the system, as was the case for canonical simulations. Indeed, that would bias the sampling of the microscopic function  $\phi$  towards the low numbers of molecules. Instead, I arbitrarily fix it to 50 steps per cycle, plus the number of particles not subject to grand canonical constraints, for instance cations in the case of a mixed cation/gas simulation.

### 3.2.3 Computational aspects

Compared to canonical MC, the efficient implementation of GCMC poses the additional challenge of changing the number of particles across the simulation. This requires almost no accommodation for the computations that operate in the real space, *i.e.* framework pre-computed grids, and pairwise interactions (including the direct part of Ewald summation). For these, the only adaptation consists in making the neighbour lists resizable, which is already implemented in `CellListMap.jl`, and otherwise keeping the list of atoms in the system up to date, to correctly check each pair of atoms.

#### Ewald summation

Although the direct part of Ewald summation can be treated like the other short-range pair interactions, the reciprocal-space part of Ewald summation requires adapting the optimization described in [section 2.4.4](#) to account for the possible introduction or removal of a species. For such a move, both values of  $S_{\mathbf{k}} = \sum_n q_n e^{-i\mathbf{k} \cdot \mathbf{r}_n}$  before and after the swap need to be computed, exactly like in [Equation \(2.21\)](#). Similar to that case, the value before the swap is already stored in memory, but the computation of the new value is slightly different: instead of computing the difference as  $\sum_n q_n (e^{-i\mathbf{k} \cdot \mathbf{r}'_n} - e^{-i\mathbf{k} \cdot \mathbf{r}_n})$ , the difference is now  $\pm \sum_n \text{swapped } q_n e^{-i\mathbf{k} \cdot \mathbf{r}_n}$ . In the case of a deletion, each element of the latter is already stored in memory, whereas in the case of an insertion, this new computation is stored in a temporary place, like for any other trial move, ready to be stored permanently if the move is accepted.

The self-interaction term is no longer constant: each new molecule contributes a term equal to  $-\sum_{m,n} \frac{q_n q_m}{8\pi\varepsilon_0} \text{erf}(\|\mathbf{r}_n - \mathbf{r}_m\|_p) / \|\mathbf{r}_n - \mathbf{r}_m\|_p$  where  $m$  and  $n$  iterate over the atoms of the molecule with  $m \neq n$ . This term is computed once for each kind of molecules and stored, so that the contribution of the self-interaction term can be updated with a single addition or subtraction when a swap move occurs. Of course, any molecule whose number can vary in the system must be electrically neutral to ensure the total system remains electrically neutral; this is also enforced in the code.

#### Tail correction

Another difference is the tail correction, which is not constant anymore either. The tail correction, whose particular relevance for the particular context of porous materials modeling was exhibited by Jablonka et al. [[122](#)], is an approximation of the energy resulting from the pair interactions further than the cutoff: if the pair interaction is shifted in the force field, then this energy is null, but otherwise it needs to be taken into account.

To do so, a useful ansatz consists in assuming that the radial distribution function  $g(r)$  is equal to 1 beyond the cutoff distance  $r_c$ , for all species. In turn, this allows analytically deriving the energy resulting from the average interaction of particles beyond the cutoff. For example, two

particles interacting with a Lennard-Jones potential (see [Equation \(2.4\)](#)) yield, for a unit cell volume  $V$  and cutoff distance  $r_c$ , a tail correction of:

$$tc^{LJ} = \frac{8\pi}{3V}\varepsilon\sigma^3 \times \left( \frac{1}{3} \left( \frac{\sigma}{r_c} \right)^9 - \left( \frac{\sigma}{r_c} \right)^3 \right) \quad (3.3)$$

Similarly, two particles interacting with a Buckingham potential (see [Equation \(2.5\)](#)) yield a tail correction of:

$$tc^{Buckingham} = \frac{2\pi}{V} \left( A \exp(-Br_c) \times \frac{2 + Br_c(2 + Br_c)}{B^3} - \frac{C}{3r_c^3} \right) \quad (3.4)$$

All tail corrections  $tc_{A,B}$  between one atom of kind A and one of kind B are precomputed for the given framework volume  $V$  and cutoff  $r_c$ , and the total tail correction is the sum

$$tc = \sum_A \sum_B N_A N_B tc_{A,B} \quad (3.5)$$

where  $N_A$  and  $N_B$  are the number of atoms of kind  $i$  and  $j$ . Knowing the number of each atom kind per molecule, it is thus possible to precompute the tail correction  $tc(i,j)$  associated with each pair of molecule kinds  $(i,j)$ , as well as the tail correction  $tc(i)$  due to the interaction of one molecule of kind  $i$  and the framework. Those terms being precomputed, the total tail correction can be expressed as

$$tc = tc_{framework} + \sum_i \left( n_i tc(i) + n_i^2 tc(i, i) \right) + \sum_i \sum_{j \neq i} n_i n_j tc(i, j) \quad (3.6)$$

where  $tc_{framework}$  is the constant tail correction due to the interaction of the framework atoms with each other, and  $n_i$ ,  $n_j$  are the number of molecules of kinds  $i$  and  $j$ .

Finally, the evolution of the tail correction when adding (+) or removing (-) one particle of kind  $i$  is thus

$$\Delta_{\pm}tc = \pm tc(i) \pm (2n_i \pm 1) tc(i, i) \pm 2 \sum_{j \neq i} n_j tc(i, j) \quad (3.7)$$

## RESIZABLE LISTS

Overall, having a variable number of species requires extra bookkeeping, to make sure that all atoms are accounted for. To maximize performance in current computers, the data structures must have good cache locality: this means that, when memory needs to be read, it should be done in contiguous accesses as much as possible. For this purpose, the positions of the atoms, the  $\kappa_k$  factors, the precomputed  $q_n e^{ik \cdot r_n}$  and  $S_k$  values, the self-interaction terms, etc., are all stored in tight arrays, with the appropriate indexing for each. When an atom or a molecule is removed, there are two choices, illustrated on [Figure 3.3](#): either leave a gap in the array, and keep track separately of which parts of the array actually refer to a valid data if need be, or move the contents of the array to fill the gap.

Both algorithmic strategies have their merit, and warrant a trial to check which performs best. I did not take the time to implement both however, and instead chose the latter systematically, because it is slightly simpler to reason about. In practice, such an approach consists in replacing

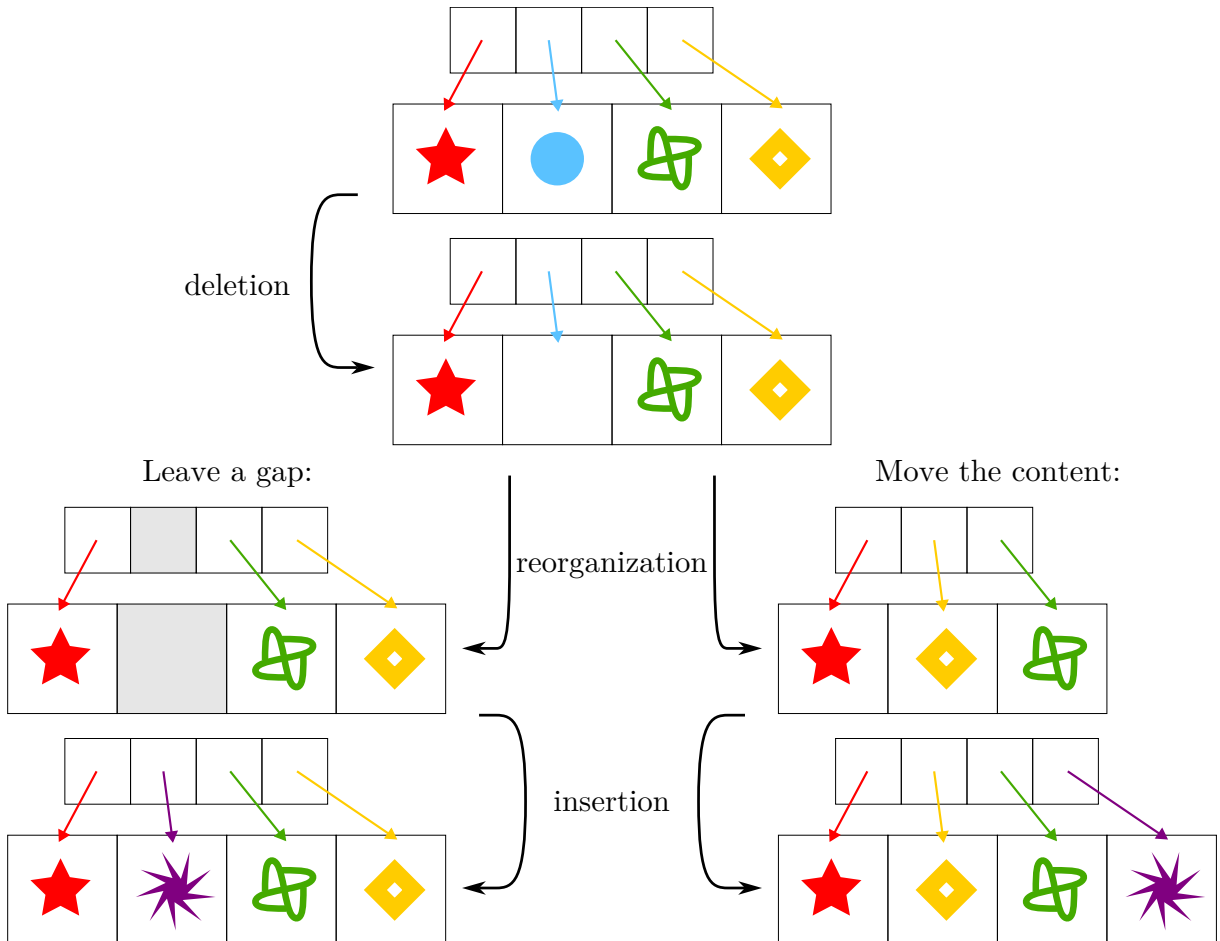


Figure 3.3: Schematic representations of the list resizing algorithmic options

the content of the gap in the array by the data at the end of the array, before reducing the size of the array, and thus removing the temporarily duplicated data at the end. The indices relative to the content of the array also need to be updated. The complexity of each array update is thus proportional to the number of elements to remove, which is generally optimal. Insertions are operated at the end of the arrays, with a likewise optimal complexity.

### 3.3 GCMC ON A GRID

Even with an efficient implementation, regular GCMC simulation remain resource-consuming, especially in the context of a large scale material screening. Improving this performance is thus valuable, especially if the precision cost can be controlled.

#### 3.3.1 Principle

Similar to the methods exposed in section 2.4.4, a typical strategy for reducing the computational cost consists in precomputing as much as possible, to decrease the workload of the main loop of the algorithm. In the case of GCMC, the main computation occurring at each trial move is that of the interactions between species, both in direct and reciprocal spaces. Since the configuration space for the molecules in the unit cell of the framework is continuous, and thus infinite, it is impossible to precompute all the possible pair interactions.

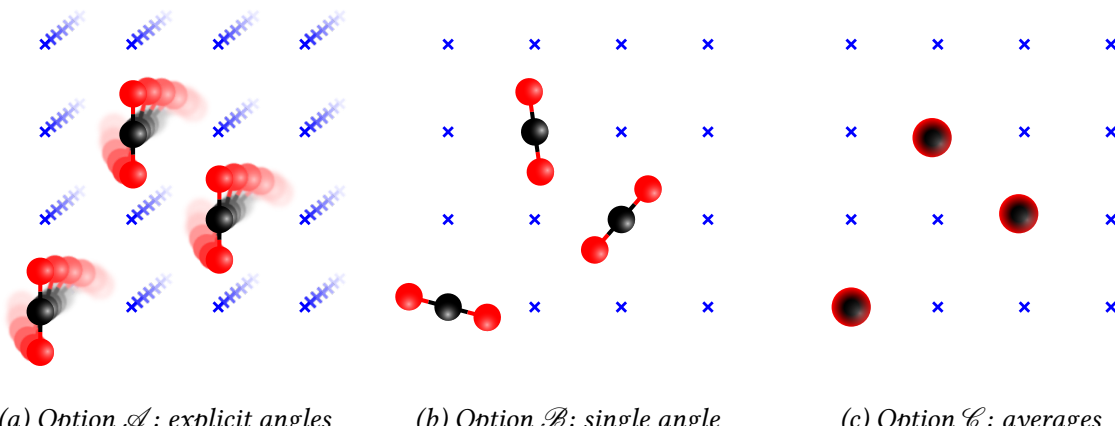


*Figure 3.4: The three considered options to account for angles on a grid*

However, that space can be discretized: to do so, the mobile species are forced to occupy one position each among a fixed set of possibilities. This principle is identical to the site hopping used in the case of cations (see [section 2.2.1](#)) except that, as explained in [section 3.1.2](#), gas species are likely to occupy many more sites than cations. Thus, the conceptually simplest set of possible positions is a regular grid: each molecule must reside atop one grid point. For polyatomic species, like all gases of interest with the exception of rare gases, this definition is incomplete however, so there are three options, also illustrated on [Figure 3.4](#):

- $\mathcal{A}$ ) the grid can include additional dimensions to account for the orientation of the molecule. In that case there must be a fixed convention dictating which atom of the molecule is placed on the grid point. That atom, called the “bead”, is typically that around which the rotation MC move operates.
- $\mathcal{B}$ ) each grid point can come with an associated fixed orientation of the molecule sitting on it. In that case, the lowest energy orientation with respect to the framework is probably the most reasonable choice, but it may grossly misrepresent the actual orientation of the molecules if those are mostly driven by the interaction with other molecules.
- $\mathcal{C}$ ) the molecule can be represented as a single point sitting on the grid, with no orientation. In that case, the interaction energy of the molecule with the framework can be taken as the average of the energies corresponding to the different orientations and, likewise, the molecule-molecule interactions can be computed by taking averages over the orientation of both molecules. These averages could be either arithmetic or Boltzmann averages, depending on the interpretation: a Boltzmann average implicitly assumes that the molecules are at equilibrium, which is not very well defined for a single molecule sitting on a grid point, while an arithmetic average implies has an orientation independent of the corresponding energy, which is not exact either.

The current study is restricted to small gases of the air which are all linear and centrosymmetric: CO<sub>2</sub>, N<sub>2</sub>, O<sub>2</sub>, etc., so the bead is conventionally chosen as the centre of the molecule. Choosing an orientation thus amounts to choosing a direction for a rod (the molecule) across all possible angles. To accurately cover this configuration space while limiting the number of studied

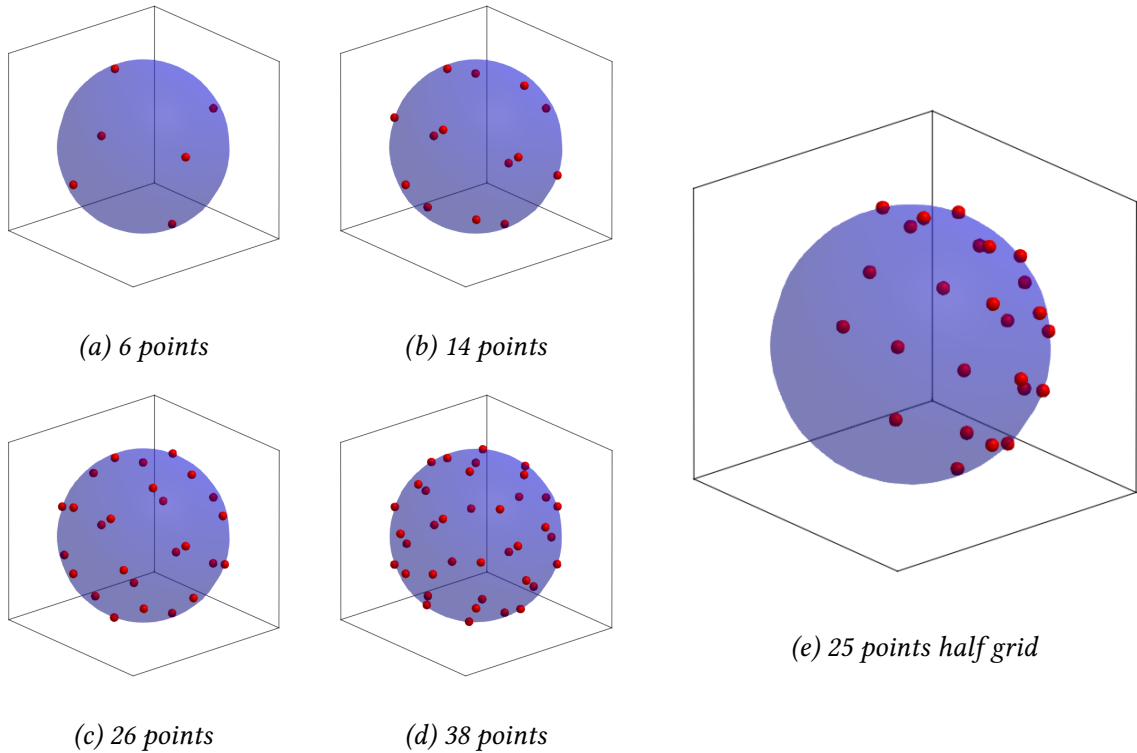


Figure 3.5: Lebedev grid points. Figure 3.5e is a half grid, used for centrosymmetric species.

angles, we use a Lebedev grid, which is a set of  $N_{\mathcal{L}}$  points  $(\theta_i, \varphi_i)$  on the surface of the sphere such that the integral of a function  $f$  can be well approximated by the sum

$$I[f] = \int_0^\pi \sin(\theta) d\theta \int_0^{2\pi} d\varphi f(\theta, \varphi) \approx 4\pi \sum_{i=1}^{N_{\mathcal{L}}} w_i f(\theta_i, \varphi_i) \quad (3.8)$$

with the appropriate weights  $w_i$ . The values of  $w_i$ ,  $\theta_i$  and  $\varphi_i$  have been precomputed once and for all for different values of  $N_{\mathcal{L}}$ . Because of orthogonality constraints on the Lebedev points, not all values of  $N_{\mathcal{L}}$  are possible: the ones which are usable in my code are  $N_{\mathcal{L}} = 6, 14, 26, 38, 50, 74, 86, 110, 146, 170, 194, 230, 266, 302, 350, 434, 590, 770, 974, 1202, 1454, 1730, 2030, 2354, 2702, 3074, 3470, 3890, 4334, 4802, 5294$  and  $5810$ , allowing for any fine-tuning of the precision level. Only half of these points are actually used since both the target gases and the Lebedev grids are centrosymmetric. A few representations of the Lebedev grid are given on Figure 3.5

The number of possible configurations of a molecule is  $\alpha \times a \times b \times c$  where  $(a, b, c)$  is the size of the spatial grid and  $\alpha$  is either  $N_{\mathcal{L}}$  in option  $\mathcal{A}$ , or 1 for options  $\mathcal{B}$  and  $\mathcal{C}$ . Since I use a Van der Waals cutoff of  $12 \text{ \AA}$ , the framework with the smallest grid will necessarily have its perpendicular lengths greater or equal to  $2 \times 12 \text{ \AA} = 24 \text{ \AA}$ . Thus, with a distance of  $0.2 \text{ \AA}$  between two grid points,  $a$ ,  $b$  and  $c$  are greater or equal to 120 so the size of the configuration space is at least  $\alpha \times 120^3$ .

The goal of the grid MC approach is to reduce the amount of computations done at each step to accelerate the GCMC simulations, by precomputing the pair interactions between grid points. The number of pair interactions to precompute is thus, in theory, at least  $(\alpha \times 120^3)^2 / 2 =$

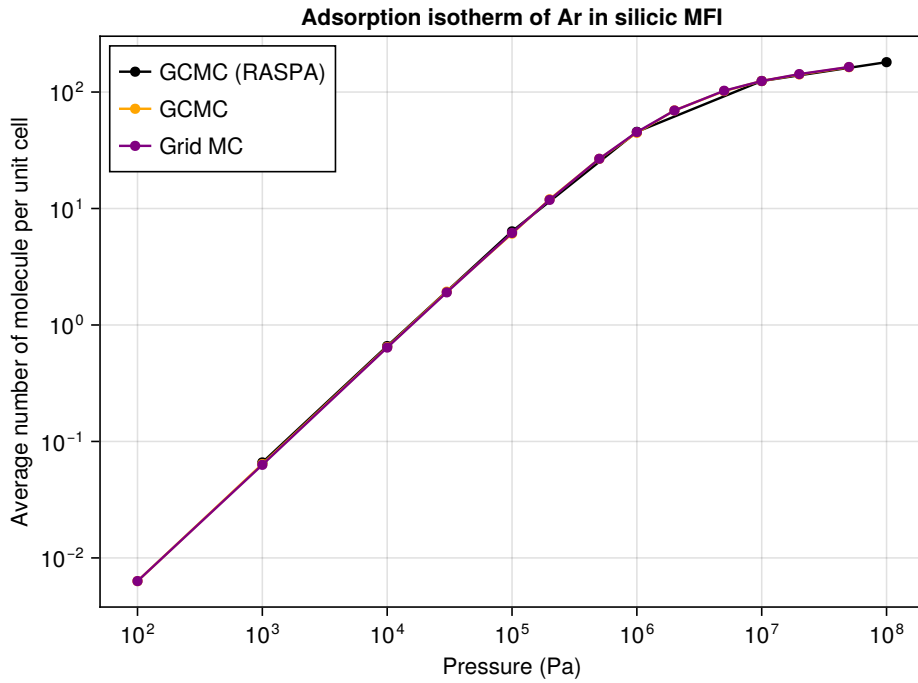


Figure 3.6: Adsorption isotherm of Ar on silicic MFI obtained with different simulation strategies. The black line is the RASPA implementation of GCMC while the orange line is my implementation.

$\alpha^2 \times 120^6/2$ . It can actually be reduced further with translation symmetry considerations: the interaction between grid points  $(x_1, y_1, z_1, \theta_1)$  and  $(x_2, y_2, z_2, \theta_2)$  is identical to that between grid points  $(x_1 + \Delta, y_1 + \Delta, z_1 + \Delta, \theta_1)$  and  $(x_2 + \Delta, y_2 + \Delta, z_2 + \Delta, \theta_2)$  for any  $\Delta$ . It is thus sufficient to precompute the interaction between  $(0, 0, 0, \theta)$  and all other grid points, so the minimum number of precomputations is actually  $\alpha^2 \times 120^3 \approx \alpha^2 \times 2 \cdot 10^6$ . Each precomputation yields an energy, represented by a floating-point number, which takes 8 B of space, and the typical RAM of a computer is on the order of 10 GB, so the maximum value of  $\alpha$  is approximately  $\sqrt{10^{10}/(8 \times 2 \cdot 10^6)} = 25$  for the smallest possible spatial grid.

In conclusion, using explicit angles (option  $\mathcal{A}$ ) is theoretically doable only for small enough unit cells and by using the smallest numbers of angles, otherwise the precomputation results cannot be stored in memory. Moreover, the numerical cost of the precomputation itself can be expected to be considerable, since it requires  $\alpha^2 \times 2 \cdot 10^6$  pair interaction computations. This is similar to the cost of simulating a system of  $N = \alpha^2$  particles in interaction across one million MC steps (which is close to a typical GCMC simulation length), since each MC trial move requires computing  $2N$  pair interactions ( $N$  for the particle before the move,  $N$  for the particle after). Therefore, option  $\mathcal{A}$  is unlikely to be applicable in most cases.

### 3.3.2 Validation

To check the validity of this simulation strategy, let's start by comparing the loading of Ar in a zeolite obtained by regular GCMC and through this grid MC approach. The result for zeolite MFI is presented on Figure 3.6, using a grid step size of 0.2 Å. The perfect superposition of the three isotherms indicate that the grid MC simulation method is apt to reproduce the adsorption property of noble gas in zeolites with great accuracy, even at high pressure.

With more complex molecules, angles have to be taken into account, using either option  $\mathcal{B}$  or  $\mathcal{C}$ . Their comparison is illustrated with the adsorption of CO<sub>2</sub> in FAU in Figure 3.7a, which shows that averaging orientations ( $\mathcal{C}$ ) provide more qualitative results compared to selecting one single orientation per grid point ( $\mathcal{B}$ ). Yet, none manage to correctly reproduce the adsorption behavior at medium/high pressures.

As evoked previously, the nature of the angular averaging of energies, either arithmetic or Boltzmannian, stems from a hypothesis on the distribution of microstates, neither of which is actually valid. The influence of this choice on the simulated loading of CO<sub>2</sub> in FAU is presented in Figure 3.7.

In Figure 3.7a, it appears that the choice of averaging for the molecule-molecule interaction has little influence on the result until the high pressures. Unsurprisingly, the Boltzmann average, which favors attractive interaction, increases the loading compared the arithmetic average, but the general trend is very similar and neither appear to be particularly more right than the other.

On the other hand, Figure 3.7b illustrates the drastic difference in the choice of averaging for the framework-molecule interaction. Only the Boltzmann average yields an isotherm closely following that of the reference GCMC simulation at low pressures: the arithmetic averaging of angles yields a large underestimation of the loading, while taking only the lowest energy across angles yields a large overestimation.

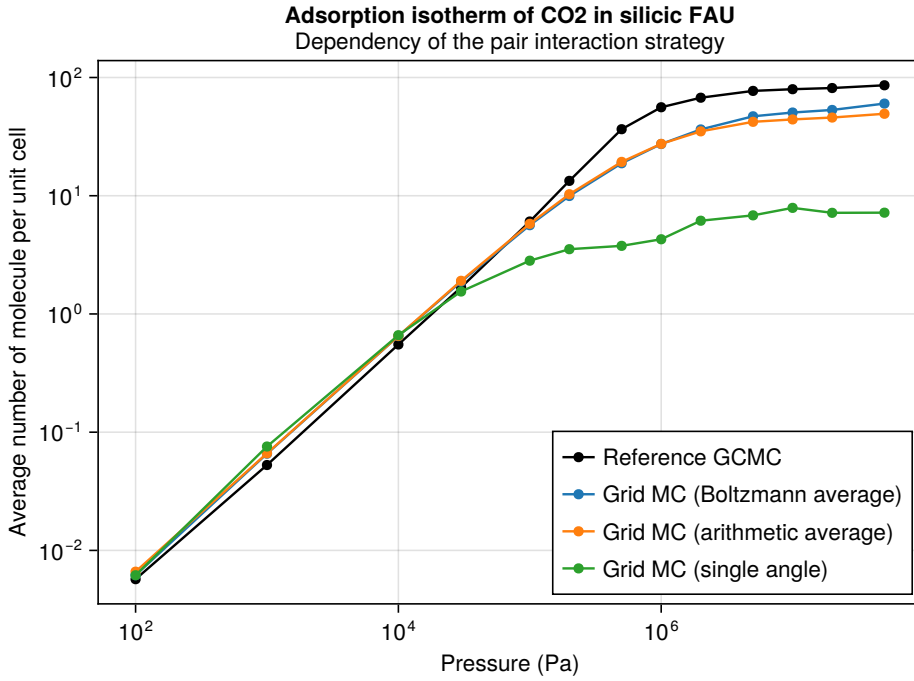
From these observations, it appears that the molecules of CO<sub>2</sub> preferentially orient themselves according to the interactions with the framework at low pressure, which should be obvious since low pressures correspond to a regime where molecule-molecule interactions are negligible. More importantly, irrespective of the pressure regime, the entropic contribution is paramount: the molecules do not simply orient themselves according to the lowest energy configuration, but freely rotate in accordance with Boltzmann distribution.

Regarding the numerical method itself, the main limit is the behaviour at intermediate and high pressure, which significantly parts from expectation. While this necessarily stems from the use of a grid, it does not depend on the grid step size: Figure 3.8 shows the evolution of the isotherm using option  $\mathcal{C}$  with Boltzmann averaging for framework-molecule interactions and arithmetic averaging for molecule-molecule interactions. The isotherm remains constant as long as the grid step size is small enough, which points to the fact the issue lies in the nature of the simulation method itself.

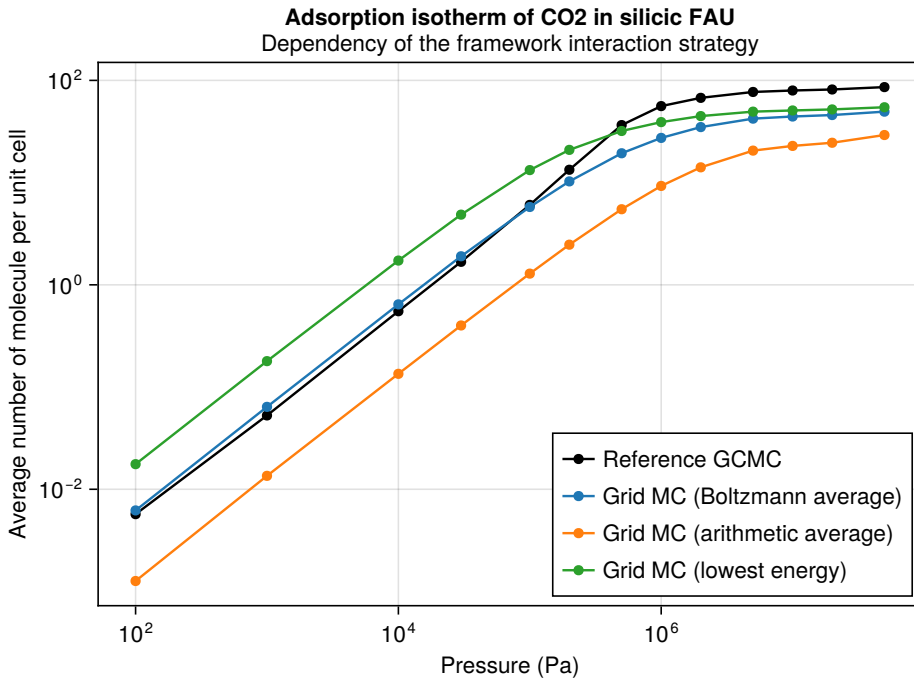
### 3.3.3 Computational aspects

The main interest of the grid MC approach is that all pair interaction energies can be precomputed, which makes each trial move much less computationally costly, and thus the overall simulation much faster. Indeed, the variation of energy due to a single MC trial move can be expressed as

$$\Delta E^{\text{grid MC}} = \begin{cases} \delta(N + 1, \mathbf{r}) & \text{if insertion of a new molecule at } \mathbf{r} \\ -\delta(i, \mathbf{r}) & \text{if deletion of the molecule } i \text{ at } \mathbf{r} \\ \delta(i, \mathbf{r}') - \delta(i, \mathbf{r}) & \text{if move of the molecule } i \text{ from } \mathbf{r} \text{ to } \mathbf{r}' \end{cases} \quad (3.9)$$



(a) Influence of the molecule-molecule interaction strategy. “single angle” refers to option  $\mathcal{B}$ , while for option  $\mathcal{C}$ , the fixed framework-molecule interaction strategy is the Boltzmann average.



(b) Influence of the framework-molecule interaction strategy with option  $\mathcal{C}$ . The fixed molecule-molecule interaction strategy is the arithmetic average. “lowest energy” refers to taking the minimum instead of taking an average.

Figure 3.7: Adsorption isotherm of CO<sub>2</sub> on silicic FAU obtained with different grid MC strategies.

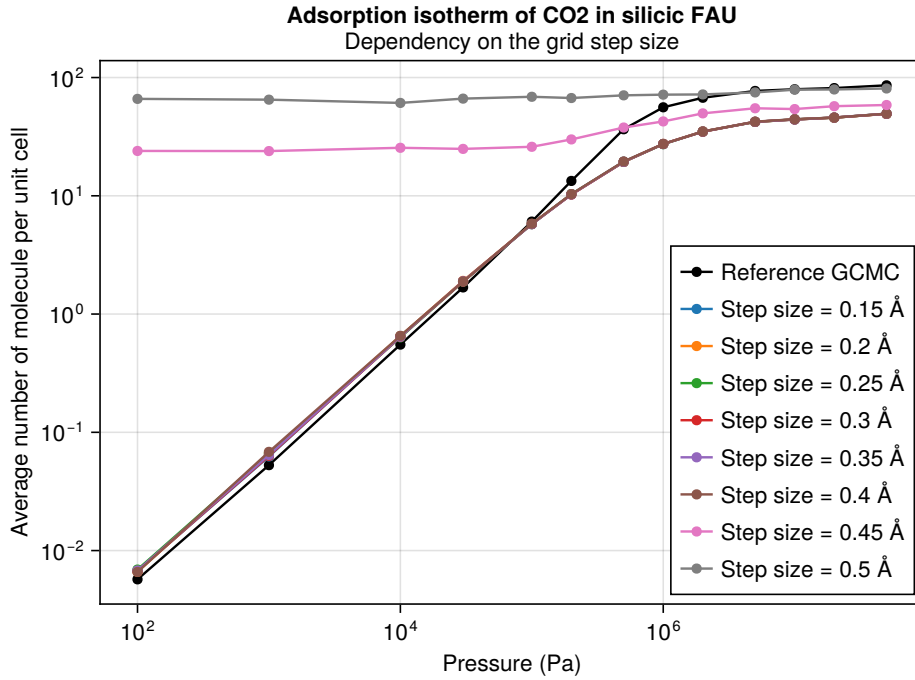


Figure 3.8: Adsorption isotherm of  $\text{CO}_2$  on silicic FAU obtained with different grid MC step sizes

where  $N$  is the number of molecules in the system and

$$\delta(i, \mathbf{r}) = \text{framework}(\mathbf{r}) + \sum_{j \neq i} \text{interaction}(\mathbf{r}, \mathbf{r}_j) + \text{tc}_{\text{framework}} + (2N + 1)\text{tc}_{\text{interaction}} \quad (3.10)$$

The different terms above are all precomputed for the different values of the grid point  $\mathbf{r}$ :

- $\text{framework}(\mathbf{r})$  refers to the framework-molecule interaction, which is computed once and for all according to either of the three options  $\mathcal{A}$ ,  $\mathcal{B}$  and  $\mathcal{C}$  discussed before.
- $\text{interaction}(\mathbf{r}, \mathbf{r}')$  is the interaction between two molecules, one at  $\mathbf{r}$  and the other at  $\mathbf{r}'$ .
- $\text{tc}_{\text{framework}}$  is the tail correction for the atoms of the framework and the atoms of the molecule, and  $\text{tc}_{\text{interaction}}$  is the tail correction for the atoms of two molecules interacting.

The tail correction terms are stored as simple numbers,  $\text{framework}(\mathbf{r})$  is stored as a tridimensional array of energies,  $\mathbf{r}$  being mapped to a triplet of integers indexing the grid points. The term that takes the most time to precompute,  $\text{interaction}(\mathbf{r}, \mathbf{r}')$ , is stored in a custom data structure made of a tridimensional index array, along the energy data, in a flat list. Due to translation symmetry, the query of the interaction between  $\mathbf{r}$  and  $\mathbf{r}'$  becomes that between the origin and  $\mathbf{r} - \mathbf{r}'$ . The corresponding triplet of integers maps to an index in the tridimensional array, and that index is the one used to retrieve the energy from the energy list. The index can also be 0, to indicate that the interaction energy is zero (i.e. beyond the cutoff): this way, the flat energy list only stores relevant values.

The precomputation itself is also optimized, to avoid making it the dominant computational cost of running grid MC simulations. To do so, the framework interactions computation benefits from all the precomputations explained in section 2.4.4, in particular the tabulated atomic grids.

For the molecule-molecule interaction averaged over the angles, the energy is interpolated from a linear grid: the interaction energy is computed by putting the bead of the first molecule at the origin and the other at a distance  $d$ , where  $d$  increments from 0 to the cutoff distance by steps of one fifth of the average MC grid step. The interpolation is done with cubic splines through the `BasicInterpolators.jl` Julia package.





# 4

---

## DATABASE APPROACH

---

---

4.1	Screening studies . . . . .	110
4.2	Adsorption isotherm . . . . .	110
4.2.1	Definition and classification . . . . .	110
4.2.2	Experimental observation and numerical prediction . . . . .	112
4.3	Database constitution. . . . .	112
4.3.1	Aluminium placement . . . . .	113
4.3.2	Cation placement . . . . .	113
4.4	Prediction . . . . .	114
4.4.1	Why isotherms? . . . . .	114
4.4.2	Adsorption models. . . . .	115
4.4.3	Isotherm fitting . . . . .	118
4.4.4	Fitting result . . . . .	119
4.4.5	Simple meta-models . . . . .	122
4.5	Perspectives . . . . .	123
	Peer-reviewed articles. . . . .	131
	Open-source software and libraries . . . . .	131

---

## 4.1 SCREENING STUDIES

Research on the adsorption properties of zeolites in particular, and nanoporous materials in general, aims at understanding the nature and respective importance of the different interactions that drive the adsorption phenomenon. This understanding can afterwards be turned into principles, which are then applied to predict the adsorption capacities of similar materials on similar gases, where these principles remain valid.

The natural starting point for this research is a study of a particular material with a particular gas, which leads to particular observations that may then be generalized. Many such studies have been performed and published on zeolites, each involving a considerable amount of work, which provide very precise results on a given topology, with up to a few different Si/Al ratios. Yet, the conclusions can seldom be carried over to provide predictions on other topologies.

The converse strategy consists in doing screening studies, in which a vast array of structures is tackled at the same time. Given the cost of doing so experimentally, these studies are mostly computational, thus providing less precise results than actual experiments, but on a broader scale.

Most zeolite screening studies focus on all-silica zeolites, an approach that sidesteps the issue of placing aluminium and cations. However, most zeolite adsorption applications require cationic zeolites, since cations critically increase the adsorption capacity of the materials.

Even among the few studies which tackle cationic zeolites across topologies and Si/Al ratios, not all properly place cations in the framework, although it is known that this can lead to incorrect subsequent adsorption measurements.<sup>106</sup> For example, Mousavi et al. [123] target 57 different topologies with 5 different possible cations, but fail to mention where these are placed before the start of the Grand Canonical Monte Carlo (GCMC) simulations, likely resulting in them being trapped in a non-optimal placement. Lin et al. [124] also screens cationic zeolites, but place cations at the so-called “minimum energy positions” instead of using a robust method like parallel tempering; they also use a force field made for FAU zeolites only, which is inadequate to screen other zeolites.

In this chapter, I explain how I constitute a database of cationic zeolite structures and how it can be used for isotherm prediction through statistical methods. This work is ongoing at the time of writing.

## 4.2 ADSORPTION ISOTHERM

### 4.2.1 Definition and classification

The behaviour of a material with respect to the adsorption of a gas is typically assessed by measuring the evolution of its adsorption capacity with external fluid pressure, at a fixed temperature. The resulting curve is called an isotherm, and it is usually classified according to its general shape into one of several possible categories, represented on [Figure 4.1](#).

The shape of the isotherm depends on the surface of the material, the strength of its interaction with the adsorbate and of the adsorbate-adsorbate interactions. For example, type I isotherms are often observed on materials with very small external surface and monodisperse pores of

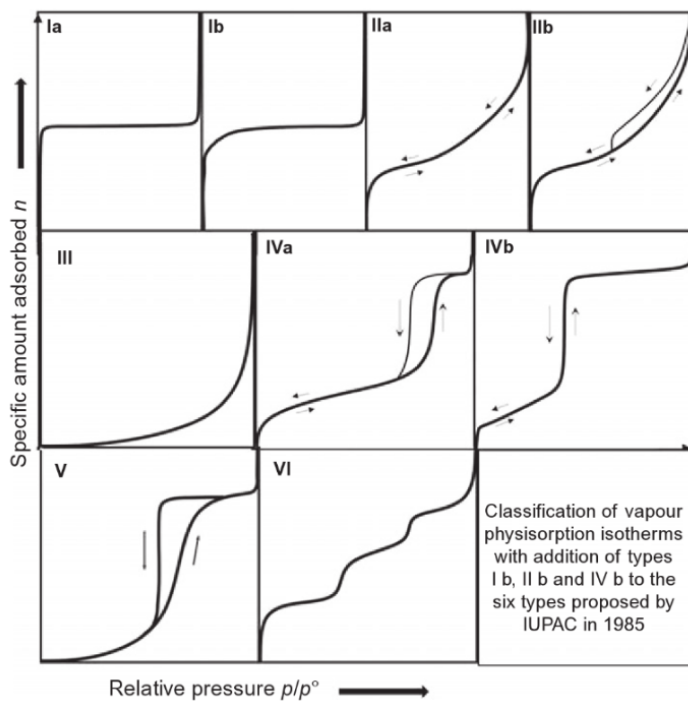


Figure 4.1: Classification of gas isotherm by IUPAC, taken from [126], itself adapted from [127].  $p^0$  designates the saturation pressure of the adsorbate.

small size, where adsorption quickly reaches saturation. On the other hand, type III isotherms occur when the adsorbent-adsorbate interaction is weak and adsorption is not limited by the pore size (either because adsorption occurs on the external surface or because the pores are very large). Some of these types exhibit hysteresis loops: for example, type IV(a) isotherms, typical of mesoporous adsorbents, have the adsorption branch lower than the desorption branch (when the gas is withdrawn), which comes from the capillary condensation of the adsorbate at high pressure. Real isotherms are often combinations or slight variations of these idealized types.<sup>125</sup>

At very low pressure, all isotherms are expected to be linear: this is Henry's law, and Henry's adsorption constant K is proportional to the slope of the isotherm. In that limit, all adsorbates behave like ideal gases since, by definition, there is no adsorbate-adsorbate interaction at low enough pressure.

The other end of the pressure spectrum is more complex. When adsorption occurs on the external surface of the adsorbent, for instance with clays, and if adsorbent-adsorbent interactions are strong enough to allow multi-layer adsorption, then the number of adsorbed species never stops growing with increasing pressures. However, with zeolites and more generally any adsorbent where adsorption occurs in finite pores, the adsorption capacity plateaus at high pressure when all the pores are filled with the adsorbate. It should be mentioned though that the adsorption capacity can still increase beyond that limit, because of the compressibility of the adsorbate in liquid or supercritical state. These regimes of extremely high pressure (above 100 MPa) are of lesser industrial relevance because reaching these conditions is costly and hazardous. They are, however, visible in simulations.

### 4.2.2 Experimental observation and numerical prediction

Experimentally, adsorption isotherms are measured by progressively increasing the input pressure of the adsorbate in the material at the fixed temperature, and measuring the amount adsorbed. The desorption isotherm follows up by progressively decreasing the input pressure, and similarly measuring the amount of adsorbate.

The measurement itself usually consists in either of the three following methods:<sup>125</sup>

- volumetry: a fixed amount of gas at the target pressure is put in contact with the adsorbent, and what is measured is the difference of pressure before and after adsorption.
- breakthrough: the gas starts flowing through the adsorbent at a given time, and the outlet concentration and volumetric flowrates are measured.
- gravimetry: the difference in mass of the sample containing the adsorbent before and after adsorption is measured by balancing its weight against buoyancy.

By reproducing the experiment with a reference gas (usually N<sub>2</sub> or Ar), these techniques give access to the net adsorption, which is the absolute amount of adsorbed species minus that which would be in a fluid occupying the same space as the adsorbent at the same pressure and temperature. Knowledge of the volume of adsorbent allows retrieving the absolute adsorption capacity, which is the thermodynamic variable directly accessible in simulations.

Some more anecdotic isotherm measurement techniques including impedance spectroscopy as well as NMR allow obtaining directly the absolute adsorption,<sup>125</sup> but these methods are much too costly to be used routinely.

The adsorption capacity can be predicted numerically through GCMC simulations, as explained in section 3.2. Beyond the limits due to the precision of the energy computation, either from a force field or from DFT, and convergence of the simulations, those are also dependent on a model of the adsorbent, which cannot take into account the complexity of real materials. In the case of zeolites, the location of the aluminium and of the cations has already been discussed through chapter 2, but more generally, all kinds of defects and small crystal size effects can lead to experimental isotherms differing from the simulated counterparts. This limits the accuracy of individual numerical simulation compared to precise experiments. They remain useful however to extract tendencies and direct the search for new adsorbents, which may be experimentally tested eventually.

## 4.3 DATABASE CONSTITUTION

Finding general tendencies in the adsorption behaviour across zeolites requires doing the analysis of many different structures. To do so, the first step consists in establishing a database of models for the materials themselves. The general workflow for creating these structures, starting from the idealized zeolite structure defined by its topology, down to the cation placement, has already been described in chapter 2. To summarize, the two steps are:

1. Aluminium placement. Start by finding the minimum Si/Al ratio by replacing as many silicon with aluminium atoms as possible, with random exchanges and restarts. Check multiple supercell sizes. Then, starting from these filled structures, replace some alu-

minium by silicon atoms at random and do more exchange steps to generate 6 aluminium placements for each target Si/Al ratio.

2. Cation placement: using either parallel tempering or “shooting star” simulations, combined with annealed site hopping once the sites are localized. The only cation used in the current study is sodium.

For the entire database, I used the same force field which is that developed by Boulfelfel et al. [105] for the adsorption of small gases on cationic zeolites with mobile cations. As with any force field, it has limited accuracy, but the goal is to develop and test a methodology with a fixed known force field to ensure the consistency of the database.

### 4.3.1 Aluminium placement

The current database contains 6 aluminium placements for all 239 known and not interrupted zeolite topologies, with Si/Al ratios of 1, 1.23, 1.4, 1.7, 2, 3, 5 and 10. The actual Si/Al ratios of each structures are those closest to the previous references, which may sometimes differ. When the minimum Si/Al ratio (presented in Table 2.1) is not among the previous references, it is added separately, and the lower Si/Al ratios cannot be generated. For example, the list of actual Si/Al ratios for topology YUG is 1.56,  $\frac{121}{71} \approx 1.704$ , 2, 3, 5 and  $\frac{349}{35} \approx 9.971$ .

The algorithm sometimes fails at finding 6 distinct aluminium placements, because of high symmetry constraints: in that case, the maximum number of distinct placements is kept. In the case where Si/Al = 1 for example, there can be up to only 2 distinct aluminium placements that obeys Löwenstein’s rule: taking an arbitrary T-atom as a reference, one placement corresponds to that reference set to Al, and the other to that reference set to Si. For many topologies, these two placements are actually symmetry-equivalent, so they share the same signature and only one of them is actually stored. This is not necessarily the case however: for example, topology JSW has two distinct aluminium placements for Si/Al = 1.

Overall, 8983 different structures with aluminium placed were generated. Each of these then need to have extra-framework cations in order to represent an electrically neutral material.

### 4.3.2 Cation placement

For all 239 known and non-interrupted topologies, and for each of the up to 6 different aluminium placements corresponding to the minimum Si/Al, a “shooting star” simulation was launched with the hot run at 2000 K for 20 000 cycles (and 2000 initialization cycles), spawning one cold simulation every 100 cycles. Each of the resulting 200 cold simulations ran at 300 K for 10 000 cycles. This served as an experiment to assess the convergence of the simulations: out of the 239 topologies, 57 converged in less than 5000 cycles (averaged across aluminium placements). For these topologies only, “shooting star” simulations were run for all previously created aluminium placements across the different Si/Al ratios, using the same parameters (except for the number of cold cycles raised to 15 000). For each “shooting star” simulation, the 200 cold simulations are divided into six groups, and for each of these groups, the structure with the lowest corresponding energy is kept. Hence, this methodology yields 6 cation placement per structure.

This methodology is a reduced version of the full cation placement strategy illustrated on the FAU topology in [section 2.3.1](#). Such a strategy starts by identifying cationic sites using the previous simulation results, then follows up by running site hopping simulations augmented by simulated annealing (or another meta-algorithm) for each desired Si / Al ratio and aluminium placement. This ensures the optimal repartition of the cations in the different sites, although the site locations themselves may not be perfectly adequate for each precise structure, since they are identified based on a cation density map averaged over different structures. The 6 placements yielding the lowest energy should thus be optimized again by running one short MC simulation each, starting from that placement and only using local translation moves. Finally, for each of these 6 simulations, one of the cycles after energy convergence picked at random can be used to yield a representative cation placement.

At the time of writing, this full methodology was not deployed yet. Although it requires more implementation effort, it should not incur a considerable computational cost compared to the initial shooting star simulations. The main reason for this is the speed of the site hopping simulations, which is considerably faster than a regular simulation.

Overall, 14 268 different structures with both aluminium and cations placed were obtained.

## 4.4 PREDICTION

Using the structures from the database, it is possible to study the adsorption behaviour of zeolites at large scale, across topologies and Si / Al ratios. To do so, one simply needs to run a GCMC simulation for each combination of zeolite structure (including Si / Al ratio, aluminium placement, nature and placement of the cations), temperature, pressure, and gas.

In order to investigate the relationship between the topology of zeolites and their adsorption properties, I attempted to build a predictive model that could output a plausible isotherm for each combination of three parameters, which are 1) the zeolite topology, 2) the Si / Al ratio and 3) the temperature, using  $\text{Na}^+$  as cation and either  $\text{CO}_2$  or  $\text{N}_2$  as gas.

### 4.4.1 Why isotherms?

Adsorption isotherms are often used for the characterization of experimental porous frameworks. One possible technique for the rationalization of unknown pore structures consists in measuring the isotherm using one of the methods presented in [section 4.2.2](#), then fitting the obtained curve against a set of pre-computed isotherms, called the kernels. Each kernel is computed based on a pore geometry (*i.e.* its shape, like a slit or a sphere, and its size) and the thermodynamical properties of the gas, often modeled using simple fluid theory. Fitting the isotherm then corresponds to finding coefficient on each kernel such that the sum of the kernels weighted by the coefficients yields the best approximation of the isotherm. The best fit thus provides the repartition of pore geometries based on their corresponding coefficients.

Another typical context of use for isotherm fitting is for the identification of a material, or the evaluation of its purity or degree of crystallization. To do so, a method consists in measuring one or more isotherms and comparing them to those obtained on a reference structure, to check if they match. In general data science, two curves can be compared by computing their root-mean-square deviation (RMSD), but this does not provide much physical meaning to the

comparison, and requires that both isotherms have points measured at the same pressures. More often, the reference isotherm has been fitted against one model, hence the isotherms of the experimental structure can be fitted against the same model, so that the coefficients of the model, which carry some physical meaning, can be compared.

In the current setting, the aim is quite different since the goal is to predict the adsorption capacity from a theoretical structure, instead of an experimental one. The concept of isotherm is actually not strictly necessary to this goal: one could imagine making a black-box model that directly outputs the adsorption capacity given the three parameters (topology, Si / Al ratio, temperature) as well as the gas pressure. This approach, however, leads to a model that cannot be physically interpreted, and that offers no guarantee on the general shape of the isotherms, with the risk of them being unphysical. On the contrary, making a model that directly predicts the coefficients of a given isotherm model from the three parameters yields a result that already embeds the physics of adsorption through the isotherm mode. Of course, it also offers the additional guarantee of a smooth and plausible interpolation of the simulated data points across pressures.

To make such a model, the first step thus consists in fitting the simulated isotherms against a given adsorption model, in order to obtain the coefficients associated with each triplet of parameters. Retrieving the relation between the parameters and the coefficient can then be cast as a data science problem.

#### 4.4.2 Adsorption models

The literature is rife with adsorption models, either grounded in theory or empirical ones. The precise choice of a model for an isotherm stems from nature of the adsorption when known, otherwise the shape of the isotherm, the nature of the material or even the scientific community. Since isotherm models are only used here as a mean for extracting a common mathematical descriptor of the isotherms across numerous settings, the only criterion is that the model should be rich enough to accurately reproduce the isotherms. Beyond that, the simpler the model, *i.e.* the smaller the number of coefficients necessary to represent an isotherm, the better it will be for prediction.

Next are the isotherm models which I investigated for this project. This list is not exhaustive, but it covers a sizeable proportion of the most commonly used models for small gas adsorption in zeolites.<sup>128</sup>

##### LANGMUIR

The simplest adsorption model corresponds to a physical situation where the adsorbate behaves as an ideal gas, and binds with the adsorbent in a reversible reaction of equilibrium constant  $\beta$ . In that setting, the Langmuir adsorption model states that the fraction of occupied adsorption sites is  $\beta P / (1 + \beta P)$  where  $P$  is the pressure, hence the total adsorption capacity is:

$$n_{\text{Langmuir}}(P) = \alpha \frac{\beta P}{1 + \beta P} \quad (4.1)$$

where  $\alpha$  is the maximum population of the site.

This very simple model is not accurate for zeolites however. One of the reasons is that zeolites contain multiple adsorption sites, both spatially – there are multiple adsorption reactions happening simultaneously – and energetically – they have different values of  $\beta$ .

**N-SITE LANGMUIR**

One simple way to circumvent the previous issues consists in simply summing multiple Langmuir adsorption models. This physically assumes some kind of independence between the different adsorption sites, which is debatable, and the general formula is

$$n_{\text{N-site Langmuir}}(P) = \sum_{i=1}^N \alpha_i \frac{\beta_i P}{1 + \beta_i P} \quad (4.2)$$

Such a general model can be made to fit any isotherm, simply by increasing the number of sites N until reaching a high enough complexity of the model. In practice, N = 3 is good enough to fit many isotherms, simply because the fit can be optimized across six coefficients, although the underlying physical model may not be accurate at all.

**FREUNDLICH**

This simple empirical model is commonly used when the adsorption is known to happen on a heterogeneous surface, and depends on two parameters A and  $\gamma$ :

$$n_{\text{Freundlich}}(P) = A \times P^\gamma \quad (4.3)$$

Beyond its simplicity, the main limit of the model is its behaviour at high pressure: the model diverges to  $+\infty$  whereas, in practice, adsorption reaches saturation (before the highly condensed phase).

**SIPS**

The Sips model combines both Langmuir and Freundlich isotherms, with the following formula:

$$n_{\text{Sips}}(P) = \alpha \frac{(\beta P)^\gamma}{1 + (\beta P)^\gamma} \quad (4.4)$$

This model has two limit regimes: at low pressure, it is equivalent to the Freundlich model while at high pressure, it reaches a plateau similarly to the Langmuir model. It also reduces to the Langmuir model in the particular case of  $\gamma = 1$ .

**TOTH**

The Toth model is another empirical variation of the Langmuir model:

$$n_{\text{Toth}}(P) = \alpha \frac{\beta P}{(1 + (\beta P)^\gamma)^{1/\gamma}} \quad (4.5)$$

Like the Sips model, it reduces to the Langmuir model for  $\gamma = 1$ , and reaches a plateau at high pressure. A slight difference with the Sips model is the adsorption capacity at low pressure, which becomes proportional to P and thus obeys Henry's law, whereas both Freundlich and Sips models have a dependency in  $P^\gamma$ .

**REDLICH-PETERSON**

Like the Sips model, the Redlich-Peterson model combines both Langmuir and Freundlich models:

$$n_{\text{Redlich-Peterson}} = \alpha \frac{P}{1 + (\beta P)^\gamma} \quad (4.6)$$

It also follows Henry's law by reducing to a linear function of  $P$  at low pressure, but its behaviour at high pressure is similar to Freundlich's, making it only adapted to pressure regions below the saturation point.

### JENSEN-SEATON

By adding a fourth parameter, Jensen and Seaton propose an adsorption model that present both Henry's law linear behaviour at low pressure, as well as a non-constant affine asymptote at high pressure that models the compressibility region.

$$n_{\text{Jensen-Seaton}} = \alpha \beta P \times \left( 1 + \left( \frac{\beta P}{1 + \delta P} \right)^\gamma \right)^{-1/\gamma} \quad (4.7)$$

This model reduces to the Toth model when  $\delta = 0$  and to the Langmuir model when  $\gamma = 1$  (with second parameter  $\beta' = \beta + \delta$ ).

### SIPS-TOTH

A custom-made adsorption model, absent from the literature, consists in using a fourth parameter  $\zeta$  to act as a continuous switch between the Toth model ( $\zeta = 0$ ) and the Sips model ( $\zeta \rightarrow +\infty$ ):

$$n_{\text{Sips-Toth}} = \alpha \times \left( \frac{(\beta P)^\gamma}{1 + (\beta P)^\gamma} \right)^{\frac{1+\gamma\zeta P}{\gamma(1+\zeta P)}} \quad (4.8)$$

Like its two building blocks, this model collapses to a simple Langmuir isotherm when  $\gamma = 1$ , and reaches a plateau at high pressure. It also obeys Henry's law at low pressure.

### SUMMARY

**Table 4.1** summarizes the key properties of the previously presented isotherm models. The number of coefficients characterizes the complexity of the model. Its behaviour at low pressure should obey Henry's law, while it should be affine at very high pressure to correctly model the compressibility phase, or at least behave as a plateau otherwise to account for the stationary phase at high pressures.

Name	Coefficients	Henry's law at low P	Behaviour at high P
Linear	1	No	Affine
N-site Langmuir	2N	Yes	Plateau
Freundlich	2	No	Polynomial
Sips	3	No	Plateau
Toth	3	Yes	Plateau
Redlich-Peterson	3	Yes	Polynomial
Jensen-Seaton	4	Yes	Affine
Sips-Toth	4	Yes	Plateau

Table 4.1: Main characteristics of different adsorption models

Several of these models can be combined by simply adding them together. For this purpose, one extra dummy model was added, which simply consists in doing a linear regression of the isotherm:

$$n_{\text{Linear}} = \eta \times P \quad (4.9)$$

Of course, this model does not fit any actual isotherm by itself, but it can be added to any model that reaches a plateau at high pressure to fix its behaviour for the compressibility phase, by making it affine as expected.

#### 4.4.3 Isotherm fitting

In practice, fitting an isotherm means finding the parameters  $\alpha, \beta, \gamma, \dots$  of the model such that the theoretical isotherm resulting from the model is as close as possible to the input one. This closeness can be properly defined through the RMSD for instance. Finding the best parameters can thus be formulated as an optimization problem, *i.e.* a problem of the form

$$\text{minimize } \mathcal{D}(\alpha, \beta, \gamma) \quad \text{such that } \alpha > 0, \beta > 0, 0 < \gamma < 5 \quad (4.10)$$

for example, where  $\mathcal{D}$  represents the deviation between the model with the given parameters and the actual isotherm.

Unfortunately, the expressions of the different adsorption models make this problem non-convex, which is a category of optimization problems generally considered difficult. To solve it, I used the `LsqFit.jl` and `BlackBoxOptim.jl` Julia packages to do global optimization. Crucially, these two packages do not rely on  $\mathcal{D}$  being differentiable, since that would require finding the derivative of the deviation with respect to the parameters for all investigated adsorption models and their combination.

#### RATIONAL INITIAL POINT

Both packages use meta-heuristic and stochastic algorithms to perform the actual optimization, but they need a starting point, *i.e.* an initial value for the parameters, to work. The result often depends on the quality of this initial point: the closer it is to the optimum, the better the final result.

To find this initial point, I tried to obtain it numerically from a linearization of the adsorption models. This operation consists in finding an equation  $y = f(x)$  verified by the adsorption model, where  $y$  and  $x$  can be expressed in terms of the pressure  $P$  and the loading  $n$ , and  $f$  is an affine function  $f : x \mapsto ax + b$ , such that the parameters of the model  $\alpha, \beta, \gamma, \dots$ , can be expressed in terms of  $a$  and  $b$ . Doing a linear fit  $y = f(x)$  using the simulated data thus allows retrieving a rational set of model parameters, which can serve as a starting point in `LsqFit.jl` to find the best model fit.

For the different adsorption models tried, this is the strategy I used, mixing linear regressions and empirical parameter tuning:

- For Langmuir, the linear regression  $n^{-1} = f(P^{-1})$  yields  $n_{\text{Langmuir}}^{-1} = \alpha'_0^{-1} \left( 1 + \beta'_0 P^{-1} \right)$ . Three different initial points are then tested:  $\alpha_0 = \alpha'_0 \times \theta$  and  $\beta_0 = \beta'_0 / \theta$  with  $\theta = 0.833$ ,  $1.44$  and  $0.579$ .
- For Freundlich, the linear regression  $\log n = f(\log P)$  directly gives  $\log n_{\text{Freundlich}} = \log A_0 + \gamma_0 \log P$ .
- For Sips, a first linear regression  $\log n = f(\log P)$  gives an approximate value  $\gamma_0$ , then a second linear regression  $n^{-1} = f(P^{\gamma_0})$  yields  $n_{\text{Sips}}^{-1} = \alpha_0 \left( 1 + \beta^{-\gamma_0} P^{-\gamma_0} \right)$ .

- For Toth, the three initial points  $\alpha_0$  and  $\beta_0$  from the Langmuir isotherm are tested with  $\gamma_0 = 0.667$ ,  $2.25$  and  $0.296$  respectively.
- For Redlich-Peterson, a first linear regression  $\log(P/n) = f(\log P)$  allows to obtain  $\log(P/n_{\text{Redlich-Peterson}}) = \gamma_0 \log P + C$ , then a second linear regression  $P/n = f(P^{\gamma_0})$  yields  $P/n_{\text{Redlich-Peterson}} = \alpha_0^{-1} (1 + \beta_0^{\gamma_0} P^{\gamma_0})$ .
- For Jensen-Seaton, the three sets of initial parameters  $\alpha_0$ ,  $\beta_0$  and  $\gamma_0$  are taken with the method for Toth, with a fixed  $\delta_0 = 8 \times 10^{-10}$ .
- For Sips-Toth, both Sips and Toth parameters are tried, with the switching parameter  $\zeta_0$  equal to either  $1$ ,  $10^{-5}$  or  $10^{-10}$ .

When adding a linear term to a model, the linear slope is taken from a linear regression of the four last point in the isotherm, then the rest of the initial point is taken from the isotherm minus this initial slope.

#### BLACK BLOX INITIAL POINT

Unfortunately, the previous rational but simplistic method does not give good results even for simple models, because the initial points are too far from the optimum. A more systematic approach consists in checking a larger set of initial parameters with the `BlackBoxOptim.jl` package. The best set of parameters found is then used as the initial point for an `LsqFit.jl` optimization, and whichever set of parameters yields the lowest RMSD is deemed the optimal fit.

The only requirement for `BlackBoxOptim.jl` is to delimit the minimum and maximum values for each parameter. I use  $0 \text{ Pa}^{-1} < \beta < 1 \text{ Pa}^{-1}$ ,  $0 < \gamma < 5$ ,  $0 \text{ Pa}^{-1} < \delta < 1 \text{ Pa}^{-1}$ ,  $0 \text{ Pa}^{-1} < \zeta < 0.5 \text{ Pa}^{-1}$ , and  $2M/3 < \alpha < 4M/3$  where  $M$  is the maximum value of the isotherm. Overall, I find that this approach, starting with `BlackBoxOptim.jl` to have an initial point followed by `LsqFit.jl` for fine-grained optimization, gives the best result.

External to the Julia ecosystem, it is also possible to perform isotherm fitting using proprietary softwares like OriginLab, or other free open-source alternatives like the PyGAPS package in Python.<sup>129</sup> The latter provides isotherm fitting capability for (up to 3-site) Langmuir, Freundlich, Toth, Jensen-Seaton and a few other models, but not Sips, Redlich-Peterson, nor custom functions like the Sips-Toth model presented before. The PyGAPS framework is flexible enough to allow adding custom models however, so it could be interesting to compare the quality of my fits with theirs.

#### 4.4.4 Fitting result

The result of isotherm fitting according to all of the previous models, with and without linear addition, and starting from the black box initial point, is represented in Figure 4.2 on a particular example, which is the adsorption of CO<sub>2</sub> in FAU with Si/Al = 1.23.

The quality of the fit generally increases with the number of parameters, simply because of the increased flexibility of the model. Similarly, adding one extra linear parameter improves the quality of the overall fit, in particular at high pressure, since it corresponds to the linear compressibility regime. The case of the Jensen-Seaton adsorption model complements this

## DATABASE APPROACH

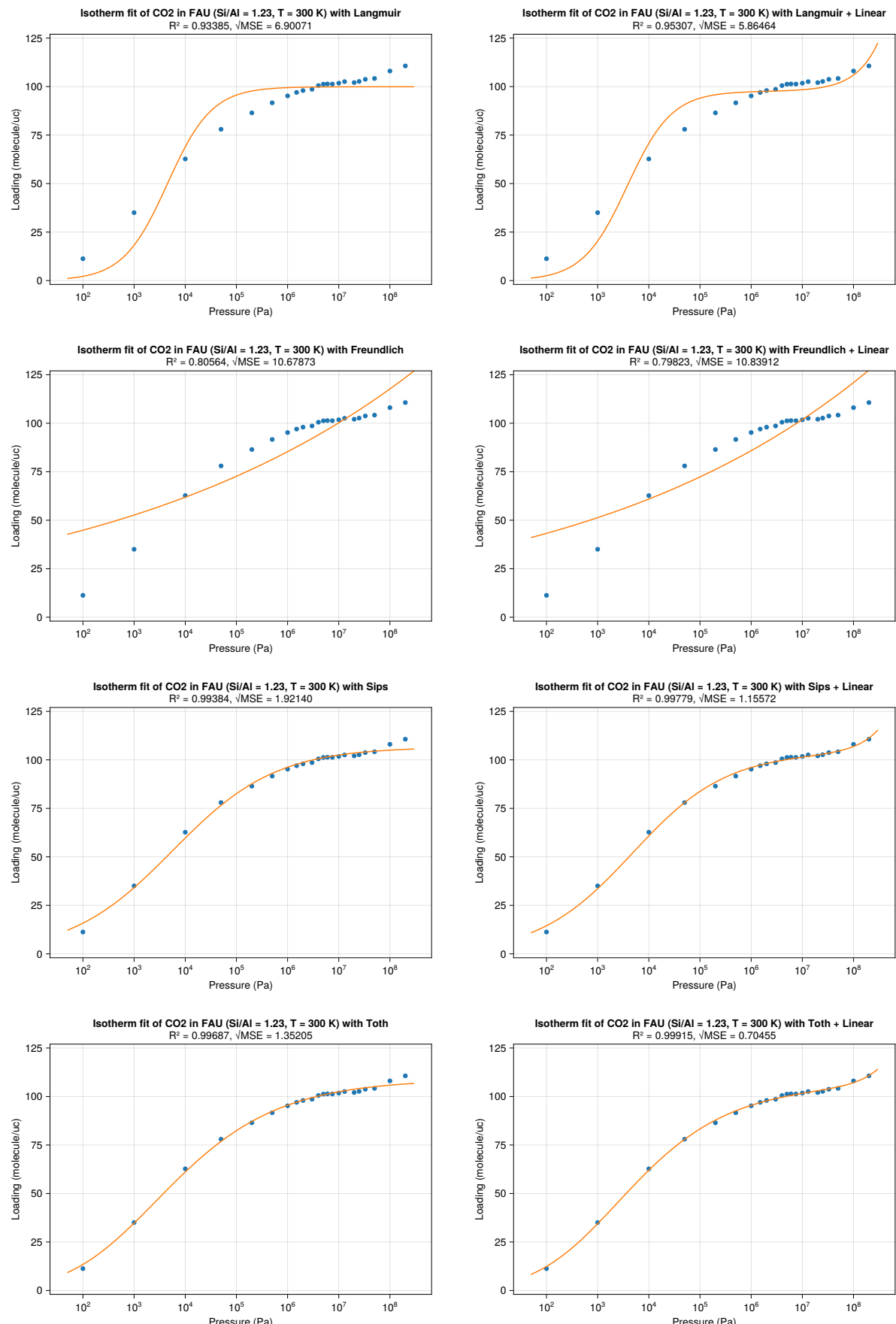


Figure 4.2: Simulated adsorption isotherm fitted with different models

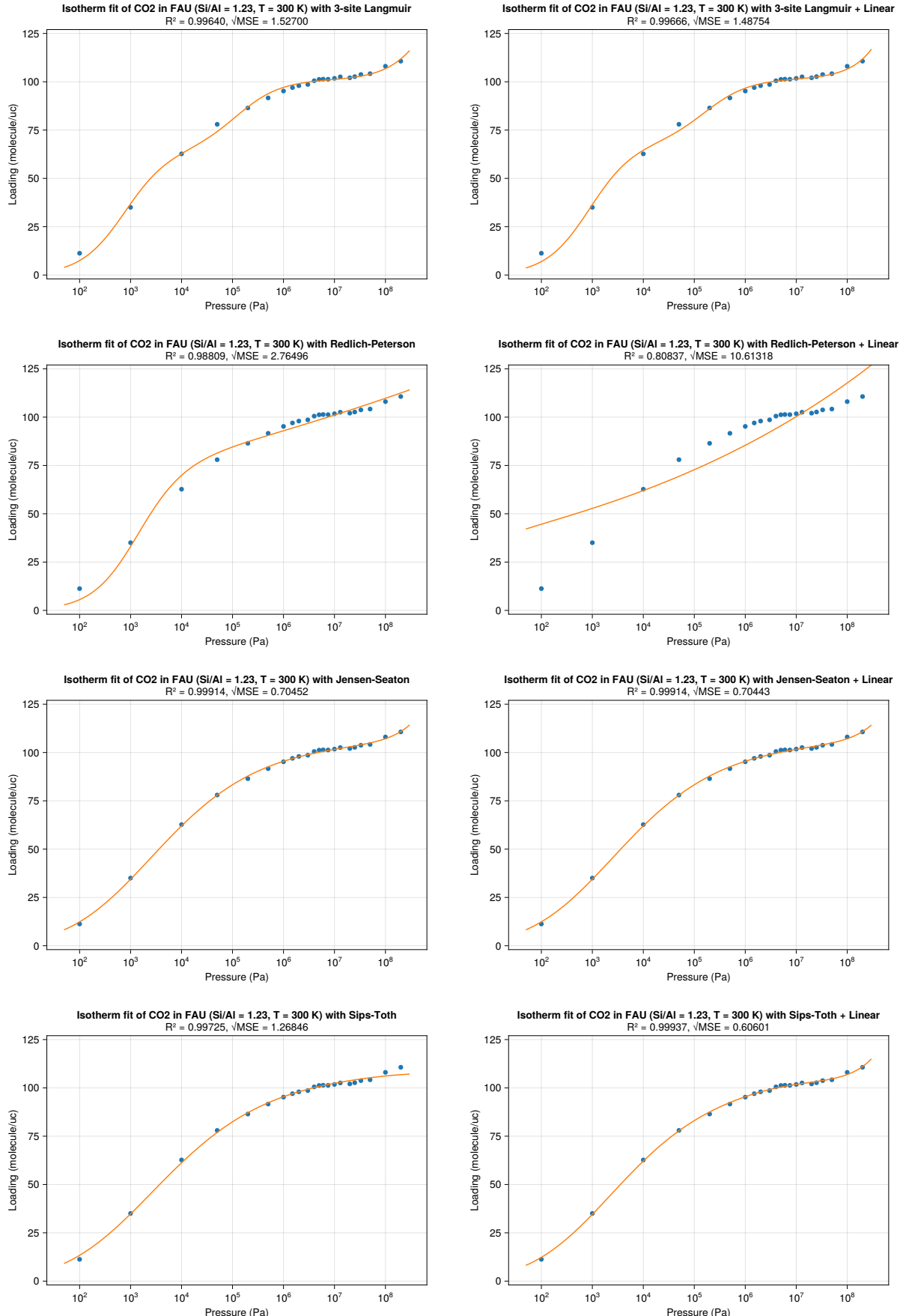


Figure 4.2: Simulated adsorption isotherm fitted with different models (continued)

point: there is no improvement in the fit due to the linear parameter in that case, because Jensen-Seaton isotherms already behave linearly at high pressure.

However, not all models perform equivalently. For example, even with 3 sites and thus 6 parameters, Langmuir fits very poorly compared to the Sips-Toth model plus linear term, which is the overall best and require one less parameter. With only 4 parameters, Toth plus linear is equivalent to Jensen-Seaton. Both Freundlich and Redlich-Peterson fail to fit because of the polynomial behaviour at high pressure.

Other isotherms of the database generally leads to the same ordering of fit quality, so the most appropriate adsorption models to use for the current purpose seem to be either Jensen-Seaton (4 parameters) or Sips-Toth plus linear (5 parameters). The next subsection presents a simple statistical methodology to predict the values of the parameters of a model, whichever it may be, hence it is assumed that one adsorption model has been chosen and fixed.

#### 4.4.5 Simple meta-models

Once a sufficient number of fitted isotherms are available, the next goal is to somehow interpolate across them across Si / Al ratio and temperatures for a given topology. Through fitting, this problem is reduced to finding function  $\alpha(r, T)$ ,  $\beta(r, T)$ ,  $\gamma(r, T)$ , ... i.e. to expressing each parameter of the adsorption model as a function of the Si / Al ratio  $r$  and the temperature  $T$ .

For each parameter  $p$ , I tried to express  $p(r, T)$  through a simple meta-model – i.e. a model of the evolution of a (sub-)model parameter –, using GLM.jl, a Julia package for fitting linear models. In detail, I tried to fit expressions of the form

$$f_p^{(p)}(p) = A^{(p)} \times f_r^{(p)}(r) + B^{(p)} \times f_T^{(p)}(T) + C^{(p)} \quad (4.11)$$

where each function  $f^{(p)}$  was either the identity, the inverse, or the log. Such a fit consists in finding the optimal parameters  $A^{(p)}$ ,  $B^{(p)}$  and  $C^{(p)}$  to minimize the RMSD between both sides of the expected equality. There are 27 such expressions to test for each parameter  $p$  since each of the three function  $f^{(p)}$  has three choices (identity, inverse, log), and the expression which yields the lowest RMSD is kept as the meta-model, along with the corresponding parameters.

For example, using the Jensen-Seaton adsorption model for CO<sub>2</sub> adsorption in FAU zeolites, the following expression is found for the  $\beta$  parameter:

$$\log \beta(r, T) = -1.8489 \times \log r + 5170.7 \times \frac{1}{T} - 22.928 \quad (4.12)$$

[Figure 4.3](#) represents the comparison between the interpolated value of  $\beta(r, T)$  and the values collected from the isotherms fitting in the previous setting. In this case, the fit works well, but the simple meta-model above does not always provide such a good level of agreement.

Overall, this approach provides a simple meta-model which works reasonably well to interpolate isotherms. For example, [Figure 4.4](#) shows the difference in quality between the direct Jensen-Seaton fit of an isotherm, and the one obtained from the simple meta-model. In this example, the simple meta-model was built using Si / Al ratios of 1, 1.23, 1.4, 2, 5 and 10 and temperatures of 300 K, 340 K and 420 K, thus excluding the investigated point with Si / Al ratio of 2.4 at

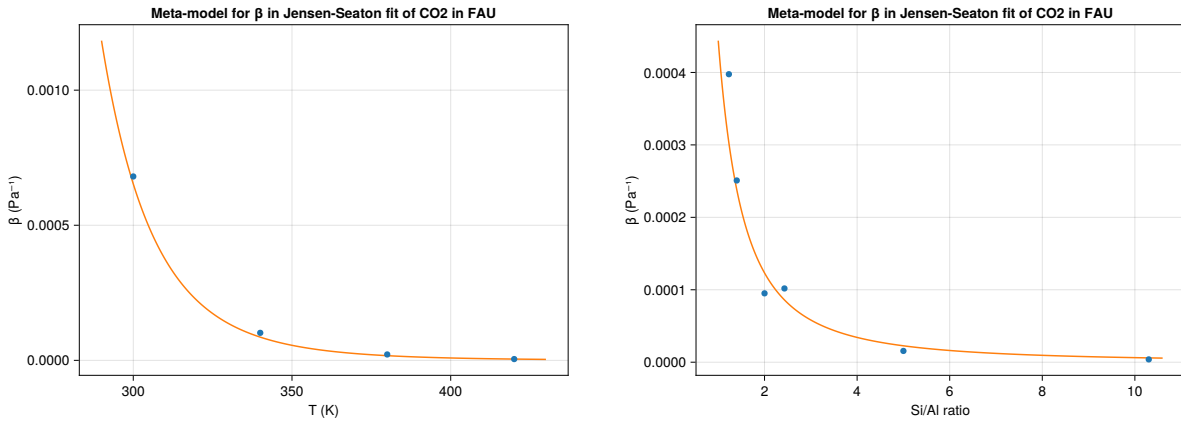
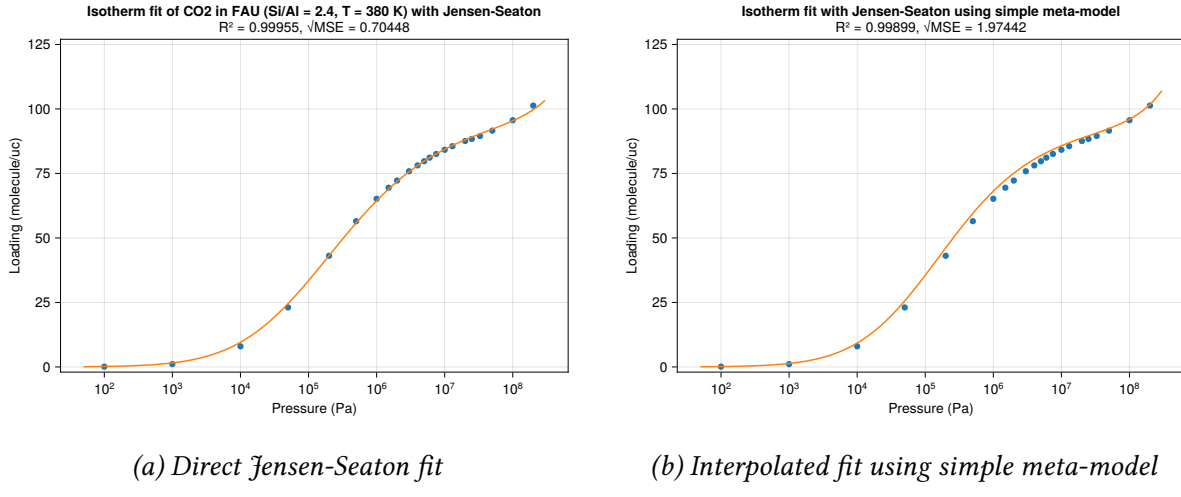
(a) Evolution with temperature for  $Si/Al = 2.43$ (b) Evolution with  $Si/Al$  ratio for  $T = 340$  K

Figure 4.3: Evolution of the  $\beta$  parameter in the Jensen-Seaton fit of  $CO_2$  adsorption isotherms on FAU. The full line is the simple meta-model obtained in Equation (4.12).



(a) Direct Jensen-Seaton fit

(b) Interpolated fit using simple meta-model

Figure 4.4: Fitted adsorption isotherms of  $CO_2$  in FAU with  $Si/Al = 2.4$  at  $T = 380$  K

$T = 380$  K. While not as quantitative as the actual fit, the simple meta-model allows retrieving an isotherm which is close to the reference without needing any additional computation.

## 4.5 PERSPECTIVES

At the time of writing, I have only computed gas adsorption isotherms on three topologies: CHA, LTA and FAU. The previous methodology using simple meta-models to interpolate isotherms constitute a convenient method to obtain adsorption capacities given enough data for the target topology, but does not allow generalizing to other topologies. To reach this target, more isotherm data is required on various topologies, from which point it would become possible to create yet another simple meta-meta-model whose target are the coefficients A, B and C of the previous simple meta-model, depending only on the topology.

Another approach consists in relying on the more general tools of machine learning, instead of the custom approach detailed before. Deep learning could be used as a black-box method to

directly learn the  $p(r, T, \tau)$  functions, where  $\tau$  designates the framework topology, numerically represented using ring statistics or coordination sequences for instance. Yet, once again, this requires much more isotherm data than what is currently available.

Fortunately, my cationic zeolite structure database now contains 64 topologies with representative structures across Si/Al ratios. Once the adsorption isotherms are computed on all of these structures, it should provide enough data to start creating a more robust predictive model.





---

# CONCLUSION AND PERSPECTIVES

---

Crystalline nanoporous frameworks constitute a major source of adsorbent candidates for gas separation applications. In order to efficiently screen through them, numerical methods rely on descriptions of the materials to predict their adsorption properties. At the most precise level, this description needs every atom of the framework to run molecular simulations, in which all atomistic interaction pairs are accounted explicitly; at the coarsest level, the bare topology of a material provides a very simplified view on its microstructure.

This notion of topology was made more accessible to the scientific community by the creation of the `CrystalNets.jl` Julia library. Its intuitive web interface<sup>\*</sup>, with a dedicated visualization panel, allows easily identifying the topology of crystalline materials without computational knowledge. I also developed additional topology analysis tools in the publicly released `PeriodicGraphs.jl` Julia package<sup>†</sup>, including an efficient ring statistics analysis component.

In the case of zeolites, an atomistic description of the microstructure of the material requires knowing the repartition of the aluminium atoms among the T-atoms and the placement of the extra-framework cations in the unit cell. These two problems are numerically difficult to solve and little experimental data is available for most zeolite topologies. I have presented a multi-step methodology to identify the different cationic sites, using a new meta-algorithm called “shooting star” to easily parallelize computations, combined with annealed site hopping to correctly populate the obtained sites. These methods have been tested using classical force fields, but they do not rely on those and could be used with other energy computation schemes such as density functional theory.

Once the atomistic structure of the adsorbent is known, its adsorption capacity for a target gas can be computed using grand canonical Monte-Carlo (GCMC) simulations. I have implemented a simplified GCMC strategy where the guest molecules have to be localized on a regular grid, to attempt to improve the performance of these simulations. The results perfectly reproduce those obtained with the initial more costly methodology for monoatomic molecules, but for polyatomic molecules the grid GCMC strategy only gives correct results at low pressure.

Another venue to predict adsorption capacities consists in using machine learning. For this purpose, I have used the previous methodologies to build a database containing adsorption

---

<sup>\*</sup>accessible at <https://progs.coudert.name/topology>

<sup>†</sup>documentation available at <https://lizou.github.io/PeriodicGraphs.jl/>

results for CO<sub>2</sub> and N<sub>2</sub> in cationic zeolites with Na<sup>+</sup> cations, at different Si/Al ratios, temperatures and pressures. From this, a few simplistic regression models already show promising results for directly predicting adsorption isotherms, hence ensuring that the yielded adsorption capacities still obey an underlying physical model.

This work could be extended in several directions. The effect of the nature of the cation on both cationic site location and adsorption across zeolites needs a separate study. For the purpose of gas separation, the prediction of coadsorption warrant a dedicated optimized methodology, although simple models already exist to predict coadsorption from pure components adsorption capacities. Due to its prevalence in many industrial aspects, the competitive adsorption of water in particular should be evaluated for all zeolites of interest. And finally, since gas adsorption is experimentally known to possibly influence the location of the cationic sites in zeolites, this observation needs to be assessed in numerical simulations and its effects carefully evaluated.

For the time being, the next step of the project consists in adding more topologies to the only three (FAU, LTA and CHA) present in the adsorption isotherms database. This would enable the construction of more refined prediction models that could take the topology of the zeolite as a parameter. To do so, different topological descriptors need to be tried to determine which ones correlate best with the computed properties. In this context, the topological tiling of the framework, which consists in its decomposition into volumes limited by the rings of its bond network, could provide key indicators of the pore structure of the zeolite, or even on the cationic sites, which is likely to strongly correlate with the adsorption capacity. Any realistic model will probably also require extra-topological information such as geometric data, to complete its description of the zeolite.

Ultimately, reaching such a model would mean that the adsorption capacity of a gas in a cationic zeolite could be given from a single mathematical formula, for all topologies, Si/Al ratios, temperatures and pressures. The constant values appearing in this formula would stem from computed correlations in simulated data, thus the uncertainty of their values could be obtained, and propagated to yield a controlled uncertainty on the result. In turn, this would pave the way for ultra-fast screening of zeolites for adsorption purposes with controlled accuracy.





---

# LIST OF PUBLICATIONS

---

## PEER-REVIEWED ARTICLES

- [1] Lionel Zoubritzky and François-Xavier Coudert. “CrystalNets.jl: Identification of Crystal Topologies”. In: *SciPost Chem.* 1 (2022), p. 005. doi: [10.21468/SciPostChem.1.2.005](https://doi.org/10.21468/SciPostChem.1.2.005).
- [2] Lionel Zoubritzky and François-Xavier Coudert. “CrystalNets online: Intuitive Identification and Visualization of Crystal Topologies”. In preparation.
- [3] Guobin Zhao et al. “CoRE-MOF 2024”. In preparation.

## OPEN-SOURCE SOFTWARE AND LIBRARIES

- CrystalNets web interface: <https://progs.coudert.name/topology>
- CrystalNets.jl: crystal net topology analysis, <https://github.com/coudertlab/CrystalNets.jl>
- PeriodicGraphs.jl: periodic graphs algorithms and ring statistics, <https://github.com/Liozou/PeriodicGraphs.jl>
- PeriodicGraphEmbeddings.jl: euclidean embeddings of periodic graphs and symmetry analysis, <https://github.com/Liozou/PeriodicGraphEmbeddings.jl>
- CrystalEnergyGrids.jl: MC simulation framework for guests in rigid crystalline materials (in development), <https://github.com/Liozou/CrystalEnergyGrids.jl>
- MolecularDFT.jl: molecular density functional theory for molecules in rigid frameworks (in development), <https://github.com/Liozou/MolecularDFT.jl>



---

# BIBLIOGRAPHY

---

- [1] L. Zoubritzky and F.-X. Coudert. “CrystalNets.jl: Identification of Crystal Topologies”. In: *SciPost Chem.* 1 (2022), p. 005. [DOI: 10.21468/SciPostChem.1.2.005](https://doi.org/10.21468/SciPostChem.1.2.005).
- [2] N. W. Ockwig, O. Delgado-Friedrichs, M. O’Keeffe, and O. M. Yaghi. “Reticular Chemistry: Occurrence and Taxonomy of Nets and Grammar for the Design of Frameworks”. In: *ChemInform* 36.24 (2005). ISSN: 0931-7597. [DOI: 10.1002/chin.200524292](https://doi.org/10.1002/chin.200524292).
- [3] O. M. Yaghi, M. O’Keeffe, N. W. Ockwig, H. K. Chae, M. Eddaoudi, and J. Kim. “Reticular Synthesis and the Design of New Materials”. In: *Nature* 423.6941 (2003), pp. 705–714. ISSN: 0028-0836. [DOI: 10.1038/nature01650](https://doi.org/10.1038/nature01650).
- [4] D. J. Tranchemontagne, J. L. Mendoza-Cortés, M. O’Keeffe, and O. M. Yaghi. “Secondary Building Units, Nets and Bonding in the Chemistry of Metal–Organic Frameworks”. In: *Chem. Soc. Rev.* 38.5 (2009), p. 1257. ISSN: 0306-0012. [DOI: 10.1039/b817735j](https://doi.org/10.1039/b817735j).
- [5] H. Furukawa, Y. B. Go, N. Ko, Y. K. Park, F. J. Uribe-Romo, J. Kim, M. O’Keeffe, and O. M. Yaghi. “Isoreticular Expansion of Metal–Organic Frameworks with Triangular and Square Building Units and the Lowest Calculated Density for Porous Crystals”. In: *Inorg. Chem.* 50.18 (2011), pp. 9147–9152. ISSN: 0020-1669. [DOI: 10.1021/ic201376t](https://doi.org/10.1021/ic201376t).
- [6] S. Bureekaew, V. Balwani, S. Amirjalayer, and R. Schmid. “Isoreticular Isomerism in 4,4-Connected Paddle-Wheel Metal–Organic Frameworks: Structural Prediction by the Reverse Topological Approach”. In: *CrystEngComm* 17.2 (2015), pp. 344–352. [DOI: 10.1039/c4ce01574f](https://doi.org/10.1039/c4ce01574f).
- [7] J. Kim, B. Chen, T. M. Reineke, H. Li, M. Eddaoudi, D. B. Moler, M. O’Keeffe, and O. M. Yaghi. “Assembly of Metal–Organic Frameworks from Large Organic and Inorganic Secondary Building Units: New Examples and Simplifying Principles for Complex Structures”. In: *J. Am. Chem. Soc.* 123.34 (Aug. 2001), pp. 8239–8247. ISSN: 0002-7863. [DOI: 10.1021/ja010825o](https://doi.org/10.1021/ja010825o).
- [8] M. O’Keeffe, M. A. Peskov, S. J. Ramsden, and O. M. Yaghi. “The Reticular Chemistry Structure Resource (RCSR) Database of, and Symbols for, Crystal Nets”. In: *Acc. Chem. Res.* 41.12 (2008), pp. 1782–1789. ISSN: 0001-4842. [DOI: 10.1021/ar800124u](https://doi.org/10.1021/ar800124u).
- [9] J. Stone. “An Efficient Library for Parallel Ray Tracing and Animation”. MA thesis. Computer Science Department, University of Missouri-Rolla, Apr. 1998.
- [10] W. Humphrey, A. Dalke, and K. Schulten. “VMD – Visual Molecular Dynamics”. In: *Journal of Molecular Graphics* 14 (1996), pp. 33–38.
- [11] M. O’Keeffe and O. M. Yaghi. “Deconstructing the Crystal Structures of Metal–Organic Frameworks and Related Materials into Their Underlying Nets”. In: *Chem. Rev.* 112.2 (2012), pp. 675–702. ISSN: 0009-2665. [DOI: 10.1021/cr200205j](https://doi.org/10.1021/cr200205j).

## BIBLIOGRAPHY

- [12] S. R. Batten. “Topology and Interpenetration”. In: *Metal-Organic Frameworks: Design and Application*. John Wiley & Sons, MacGillivray, L. R., 2010, pp. 91–130.
- [13] S. Hyde, O. D. Delgado-Friedrichs, S. Ramsden, and V. Robins. “Towards Enumeration of Crystalline Frameworks: The 2D Hyperbolic Approach”. In: *Solid State Sci.* 8.7 (2006), pp. 740–752. ISSN: 1293-2558. DOI: [10.1016/j.solidstatesciences.2006.04.001](https://doi.org/10.1016/j.solidstatesciences.2006.04.001).
- [14] S. Ramsden, V. Robins, and S. Hyde. “Three-Dimensional Euclidean Nets from Two-Dimensional Hyperbolic Tilings: Kaleidoscopic Examples”. In: *Acta Cryst. A* 65.2 (2009), pp. 81–108. DOI: [10.1107/s0108767308040592](https://doi.org/10.1107/s0108767308040592).
- [15] J. C. Tan, T. D. Bennett, and A. K. Cheetham. “Chemical Structure, Network Topology, and Porosity Effects on the Mechanical Properties of Zeolitic Imidazolate Frameworks”. In: *Proc. Nat. Acad. Sci.* 107.22 (2010), pp. 9938–9943. ISSN: 0027-8424. DOI: [10.1073/pnas.1003205107](https://doi.org/10.1073/pnas.1003205107).
- [16] M. Fischer and R. G. Bell. “Influence of zeolite topology on CO<sub>2</sub>/N<sub>2</sub> separation behavior: force-field simulations using a DFT-derived charge model”. In: *The Journal of Physical Chemistry C* 116.50 (2012), pp. 26449–26463.
- [17] V. A. Blatov, A. P. Shevchenko, and D. M. Proserpio. “Applied Topological Analysis of Crystal Structures with the Program Package ToposPro”. In: *Cryst. Growth Des.* 14.7 (2014), pp. 3576–3586. ISSN: 1528-7483. DOI: [10.1021/cg500498k](https://doi.org/10.1021/cg500498k).
- [18] V. A. Blatov. “Multipurpose Crystallochemical Analysis with the Program Package TOPOS”. In: *IUCr CompComm Newsletter* 7.4 (2006), pp. 4–38.
- [19] O. Delgado-Friedrichs and M. O’Keeffe. “Identification of and Symmetry Computation for Crystal Nets”. In: *Acta Cryst. A* 59.4 (2003), pp. 351–360. ISSN: 0108-7673. DOI: [10.1107/s0108767303012017](https://doi.org/10.1107/s0108767303012017).
- [20] E. V. Alexandrov, A. P. Shevchenko, and V. A. Blatov. “Topological Databases: Why Do We Need Them for Design of Coordination Polymers?” In: *Cryst. Growth Des.* 19.5 (2019), pp. 2604–2614. ISSN: 1528-7483. DOI: [10.1021/acs.cgd.8b01721](https://doi.org/10.1021/acs.cgd.8b01721).
- [21] S. R. Hall, F. H. Allen, and I. D. Brown. “The Crystallographic Information File (CIF): A New Standard Archive File for Crystallography”. In: *Acta Cryst. A* 47.6 (1991), pp. 655–685. ISSN: 0108-7673. DOI: [10.1107/s010876739101067x](https://doi.org/10.1107/s010876739101067x).
- [22] O. Delgado-Friedrichs and M. O’Keeffe. “Crystal Nets as Graphs: Terminology and Definitions”. In: *J. Sol. State Chem.* 178.8 (2005), pp. 2480–2485. ISSN: 0022-4596. DOI: [10.1016/j.jssc.2005.06.011](https://doi.org/10.1016/j.jssc.2005.06.011).
- [23] V. Blatov, M. O’keeffe, and D. Proserpio. “Vertex-, Face-, Point-, Schläfli-, and Delaney-symbols in Nets, Polyhedra and Tilings: Recommended Terminology”. In: *CrystEngComm* 12.1 (2010), pp. 44–48. DOI: [10.1039/b910671e](https://doi.org/10.1039/b910671e).
- [24] O. Delgado-Friedrichs, S. T. Hyde, M. O’Keeffe, and O. M. Yaghi. “Crystal Structures as Periodic Graphs: The Topological Genome and Graph Databases”. In: *Struct. Chem.* 28.1 (2017), pp. 39–44. ISSN: 1572-9001. DOI: [10.1007/s11224-016-0853-3](https://doi.org/10.1007/s11224-016-0853-3).
- [25] O. Delgado-Friedrichs. “Barycentric Drawings of Periodic Graphs”. In: *International Symposium on Graph Drawing*. Springer, 2003, pp. 178–189.
- [26] M. Treacy, M. Foster, and K. Randall. “An Efficient Method for Determining Zeolite Vertex Symbols”. In: *Micropor. Mesopor. Mater.* 87.3 (2006), pp. 255–260. ISSN: 1387-1811. DOI: [10.1016/j.micromeso.2005.08.024](https://doi.org/10.1016/j.micromeso.2005.08.024).

- [27] V. A. Blatov, O. Delgado-Friedrichs, M. O’Keeffe, and D. M. Proserpio. “Three-Periodic Nets and Tilings: Natural Tilings for Nets”. In: *Acta Cryst. A* 63.5 (Sept. 2007), pp. 418–425. ISSN: 0108-7673. DOI: [10.1107/s0108767307038287](https://doi.org/10.1107/s0108767307038287).
- [28] K. Theisen, B. Smit, and M. Haranczyk. “Chemical Hieroglyphs: Abstract Depiction of Complex Void Space Topology of Nanoporous Materials”. In: *Journal of chemical information and modeling* 50.4 (2010), pp. 461–469. DOI: [10.1021/ci900451v](https://doi.org/10.1021/ci900451v).
- [29] A. Gandhi and M. F. Hasan. “A Graph Theoretic Representation and Analysis of Zeolite Frameworks”. In: *Comput. Chem. Eng.* 155 (2021), p. 107548. ISSN: 0098-1354. DOI: [10.1016/j.compchemeng.2021.107548](https://doi.org/10.1016/j.compchemeng.2021.107548).
- [30] D. Weininger. “SMILES, a Chemical Language and Information System. 1. Introduction to Methodology and Encoding Rules”. In: *J. Chem. Inf. Comput. Sci.* 28.1 (1988), pp. 31–36. ISSN: 0095-2338. DOI: [10.1021/ci00057a005](https://doi.org/10.1021/ci00057a005).
- [31] S. R. Heller, A. McNaught, I. Pletnev, S. Stein, and D. Tchekhovskoi. “InChI, the IUPAC International Chemical Identifier”. In: *J. Cheminformatics* 7.1 (2015), pp. 1–34. DOI: [10.1186/s13321-015-0068-4](https://doi.org/10.1186/s13321-015-0068-4).
- [32] J. Bezanson, A. Edelman, S. Karpinski, and V. B. Shah. “Julia: A Fresh Approach to Numerical Computing”. In: *SIAM review* 59.1 (2017), pp. 65–98. ISSN: 0036-1445. DOI: [10.1137/141000671](https://doi.org/10.1137/141000671).
- [33] J. Bezanson, J. Chen, B. Chung, S. Karpinski, V. B. Shah, J. Vitek, and L. Zoubritzky. “Julia: Dynamism and Performance Reconciled by Design”. In: *Proceedings of the ACM on Programming Languages* 2.OOPSLA (2018), pp. 1–23. ISSN: 2475-1421. DOI: [10.1145/3276490](https://doi.org/10.1145/3276490).
- [34] C. Bonneau, M. O’Keeffe, D. M. Proserpio, V. A. Blatov, S. R. Batten, S. A. Bourne, M. S. Lah, J.-G. Eon, S. T. Hyde, and S. B. Wiggin. “Deconstruction of Crystalline Networks into Underlying Nets: Relevance for Terminology Guidelines and Crystallographic Databases”. In: *Cryst. Growth Des.* 18.6 (2018), pp. 3411–3418. ISSN: 1528-7483. DOI: [10.1021/acs.cgd.8b00126](https://doi.org/10.1021/acs.cgd.8b00126).
- [35] F. M. A. Noa, M. Abrahamsson, E. Ahlberg, O. Cheung, C. R. Göb, C. J. McKenzie, and L. Öhrström. “A Unified Topology Approach to Dot-, Rod-, and Sheet-MOFs”. In: *Chem* 7.9 (2021), pp. 2491–2512. ISSN: 2451-9294. DOI: [10.1016/j.chempr.2021.07.006](https://doi.org/10.1016/j.chempr.2021.07.006).
- [36] A. Schoedel, M. Li, D. Li, M. O’Keeffe, and O. M. Yaghi. “Structures of Metal–Organic Frameworks with Rod Secondary Building Units”. In: *Chem. Rev.* 116.19 (2016), pp. 12466–12535. ISSN: 0009-2665. DOI: [10.1021/acs.chemrev.6b00346](https://doi.org/10.1021/acs.chemrev.6b00346).
- [37] L. S. Xie, E. V. Alexandrov, G. Skorupskii, D. M. Proserpio, and M. Dincă. “Diverse  $\pi$ – $\pi$  Stacking Motifs Modulate Electrical Conductivity in Tetrathiafulvalene-Based Metal–Organic Frameworks”. In: *Chem. Sci.* 10.37 (2019), pp. 8558–8565. DOI: [10.1039/c9sc03348c](https://doi.org/10.1039/c9sc03348c).
- [38] A. P. Shevchenko and V. A. Blatov. “Simplify to Understand: How to Elucidate Crystal Structures?” In: *Struct. Chem.* 32.2 (2021), pp. 507–519. ISSN: 1572-9001. DOI: [10.1007/s11224-020-01724-4](https://doi.org/10.1007/s11224-020-01724-4).
- [39] E. Alexandrov, V. Blatov, A. Kochetkov, and D. Proserpio. “Underlying Nets in Three-Periodic Coordination Polymers: Topology, Taxonomy and Prediction from a Computer-Aided Analysis of the Cambridge Structural Database”. In: *CrystEngComm* 13.12 (2011), pp. 3947–3958. DOI: [10.1039/c0ce00636j](https://doi.org/10.1039/c0ce00636j).

## BIBLIOGRAPHY

- [40] M. Li, D. Li, M. O’Keeffe, and O. M. Yaghi. “Topological Analysis of Metal–Organic Frameworks with Polytopic Linkers and/or Multiple Building Units and the Minimal Transitivity Principle”. In: *Chem. Rev.* 114.2 (2014), pp. 1343–1370. ISSN: 0009-2665. DOI: [10.1021/cr400392k](https://doi.org/10.1021/cr400392k).
- [41] B. J. Bucior, A. S. Rosen, M. Haranczyk, Z. Yao, M. E. Ziebel, O. K. Farha, J. T. Hupp, J. I. Siepmann, A. Aspuru-Guzik, and R. Q. Snurr. “Identification Schemes for Metal–Organic Frameworks to Enable Rapid Search and Cheminformatics Analysis”. In: *Cryst. Growth Des.* 19.11 (2019), pp. 6682–6697. ISSN: 1528-7483. DOI: [10.1021/acs.cgd.9b01050](https://doi.org/10.1021/acs.cgd.9b01050).
- [42] S. J. Chung, T. Hahn, and W. Klee. “Nomenclature and Generation of Three-Periodic Nets: The Vector Method”. In: *Acta Cryst. A* 40.1 (1984), pp. 42–50. ISSN: 1600-5724. DOI: [10.1107/s0108767384000088](https://doi.org/10.1107/s0108767384000088).
- [43] A. Ching, S. Edunov, M. Kabiljo, D. Logothetis, and S. Muthukrishnan. “One Trillion Edges: Graph Processing at Facebook-scale”. In: *Proceedings of the VLDB Endowment* 8.12 (2015), pp. 1804–1815. ISSN: 2150-8097. DOI: [10.14778/2824032.2824077](https://doi.org/10.14778/2824032.2824077).
- [44] T. Granlund et. al. *The GNU Multiple-Precision (GMP) Arithmetic Library*. <https://gmplib.org/>.
- [45] W. Eberly, M. Giesbrecht, P. Giorgi, A. Storjohann, and G. Villard. “Solving Sparse Rational Linear Systems”. In: *Proceedings of the 2006 International Symposium on Symbolic and Algebraic Computation*. 2006, pp. 63–70. DOI: [10.1145/1145768.1145785](https://doi.org/10.1145/1145768.1145785).
- [46] W. Eberly, M. Giesbrecht, P. Giorgi, A. Storjohann, and G. Villard. “Faster Inversion and Other Black Box Matrix Computations Using Efficient Block Projections”. In: *Proceedings of the 2007 International Symposium on Symbolic and Algebraic Computation*. 2007, pp. 143–150. DOI: [10.1145/1277548.1277569](https://doi.org/10.1145/1277548.1277569).
- [47] J. D. Dixon. “Exact Solution of Linear Equations Using P-adic Expansions”. In: *Numer. Math.* 40.1 (1982), pp. 137–141. ISSN: 0029-599X. DOI: [10.1007/bf01459082](https://doi.org/10.1007/bf01459082).
- [48] E. Kaltofen and B. D. Saunders. “On Wiedemann’s Method of Solving Sparse Linear Systems”. In: *International Symposium on Applied Algebra, Algebraic Algorithms, and Error-Correcting Codes*. Springer, 1991, pp. 29–38. DOI: [10.1007/3-540-54522-0\\_93](https://doi.org/10.1007/3-540-54522-0_93).
- [49] O. Delgado-Friedrichs, S. T. Hyde, S.-W. Mun, M. O’Keeffe, and D. M. Proserpio. “Nets with Collisions (Unstable Nets) and Crystal Chemistry”. In: *Acta Cryst. A* 69.6 (2013), pp. 535–542. ISSN: 0108-7673. DOI: [10.1107/s0108767313020655](https://doi.org/10.1107/s0108767313020655).
- [50] B. Delaunay. “Neue Darstellung der geometrischen Kristallographie”. In: *Z. Kristallogr. Cryst. Mater.* 84.1-6 (1933), pp. 109–149. ISSN: 2196-7105. DOI: [10.1524/zkri.1933.84.1.109](https://doi.org/10.1524/zkri.1933.84.1.109).
- [51] P. Niggli, W. Wien, and F. Harms. *Handbuch Der Experimentalphysik*. Leipzig: Akademische Verlagsgesellschaft, 1928.
- [52] A. Santoro and A. Mighell. “Determination of Reduced Cells”. In: *Acta Cryst. A* 26.1 (1970), pp. 124–127. ISSN: 0567-7394. DOI: [10.1107/s0567739470000177](https://doi.org/10.1107/s0567739470000177).
- [53] A. Togo and I. Tanaka. “Spglib: A Software Library for Crystal Symmetry Search”. In: *arXiv preprint arXiv:1808.01590* (2018). arXiv: [1808.01590](https://arxiv.org/abs/1808.01590).
- [54] R. W. Grosse-Kunstleve, N. K. Sauter, N. W. Moriarty, and P. D. Adams. “The Computational Crystallography Toolbox: Crystallographic Algorithms in a Reusable Software Framework”. In: *J. Appl. Cryst.* 35.1 (2002), pp. 126–136. ISSN: 0021-8898. DOI: [10.1107/s0021889801017824](https://doi.org/10.1107/s0021889801017824).

- [55] G. Havas, B. S. Majewski, and K. R. Matthews. “Extended Gcd and Hermite Normal Form Algorithms via Lattice Basis Reduction”. In: *Exp. Math.* 7.2 (1998), pp. 125–136. ISSN: 1058-6458. doi: [10.1080/10586458.1998.10504362](https://doi.org/10.1080/10586458.1998.10504362).
- [56] E. Ren, P. Guilbaud, and F.-X. Coudert. “High-Throughput Computational Screening of Nanoporous Materials in Targeted Applications”. In: *arXiv preprint arXiv:2202.09886* (2022). arXiv: [2202.09886](https://arxiv.org/abs/2202.09886).
- [57] N. Castel and F.-X. Coudert. “Atomistic Models of Amorphous Metal–Organic Frameworks”. In: *J. Phys. Chem. C* (2022). doi: [10.1021/acs.jpcc.2c01091](https://doi.org/10.1021/acs.jpcc.2c01091).
- [58] C. Baerlocher and L. B. McCusker. *Database of Zeolite Structures*. [https://europe.iza-structure.org/IZA-SC/ftc\\_table.php](https://europe.iza-structure.org/IZA-SC/ftc_table.php).
- [59] Y. G. Chung, E. Haldoupis, B. J. Bucior, M. Haranczyk, S. Lee, H. Zhang, K. D. Vogiatzis, M. Milisavljevic, S. Ling, J. S. Camp, B. Slater, J. I. Siepmann, D. S. Sholl, and R. Q. Snurr. “Advances, Updates, and Analytics for the Computation-Ready, Experimental Metal–Organic Framework Database: CoRE MOF 2019”. In: *J. Chem. Eng. Data* 64.12 (2019), pp. 5985–5998. ISSN: 0021-9568. doi: [10.1021/acs.jced.9b00835](https://doi.org/10.1021/acs.jced.9b00835).
- [60] F. Hoffmann. *The Fascination of Crystals and Symmetry*. Blog post “CrystalNets vs. TopCryst” at <https://crystalsymmetry.wordpress.com/2023/07/17/crystalnets-vs-topcryst/> and <https://crystalsymmetry.wordpress.com/2023/07/27/crystalnets-vs-topcryst-follow-up/>. July 2023.
- [61] C. R. Groom, I. J. Bruno, M. P. Lightfoot, and S. C. Ward. “The Cambridge Structural Database”. In: *Acta Cryst. B* 72.2 (2016), pp. 171–179. doi: [10.1107/s2052520616003954](https://doi.org/10.1107/s2052520616003954).
- [62] H. Xu, W. Bao, Y. Xu, X. Liu, X. Shen, and D. Zhu. “An unprecedented 3D/3D hetero-interpenetrated MOF built from two different nodes, chemical composition, and topology of networks”. In: *CrystEngComm* 14.18 (2012), pp. 5720–5722.
- [63] C. Zheng, Y. Li, and J. Yu. “Database of Open-Framework Aluminophosphate Structures”. In: *Sci. Data* 7.1 (2020). ISSN: 2052-4463. doi: [10.1038/s41597-020-0452-4](https://doi.org/10.1038/s41597-020-0452-4).
- [64] J. V. Smith. “Topochemistry of Zeolites and Related Materials. 1. Topology and Geometry”. In: *Chem. Rev.* 88.1 (1988), pp. 149–182. ISSN: 0009-2665. doi: [10.1021/cr00083a008](https://doi.org/10.1021/cr00083a008).
- [65] M. Treacy, I. Rivin, E. Balkovsky, K. Randall, and M. Foster. “Enumeration of Periodic Tetrahedral Frameworks. II. Polynodal Graphs”. In: *Micropor. Mesopor. Mater.* 74.1-3 (2004), pp. 121–132. ISSN: 1387-1811. doi: [10.1016/j.micromeso.2004.06.013](https://doi.org/10.1016/j.micromeso.2004.06.013).
- [66] R. Pophale, P. A. Cheeseman, and M. W. Deem. “A Database of New Zeolite-like Materials”. In: *Phys. Chem. Chem. Phys.* 13.27 (2011), pp. 12407–12412. doi: [10.1039/c0cp02255a](https://doi.org/10.1039/c0cp02255a).
- [67] N. Rego and D. Koes. “3Dmol.js: molecular visualization with WebGL”. In: *Bioinformatics* 31.8 (2015), pp. 1322–1324.
- [68] S. R. Balestra, N. Rodríguez-Sánchez, D. Mena-Torres, and A. R. Ruiz-Salvador. “Structural Features and Zeolite Stability: A Linearized Equation Approach”. In: *Crystal Growth & Design* 24.3 (2024), pp. 938–946.
- [69] J. Li, M. Gao, W. Yan, and J. Yu. “Regulation of the Si/Al ratios and Al distributions of zeolites and their impact on properties”. In: *Chemical Science* 14.8 (2023), pp. 1935–1959.
- [70] A. Deneyer, Q. Ke, J. Devos, and M. Dusselier. “Zeolite synthesis under nonconventional conditions: reagents, reactors, and modi operandi”. In: *Chemistry of Materials* 32.12 (2020), pp. 4884–4919.

## BIBLIOGRAPHY

- [71] R. Bandyopadhyay, Y. Kubota, N. Sugimoto, Y. Fukushima, and Y. Sugi. “Synthesis of borosilicate zeolites by the dry gel conversion method and their characterization”. In: *Microporous and mesoporous materials* 32.1-2 (1999), pp. 81–91.
- [72] R. Fricke, H. Kosslick, G. Lischke, and M. Richter. “Incorporation of gallium into zeolites: syntheses, properties and catalytic application”. In: *Chemical reviews* 100.6 (2000), pp. 2303–2406.
- [73] R. T. Pabalan and F. P. Bertetti. “Cation-exchange properties of natural zeolites”. In: *Reviews in mineralogy and geochemistry* 45.1 (2001), pp. 453–518.
- [74] T. Frising and P. Leflaive. “Extraframework cation distributions in X and Y faujasite zeolites: A review”. In: *Microporous and Mesoporous materials* 114.1-3 (2008), pp. 27–63.
- [75] M. Opanasenko, M. Shamzhy, Y. Wang, W. Yan, P. Nachtigall, and J. Čejka. “Synthesis and post-synthesis transformation of germanosilicate zeolites”. In: *Angewandte Chemie International Edition* 59.44 (2020), pp. 19380–19389.
- [76] M. Moliner. “State of the art of Lewis acid-containing zeolites: lessons from fine chemistry to new biomass transformation processes”. In: *Dalton transactions* 43.11 (2014), pp. 4197–4208.
- [77] L. Nemeth and S. R. Bare. “Science and technology of framework metal-containing zeotype catalysts”. In: *Advances in Catalysis*. Vol. 57. Elsevier, 2014, pp. 1–97.
- [78] M. Jiménez-Reyes, P. Almazán-Sánchez, and M. Solache-Ríos. “Radioactive waste treatments by using zeolites. A short review”. In: *Journal of environmental radioactivity* 233 (2021), p. 106610.
- [79] Y. T. Tran, J. Lee, P. Kumar, K.-H. Kim, and S. S. Lee. “Natural zeolite and its application in concrete composite production”. In: *Composites Part B: Engineering* 165 (2019), pp. 354–364.
- [80] D. E. Resasco, S. P. Crossley, B. Wang, and J. L. White. “Interaction of water with zeolites: a review”. In: *Catalysis Reviews* 63.2 (2021), pp. 302–362.
- [81] J. A. Ippolito, D. D. Tarkalson, and G. A. Lehrsch. “Zeolite soil application method affects inorganic nitrogen, moisture, and corn growth”. In: *Soil science* 176.3 (2011), pp. 136–142.
- [82] A. Amedlous, C. Hélaine, R. Guillet-Nicolas, O. Lebedev, S. Valable, and S. Mintova. “Gadolinium-loaded LTL nanosized zeolite for efficient oxygen delivery and magnetic resonance imaging”. In: *Inorganic Chemistry Frontiers* 10.9 (2023), pp. 2665–2676.
- [83] S. R. Balestra, S. Hamad, A. R. Ruiz-Salvador, V. Domínguez- García, P. J. Merkling, D. Dubbeldam, and S. Calero. “Understanding nanopore window distortions in the reversible molecular valve zeolite RHO”. In: *Chemistry of Materials* 27.16 (2015), pp. 5657–5667.
- [84] H. Xiong, Z. Liu, X. Chen, H. Wang, W. Qian, C. Zhang, A. Zheng, and F. Wei. “In situ imaging of the sorption-induced subcell topological flexibility of a rigid zeolite framework”. In: *Science* 376.6592 (2022), pp. 491–496.
- [85] V. Kapko, C. Dawson, M. Treacy, and M. Thorpe. “Flexibility of ideal zeolite frameworks”. In: *Physical Chemistry Chemical Physics* 12.30 (2010), pp. 8531–8541.
- [86] B. Ilić and S. G. Wettstein. “A review of adsorbate and temperature-induced zeolite framework flexibility”. In: *Microporous and Mesoporous Materials* 239 (2017), pp. 221–234.

- [87] W. H. Baur and R. X. Fischer. "The floppiness of it all: bond lengths change with atomic displacement parameters and the flexibility of various coordination tetrahedra in zeolitic frameworks. An empirical structural study of bond lengths and angles". In: *Chemistry of Materials* 31.7 (2019), pp. 2401–2420.
- [88] W. Loewenstein. "The distribution of aluminum in the tetrahedra of silicates and aluminates". In: *American Mineralogist: Journal of Earth and Planetary Materials* 39.1-2 (1954), pp. 92–96.
- [89] C. A. Fyfe, J. M. Thomas, J. Klinowski, and G. C. Gobbi. "Magic-Angle-Spinning NMR (MAS-NMR) Spectroscopy and the Structure of Zeolites". In: *Angewandte Chemie International Edition in English* 22.4 (1983), pp. 259–275.
- [90] J. Dědeček, D. Kaucký, B. Wichterlová, and O. Gonsiorová. " $\text{Co}^{2+}$  ions as probes of Al distribution in the framework of zeolites. ZSM-5 study". In: *Physical Chemistry Chemical Physics* 4.21 (2002), pp. 5406–5413.
- [91] V. Gábová, J. Dědeček, and J. Čejka. "Control of Al distribution in ZSM-5 by conditions of zeolite synthesis". In: *Chemical communications* 10 (2003), pp. 1196–1197.
- [92] F. I. Pambudi and N. Prasetyo. "Insight into the structure of the heulandite-type zeolite containing aromatic compounds using periodic density functional theory". In: *Materials Today Communications* 26 (2021), p. 102028.
- [93] E. Dempsey, G. Kühl, and D. H. Olson. "Variation of the lattice parameter with aluminum content in synthetic sodium faujasites. Evidence for ordering of the framework ions". In: *The Journal of Physical Chemistry* 73.2 (1969), pp. 387–390.
- [94] S. J. Kwak, H. S. Kim, N. Park, M.-J. Park, and W. B. Lee. "Recent progress on Al distribution over zeolite frameworks: Linking theories and experiments". In: *Korean Journal of Chemical Engineering* 38.6 (2021), pp. 1117–1128.
- [95] N. Wang, M. Zhang, and Y. Yu. "Distribution of aluminum and its influence on the acid strength of Y zeolite". In: *Microporous and mesoporous materials* 169 (2013), pp. 47–53.
- [96] M. Jeffroy. "Simulation moléculaire des propriétés des zéolithes cationiques : Propriétés thermodynamiques et propriétés structurales". PhD thesis. Université Paris-Sud 11, 2010.
- [97] E. García-Pérez, D. Dubbeldam, B. Liu, B. Smit, and S. Calero. "A computational method to characterize framework aluminum in aluminosilicates". In: *Angewandte Chemie* 119.1-2 (2007), pp. 280–282.
- [98] B. Liu, E. García-Pérez, D. Dubbeldam, B. Smit, and S. Calero. "Understanding aluminum location and non-framework ions effects on alkane adsorption in aluminosilicates: A molecular simulation study". In: *The Journal of Physical Chemistry C* 111.28 (2007), pp. 10419–10426.
- [99] J. M. Findley, P. I. Ravikovitch, and D. S. Sholl. "The effect of aluminum short-range ordering on carbon dioxide adsorption in zeolites". In: *The Journal of Physical Chemistry C* 122.23 (2018), pp. 12332–12340.
- [100] M. Erdős, D. F. Geerdink, A. Martin-Calvo, E. A. Pidko, L. J. Van Den Broeke, S. Calero, T. J. Vlugt, and O. A. Moulton. "In silico screening of zeolites for high-pressure hydrogen drying". In: *ACS applied materials & interfaces* 13.7 (2021), pp. 8383–8394.
- [101] H. Fang, A. S. Daou, S. E. Boulfelfel, J. M. Findley, P. I. Ravikovitch, and D. S. Sholl. "Computational Screening of Cationic Zeolites for n-Butane/Methane Separations Us-

## BIBLIOGRAPHY

- ing Quantitatively Accurate First-Principles-Derived Force Fields”. In: *The Journal of Physical Chemistry C* 127.49 (2023), pp. 23941–23955.
- [102] A. S. Daou, H. Fang, S. E. Boulfelfel, P. I. Ravikovitch, and D. S. Sholl. “Machine Learning and IAST-Aided High-Throughput Screening of Cationic and Silica Zeolites for Alkane Capture, Storage, and Separations”. In: *The Journal of Physical Chemistry C* 128.14 (2024), pp. 6089–6105.
- [103] P. Nachtigall, M. R. Delgado, D. Nachtigallova, and C. O. Areán. “The nature of cationic adsorption sites in alkaline zeolites—single, dual and multiple cation sites”. In: *Physical Chemistry Chemical Physics* 14.5 (2012), pp. 1552–1569.
- [104] D. Frenkel and B. Smit. “Chapter 3 - Monte Carlo Simulations”. In: *Understanding Molecular Simulation (Second Edition)*. Ed. by D. Frenkel and B. Smit. Second Edition. San Diego: Academic Press, 2002, pp. 23–61. ISBN: 978-0-12-267351-1. doi: <https://doi.org/10.1016/B978-012267351-1/50005-5>.
- [105] S. E. Boulfelfel, J. M. Findley, H. Fang, A. S. Daou, P. I. Ravikovitch, and D. S. Sholl. “A Transferable Force Field for Predicting Adsorption and Diffusion of Small Molecules in Alkali Metal Exchanged Zeolites with Coupled Cluster Accuracy”. In: *The Journal of Physical Chemistry C* 125.48 (2021), pp. 26832–26846.
- [106] H. Fang, A. Kulkarni, P. Kamakoti, R. Awati, P. I. Ravikovitch, and D. S. Sholl. “Identification of high-CO<sub>2</sub>-capacity cationic zeolites by accurate computational screening”. In: *Chemistry of Materials* 28.11 (2016), pp. 3887–3896.
- [107] S. Buttefey, A. Boutin, C. Mellot-Draznieks, and A. H. Fuchs. “A simple model for predicting the Na<sup>+</sup> distribution in anhydrous NaY and NaX zeolites”. In: *The Journal of Physical Chemistry B* 105.39 (2001), pp. 9569–9575.
- [108] C. Beauvais. “Effet de l'eau sur les propriétés d'adsorption d'un solide nanoporeux : Étude par simulation moléculaire de la zéolithe faujasite”. PhD thesis. Université Paris-Sud 11, 2004.
- [109] G. Maurin, P. Llewellyn, and R. Bell. “Adsorption mechanism of carbon dioxide in faujasites: grand canonical Monte Carlo simulations and microcalorimetry measurements”. In: *The Journal of Physical Chemistry B* 109.33 (2005), pp. 16084–16091.
- [110] C. Abrioux, B. Coasne, G. Maurin, F. Henn, A. Boutin, A. Di Lella, C. Nieto-Draghi, and A. Fuchs. “A molecular simulation study of the distribution of cation in zeolites”. In: *Adsorption* 14 (2008), pp. 743–754.
- [111] A. Di Lella, N. Desbiens, A. Boutin, I. Demachy, P. Ungerer, J.-P. Bellat, and A. H. Fuchs. “Molecular simulation studies of water physisorption in zeolites”. In: *Physical Chemistry Chemical Physics* 8.46 (2006), pp. 5396–5406.
- [112] J. Hunger, I. A. Beta, H. Böhlig, C. Ling, H. Jobic, and B. Hunger. “Adsorption structures of water in NaX studied by DRIFT spectroscopy and neutron powder diffraction”. In: *The Journal of Physical Chemistry B* 110.1 (2006), pp. 342–353.
- [113] D. Dubbeldam, S. Calero, D. E. Ellis, and R. Q. Snurr. “RASPA: molecular simulation software for adsorption and diffusion in flexible nanoporous materials”. In: *Molecular Simulation* 42.2 (2016), pp. 81–101.
- [114] L. Martínez. “CellListMap.jl: Efficient and customizable cell list implementation for calculation of pairwise particle properties within a cutoff”. In: *Computer Physics Communications* 279 (2022), p. 108452.

- [115] F. Lekien and J. Marsden. “Tricubic interpolation in three dimensions”. In: *International Journal for Numerical Methods in Engineering* 63.3 (2005), pp. 455–471.
- [116] S. P. Bates, W. J. van Well, R. A. van Santen, and B. Smit. “Energetics of n-alkanes in zeolites: a configurational-bias Monte Carlo investigation into pore size dependence”. In: *Journal of the American Chemical Society* 118.28 (1996), pp. 6753–6759.
- [117] A. Laio and M. Parrinello. “Escaping free-energy minima”. In: *Proceedings of the national academy of sciences* 99.20 (2002), pp. 12562–12566.
- [118] T. Marqueño, D. Santamaría-Perez, J. Ruiz-Fuertes, R. Chuliá-Jordán, J. L. Jordá, F. Rey, C. McGuire, A. Kavner, S. MacLeod, D. Daisenberger, C. Popescu, P. Rodriguez-Hernandez, and A. Muñoz. “An Ultrahigh CO<sub>2</sub>-Loaded Silicalite-1 Zeolite: Structural Stability and Physical Properties at High Pressures and Temperatures”. In: *Inorganic Chemistry* 57.11 (2018). PMID: 29737842, pp. 6447–6455. doi: [10.1021/acs.inorgchem.8b00523](https://doi.org/10.1021/acs.inorgchem.8b00523).
- [119] D.-Y. Peng and D. B. Robinson. “A new two-constant equation of state”. In: *Industrial & Engineering Chemistry Fundamentals* 15.1 (1976), pp. 59–64.
- [120] O. Kunz and W. Wagner. “The GERG-2008 wide-range equation of state for natural gases and other mixtures: an expansion of GERG-2004”. In: *Journal of chemical & engineering data* 57.11 (2012), pp. 3032–3091.
- [121] P. J. Walker, H.-W. Yew, and A. Riedemann. “Clapeyron.jl: an extensible, open-source fluid thermodynamics toolkit”. In: *Industrial & Engineering Chemistry Research* 61.20 (2022), pp. 7130–7153.
- [122] K. M. Jablonka, D. Ongari, and B. Smit. “Applicability of tail corrections in the molecular simulations of porous materials”. In: *Journal of chemical theory and computation* 15.10 (2019), pp. 5635–5641.
- [123] S. H. Mousavi, K. Chen, J. Yao, A. Zavabeti, J. Z. Liu, and G. K. Li. “Screening of alkali metal-exchanged zeolites for nitrogen/methane separation”. In: *Langmuir* 39.3 (2023), pp. 1277–1287.
- [124] L.-C. Lin, A. H. Berger, R. L. Martin, J. Kim, J. A. Swisher, K. Jariwala, C. H. Rycroft, A. S. Bhowm, M. W. Deem, M. Haranczyk, et al. “In silico screening of carbon-capture materials”. In: *Nature materials* 11.7 (2012), pp. 633–641.
- [125] S. Brandani, E. Mangano, and L. Sarkisov. “Net, excess and absolute adsorption and adsorption of helium”. In: *Adsorption* 22 (2016), pp. 261–276.
- [126] J. Rouquerol, F. Rouquerol, P. Llewellyn, G. Maurin, and K. Sing. *Adsorption by powders and porous solids: principles, methodology and applications*. Academic press, 2013.
- [127] K. Sing, D. Everett, R. Haul, L. Moscou, R. Pierotti, J. Rouquerol, and T. Siemieniewska. “International union of pure and applied chemistry physical chemistry division commission on colloid and surface chemistry including catalysis. vol. 57, issue 4”. In: *Pure Appl Chem* (1985), pp. 603–619.
- [128] N. Ayawei, A. N. Ebelegi, and D. Wankasi. “Modelling and interpretation of adsorption isotherms”. In: *Journal of chemistry* 2017.1 (2017), p. 3039817.
- [129] P. Iacomi and P. L. Llewellyn. “pyGAPS: a Python-based framework for adsorption isotherm processing and material characterisation”. In: *Adsorption* 25.8 (2019), pp. 1533–1542.





## RÉSUMÉ

---

La séparation et purification des gaz est un enjeu industriel majeur, qui nécessite l'emploi d'adsorbants spécifiques à certaines espèces moléculaires. Afin d'accélérer le développement de nouveaux adsorbants d'intérêt, il peut être utile d'avoir recours à des méthodes de simulations numériques permettant d'identifier des candidats potentiels.

Ces méthodes restent cependant coûteuses en temps et en énergie. Pour tenter d'améliorer leurs performances, cette thèse propose et explore plusieurs avancées méthodologiques sur les différentes étapes de la simulation. En particulier, de nouveaux algorithmes et outils sont présentés pour l'identification de la topologie des matériaux cristallins, pour localiser les cations dans les charpentes zéolitiques, et pour déterminer la capacité d'adsorption d'un gaz dans un matériau poreux. Les résultats de simulation alimentent une base de donnée qui est aussi exploitée pour proposer une prédition approximative mais ultra-rapide d'isothermes d'adsorption, ouvrant la voie à des stratégies de criblage de matériaux nanoporeux à haute performance.

## MOTS CLÉS

---

simulation moléculaire, matériaux nanoporeux, adsorption, topologie cristalline, zéolites

## ABSTRACT

---

Gas separation and purification is a crucial industrial issue, which is technologically addressed by fine-tuning the gas specificity of adsorbents. However, the experimental development of new adsorbents is a costly process, hence the need for preliminary computer simulations to test only the most promising candidates.

These simulation techniques remain costly in themselves. In order to improve their performance, this thesis proposes and explores new methodological options across the different steps of the simulation. In particular, new algorithms and tools are presented to tackle the identification of the topology of crystalline materials, the location of cations in zeolitic frameworks, and the adsorption capacity of a gas in porous materials. The simulation results are then used to feed a database, which allows using a statistical approach to provide coarse but ultra-fast predictions of adsorption isotherms, paving the way for high-performance screening strategies of nanoporous materials.

## KEYWORDS

---

molecular simulation, nanoporous materials, adsorption, crystal topology, zeolites